

**INVESTIGATION OF GAS – SOLID CIRCULATING  
FLUIDIZED BED AT TWO SCALES USING EXPERIMENTAL  
AND NUMERICAL TECHNIQUES**

*A thesis  
submitted in partial fulfillment of the  
requirements for the degree of*

**DOCTOR OF PHILOSOPHY**

*by*

**PREMKUMAR K  
(126107013)**



**DEPARTMENT OF CHEMICAL ENGINEERING  
INDIAN INSTITUTE OF TECHNOLOGY GUWAHATI  
GUWAHATI-781039  
DECEMBER 2016**

# CERTIFICATE

---

It is certified that the work contained in the thesis entitled **Investigation of Gas – Solid Circulating Fluidized Bed at Two Scales Using Experimental and Numerical Techniques** by **Premkumar K**, a student in the Department of Chemical Engineering, Indian Institute of Technology Guwahati, Guwahati, India, for the award of the degree of **Doctor of Philosophy** has been carried out under my supervision and this work has not been submitted elsewhere for the degree.

**Dr. Rajesh Kumar Upadhyay**

Assistant Professor

Department of Chemical Engineering  
Indian Institute of Technology Guwahati

Guwahati – 781039, Assam, India.

## ACKNOWLEDGEMENTS

I wish to express my heartily indebtedness and deep sense of gratitude to my supervisor, Dr. Rajesh Kumar Upadhyay, Department of Chemical Engineering, Indian Institute of Technology Guwahati, India for his inspiring guidance, suggestions throughout the course of this work. His keen interest and experience helped this research work always on a smooth and steady path. His management skills always inspired me, in particular, his patience on handling the difficult situations and an ignorant student like me.

I am grateful to my doctoral committee members Prof. Pinakeswar Mahanta, Dr. S.K.Majumder, Dr. Nanda Kishore and Dr. Vinayak Kulkarani who gave critical comments on the research findings. Particularly, Dr.S.K.Majumder comments provided critical insights on residence time distribution studies.

I am thankful to present and previous Head of Department of Chemical Engineering, Prof. Bishnupada Mandal and Prof. V.S.Moholkar for providing me the necessary facilities in the department during my research work. Also, I would like to thank all the faculty members of Chemical Engineering Department, in particular Prof. Anugrah Singh, Prof. Sasidhar Gumma, Dr. Raghavendra Gupta and Dr. Pankaj Tiwari for thought provoking discussions and support.

I am thankful to Dr. S. Senthivelan, Department of Mechanical Engineering, IIT Guwahati for providing motor to conduct the test runs.

I express my sincere thanks to Dr. H. J. Pant, Isotope Applications Division for helping me on radioactive particle tracer handling and fruitful discussion on applications of RTD in day to day life.

Progress made by a researcher is a combined effort of all the past works put together. I am aware of the fact that I cannot mention the endless list of past contributors. I feel I

should express my gratitude to all the researchers who developed all the tools for this thesis.

Discussion with Prof. Shantanu Roy, Department of Chemical Engineering, Indian Institute of Technology Delhi, on solid flux provided significant insights on measurements in CFB. Discussion with Prof. Muthanna Al- Dahhan, Department of Chemical and Biochemical Engineering, Missouri University of Science and Technology, USA on calibration in RPT and development of new methods for calibration, inspired me to have new direction for research in RPT.

Several people have made significant contributions in making my work and life at IIT Guwahati a memorable experience. In particular, I would like to express my gratitude to Lipika Kalo for her encouragement, extensive discussion and constant help. She taught me the method of preparation of radioactive particle, preparation of experimental setups for RPT experiments and in fact, without her support none of my experiments would not be possible. I am greatly indebted to all my colleagues and friends beyond words, the list is infinite but to name a few, Trilok Tribedi, Rajani kant Boro, Jitendra, Dr. Shilpi, Roopesh, Soorya, Karan, Sonit, Premsagar, Kuldeep, Shyam, Sandeep, Tarang, Dr. Johnney and Vivek. They have been always there for me with their suggestions, moral support and hand of help for everything I needed. Trilok Tribedi's out of box thinking always gave excellent outputs. Rajani kant boro taught me work and life balance. Moral support by Richa Sharma was unparalleled, during the whole duration of Ph.D.

It is my friends from undergraduate days, D.V.Kaushika, Dr. G. Keerthiga and M. Vivekanadan who are always there for me, sometimes painstakingly find the ways to support me even though it is physically impossible for them to do so.

My parent's unconditional love and support always motivates me to go one step further.

Without my sister's financial support I would not been here.

I would like to thank BRNS (Board of Research in Nuclear Sciences) to fund this project and MHRD (Ministry of Human Resource and Development) for providing the assistantship during Ph.D.

Finally, I would like to thank all those who have helped me during the research work.

Premkumar K  
IIT Guwahati



# TABLE OF CONTENTS

|   |     |
|---|-----|
| <b>ABSTRACT</b>   | i   |
| <b>TABLE OF CONTENTS</b>  | ii  |
| <b>LIST OF FIGURES</b>  | vii |
| <b>LIST OF TABLES</b>   | xvi |
| <b>1. INTRODUCTION</b>  | 1   |
| 1.1 Introduction  | 1   |
| 1.2 Circulating fluidized Bed   | 6   |
| 1.3 Hydrodynamics of circulating fluidized bed  | 10  |
| 1.3.1 Macro-scale hydrodynamics   | 11  |
| 1.3.2 Meso-scale hydrodynamics  | 14  |
| 1.4 Scale up of circulating fluidizing bed (CFB)  | 16  |
| 1.5 Motivation  | 17  |
| 1.6 Objectives  | 19  |
| 1.7 Structure of the thesis   | 20  |
| Notations   | 21  |
| References  | 22  |
| <b>2. RADIOACTIVE PARTICLE TRACKING (RPT) AND BENCHMARKING FOR HIGH VELOCITY CONDITIONS</b> | 31  |
| 2.1 Introduction  | 31  |
| 2.2 Radioactive particle tracking technique   | 42  |
| 2.2.1 Methodology   | 42  |
| 2.2.2 Implementation of RPT   | 45  |
| 2.2.3 Calibration   | 49  |

|           |   |           |
|-----------|---|-----------|
| 2.2.4     | Reconstruction algorithm  | 54        |
| 2.2.5     | Optimal design of RPT experiments   | 56        |
| 2.3       | Implementation of RPT technique for high velocity system                        | 58        |
| 2.3.1     | Experimental setup  | 63        |
| 2.3.2     | Resolution and sensitivity  | 64        |
| 2.3.3     | Results and discussions   | 65        |
| 2.3.4     | Conclusions   | 74        |
| 2.4       | Summary   | 76        |
|           | Notations   | 77        |
|           | References  | 79        |
| <b>3.</b> | <b>EXPERIMENTAL INVESTIGATION OF LABORATORY SCALE CIRCULATING FLUIDIZED BED</b> | <b>85</b> |
| 3.1       | Introduction  | 85        |
| 3.2       | Literature on velocity studies in CFB   | 86        |
| 3.3       | Experimental setup  | 93        |
| 3.4       | Solid flux measurement  | 96        |
| 3.4.1     | Velocity and volume fraction measurement methods                                | 97        |
| 3.5       | Radioactive particle tracking (RPT) measurements                                | 105       |
| 3.6       | Results and discussions   | 110       |
| 3.6.1     | Visual observation of riser   | 111       |
| 3.6.2     | Lagrangian track of particle position   | 113       |
| 3.6.3     | Lagrangian velocity of the solids   | 115       |
| 3.6.4     | PDF of instantaneous velocity   | 119       |
| 3.6.5     | Velocity vector plots   | 120       |
| 3.6.6     | Number of occurrences   | 123       |

|           |  |            |
|-----------|--|------------|
| 3.6.7     | Ensemble averaged velocity   | 124        |
| 3.6.8     | Solid velocity fluctuations  | 126        |
| 3.6.9     | Turbulent kinetic energy   | 130        |
| 3.7       | Effect of superficial gas velocity   | 132        |
| 3.8       | Effect of solid flux   | 142        |
| 3.9       | Solid mixing studies   | 147        |
| 3.9.1     | Residence time distribution  | 147        |
| 3.9.2     | Trajectory length distribution (TLD)   | 162        |
| 3.9.3     | Local solids mixing  | 164        |
| 3.10      | Summary  | 166        |
|           | Notations  | 169        |
|           | References   | 170        |
| <b>4.</b> | <b>EXPERIMENTAL INVESTIGATION OF PILOT SCALE<br/>CIRCULATING FLUIDIZED BED</b> | <b>179</b> |
| 4.1       | Introduction   | 179        |
| 4.2       | Present state of the art of scale study  | 181        |
| 4.3       | Experimental setup   | 183        |
| 4.4       | Solid motion using radioactive particle tracking (RPT)<br>technique            | 185        |
| 4.4.1     | Instantaneous position   | 188        |
| 4.4.2     | PDF of instantaneous velocity  | 191        |
| 4.4.3     | Velocity vector plots  | 194        |
| 4.4.4     | Contour of occurrences   | 195        |
| 4.4.5     | Ensemble averaged velocity   | 196        |
| 4.4.6     | Solid velocity fluctuations  | 198        |

|           |   |            |
|-----------|---|------------|
| 4.4.7     | Turbulent kinetic energy                                      | 201        |
| 4.4.8     | Effect of scale   | 203        |
| 4.5       | Hydrodynamic similarity                                       | 204        |
| 4.5.1     | Development of the empirical equation for mean solid velocity | 208        |
| 4.6       | Solid mixing studies  | 211        |
| 4.6.1     | Residence time distribution                                   | 211        |
| 4.6.2     | Trajectory length distribution (TLD)                          | 217        |
| 4.6.3     | Local solids mixing   | 218        |
| 4.7       | Summary   | 219        |
|           | Notations   | 221        |
|           | References  | 222        |
| <b>5.</b> | <b>NUMERICAL INVESTIGATION OF CIRCULATING FLUIDIZED BED</b>   | <b>227</b> |
| 5.1       | Introduction  | 227        |
| 5.2       | Literature on Euler – Euler modelling of gas solid riser      | 229        |
| 5.3       | Euler – Euler modelling approach                              | 234        |
| 5.3.1     | Conservation equations  | 235        |
| 5.3.2     | Solid phase fluctuations                                      | 237        |
| 5.3.3     | Drag closure  | 241        |
| 5.3.4     | Gas phase turbulence  | 242        |
| 5.4       | Base case formulation   | 245        |
| 5.5       | Effect of superficial gas velocity                            | 258        |
| 5.6       | Effect of solid flux  | 260        |
| 5.7       | Pilot scale setup   | 261        |

|   |            |
|---|------------|
| 5.8 Summary                               | 264        |
| Notations                                 | 266        |
| References                                | 268        |
| <b>6. CONCLUSIONS AND RECOMMENDATIONS</b> | <b>275</b> |
| 6.1 Conclusions                           | 275        |
| 6.2 Recommendations and future directions | 278        |
| References                                | 280        |



## List of Figures

| <b>Figure No.</b> | <b>Figure Title</b>  | <b>Page No.</b> |
|-------------------|--|-----------------|
| 1.1               | Flow patterns in gas solids fluidized beds (adapted from Grace, 1997)                          | 2               |
| 1.2               | Geldart classification of particles for air at ambient conditions (adapted from Geldart, 1973) | 4               |
| 1.3               | Flow regime diagram for gas - solids (adapted from Bi and Grace, 1995)                         | 5               |
| 1.4               | Schematic diagram of Circulating Fluidized bed   | 7               |
| 2.1               | Five fiber optical probe (adapted from Zhu et al. (2001))                                      | 33              |
| 2.2               | Schematic of LDA (Courtesy Dantec Dynamics)  | 35              |
| 2.3               | Schematic of PIV measurement principle   | 37              |
| 2.4               | Schematic of PEPT measurement principle  | 38              |
| 2.5               | Photograph of RPT setup  | 40              |
| 2.6               | Flow chart for RPT data acquisition and processing   | 45              |
| 2.7               | Schematic diagram of data acquisition system   | 47              |
| 2.8               | Schematic diagram of NaI(Tl) detector  | 48              |
| 2.9               | Energy spectra of Scandium - 46  | 49              |
| 2.10              | Schematic diagram for relative positioning of source and detector                              | 52              |

|       |  |    |
|-------|--|----|
| 2.11  | Four possible cases in which photon can travel through a cylindrical detector  | 53 |
| 2.12  | Representation of dynamic bias   | 59 |
| 2.13  | Photograph and schematic of experimental setup   | 64 |
| 2.14  | Resolution and sensitivity of the accuracy experiment  | 65 |
| 2.15  | Stationary bias  | 67 |
| 2.16a | PDF of error in displacement at different acquisition frequency for tracer particle velocity of 0.85 m/s                                 | 69 |
| 2.16b | PDF of instantaneous velocity at different acquisition frequency for tracer particle velocity of 0.85 m/s                                | 70 |
| 2.17a | PDF of error in displacement at different acquisition frequency for tracer particle velocity of 2.686 m/s                                | 71 |
| 2.17b | PDF of instantaneous velocity at different acquisition frequency for tracer particle velocity of 2.686 m/s                               | 71 |
| 2.18a | PDF of error in displacement at different acquisition frequency for tracer particle velocity of 4.852 m/s                                | 72 |
| 2.18b | PDF of instantaneous velocity at different acquisition frequency for tracer particle velocity of 4.852 m/s                               | 72 |
| 2.19a | PDF of error in displacement at different acquisition frequency for tracer particle velocity of 8.203 m/s                                | 73 |
| 2.19b | PDF of instantaneous velocity at different acquisition frequency for tracer particle velocity of 8.203 m/s.                              | 74 |
| 2.20  | Comparison of standard deviation in displacement and velocity prediction for different value of tracer velocity at different frequencies | 74 |

|      |  |     |
|------|--|-----|
| 3.1  | Photograph of laboratory scale experimental setup  | 94  |
| 3.2  | Schematic of laboratory scale experimental setup   | 95  |
| 3.3  | Photograph showing the detector position for RTD measurements (Lead sheets are removed for the sake of clarity)                                    | 99  |
| 3.4  | Count – time series for a single circulation   | 99  |
| 3.5  | Schematic diagram of densitometry setup  | 101 |
| 3.6a | Variation of solid flux with solid inventory   | 102 |
| 3.6b | Variation of superficial gas velocity with solid inventory for solid flux of 110 kg/m <sup>2</sup> s   | 103 |
| 3.7  | Photograph of RPT test facility for laboratory scale CFB   | 109 |
| 3.8  | Contours of resolution and sensitivity for RPT experiments   | 110 |
| 3.9  | Photographs of metastable structures (a) $U_g - 7$ m/s and $G_s - 110$ kg/m <sup>2</sup> s (b) $U_g - 8.8$ m/s and $G_s - 144$ kg/m <sup>2</sup> s | 112 |
| 3.10 | Typical position map of a single trajectory in different planes ( $U_g - 8.8$ m/s, $G_s - 110$ kg/m <sup>2</sup> s)                                | 114 |
| 3.11 | Axial Lagrangian velocity of solids for a single trajectory ( $U_g - 8.8$ m/s and $G_s - 110$ kg/m <sup>2</sup> s)                                 | 116 |
| 3.12 | Effect of grid on mean axial velocity at h - 1.65 m. ( $U_g - 8.8$ m/s, $G_s - 110$ kg/m <sup>2</sup> s)   | 117 |
| 3.13 | Validation of stationarity (a) Axial mean velocity (b) Axial RMS velocity at h = 1.5 m ( $U_g - 8.8$ m/s, $G_s - 110$ kg/m <sup>2</sup> s)         | 118 |
| 3.14 | PDF of axial instantaneous velocities for the operating condition of $U_g - 8.8$ m/s and $G_s - 110$ kg/m <sup>2</sup> s at theta plane = 0°       | 121 |

|      |  |     |
|------|--|-----|
| 3.15 | PDF of radial instantaneous velocities for the operating condition of $U_g = 8.8$ m/s and $G_s = 110$ Kg/m <sup>2</sup> s at theta plane = 0° at height of H = 1.5 m | 121 |
| 3.16 | Vector plot at different planes for the operating condition of $U_g = 8.8$ m/s and $G_s = 110$ kg/m <sup>2</sup> s   | 122 |
| 3.17 | Contour map showing the azimuthal averaged occurrence for the operating condition of $U_g = 8.8$ m/s and $G_s = 110$ kg/m <sup>2</sup> s                             | 123 |
| 3.18 | Azimuthally averaged mean axial velocities at different heights for operating condition of $U_g = 8.8$ m/s and $G_s = 110$ kg/m <sup>2</sup> s                       | 125 |
| 3.19 | Azimuthally averaged RMS velocities at different heights for operating condition of $U_g = 8.8$ m/s and $G_s = 110$ kg/m <sup>2</sup> s                              | 129 |
| 3.20 | Azimuthally averaged Reynolds stress at different heights for operating condition of $U_g = 8.8$ m/s and $G_s = 110$ kg/m <sup>2</sup> s                             | 130 |
| 3.21 | Azimuthally averaged Turbulent kinetic energy at different heights for operating condition of $U_g = 8.8$ m/s and $G_s = 110$ kg/m <sup>2</sup> s                    | 131 |
| 3.22 | PDF of axial instantaneous velocity of solids for different gas velocity at the flux of 110 kg/m <sup>2</sup> s  | 134 |
| 3.23 | Azimuthally and axially averaged mean velocities for different gas velocity for the flux of 110 kg/m <sup>2</sup> s  | 136 |
| 3.24 | Azimuthally and axially averaged RMS velocities for different gas velocity for the flux of 110 kg/m <sup>2</sup> s   | 138 |
| 3.25 | Azimuthally and axially averaged turbulent stresses for different gas velocity for the flux of 110 kg/m <sup>2</sup> s   | 139 |

|      |  |     |
|------|--|-----|
| 3.26 | Azimuthally and axially averaged turbulent kinetic energy for different gas velocity for the solid flux of 110 kg/m <sup>2</sup> s | 140 |
| 3.27 | PDF of instantaneous velocity of different operating conditions  | 141 |
| 3.28 | Azimuthally and axially averaged mean velocities for different operating conditions  | 143 |
| 3.29 | Azimuthally and axially averaged RMS velocities for different operating conditions   | 145 |
| 3.30 | Azimuthally and axially averaged turbulent stresses for different operating conditions   | 146 |
| 3.31 | Azimuthally and axially averaged turbulent kinetic energy for different operating conditions                                       | 147 |
| 3.32 | Schematic of experimental setup showing different sections of RTD measurements   | 152 |
| 3.33 | Schematic explaining the equivalence of E – Curve from the single particle tracking and conventional tracer techniques             | 153 |
| 3.34 | Residence time distribution for the bottom region  | 158 |
| 3.35 | Residence time distribution for the middle (RPT) region  | 159 |
| 3.36 | Residence time distribution for the top region   | 160 |
| 3.37 | Residence time distribution for the entire riser   | 161 |
| 3.38 | Trajectory time distribution for the middle region (RPT measurement section) for the length of L = 48 cm                           | 163 |
| 3.39 | Axially and azimuthally averaged axial solids diffusivity  | 166 |
| 4.1  | Photograph and schematic of pilot scale experimental setup   | 184 |
| 4.2  | Photograph detailing the detector arrangement in the investigation zone  | 185 |

|      |  |     |
|------|--|-----|
| 4.3  | Contours of resolution and sensitivity for RPT experiments used in current work  | 186 |
| 4.4  | Typical position map of single trajectory in different planes ( $U_g - 9.6$ m/s, $G_s - 110$ kg/m <sup>2</sup> s)                                  | 189 |
| 4.5  | Effect of grid on mean axial velocity at $h - 3.75$ m. ( $U_g - 9.6$ m/s, $G_s - 110$ kg/m <sup>2</sup> s)   | 190 |
| 4.6  | Validation of stationarity (a) Axial mean velocity (b) Axial RMS velocity at $h = 3.75$ m ( $U_g - 9.6$ m/s, $G_s - 110$ kg/m <sup>2</sup> s)      | 191 |
| 4.7  | PDF of axial instantaneous velocity of solids for the operating condition of $U_g - 9.6$ m/s and $G_s - 110$ kg/m <sup>2</sup> s                   | 193 |
| 4.8  | Vector plot at different planes for the operating condition of $U_g - 9.6$ m/s and $G_s - 110$ kg/m <sup>2</sup> s                                 | 194 |
| 4.9  | Contour map showing the normalized occurrence for the all operating conditions   | 196 |
| 4.10 | Azimuthally and axially averaged mean velocities   | 197 |
| 4.11 | Azimuthally and axially averaged RMS velocities  | 199 |
| 4.12 | Azimuthally and axially averaged turbulent stresses  | 201 |
| 4.13 | Azimuthally and axially averaged turbulent kinetic energy  | 202 |
| 4.14 | Azimuthally and axially averaged Mean axial velocity and Axial RMS velocity showing effect of scale  | 203 |
| 4.15 | Azimuthally and axially averaged Mean axial velocity and Axial RMS velocity at the laboratory scale setup having same $Fr_D^{-0.3} G_s / \rho U_g$ | 206 |

|      |  |     |
|------|--|-----|
| 4.16 | Azimuthally and axially averaged Mean axial velocity and Axial RMS velocity at the pilot scale setup having same $Fr_D^{-0.3}G_s/\rho U_g$                         | 207 |
| 4.17 | Azimuthally and axially averaged Mean axial velocity and Axial RMS velocity at laboratory and pilot scale setup having same $Fr_D^{-0.3}G_s/\rho U_g$              | 208 |
| 4.18 | Pox diagram for predicted Mean solid velocities from empirical correlation and measured solid velocity   | 211 |
| 4.19 | Schematic showing different RTD sections in pilot scale setup  | 213 |
| 4.20 | Residence time distribution for the section 1 (bottom)   | 215 |
| 4.21 | Residence time distribution for the section 2 (Intermediate)   | 215 |
| 4.22 | Residence time distribution for the section 3 (middle / RPT)   | 216 |
| 4.23 | Residence time distribution for the section 4 (Top)  | 216 |
| 4.24 | Residence time distribution for the overall column   | 217 |
| 4.25 | Trajectory time distribution for the RPT region for the length of $L = 53$ cm  | 218 |
| 4.26 | Axially and azimuthally averaged axial solids diffusivity  | 219 |
| 5.1  | Schematic of computational domain of laboratory and pilot scale setup  | 246 |
| 5.2  | Axial profile of mean axial velocity and mean volume fraction for different grids at the axis of the riser ( $U_g = 8.8$ m/s and $G_s = 144$ kg /m <sup>2</sup> s) | 249 |

|      |   |     |
|------|---|-----|
| 5.3  | Axial profile of mean axial velocity and mean volume fraction for different drag model at the axis of the riser ( $U_g = 8.8$ m/s and $G_s = 144$ kg /m <sup>2</sup> s)                   | 250 |
| 5.4  | Axial profile of mean axial velocity and mean volume fraction for different specularity coefficient at the axis of the riser ( $U_g = 8.8$ m/s and $G_s = 144$ kg /m <sup>2</sup> s)      | 253 |
| 5.5  | Axial profile of mean axial velocity and mean volume fraction for different restitution coefficient at the axis of the riser ( $U_g = 8.8$ m/s and $G_s = 144$ kg /m <sup>2</sup> s)      | 254 |
| 5.6  | Radial profile of mean axial velocity and mean volume fraction for different specularity coefficient at the height of $H = 1.5$ m ( $U_g = 8.8$ m/s and $G_s = 144$ kg /m <sup>2</sup> s) | 257 |
| 5.7  | Radial profile of mean axial velocity for different superficial gas velocity at the same flux of 110 kg/m <sup>2</sup> s at the height of $H = 1.5$ m                                     | 259 |
| 5.8  | Radial profile of mean granular temperature for different superficial gas velocity at the same flux of 110 kg/m <sup>2</sup> s at the height of $H = 1.5$ m                               | 259 |
| 5.9  | Radial profile of mean axial velocity for different solid flux at the same superficial gas velocity of 8.8 m/s at the height of $H = 1.5$ m   | 260 |
| 5.10 | Radial profile of mean granular temperature for different solid flux at the same superficial gas velocity of 8.8 m/s at the height of $H = 1.5$ m   | 261 |

|      |  |     |
|------|--|-----|
| 5.11 | Axial profile of the mean axial velocity and mean volume fraction for different grids at the axis of the riser                           | 262 |
| 5.12 | Radial profile of mean axial velocity for different operating conditions at the pilot plant scale setup at the height of $H = 4$ m       | 263 |
| 5.13 | Radial profile of mean granular temperature for different operating conditions at the pilot plant scale setup at the height of $H = 4$ m | 264 |



## List of Tables

| <b>Table No.</b> | <b>Title</b>  | <b>Page No.</b> |
|------------------|---|-----------------|
| 1.1              | Applications of CFB   | 9               |
| 1.2              | Operating Characteristics of FCC and CFBC   | 10              |
| 2.1              | Quantities calculated from RPT experimental data (Roy et al., 2005; Upadhyay, 2010) | 44              |
| 2.2              | Look up table showing calibration data  | 55              |
| 2.3              | Experimental conditions   | 64              |
| 2.4              | Standard error in position reconstruction for stationary tracer position            | 67              |
| 3.1              | Literature review of experimental work on solid velocities in CFB                   | 90              |
| 3.2              | Comparison of solid flux by two methods   | 104             |
| 3.3              | Operating conditions in laboratory scale experiment                                 | 111             |
| 3.4              | Axial dispersion number for the bottom region ( $\Delta L = 1.309$ m)               | 155             |
| 3.5              | Axial dispersion number for the RPT region ( $\Delta L = 0.5215$ m)                 | 155             |
| 3.6              | Axial dispersion number for the top region ( $\Delta L = 0.9985$ m)                 | 156             |
| 3.7              | Axial dispersion number for the overall column                                      | 156             |
| 4.1              | Operating conditions of pilot scale setup   | 187             |
| 4.2              | Experimental and solid particles used for empirical correlation                     | 209             |
| 4.3              | Residence time distribution and dispersion number at different sections             | 214             |

|     |  |     |
|-----|--|-----|
| 4.4 | Residence time distribution and dispersion number for the entire riser | 214 |
| 5.1 | Literature on Euler – Euler simulations using Geldart’s B particle     | 232 |
| 5.2 | Interphase momentum exchange coefficients                              | 241 |
| 5.3 | Simulation conditions and parameters                                   | 247 |



## ABSTRACT

Gas – solid Circulating fluidized bed (CFB) finds application in industrial process like cracking, combustion, gasification, drying, etc. The major reasons cited being operation flexibility, efficiency, short residence time, etc. Even though, CFB is in use for more than three decades, fundamental understanding is still insufficient. Design and scale up of CFB is still empirical and based on experience rather than science. This is mainly due to the complexity of gas – solid, solid – solid and solid-wall interactions. Multi-scale nature of these interactions, both in length and time scale, makes it more difficult to delineate the hydrodynamics. These interactions are also a function of geometry and scale, which makes scale-up of CFB more challenging. Numerical simulation is cost effective approach however, has been largely suffering from lack of experimental data. Further, most of the studies on scale effect are limited to the mean values. Very few studies are available on the fluctuations at different scales. Further no study is available on scale study using noninvasive techniques and also unbiased with scale.

In current study, solid velocity field and solid mixing are investigated using radiation based noninvasive technique, radioactive particle tracking (RPT). Studies are conducted at two different scales, laboratory and pilot plant scales. Eulerian and Lagrangian velocity field of solid is estimated for different gas inlet velocity and solid inlet flux. Further turbulent parameters like Reynolds stress, turbulent kinetic energy are estimated for all the conditions. Global mixing is studied using residence time distribution and Trajectory length distribution studies. Further, local mixing is estimated by solid diffusivity which is calculated by using the first principles. A new scaling law based on solid velocity is developed to predict the effect of operating conditions and scale. Finally, numerical simulations are conducted to augment the experiments and validated with the experimental data.

# Chapter 1

## Introduction

### Scope

In this chapter, introduction to gas - solid fluidization and circulating fluidization bed are presented. Hydrodynamics of circulating fluidized bed are briefed. Then, motivations for current work are presented. Objectives of current work are presented. The structure of the thesis has been presented at the last section of this chapter.

### 1.1 Introduction

Multiphase reactors are very common in chemical process industries. Around 90% of the industrial chemical reaction uses catalysis and most of them are multiphase in nature (Pangarkar, 2015). Often catalysts used are solids, because solids are easy to separate and can be reused. Gas-solid multiphase flow reactors are perhaps the most commonly used reactor in many industries like pharmaceuticals, petroleum refinery, power plants, mineral processing, metallurgical, etc. Efficiency of these reactors largely depends on the contacting pattern, which is more critical if high degree of conversion is required. Based on the contacting pattern, gas-solid multiphase flow reactors/contactors are divided in several regimes which are shown in Figure 1.1.

At low gas velocity, gas merely percolates through the void spaces without disturbing the bed of solids. This regime is called as fixed bed. With increase in gas velocity, drag force acting on the solids, balances the weight of the solids. At this point, solids in the bed start to move and bed expands. The superficial gas velocity at which bed completely fluidize is called minimum fluidization velocity,  $U_{mf}$ . In comparison with packed beds, fluidized beds

offer better contacting and provide better heat and mass transfer rates, due to increased surface area. Hence, fluidized beds are widely used for gas-solids contacting.

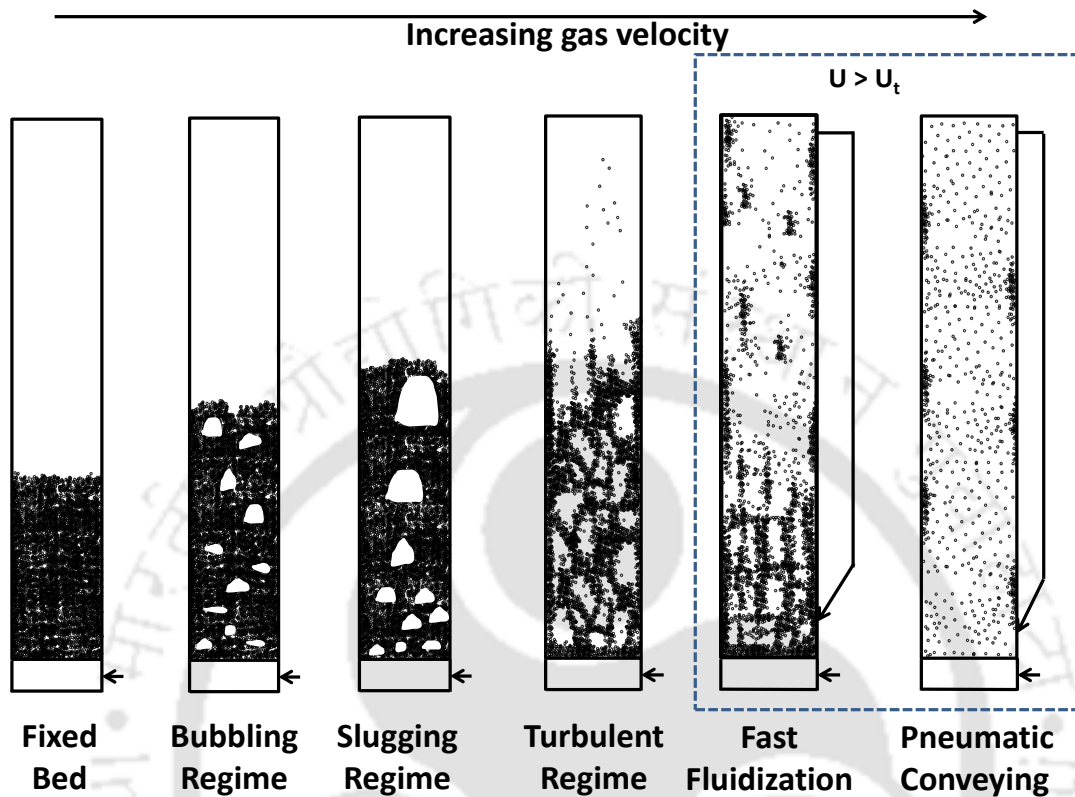


**Figure 1.1** Flow patterns in gas solids fluidized beds (adapted from Grace (1997))

Further increase in gas velocity, bed porosity increases and excess gas starts to form bubbles which significantly reduces the gas-solids contacting. This regime is called as bubbling fluidization. Onset of bubbling regime can be calculated from the equation 1.1, which is given by Geldart and Abrahamsen (1978).

$$U_{mb} = 33d_p \left( \frac{\rho_g}{\mu_g} \right)^{0.1} \tag{1.1}$$

Bubbles may grow to the size of the column diameter depending on the solid size, density and diameter of the column, characterized as slugging fluidization. Slugging is generally undesirable because of the reduced gas – solid contacting and vibration of the bed. Further

increase in gas velocity leads to turbulent fluidization. Onset of turbulent fluidization is characterized by maximum pressure fluctuations at the bottom of the column. In turbulent fluidization regime, no visible upper surface of the bed is observed. Gas-solid contacting is better than the bubbling regime due to the reduced gas bypassing in form of bubbles. However, turbulent regimes are considered as highly unstable and significant loss of solids is reported due to entrainment. Correlation of Bi and Grace (1995), can be used to predict the onset of turbulent regime (equation 1.2).

$$\text{Re}_c = 1.24Ar^{0.45} \quad (2 < Ar < 10^8) \quad (1.2)$$

If the gas velocity is increased further beyond the turbulent regime, entrainment increases and system reaches the condition where stable operation is not possible without recycling of solids.

Usually, gas - solid separation systems are used to capture the solids and feed back to the bottom of the column. This closed loop operation of solids is called as circulating fluidized bed (CFB). In CFB, gas and solids move upward in a column, commonly known as *Riser*, which are separated on the top of the column through cyclones. Two distinct regions can be observed in CFB, dense region at the bottom of the column and dilute region at the upper section. This distinct regime is classified as fast fluidization regime. Slip velocity based on the average velocity of solid and gas is highest in the fast fluidization regime. Thus it is generally expected that the gas solid contact efficiency is higher in CFB compared to the bubbling and turbulent fluidized beds. Transition from turbulent to fast fluidization can be computed by the correlation given by Bi et al. (1995), which is given by equation 1.3.

$$\text{Re}_{se} = 1.53Ar^{0.5} \quad (2 < Ar < 4 \times 10^6) \quad (1.3)$$

At sufficient high gas velocity, lower dense region of fast fluidized bed disappears. This regime is called as pneumatic conveying. The superficial gas velocity at which the solid accumulation in the bottom region disappears is called as accumulative choking, which signifies the transition from fast fluidization to the pneumatic regime. The equation of Yang (1983) can be used to predict the accumulative choking,  $U_{CA}$ ,

$$\frac{2gD(\varepsilon_{CA}^{-4.7} - 1)}{\left(\frac{U_{CA} - U_t}{\varepsilon_{CA}}\right)^2} = 6.81 \times 10^5 \left(\frac{\rho_g}{\rho_p}\right)^{2.2} \quad (1.4)$$

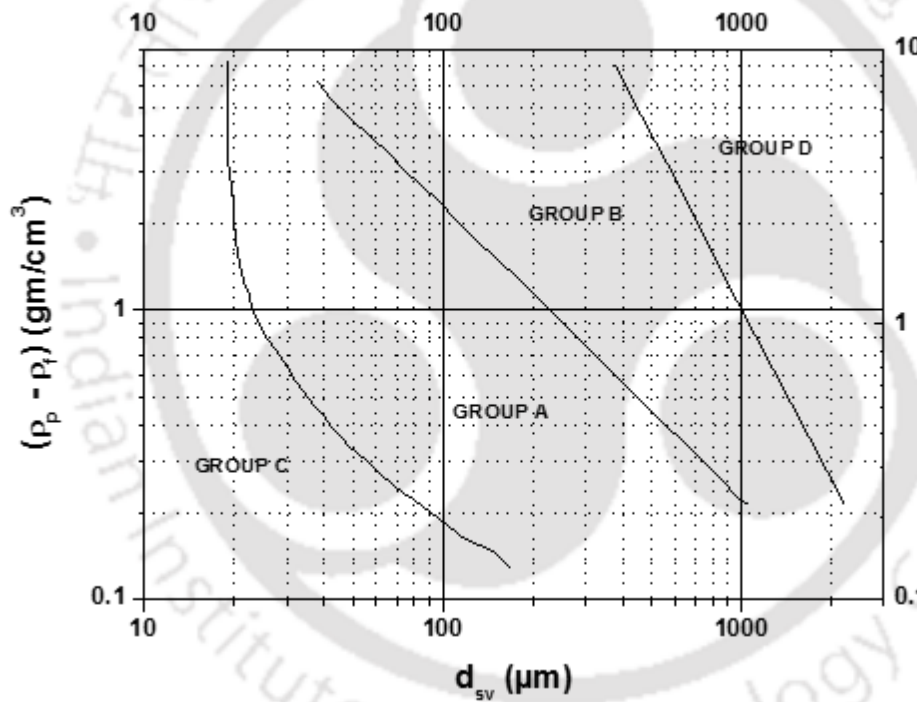


**Figure 1.2 Geldart classification of particles for air at ambient conditions (adapted from Geldart (1973))**

The behavior of fluidized bed and risers also depend on the particle characteristics. Geldart (1973) has classified solids into four groups A, B, C and D based on their size and relative fluid-solids density which is shown in the Figure 1.2. Group A particles are having small mean particle size and / or low particle density ( $\leq 1400 \text{ kg/m}^3$ ), for example, FCC particles.

They fluidize easily, expands smoothly and bubbles are formed once the gas velocity reaches minimum bubbling velocity. Group B particles are having size range of 40 $\mu\text{m}$  to 500 $\mu\text{m}$  and density in the range of 1400 kg/m<sup>3</sup> to 4000 kg/m<sup>3</sup>, for example, sand. They fluidize well with vigorous bubbling action and bubbles are formed at the minimum fluidization velocity itself. Group C particles are cohesive and very fine, where fluidization is very difficult. e.g. talcum powder. Group D particles are large and / or dense particles. e.g. coffee beans. They fluidize with exploding bubbles severe channeling and spouting. are observed.

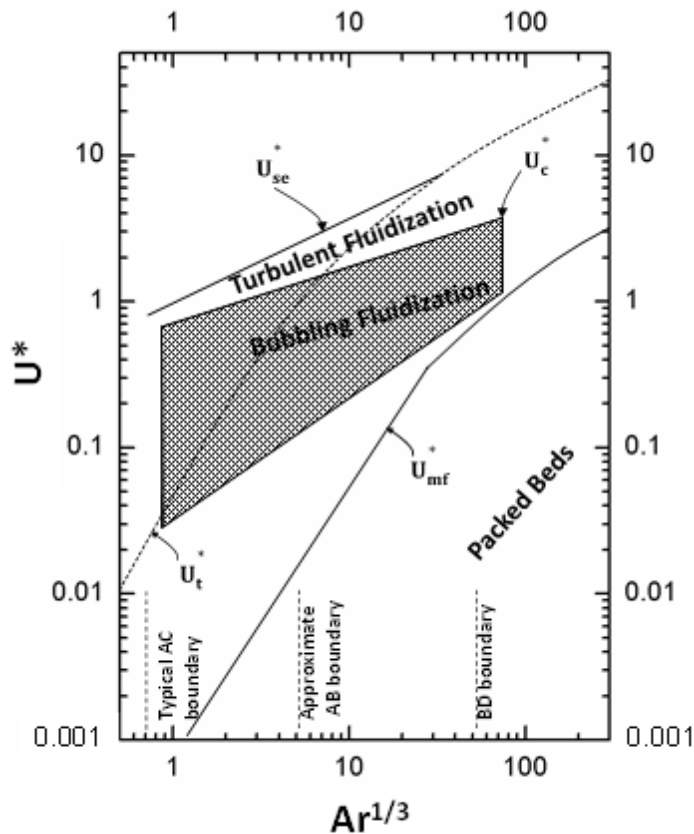


**Figure 1.3 Flow regime diagram for gas - solids (adapted from Bi and Grace (1995))**

Further, behavior of fluidized beds also depends on column diameter, shape of the particles, fluid properties (density and viscosity), column roughness, internals, inter-particle forces

and particle collisions. Several researchers (Reh, 1971; Grace, 1986; Bi and Grace, 1995; Das et al., 2008, Rabinovich and Kalman, 2011) have developed regimes maps to know *a priori*, about the regime in which the operating conditions fall. Bi and Grace (1995) flow regime map is the one most widely used and shown in the Figure 1.3. However, till now, no fundamental model or regime map is available which can accurately predict the behavior of the bed. This is mainly because of poor understanding of flow behavior of such beds which depends on several parameters. Additionally, the role of individual parameters on column behavior is not known and till now no single model or combination of models (both phenomenological and computation model) are available which can accurately determine the effect of these parameters.

## 1.2 Circulating fluidized bed

Gas-solid circulating fluidized beds have been an active area of research in the past few decades mainly because of its wide use in energy and chemical process industries. Typical CFB consists of riser (long section of vertical pipe), cyclone separator, standpipe (regenerator) and feed system as shown in Figure 1.4. Gas-solids reactions are primarily taking place in riser section, where gas and solids flow concurrently upwards. Solids are separated from the gas stream in cyclone separator. Separated solids are recirculated back to the system through the standpipe, which provides the necessary pressure head. CFB can be operated in fast fluidization, pneumatic transport and dense suspension upflow regimes depending upon the process requirement (Berruti et al., 1995; Zhu, 2010; Grace, 1999). Operational flexibility is the major advantage of CFB over the conventional bubbling / turbulent fluidization beds. Some of the examples are: catalyst can be regenerated continuously during the recirculation, gas and solid fluxes can be controlled independently

by varying the inventory (Reh, 1995), etc. The other advantages of CFB are: better gas-solid contact in short residence time ( $<10s$ ) due to the lack of bubbles, high heat and mass transfer rate, high gas and solid throughput, reduced axial gas and solids back mixing, almost isothermal condition throughout the reactor and reduced tendency for particles to agglomerate (Grace, 1990; Berruti et al., 1995). Restricted range of particle properties and complexities in designing the recirculation loop are the major limitations of CFB.

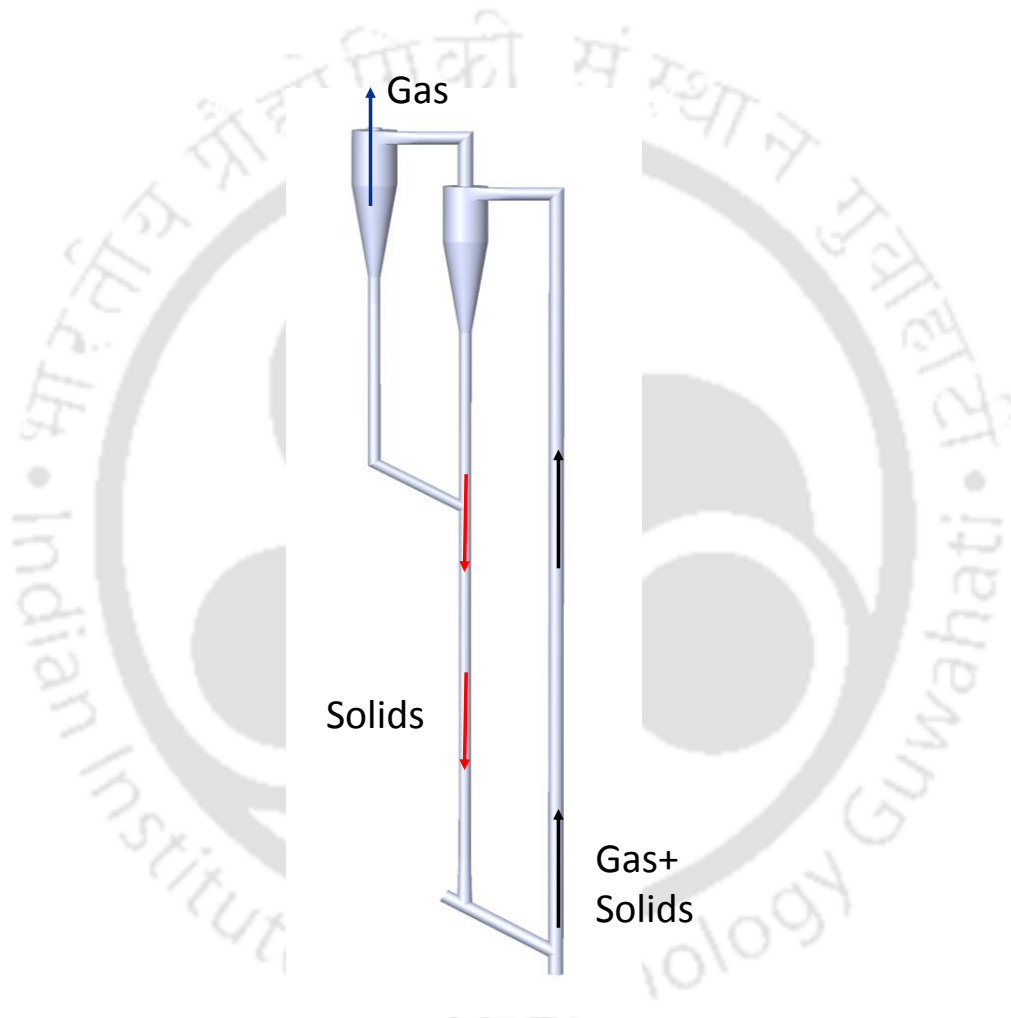


**Figure 1.4 Schematic diagram of Circulating Fluidized bed**

First commercial CFB unit was used for fluid catalytic cracking (FCC) in 1942. In 1960s, when Mobil came up with zeolite cracking catalyst, CFB became prominent reactor for fluid catalytic cracking (Grace, 1997). For the past 60 years, CFB has been used for the fluid catalytic cracking. Around 350 CFB catalytic crackers are operating worldwide

processing 14.7 million barrels per day as of 2010 (Lyn, 2010). Around 45% of all the gasoline produced worldwide is processed through FCC and ancillary units such as the alkylation unit (Sadeghbeigi, 2012). Value addition of FCC is as high as US \$ 10 per barrel (Grace, 1997).

Other prominent CFB application in terms of throughput is the circulating fluidized bed combustion (CFBC). CFBC is widely used because of fuel flexibility and environmental regulations. First commercial scale CFBC for power production was commissioned in 1982. Today, around 600 units of CFBC are operating worldwide with a capacity of 46 GWe power supply (Platts, 2012). Other industrial processes that use CFB are discussed in detail by Berruti et al. (1995), Reh (1995), Grace and Bi (1997), Avidan (1997) and Matsen (1997). Table 1.1 adapted from Grace and Bi (1997) lists few of the applications of CFB. Recent studies have found CFB as viable option for chemical looping combustion (CLC) and steam reforming (Hossain and Lasa, 2008; Mousa et al., 2014). However, in terms of throughput, circulating fluidized bed combustion (CFBC) and fluid catalytic cracking (FCC) are the principal applications.

CFBC is usually operated at solid flux,  $G_s < 100 \text{ kg/m}^2\text{s}$ , while for FCC it is  $> 400 \text{ kg/m}^2\text{s}$ . In CFBC, high axial and radial mixing is required to maintain the isothermal condition throughout the bed. However, the same will reduce the desired product (gasoline production) selectivity for FCC. Typical operating characteristics of FCC and CFBC are listed in Table 1.2, which shows significant difference in design, particle type, superficial velocity, solid flux, etc. for both the applications.

**Table 1.1 Applications of CFB**

---

**I. Gas – Solids reactions**

Combustion of coal, wood and shale

Incineration of solid waste

Synthesis of  $\text{AlF}_3$  and  $\text{SiC}$

Recovery / cleaning of off-gases

Desulphurization of flue gas

Gasification of coal, biomass, etc

Calcination of alumina, phosphate rock, clay, etc

Reduction of iron ore, lateritic nickel ore, etc

Roasting of sulphidic ores ( $\text{ZnS}$ ,  $\text{Cu}_2\text{S}$ , gold ores)

Dehydration of boric acid

Decomposition of sulphate, chloride and carbonate

Cement production

**II. Solid-catalyzed gas-phase reactions**

Fluid catalytic cracking

Fischer – Tropsch synthesis

Butane oxidation to maleic anhydride

Oxidation of *o*-xylene / naphthalene to phthalic anhydride

Ethylene epoxidation

Oxidative dehydrogenation of butene to butadiene

Oxidative coupling of methane to ethylene and ethane

Methanol to olefins

Simultaneous  $\text{NO}_x$  and  $\text{SO}_2$  removal from off- gases

---

**Table 1.2 Operating characteristics of FCC and CFBC**

| <b>Operating parameters</b> | <b>FCC</b>                    | <b>CFBC</b>                   |
|-----------------------------|-------------------------------|-------------------------------|
| Particle density            | 1100 – 1500 kg/m <sup>3</sup> | 1800 – 2600 kg/m <sup>3</sup> |
| Particle diameter           | 50 -150 $\mu$ m               | 250 – 500 $\mu$ m             |
| Geldart Classification      | Group A                       | Group B                       |
| Temperature                 | 250 – 650°C                   | >800°C                        |
| Superficial velocity        | 6 - 28 m/s                    | 2-6 m/s                       |
| Solid circulation rate      | > 400 kg/m <sup>2</sup> s     | 5 - 100 kg/m <sup>2</sup> s   |
| Pressure                    | $\geq$ 100 KPa                | 100 KPa                       |
| Exit Geometry               | Smooth, abrupt                | Abrupt                        |

### **1.3 Hydrodynamics of circulating fluidized bed**

In CFB, both gas and solids move upward in riser section. In all the applications stated above, CFB is mainly used to attain short residence time to achieve maximum product yield per unit volume. The performance of these reactors mainly depends on flow behavior of individual phases, contacting between gas and solids and mixing of phases. However design, scale-up and performance of CFB are still challenging due to the complexity of the interaction occurring between inter and intra phases. To achieve optimal design and desirable performance from CFB, precise description of reactor scale phase distribution, phase recirculation, hydrodynamic and transport of phases are required. Further, it is also important to find the solid distribution, circulation rate and mixing pattern, which majorly determines the gas-solids contact time.

Reh (1971), Yerushalmi et al. (1976), Li and Kwauk (1980) have measured axial solid distribution profile in riser which ascertains fast fluidization (FF) as different regime. Excellent reviews are available in the literature on hydrodynamics (Berutti et al., 1995; Lim

et al., 1995), gas - solid contact efficiency (Wang and Zhu, 2016) and dispersion and mass transfer rates (Breault, 2006) in CFB. These studies clearly depicts the presence of different length scale (particle and reactor scale) and time scale phenomena in CFB, which needs to be inferred for better description of flow in CFB. Therefore, for better understanding, hydrodynamics of CFB are analyzed at two different scales, viz., macro and meso scales.

### **1.3.1 Macro-scale hydrodynamics**

The event/structures which occurs at reactor scale is classified as macroscale phenomenon. Macro scale hydrodynamics can be analyzed as axial and radial flow structures which largely depend on operating conditions.

#### ***Axial flow structure***

At the outset of CFB research, axial and radial distribution of solids was the peculiarity of the CFB. The cross sectional averaged axial solid volume fraction follows 'S'-shaped profile which consists of dense bottom region, dilute top region and in between transition region. Later other kind of profiles viz, exponential, linear, 'C'-shaped curves are also reported in CFB. The axial solid hold up profile depends on solid circulation rate, total solids inventory, particle size and density, solids inlet configuration, secondary air injection and the level of solids reintroduction into the riser (Lim et al., 1995). Riser entry and exit configurations also affect the axial flow structure (Fan and Zhu, 1998).

Ratio of the solid circulation rate to the saturation carrying capacity of gas also influences the shape of axial solid holdup profile (Li et al., 1988). If the solid circulation rate is more than the saturation carrying capacity, S-shape or linear solid holdup profiles are observed. However, if solid circulation rate is lower than the saturation carrying capacity of the gas (entered solids are immediately entrained from the system), exponential profile is observed. In case of restricted/tapered exits, the solid volume fraction increases significantly at the top section of the riser which leads to C-shaped solid holdup profile in CFB (Martin et al.,

1992). Yang et al. (1988) have classified regimes in CFB based on axial solid holdup profiles. These are dilute bed, fast fluidized bed and dense transport bed where axial solid holdup profiles are exponential, S-shaped and linear respectively.

Axial solid holdup profile also depends on geometrical and operational parameters. Increasing the solid circulation rate or decreasing the superficial gas velocity increases the cross-sectional averaged axial solid fraction in riser, primarily in the bottom dense region (Bai et al., 1992; Issangya et al., 1999; Wang et al., 2014). Similarly, increase in particle size and/or solid density, increases the solid fraction in the bottom region however at the same time slight decrease in solid holdup at the top region is also observed (Bai et al., 1992). It has also been noted that with increase in riser diameter cross-sectional averaged axial solid holdup decreases, particularly in the bottom region.

Acceleration zone is defined as zone extending from the bottom of the riser to the point where the solids attain constant velocity (Weinstein and Li, 1989) or where pressure gradient is constant (Arena et al., 1986; Bai et al., 1990). Acceleration length may occupy 1/3 to 2/3 length of the riser. In other words, solids attain approximately constant average velocity after 1/3 to 2/3 length of the riser. However, most of the acceleration occurs in transition zone (90 to 95%), suggesting as the boundary of the accelerating zone for all the practical purposes (Arena et al., 1986; Bai et al., 1990; Parssinen and Zhu, 2001; Wang et al., 2014). Acceleration length or axial particle velocity development varies with distributor, solid circulation rate and riser diameter (Yan et al., 2008; Bai et al., 1990; Yan et al., 2008; Wang et al., 2014). It increases with the solid circulation rate and riser diameter and decreases with superficial gas velocity.

### ***Radial flow structure***

The radial distribution of solids is one of the most critical aspects of the CFB. Most of the researches have reported, 'core - annular' structure where dilute core (low solid fraction) exist at the center and dense annulus region is found near the wall (Bader et al., 1988; Rhodes et al., 1988; Bolton and Davidson, 1988; Brereton and Grace, 1993). The thickness of annular region increases with an increase in diameter (Werther, 1994; Zhang et al., 1995) and height of the riser (Kim et al., 2004). It is also a function of cross sectional averaged solid volume fraction (Bi et al., 1996). Further, the radial diffusion of solids from low concentration (at center) to high concentration (at wall) is also observed which has been explained by various theories given by several researchers (Berruti and kalogerakis, 1989, Bolton and Davidson, 1988, Li et al., 1991 etc.). However, none of these theories are well accepted due to their limited applicability.

In literature, several authors have also reported uniform solid holdup at the centre region of the riser which increases dramatically near the wall. The center dilute region can be extended up to 70 – 85% of the column radius (Hartge et al., 1988; Parssinen and Zhu, 2001). Parabolic and M shaped radial voidage profile are also widely reported (Weinstein et al., 1986; Hartge et al., 1988; Bai et al., 1991; Kato et al., 1991; Herb et al., 1992; Zhou et al., 1994). The shape of radial profile changes significantly with the operating conditions (Zhang et al., 1991; Brereton and Grace, 1993; Lim et al., 1995; Issangya et al., 2000; Wang et al., 2014). It has also been reported that superficial air velocity and solid circulation rate greatly influences the solid holdup near the wall (Issangya et al., 2000; Wang et al., 2014). Relative increase in solid hold up near the wall and simultaneous decrease in dilute central core region is observed for an increase in the solid circulation rate or decrease in the superficial gas velocity. In the high solid flux condition ( $G_s > 700 \text{ Kg/m}^2\text{s}$ ), dilute core region shrinks up to 20% of the radius (Wang et al., 2014).

Mean solid velocity along the radius is positive in the dilute core and negative near the wall. Negative velocity near the wall greatly depends on the operating conditions. However, in case of the dense suspension upflow or dilute flow, mean axial velocities of solids are reported positive all along the column. Several profiles for mean axial solids velocity, parabolic, horizontal S, power law, boltzman function, linear etc., are reported in literature. The shape of the solid axial velocity strongly depends on the operating condition i.e. superficial gas velocity and solid circulation rate.

Lastly, flow development in the riser depends on the operating conditions, diameter of riser, distributor, inlet and exit configuration. The length required for flow development decreases with the increase in the superficial gas velocity and increases with the increase in solid circulation rate. Flow develops faster in the core region compared to the annulus. In high density riser, three or four distinct radial profiles of velocity are observed in the riser up to flow development. Mostly parabolic or horizontal S shaped profile is observed in the bottom or distributor controlled region. In the middle section steep or linear profile is observed and at the top parabolic profile is observed.

### **1.3.2 Meso-scale hydrodynamics**

In gas-solid risers, several authors have reported the existence of meso-scale meta-stable structures, commonly known as 'clusters' (Li et al., 1991; Horio and Kuroki, 1994; Lacknermeier et al., 2001). It is observed that in many cases slip velocity, defined as the difference between the interstitial gas velocity and solid velocity, in the riser exceeds the single particle terminal velocity by two orders of magnitude (Squires, 1986). Li and Kwauk (1980) and Li et al. (1988) proposed that this might be due to the presence of large coherent structures which is larger than the single particle by several orders of magnitude. Cluster formation in the CFB riser was first captured using video camera by Li et al. (1991) and by

photographic analysis using laser sheet technique by Horio and Kuroki (1994). However, the above mentioned studies were mainly in dense riser. Kuroki and Horio (1994), and Lacknermeier et al. (2001) have confirmed existence of clusters even in the dilute flow riser. In literature, various irregular shapes of cluster structures are reported viz., strands, streamers, U shaped, near spherical (Li et al., 1991; Kuroki and Horio, 1994; Zou et al., 1994; Lacknermeier et al., 2001; Xu and Zhu, 2011; Shaffer et al., 2013; Mondal et al., 2015). However, mechanism of cluster formation is still not well understood (Fan and Zhu, 1998). Researchers have proposed different theories for the formation of clusters (Glasser et al., 1998; Li and Kupiers, 2003; Cocco et al., 2010). Glasser et al. (1998) have suggested that solid inertia, fluid-solids drag, gravity and solid phase stress are responsible for cluster formation. However, Li and Kupiers (2003), and Cocco et al. (2010) have proposed that inelastic collisions and cohesive forces play critical role in cluster formation

Clusters are characterized by their size, frequency and duration. Clusters characteristics varies with axial and radial position in the riser, solid properties, solid size distribution, solid flux, superficial gas velocity and local mean solids concentration (Manyele et al., 2002; Guenther and Breault, 2007; Chew et al., 2012; Kiani et al., 2013; Mondal et al., 2015). Cluster duration and frequency is highly influenced by the material properties and operating conditions, while axial position has secondary effect (Chew et al., 2012).

Cluster structure and size characterization has been difficult due to the time and length scales involved. In addition to that, mostly optical fiber probes or photographic techniques are used for the identification of clusters which are inherently a two dimension measurement. Cluster size are characterized by vertical length of the clusters (Zou et al., 1994)). Few studies have also reported the width and length of the clusters (Mondal et al., 2015). In any case, definition of cluster dimension is difficult due to the irregular shape. In literature, U shaped clusters are observed for higher solid holdup and strands are observed

for lower solid holdups (Bai et al., 1991; Lackemeirer et al., 2001). Elliptical shaped clusters are also reported (Lim et al., 1996; Rhodes et al., 1990). Further, size and shape of the clusters also depends on the location inside the riser. Similar to the other characteristics, cluster size also varies with elevation, operating conditions, radial position and material properties.

Existence of clusters significantly modify the performance of CFB by changing the dispersion (axial and radial) values, heat and mass transfer characteristics. Mostly, gases prefer to bypass the cluster, thereby limiting the contact with the solids. Thus, effective mass transfer coefficient is two or more order of magnitude less than the 'cluster free' phase (Sundaresan, 2013). Fluctuating motion of clusters leads to the segregation towards the wall which reduces the contact efficiency. This may be critical during the scale up process (Sundaresan, 2013).

#### **1.4 Scale up of circulating fluidizing bed**

Scale up of the circulating fluidized bed is very challenging task. In fact knowledge of scale up on CFB is very limited in the open domain. Due to the expense involved and commercial interests, data available with the industries are not available in the open domain. Even with whatever the data are available with industries, scale up of CFB is still a challenge, which can be proven by two classical commercial level failures. Sasol Synthol Fischer-Tropsch reactors changed back to the turbulent fluidized bed from circulating fluidized bed and saved 18% on the total plant cost (Steynberg et al. (1991)). In another example, DuPont's maleic anhydride production by partial oxidation of butane failed to give the desired performance in CFB when scaled to the commercial scale. Though, the performance was reported better at laboratory and pilot plant scales (Contractor, 1999). This leads to the decommissioning of the commercial plant (Duduvokic, 2010). In fact, FCC is the only

successful commercial solid catalytic gas phase reaction in the circulating fluidized bed. This is mainly due to the lack of understanding of the scale effects in circulating fluidized bed.

Some researchers have proposed scaling laws as an alternative method for the design of commercial CFB plants. Glicksman (1984) developed scaling laws from dimensional analysis of governing equations derived by Anderson and Jackson (1967). All the scaling laws suffer from the lack of accounting of the meso-scale meta-stable structures. Moreover, solid properties are not accounted in most of the scaling law developed (Knowlton et al., 2005).

Further, studies on effect of the diameter of the riser on the solid fraction show that at the same operating conditions, bed density is higher in larger diameter riser than the smaller diameter riser (Yan and Zhu, 2004). Radial profile of solid fraction becomes steeper in large diameter riser for the same operating conditions. Further, particle velocity is observed to be lower in the large diameter riser at the same operating conditions. It is also observed that flow development length is high in the larger diameter riser (Yan et al., 2005) compared to smaller diameter. However, most of the scale studies were focused on the solid distribution, studies on particle velocity and fluctuations are largely missing.

## **1.5 Motivation**

Reactor performance decides the profitability of any chemical plant. Reactor performance is the function of feed condition, reaction kinetics and contacting (Levenspiel, 1999). In case of fast reactions, which is typical in CFB, yield and selectivity of the desired product(s) are mainly controlled by local hydrodynamics. In FCC, propylene (which is in high demand, 4.7 % annual growth rate in demand) yield can be increased by severe operating conditions like high reaction temperature and high catalyst to oil ratio which affects the

hydrodynamics. So, quantitative understanding of hydrodynamics of CFB is very important for scale up, improving the performance of existing CFBs and utilizing the CFB for new processes. In literature large number of studies are reported on hydrodynamics of the CFB (Parssinen and Zhu, 2001; Wang et al., 1998; Issangya et al., 2000; Zhang et al., 2003; Miller and Gidaspow, 1992; Weinstein et al., 1986; Wang et al., 2014). However, most of these studies have used intrusive techniques and gives mean values of the solid fraction or concentration. Further, very few studies are available on velocity measurement including fluctuations and other turbulent quantities (Tartan and Gidaspow, 2004; Bhusarapu, 2005; Ibsen, 2002; Gopalan and Shaffer, 2013; Chan et al., 2010; Pantzali et al., 2013). Systematic studies on effect of operating conditions and riser diameter on particle mean and fluctuation velocities, and other turbulent quantities are still limited in literature.

Scale up of CFB is too expensive as it involves stepwise process of constructing and macroscopically testing various sizes of pilot units (Cheremisinoff, 1986). Even though various scaling laws has been developed (mostly empirical), success of commercial operation is uncertain as explained in the previous section. This is due to the flow phenomenon involved in CFB is very complex which involves interactions at different length and time scales. Particle – particle, particle – wall, and particle - gas interactions are least understood in CFB till date. Further, change in these interactions with change in diameter is also not known. These interactions severely affect the flow distributions in the riser. Dudukovic (2010) has reported that scale up challenges can be met out by implementation of perfect flow distribution and control from proven laboratory scale process. However, these challenges get bigger in CFB due to the multiscale nature of interactions between the phases, demanding studies on fluctuations in addition to the mean local values. Very few studies are reported on scale effects (Chang and Louge, 1991; Yan and Zhu, 2004, 2005; Caloz, 2000). Accuracy of most of the optical techniques and

intrusive techniques depends on the scale and operating conditions. It is imperative to have a technique which doesn't depend on the scale and operating conditions for comparison at different scales. To the best of author's knowledge there is no study available on scale effect on local velocity using noninvasive technique.

Reactor modeling can reduce the effort and cost of design and scale up. However reactor modeling requires detailed understanding of underlying local structures and interactions of particle – gas, particle – particle and particle – wall. Significant progress has been made in the modeling based on Computational fluid dynamics (CFD) but still prediction of models developed is not satisfactory. This is due to empirical inputs used in the modeling is not able to account all the interactions and needs rigorous validation at different scales. However, in literature most of the validations are reported for the first order moment (mean velocity or mean solid distribution) which is not sufficient to verify the model effectiveness. For more reliable CFD model, validation of higher order moments (RMS velocities, granular temperature, stress, etc.) are required. However, such validations are limited due to the availability of accurate data at different operating conditions and at different scales. Hence, a systematic high accuracy data is required for different operating conditions at different scales.

## **1.6 Objectives**

The global aim of the current work is to improve the understanding of scale effect using state-of-the-art experimental and numerical techniques and generate detailed data for validation of numerical models. The specific objectives of the work are as follows,

1. Implementation of radioactive particle tracking (RPT) technique in a relatively high velocity gas-solid CFB system

2. Experimental investigation of laboratory scale CFB setup through radio isotope based techniques
  - Effect of solid flux
  - Effect of fluid inlet velocity
3. Analysis of pilot plant scale CFB through RPT technique
  - Effect of solid flux and fluid inlet velocity
  - Effect of scale
4. Numerical investigation of CFB to study the hydrodynamics at different scales using Euler – Euler approach emphasizing the effect of solid flux, fluid velocity and scale.

## 1.7 Structure of the thesis

This thesis is structured in the following manner. Chapter 2 discusses about radioactive particle tracking and accuracy of radioactive particle tracking at high velocity conditions. Discussion about the radioactive particle tracking technique and implementation of radioactive particle tracking have also been done. Next section discuss about the issues in implementation of radioactive particle tracking and sources of error in radioactive particle tracking. Then, discussion progresses on quantifying the accuracy of the radioactive particle tracking at stationary and dynamic conditions.

Chapter 3 discuss about the particle velocity field and residence time distribution study in the laboratory scale setup. First, solid flux measurements are discussed. Then, Lagrangian motion of the solids are discussed. Thereafter, Eulerian mean and fluctuations are discussed. Effect of superficial gas velocity and effect of solid flux are discussed. Then, residence time distribution and diffusivity are discussed.

In chapter 4, experiments on pilot scale setup are discussed. Similar to laboratory scale study, Lagrangian motion of solids and Eulerian velocity field are discussed. Thereafter, the effect of scale up is discussed. Further, hydrodynamic similarity laws are validated. Later, global and local solid mixing in pilot scale setup are discussed.

Chapter 5 discusses about the numerical investigation of CFB. First, the development of model is discussed. Then, base case simulation in laboratory scale setup is discussed. Later, effect of solid flux and superficial gas velocity are discussed. Finally, effect of scale-up is discussed. Chapter 6 gives the overall conclusion and future recommendations emerge out of the thesis.

### Notations

|       |                                    |                    |
|-------|------------------------------------|--------------------|
| $Ar$  | Archimedes number                  | [-]                |
| $d_p$ | Particle diameter                  | [ $\mu\text{m}$ ]  |
| $D$   | Column diameter                    | [m]                |
| $g$   | Acceleration due to gravity        | [ $\text{m/s}^2$ ] |
| $Re$  | Reynolds number                    | [-]                |
| $U$   | Superficial gas velocity           | [m/s]              |
| $U^*$ | Dimensionless superficial velocity | [-]                |

### Greek letters

|                    |               |                     |
|--------------------|---------------|---------------------|
| $\varepsilon_{CA}$ | Void fraction | [-]                 |
| $\rho$             | Density       | [ $\text{kg/m}^3$ ] |
| $\mu_g$            | Gas viscosity | [kg/ms]             |

### Subscript

|     |  |
|-----|--|
| $C$ | Transition from bubbling to turbulent fluidization |
|-----|--|

|           |   |
|-----------|---|
| <i>CA</i> | Type A or accumulative choking          |
| <i>f</i>  | Fluid                                   |
| <i>g</i>  | Gas                                     |
| <i>mb</i> | Minimum bubbling                        |
| <i>mf</i> | Minimum fluidization                    |
| <i>p</i>  | Particle                                |
| <i>s</i>  | Solids                                  |
| <i>se</i> | Onset of significant solids entrainment |
| <i>t</i>  | Terminal settling of single particles   |

## References

- Arena, U., Cammarota, A., Pistane, L., 1986. High velocity fluidization behaviour of solids in a laboratory scale circulating fluidized bed. In *Circulating Fluidized Bed Technology* (eds Basu, P.), Pergamon Press, Toronto. 119-125.
- Anderson, T.B., Jackson. R., 1967. A fluid mechanical description of fluidized beds. *Ind. Eng. Chem. Fundamen.* 6, 527- 535.
- Avidan, A. A., 1997. Fluid Catalytic Cracking, in *Circulating Fluidized Beds*. (eds. Grace, J. R., Avidan A. A., Knowlton T.M.), Blackie Academic & Professional, New York.
- Bader, R.J., Findlay, J., Knowlton, T.M., 1988. Gas/solids flow patterns in a 30.5 cm diameter circulating fluidized bed. In *Circulating Fluidized Bed Technology II* (eds by Basu, P. and Large, J.F.), Pergamon Press, Toronto. 123-137.
- Bai, D.R., Jin, Y., Yu, Z.Q. 1990. Particle acceleration length in a circulating fluidized bed. *Chem. Reaction Eng. & Technol.* 6, 34-39.

- Bai, D.R., Jin, Y., and Yu, Z.Q., 1991. Cluster observation in a two-dimensional fast fluidized bed, in *Fluidization '91: Science and Technology* (eds. Kwauk, M., and Hasatani, M.), Science Press, Beijing. 110-115.
- Berruti, F., Chaouki, J., Godfroy, L., Pugsley, T.S., Patience, G.S., 1995. *Can. J. Chem. Eng.* 73, 579-602.
- Berruti, F., Kalogerakis, N., 1989. Modelling the internal flow structure of circulating fluidized beds. *Can. J. Chem. Eng.* 67, 1010-1014.
- Bhusarapu, S., 2005. *Solid Flow Mapping in Gas-Solid Risers* (D.Sc. Thesis). Washington University, USA.
- Bi, H.T., Grace, J.R., 1995. Flow Regime Diagrams for Gas-Solid Fluidization and Upward Transport. *Int. J. Multiphase Flow* 21, 1229-1236.
- Bolton, L.W., Davidson, J.F., 1988. Recirculating of Particles in Fast Fluidized Risers. In *Circulating Fluidized Bed Technology*. (eds Basu, P.), Pergamon, Oxford.
- Breault, R.W., 2006. A review of gas-solid dispersion and mass transfer coefficient correlations in circulating fluidized beds. *Powder Technol.* 163, 9–17.
- Brereton, C.M.H., and Grace, J.R., 1993. End effects in circulating fluidized bed hydrodynamics, in *Circulating Fluidized Bed Technology IV* (ed. A. Avidan), *AIChE J. New York.* 137-144.
- Chan, C.W., Seville, J.P.K., Parker, D.J., Baeyens, J., 2010. Particle velocities and their residence time distribution in the riser of a CFB. *Powder Technol.* 203, 187–197.
- Chang, H., Louge, M., 1992. Fluid dynamic similarity of circulating fluidized beds. *Powder Technol.* 70, 259–270.
- Cheremisinoff, N.P., 1986. Review of experimental methods for studying the hydrodynamics of gas-solid fluidized beds. *Ind. Eng. Chem. Process Des. Dev.*, 25, 329-351.
- Chew, J.W., Hays, R., Findlay, J.G., Knowlton, T.M., Reddy Karri, S.B., Cocco, R.A., Hrenya, C.M., 2012. Cluster characteristics of Geldart Group B particles in a pilot-scale CFB riser. II. Polydisperse systems. *Chem. Eng. Sci.* 68, 72–81.

- Cocco, R., Shaffer, F., Hays, R., Karri, S.B.R., Knowlton, T., 2010. Particle clusters in and above fluidized beds 203, 3–11.
- Contractor, R.M., 1999. Dupont's CFB technology for maleic anhydride. *Chem. Eng. Sci.* 54, 5627–5632.
- Das, M., Meikap, B.C., Saha, R.K., 2008. Prediction of cluster diameter for a wide range of particles for gas–solid dispersed phase in a fast fluidized-bed reactor. *Asia-Pac. J. Chem. Eng.* 3, 223–229.
- Dudukovic, M. P., 2010. Reaction engineering: Status and future challenges. *Chem. Eng. Sci.* 65, 3–11.
- Fan, L.S. and C. Zhu, C., 1998. *Principles of Gas–Solid Flows*, Cambridge University Press, 396–400.
- Geldart, D., Abrahamsen, A. R., 1978. Homogeneous fluidisation of fine powders using various gases and pressures, *Powder Technol.* 19, 133–134.
- Geldart, D., 1973. Types of Gas Fluidization. *Powder Technol.* 7, 285–292.
- Glicksman L.R., 1984. Scaling relationships for fluidized beds. *Chem. Eng. Sci.* 39 (9), 1373–1379.
- Glasser, B., Sundaresan, S., Kevrekidis, I., 1998. From Bubbles to Clusters in Fluidized Beds. *Phys. Rev. Lett.* 81, 1849–1852.
- Gopalan, B., Shaffer, F., 2013. Higher order statistical analysis of Eulerian particle velocity data in CFB risers as measured with high speed particle imaging. *Powder Technol.* 242, 13–26.
- Grace, J.R., 1990. High velocity fluidized bed reactors. *Chem. Eng. Sci.* 45(8), 1953–1966.
- Grace J.R., Bi H., 1997. Introduction to circulating fluidized beds, in *Circulating Fluidized Beds* (eds, Grace J.R., Avidan A.A. & Knowlton T.M.), Engineering Foundation, New York, 1–19.
- Grace, J.R., 1986. Fluid Beds as Chemical Reactors. Chap. 11 in *Gas Fluidization Technology*. (eds D. Geldart) Wiley and Sons, Chichester, UK, 287–341.

- Guenther, C., Breault, R., 2007. Wavelet analysis to characterize cluster dynamics in a circulating fluidized bed. *Powder Technol.* 173, 163–173.
- Herb, B., Dou, S., Tuzla, K., Chen, J. C., 1992. Solid mass fluxes in circulating fluidized beds. *Powder Technol.* 70(3), 197-205.
- Hartge, E.D., Rensner, D., Werther, J., 1988. Solid concentration and velocity patterns in circulating fluidized beds. In *Circulating Fluidized Bed Technology II* (eds Basu, P. and J.F. Large, J. F.), Pergamon Press, Oxford. 165-180.
- Horio, M., Kuroki, H., 1994. Three-dimensional flow visualization of dilutely dispersed solids in bubbling and circulating fluidized beds. *Chem. Eng. Sci.* 49, 2413–2421.
- Hossain, M.M., de Lasa, H.I., 2008. Chemical-looping combustion (CLC) for inherent separations—a review. *Chem. Eng. Sci.* 63, 4433–4451.
- Ibsen, C.H., 2002. An Experimental and Computational Study of Gas-Particle Flow in Circulating Fluidised Reactors (PhD Thesis). Aalborg University, Denmark.
- Issangya, A.S., Bai, D., Bi, H.T., Lim, K.S., Zhu, J., Grace, J.R., 1999. Suspension densities in a high-density circulating fluidized bed riser. *Chem. Eng. Sci.* 54, 5451–5460.
- Issangya, A.S., Grace, J.R., Bai, D., Zhu, J., 2000. Further measurements of flow dynamics in a high-density circulating fluidized bed riser. *Powder Technol.* 111, 104–113.
- Lackermeier, U., Rudnick, C., Werther, J., Bredebusch, A., Burkhardt, H., 2001. Visualization of flow structures inside a circulating fluidized bed by means of laser sheet and image processing. *Powder Technol.* 114, 71–83.
- Levenspiel, O., 1999. *Chemical Reaction Engineering*, 3rd Ed., John Wiley & Sons, New York, USA.
- Li, Y., Kwauk, M., 1980. The dynamics of fast fluidization. In: Grace, J.R., Matsen, J.M. (Eds.), *Fluidization-III*. Plenum Press, New York. 537–544.

- Li, J., Tung, Y., Kwauk, M., 1988. Axial voidage profile of fluidized beds in different operating regions. In *Circulating Fluidized Bed Technology II* (eds Basu, P. & Large, J. F.). Pergamon Press, Toronto. 193-203.
- Li, J., Reh, L., Kwauk, M., 1991. Application of the principle of energy minimization to the fluid dynamics of circulating fluidized beds. in *Circulating Fluidized Bed Technology III*, Eds. P. Basu, M. Horio and M. Hasatani, Pergamon Press, Oxford, 105-111.
- Li, H., Zhu, Q., Liu, H., Zhou, Y., 1995. The cluster size distribution and motion behavior in a fast fluidized bed. *Powder Technol.* 84, 241–246.
- Li, J., Kuipers, J.A.M., 2003. Gas-particle interactions in dense gas-fluidized beds. *Chem. Eng. Sci.* 58, 711–718.
- Lim, K.S., Zhu, J., Grace, J.R., 1995. Hydrodynamics of gas solid fluidization. *Int. J. Multiph. Flow* 21, 141–193.
- Lyn, R. M., 2010. Worldwide refining, *Oil Gas J.* 108(46), 52.
- Kato, K., Takarada, T., Tamura, T. and Nishino, K., 1991. Particle hold up distribution in a circulating fluidized bed. *Circulating Fluidized Bed Technology III*, (eds. Basu, P., Horio, M., and Hasatani, M.) Pergamon press, New York. 145-150.
- Kiani, A., Sotudeh-Gharebagh, R., Mostoufi, N., 2013. Cluster size distribution in the freeboard of a gas–solid fluidized bed. *Powder Technol.* 246, 1–6.
- Kim, S. W., Kirbas, G., Bi, H., Lim, C. J., Grace, J. R., 2004. Flow structure and thickness of annular downflow layer in a circulating fluidized bed riser. *Powder Technol.* 142, 48–58.
- Knowlton, T. M., Karri, S. B. R., Issangya, A., 2005. Scale-up of fluidized-bed hydrodynamics. *Powder Technol.* 150, 72–77.
- Manyele, S.V, Pärssinen, J.H., Zhu, J., 2002. Characterizing particle aggregates in a high-density and high-flux CFB riser. *Chem. Eng. J.* 88, 151–161.
- Martin, M.P., Turlier, P., Bernard, J.R., Wild, G., 1992. Gas and solid behaviour in cracking circulating fluidized beds. *Powder Technol.* 70, 249–258.

- Matsen, J.M., 1997. Design and scale up of CFB catalytic Cracking, in *Circulating Fluidized Beds* (editor(s), Grace J.R., Avidan A.A. & Knowlton T.M.), Blackie Academic & Professional, New York.
- Miller, A., Gidaspow, D., 1992. Dense, Vertical Gas-Solid Flow in a Pipe. *AIChE J.* 38, 1801–1815.
- Mondal, D. N., Kallio, S., Saxén, H., 2015. Length scales of solid clusters in a two-dimensional circulating fluidized bed of Geldart B particles. *Powder Technol.* 269, 207–218.
- Mousa, M. B. M., Fateen, S. K., Ibrahim, E. A., 2014. Hydrodynamics of a Novel Design Circulating Fluidized Bed Steam Reformer Operating in the Dense Suspension Up flow Regime. *ISRN Chem. Eng.* 2014, 1-13.
- Pangarkar, V.G., 2015. *Design of Multiphase Reactors*, John Wiley & Sons, USA.
- Pantzali, M.N., Lozano Bayón, N., Heynderickx, G.J., Marin, G.B., 2013. Three-component solids velocity measurements in the middle section of a riser. *Chem. Eng. Sci.* 101, 412–423.
- Parssinen, J.H. and Zhu, J.X., 2001. Particle velocity and flow development in a long and high-flux circulating fluidized bed riser. *Chem. Eng. Sci.* 56, 5295-5303.
- Platts, 2012. *World Electric Power Plants Database*. New York, USA, Platts, The McGraw- Hill Companies Inc, CD-ROM.
- Reh, L., 1995. Fluid dynamics of CFB combustors. In: Kwauk, M., Li, J. (Eds.), *Circulating Fluidized Bed Technology V: Proceedings of the fifth International Conference on Circulating Fluidized Beds*. Beijing. 1–15.
- Reh, L., 1971. Fluid bed processing. *Chem. Engg. Progr.* 67, 58-63.
- Rhodes, M. J., Lausmann, P., Villain, F., Geldart, D., 1988. Measurement of radial and axial solids flux variations in the riser of a circulating fluidized bed. In *Circulating Fluidized Bed Technology*, Vol. 2 (eds by Basu, P. & Large, J. F.). Pergamon Press, Oxford. 155-164.

- Rabinovich, E., Kalman, H., 2011. Threshold velocities of particle-fluid flows in horizontal pipes and ducts : literature review. *Rev Chem. Eng.* 27, 215–239.
- Sadeghbeigi, R., 2012 Fluid catalytic cracking hand book. 3rd Ed, Butterworth-Heinemann. Oxford. UK.
- Shaffer, F., Gopalan, B., Breault, R.W., Cocco, R., Karri, S.B.R., Hays, R., Knowlton, T., 2013. High speed imaging of particle flow fields in CFB risers. *Powder Technol.* 242, 86–99.
- Sharma, A.K., Tuzla, K., Matsen, J., Chen, J.C., 2000. Parametric effects of particle size and gas velocity on cluster characteristics in fast fluidized beds. *Powder Technol.* 114–122.
- Steynberg, A.P., Shingles, T., Dry, M.E., Jager, B., and Yukawa, Y., 1991. Sasol commercial scale experience with LFB and CFB Fischer-Tropsch Reactors. In *Circulating Fluidized Bed Technology III* (eds. Basu, P, Horio, M., and Hasatani, M.), Pergamon Press, Oxford. 527-532.
- Sundaresan, S., 2013. Role of hydrodynamics on chemical reactor performance. *Curr. Opin. Chem. Eng.* 2, 325–330.
- Tartan, M., Gidaspow, D., 2004. Measurement of Granular Temperature and Stresses in Risers. *AIChE J.* 50, 1760–1775.
- Wang, Y., Wei, F., Wang, Z., Jin, Y., Yu, Z., 1998. Radial profiles of solids concentration and velocity in a very fine particle (36  $\mu\text{m}$ ) riser. *Powder Technol.* 96, 262-266.
- Wang, C., Zhu, J., Li, C., Barghi, S., 2014. Detailed measurements of particle velocity and solids flux in a high density circulating fluidized bed riser. *Chem. Eng. Sci.* 114, 9–20.
- Wang, C., Zhu, J., 2016. Developments in the understanding of gas-solid contact efficiency in the circulating fluidized bed riser reactor: A review. *Chinese J. Chem. Eng.* 24, 53–62.
- Wei, F., Yang, G.Q., Jin, Y., Yu, Z., 1995. The characteristics of cluster in a High density circulating fluidized bed. *Can. J. Chem. Eng.* 73, 650–655.

- Weinstein, H., Shao, H., Schnitzlein, M., 1986. Radial Variation of Solids Density in High Velocity Fluidization. In *Circulating Fluidization Bed Technology II* (eds. Basu P., and Large, J. F., eds.), Pergamon Press, New York, 201.
- Weinstein, H., and Li, J., 1989. An evaluation of the actual density in the acceleration section of vertical risers. *Powder Technol.* 52, 77-79.
- Werther, J., 1994. *Circulating Fluidized Bed Technology*. Vol. V, (eds Kwauk, M., Li, J.) Science Press, Beijing, China. 1–14.
- Xu, J., Zhu, J., 2011. Visualization of particle aggregation and effects of particle properties on cluster characteristics in a CFB riser. *Chem. Eng. J.* 168, 376–389.
- Yan, A., Zhu, J. J., 2004. Scale-Up Effect of Riser Reactors (1): Axial and Radial Solids Concentration Distribution and Flow Development. *Ind. Eng. Chem. Res.* 43, 5810–5819.
- Yan, A., Zhu, J. (Jingxu), 2005. Scale-up effect of riser reactors: Particle velocity and flow development. *AIChE J.* 51, 2956–2964.
- Yan, A., Huang, W., Zhu, J. (Jingxu), 2008. The influence of distributor structure on the solids distribution and flow development in circulating fluidized beds. *Can. J. Chem. Eng.* 86, 1023–1031.
- Yang, W.C. 1988. A model for the dynamics of a circulating fluidized bed loop. In *Circulating Fluidized Bed Technology H* (Edited by Basu, P. & Large, J. F.). Pergamon Press, Toronto. 181-191.
- Yerushalmi, J., Turner, D.H., Squires, A.M., 1976. The fast fluidization bed. *Ind. Eng. Chem. Process Des. Dev.* 15, 47-53.
- Zhang, W., Johnson, F., Leckner, B., 1995. Fluid-dynamic boundary layers in CFB boilers. *Chem. Eng. Sci.* 50, 201–210.
- Zhang, W., Tung, Y., Johnson, F., 1991. Radial voidage profiles in fast fluidized beds of different diameters. *Chem. Eng. Sci.* 46, 3045-3052.
- Zhang, M., Qian, Z., Yu, H., Wei, F., 2003. The solid flow structure in a circulating fluidized bed riser / downer of 0.42-m diameter. *Powder Technol.* 129, 46–52.

Zhou J., Grace J.R., Lim C.J., Brereton C.M., 1994. Particle velocity profiles in a circulating fluidized bed riser of square cross-section. Chem. Eng. Sci. 50, 237-244.

Zhu, J., 2010. Circulating turbulent fluidization - A new fluidization regime or just a transitional phenomenon. Particuology 8, 640–644.

Zou, B., Li, H. Z., Xia, Y.S., Ma, X. H., 1994. Cluster structure in a circulating fluidized-bed. Powder Technol. 78, 173–178.



## Chapter 2

# Radioactive Particle Tracking (RPT) and Benchmarking for High Velocity Conditions

### Scope

In this chapter, measurement techniques available for solid velocity measurement in gas - solids flow are briefed. Radioactive particle tracking (RPT) technique and implementation of RPT technique are explained. Further, the sources of error in RPT technique are explained. A methodology has been developed to quantify the suitable acquisition frequency for RPT experiments and accuracy which can be achieved at optimized frequency. Finally effect of dynamic bias on RPT performance for high velocity system is discussed.

### 2.1 Introduction

Investigation of multiphase flow reactors demands the use of sophisticated measuring techniques with capability to provide the required information over the entire flow field, both global (time averaged) and local, at multiple scales (Chaouki et al., 1997). Aside from the mean velocities and volume fractions, information about fluctuations is also needed. While such data are “stand-alone” sets of information and can be directly used to develop design and scale-up strategies, it also provides information that is crucial to establish the validity of phenomenological flow models and Computational Fluid Dynamics (CFD) models. A fair validation of CFD models must involve validation at multiple scales, for which one needs experimental information also at multiple scales (and not just spatial and temporal averages). Detailed review of the measurement techniques are given in Nieuwland et al. (1996), Chaouki et al. (1997), Boyer et al. (2002), van Ommen and Mudde

(2008), Upadhyay (2010). A brief review of different velocity measurement techniques used in circulating fluidized bed (CFB) is presented here. Techniques used in the literature can be classified as: invasive and non-invasive.

### **Invasive techniques**

In Invasive techniques, a probe is inserted inside the vessel to measure the flow field. The presence of a foreign element inside the vessel disturbs the flow field at the point of measurement itself, though the thickness of the probe is very small (sometimes in order of few  $\mu\text{m}$ ). Further, presence of solid particles, which are moving at relatively higher velocity ( $\sim$  few m/s), can damage the probe. However, due to the ease of application to obtain local values, invasive techniques are widely used. Optical fiber probes, Pitot tube, extraction and capacitance probes are the commonly used invasive technique. Except optical fiber probes, other techniques are bulky and thus disturb the flow considerably. Pitot tube and extraction probe measure mixture properties and/or require separation of phases to obtain the solids velocity (Ligrani et al., 1989). However, they have found limited application in CFB particularly in last two decades.

#### ***Optical fiber probe***

Optical fiber probe can be used to measure both velocity and solid volume fraction. It works based on the light reflection by the solids. Intensity of reflected light depends on the solid concentration, size and material properties of solids (Werther and Molerus, 1973; Caloz, 2000). In literature different types of optical fiber probes are used which primarily differs in number of fibers used for receiving and transmitting light signal. For velocity measurement, time taken by the solids to travel between two receiving probes is measured. Cross correlation is used to find the time traveled between the two probe points by assuming constant solids concentration between the two points. For better measurement of particle

velocities, probe diameter should be small. If the diameter of probe is in the order of 1.5 mm to 2 mm, reflection measured by the receiving probe is of group of particles. Hence, in this case, cross-correlation will have preference for the solid clusters and individual particle velocity is missed. Further, in case of optical fiber probe, measured velocity is a function of the distance between the receiving probes and acquisition frequency. If the distance between the probe points is high or acquisition frequency is quite low then particle may travel in the lateral direction leading to the disparities in the measurement. Hence, the probe must be compact and aligned in the direction of flow. To overcome the above limitations five point optical fiber probe is generally used in CFB. Typical size of a five point optical fiber probe is of 200  $\mu\text{m}$ . This helps in acquiring signal from a single or a group of smaller number of particle depending upon particle size. Velocity values are accepted only when the velocity evaluated by both pairs of fibers fall within the tolerance limit. This minimizes the error and increases the reliability of probe. Figure 2.1 shows the schematic of five fiber probe aligned in the axis.

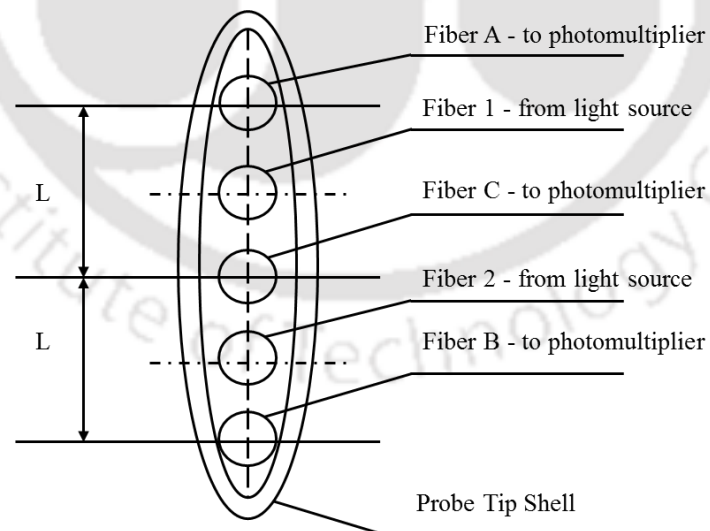


**Figure 2.1 Five fiber optical probe (adapted from Zhu et al. (2001))**

## **Noninvasive techniques**

Measurement techniques which are not intrusive and do not affect the flow are called as non-invasive techniques. Laser Doppler Velocimetry (LDV / LDA), Positron Emission Particle Tracking (PEPT), Particle Image Velocimetry (PIV), Radioactive Particle Tracking (RPT), are the widely used non-invasive techniques in CFB for local velocity measurement. Even though noninvasive techniques exist for a long time, it has been found profound use in CFB for the past two decades. Each of these techniques is briefly explained below.

### ***Laser Doppler Velocimetry (LDV)***

LDV uses the Doppler effects to measure velocity of solids in CFB. Doppler Effect is defined as the change in the frequency of light or sound, which is observed when the source, observer or both is in motion. This change is proportional to the distance between the source and observer. With increase in the distance observed frequency decreases while frequency increases with decrease in the distance. In LDA experiments, for the light source, particle acts as a moving observer and which in turn acts as a moving source for the detector / receiver. Light scattered by the seeded particles is proportional to the velocity of the particle. Solids, bubbles or droplets are used as the seeded particles. LDA technique can be operated in dual beam mode or fringe mode. Fringe mode is more commonly used as shown in the Figure 2.2. In fringe mode, two laser beams are used to form a measurement volume. Due to the interference of two different beams of same amplitude and frequency, alternating bands called fringes are formed. Fringe spacing is a function of angle between incident beams and wavelength of the beam. When the particle passes through the measurement volume, change in the frequency is observed in the detector, called as Doppler bursts. Velocity is calculated from the fringe spacing and time (from Doppler bursts). Velocity

calculated is independent of the direction. To obtain the directional velocity, one of the beam frequency is shifted, thereby creating fringe motion in the predefined direction. 3D components of velocity are measured with increased number of probes. Volume formed of three laser beams are used for this purpose.

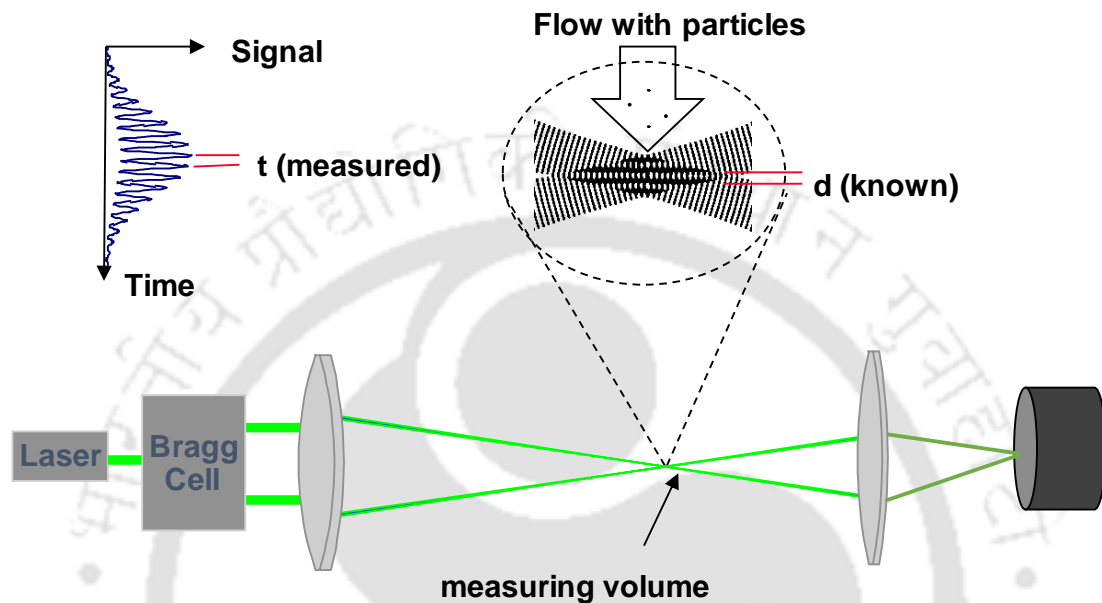


**Figure 2.2 Schematic of LDA (Courtesy Dantec Dynamics)**

Advantages of LDA technique are

1. Spatial and temporal resolution is very high
2. Calibration is not required

Disadvantages of LDA techniques are

1. Due to scattering of light, volume fraction more than 5% cannot be used
2. Transparent investigation zone is necessary
3. Optical arrangement is tedious
4. Provides point measurement

### ***Particle image velocimetry (PIV)***

Particle image velocimetry is also an optical based technique. However, PIV measurements are for field values where all the values in the predefined area can be measured. In PIV, seeded particles are photographed at sufficiently short interval whose subsequent images give the movement of the seeded particle within that interval. Typical PIV system consists of laser light, image recorder and image processing software (Figure 2.3). Laser lights are used to form laser sheet. Laser sheet illuminates the tracer particles in the imaging field. To avoid blurring of image, illumination duration of light should be short enough that the particles / tracers are frozen for the duration of imaging (Prasad, 2000). Pulsed lasers are used for illumination. Since the pulsed lasers operate at a fixed frequency, more than one laser is used to obtain the desired interval of pulse train. Using mirrors, lights are adjusted to form laser sheet at the desired region. The light scattered by the tracer particles are recorded by cameras such as CCD (Charge Coupled Device) or CMOS (Complementary Metal Oxide Semiconductor). The CCD sensors are more sensitive and less noisy; however, CMOS sensors are faster. From the subsequent images, particle movements are obtained. The recorded images are divided into smaller sub-areas called interrogation areas. By evaluation of the subsequent images, displacement vector in the interrogation area is obtained. For evaluation, statistical methods like cross correlation, adaptive correlation, etc. are used. Typically, 2D planar PIV is the most used one. Recently, 3D volumetric PIV is also introduced to measure all the three components of the velocity. Major issues in PIV include its inability to measure in the high volume fraction systems and matching refractive index at the different interfaces. Further, temporal resolution is limited. Recently, High-Speed Particle Image Velocimetry (HSPIV) is used to overcome the temporal resolution limitation, which has a sampling rate up to 1 million / sec. Still the local measurements inside the virtually opaque system are a challenge. Few PIV studies on CFB uses especially

designed borescope to overcome this limitation (Tartan and Gidaspow, 2004; Gopalan and Shaffer, 2013). However, use of borescope which is placed locally at different locations to measure the velocity field in the region of interest, makes the technique intrusive.

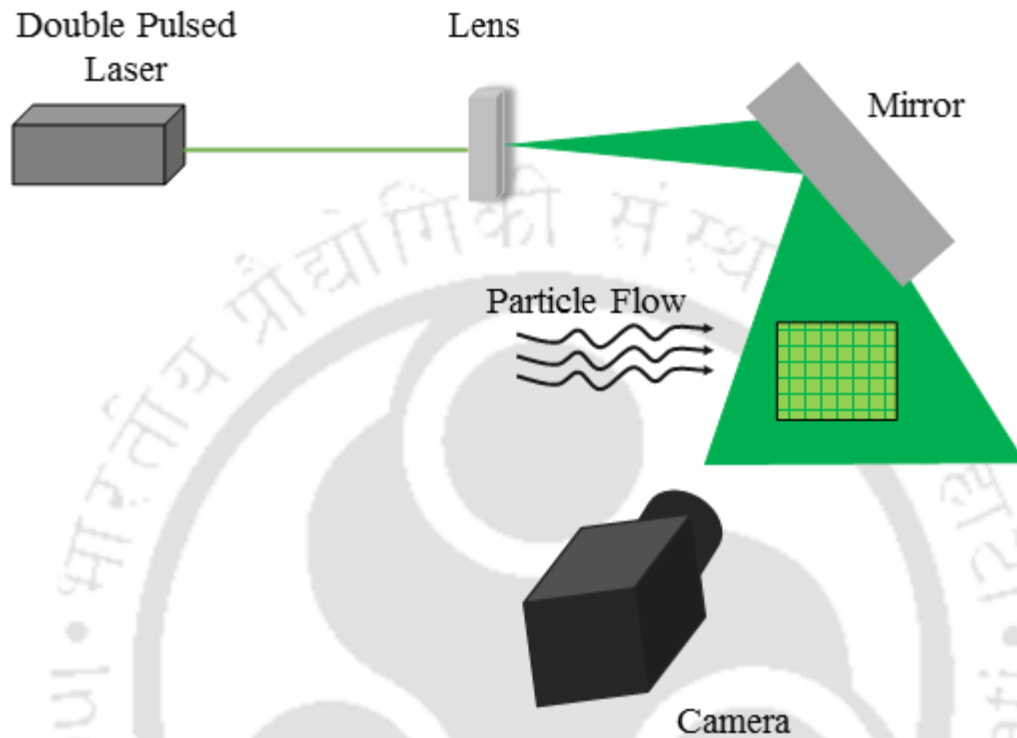


**Figure 2.3 Schematic of PIV measurement principle**

***Positron emission particle tracking (PEPT)***

Positron emission particle tracking (PEPT) is a radiation based non-invasive technique. Annihilation occurs when the positron and electron collide, producing two anti-parallel gamma rays of equal energy. PEPT involves detecting the pair of gamma rays from the same annihilation and uses multiple such instances for finding the position of the tracer. Typically,  $^{18}\text{F}$ ,  $^{61}\text{Cu}$ ,  $^{66}\text{Ga}$  radionuclides are used to prepare tracer, which is similar to the phase of interest. Position sensitive gamma ray cameras are used. Cameras are placed on either side of the column as shown in the Figure 2.4. Earlier, gas filled multi-wire proportional chambers were used as detectors, however, with recent developments NaI (TI)

and BGO are used for scintillation in the positron camera. Positron cameras having surface area of  $0.59 \times 0.47 \text{ m}^2$  are used in University of Birmingham recently (Parker and Fan, 2008; Chan et al., 2009). A single tracer particle, which emits positron, is introduced into the system. Positron emitted by tracer annihilates with the electron present in the material surrounding the tracer which produces two back to back gamma rays, representing the line passing through the tracer. Multiple such lines of resolution is used for position reconstruction, by triangulation. In theory, two such lines are enough for reconstruction. However, in practice, about 50 are used. This is because many of the events detected may be corrupt due to the Compton scattering and/or two detected gamma rays may not originated from the same annihilation event. These corrupted events are removed before finding the position by triangulation. The detectors at both ends are operated in coincidence with resolving time of 7 ns (Parker et al., 2002). Thus, events recorded within this resolving time can be considered from same annihilation.

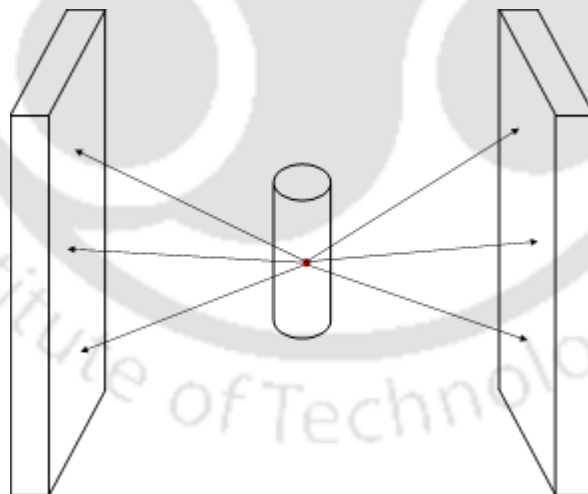


**Figure 2.4 Schematic of PEPT measurement principle**

Spatial accuracy of 1 mm is reported for the speed of 1 m/s. (Seville et al., 2005). However, the temporal resolution is in the order of milliseconds (Chan et al., 2009). The major advantage of PEPT technique is that it does not require pre calibration. However, limited

energy of the gamma-rays produced due to annihilation (512 keV) and cost is the major drawback of this technique which makes it of limited use. Further with change in the attenuation of the system, spatial and temporal resolution varies as the corrupted event increases with attenuation of the system.

### ***Radioactive particle tracking (RPT)***

Radioactive particle tracking (RPT) is a radiation based non-invasive technique like PEPT. In RPT, motion of a single gamma ray emitting tracer particle is tracked using series of scintillation detectors placed around the system of interest (Figure 2.5). The intensity of radiation emitted by tracer particle is recorded by each detector. The basic underlying principle is counts (photons) recorded varies with position. Recorded counts are a unique function of distance between tracer particle and detector, solid angle, attenuation and time of acquisition. Since the solid angle and attenuation changes with the position in the system, calibration is required. In calibration, tracer is kept at known positions and counts recorded on each detector for this known position is noted down. Similarly, a distance count map is generated for all the detectors used in the measurement for all the locations inside the column of interest at 'in-situ' condition. The position of tracer particle is reconstructed during the actual experiments by comparing the counts recorded by each detector during the experiments with counts recorded during the calibration. Thus, Lagrangian position time series of the tracer particle is obtained. Instantaneous velocity of the tracer particle is calculated by time differencing of two successive Lagrangian particle positions. The tracer particle used in experiments should be identical to the phase of interest whose velocity is to be mapped. In case of tracking solid phase, size, shape and density of the tracer particle should be same as of the solids present in the system. In case of liquid, tracer particle should be neutrally buoyant. NaI (Tl) is the most commonly used scintillation detectors because of the cost factor, others like BGO are also in use. In principle, to obtain a position in three

dimension, minimum four detectors are required. However, due to the statistical nature of gamma-ray emission and to cover region of interest more than four detectors are used.

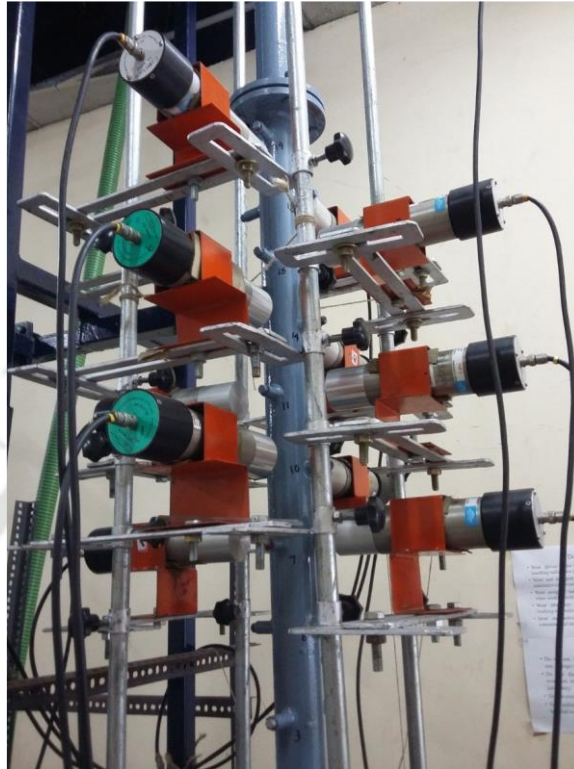


**Figure 2.5 Photograph of RPT setup**

Spatial resolution upto 1.0 mm at 50 Hz is reported (Upadhyay, 2010). Temporal resolution upto 200 Hz is reported (Bhusarapu et al., 2006). Versatility, scalability and portability are the major advantage of the RPT technique which allows the use of RPT technique for any system (gas-liquid, gas-solids, liquid-solids and gas-liquid-solids) at any scale (laboratory and pilot plant scale) of any dimension (from few cm to few m range). However, requirement of calibration at in-situ condition is the major drawback of the technique which limits the application of the technique at high pressure and high temperature environment. Though, few authors (Rados et al., 2005; Sanaei et al., 2010) have implemented RPT at relatively high pressure and temperature and have shown that fundamentally this technique

is also applicable in these environments. However, such applications are quite a few in the literature.

### ***Selection of experimental technique for measurements in CFB***

To investigate any multiphase flow reactor/contactors, it is important to understand the phenomena occurring at different length and time scale. Therefore, implemented technique should have high spatial and temporal resolution, which can resolve the flow at all scale. Further, technique should be versatile enough to be used at laboratory as well as pilot plant scale with the same accuracy. Clearly, none of the technique available till date has all the features. Tebianian et al. (2015) compared PEPT, PIV, RPT and optical fiber probe techniques and concluded that all the techniques are qualitatively able to predict the profile. However, quantitatively the results do not match. Further, it has been reported that these quantitative differences might be due to the experimental limitation of each technique. For example, terminal settling velocity of tracer in RPT experiments is 5.4 times greater than solids used in the system.

Techniques discussed here are the most commonly used for investigation of circulating fluidized bed (CFB). Optical based techniques like PIV, LDA have high temporal and spatial accuracy compared with the radiation techniques. However, these techniques cannot be applied for dense flow conditions and accuracy of these techniques differs with the position and scale of the column.

The primary aim of current work involves investigation of flow dynamics in CFB at different scales and generation of reliable data for validation of advanced computational fluid dynamics (CFD) predictions. Therefore, a technique is needed which is modular, portable, non-invasive and accuracy should not vary with the scale. PEPT can be used only for low diameter system and hence, cannot be used for different diameter system. Further,

this technique is very expensive and bulky. Radioactive particle tracking (RPT) offers all the requirements of this work and also well-proven technique. Therefore, RPT is used for this investigation. In the subsequent sections, methodology, hardwares and softwares for implementation of RPT are discussed. Further, experiments to quantify the accuracy of RPT technique are also discussed.

## **2.2 Radioactive particle tracking technique**

RPT is not a new technique and has been implemented by several authors in past. The first generation RPT was reported by Kondukov et al. (1964) for flow mapping of solids in a gas-solid fluidized bed. However, only qualitative information was able to gather due to lack of suitable hardware and data processing. Later on the technique was improved by various researchers such as Meek (1972), Lin et al. (1985), Devanathan (1991), Larachi et al. (1997), Degaleesan (1997), Roy et al. (2000), Upadhyay (2010) who have used new hardware and developed various post processing methodology to improve the resolution and sensitivity of the technique to obtain rich data base for detailed investigation of multiphase flow system. Historical development of RPT technique was reviewed in detail by Upadhyay (2010). In current thesis, RPT is explained in brief with current state of art instrumentation.

### **2.2.1 Methodology**

In RPT, a tracer particle encapsulating a radioactive source is used as a marker of the phase. For liquid tracking, particle is made neutrally buoyant with the liquid and for the solid tracking, the size, shape and density of the tracer is made approximately same. RPT consists of two steps, viz calibration and experiment. In calibration, radioactive particle emitting gamma ray is kept at several known position and counts are recorded through the scintillation detectors, which are strategically placed around the vessel of interest. Thus,

distance - count map is generated. In experiments, tracer particle is free to move, similar to the phase of interest and it radiates gamma-rays (photons) during its path which is absorbed by the detectors placed around the vessel. The best possible position of tracer is obtained by comparing the counts recorded by the detectors during experiments and from the distance-count map generated during the calibration. Since the frequency of data acquisition is known, time differencing of the two successive instantaneous particle position gives instantaneous velocity (Lagrangian velocity). Ensemble averaged velocity is obtained by dividing the whole column into the small cells, much like the way it is done in computational fluid dynamics (CFD). The difference between instantaneous velocity and ensemble averaged velocity gives fluctuation velocity. RPT measurement not only provide, instantaneous, mean and fluctuation velocities, it also provides PDF of instantaneous velocities at all the locations. Flow chart explaining the methodology of obtaining various quantities is given in Figure 2.6. Various turbulence parameters calculated from the velocities are given in Table 2.1. In addition to turbulence parameters, dispersion coefficient, autocorrelation coefficient, hurst exponent, time of flight, circulation time distribution, RTD can also be calculated (Larachi et al., 1997; Degaleesan, 1997; Roy et al., 2000; Bhusarapu, 2005).

**Table 2.1 Quantities calculated from RPT experimental data (Roy et al., 2005; Upadhyay, 2010)**

|  |  |
|--|--|
| Instantaneous Velocity                     | $v_r = \frac{2}{\Delta t} [r_2 \cos(\theta_2 - \theta_1) - r]$ $v_\theta = \frac{2}{\Delta t} [r_2 \sin(\theta_2 - \theta_1)]$ $v_z = \frac{\Delta z}{\Delta t}$ <p>Where-</p> $r = \frac{1}{2} \sqrt{r_1^2 + r_2^2 + 2r_1 r_2 \cos(\theta_1 - \theta_2)}$ |
| Ensemble average velocity                  | $\langle v_q(i, j, k) \rangle = \frac{1}{N(i, j, k)} \sum_{n=1}^{N(i, j, k)} v_{q,n}(i, j, k)$   |
| Fluctuating velocity component             | $v'_q(i, j, k) = v_q(i, j, k) - \langle v_q(i, j, k) \rangle$  |
| Azimuthally average velocity component     | $\langle v_q(i, k) \rangle^{az} = \frac{\sum_{j=1}^{T_{dim}(i)} \langle v_q(i, j, k) \rangle N(i, j, k)}{\sum_{j=1}^{T_{dim}(i)} N(i, j, k)}$  |
| RMS velocity                               | $\langle v_q \rangle^{RMS} = \sqrt{\langle v_q'^2 \rangle}$  |
| Stress                                     | $\tau_{qs} = \rho_p \langle v'_q(i, j, k) v'_s(i, j, k) \rangle$   |
| Fluctuating kinetic energy per unit volume | $KE = \frac{1}{2} \rho_p [\langle v_r'^2 \rangle + \langle v_\theta'^2 \rangle + \langle v_z'^2 \rangle]$  |

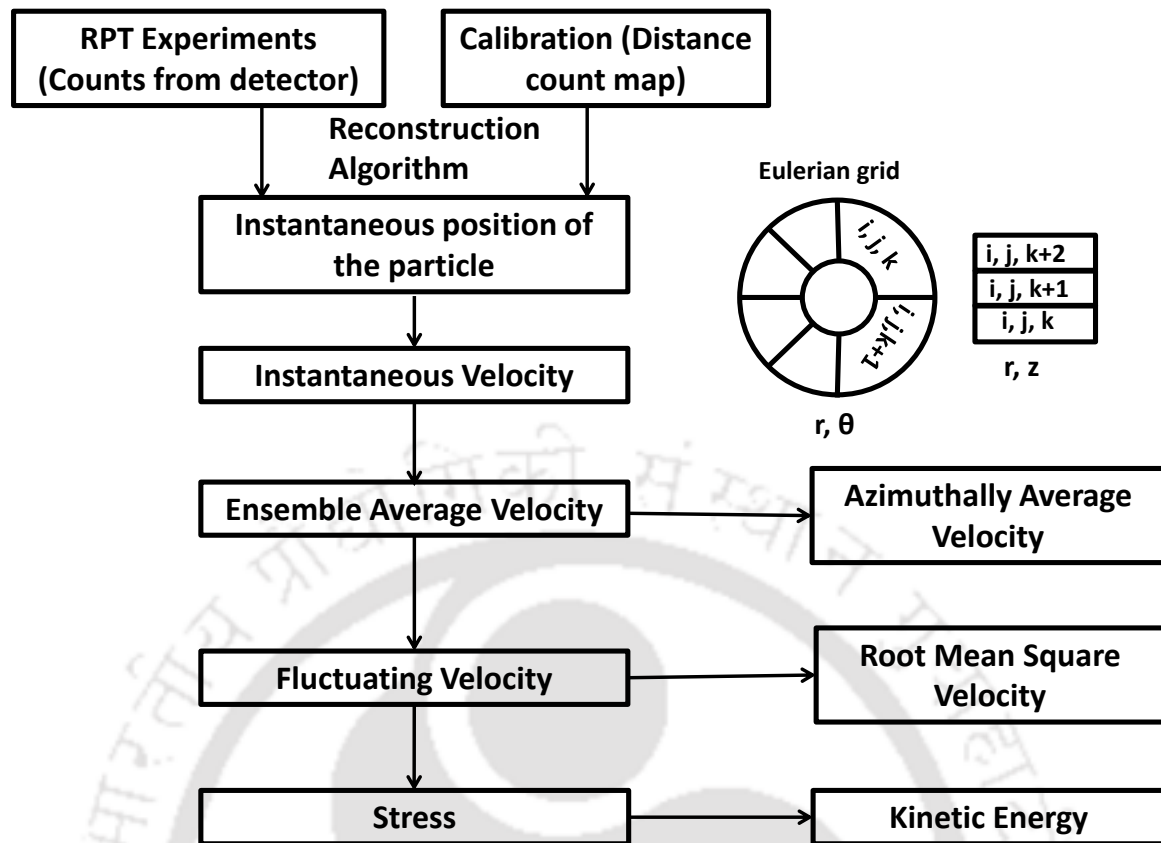


Figure 2.6 Flow chart for RPT data acquisition and processing

### 2.2.2 Implementation of RPT

In this section, various hardware and electronics, mechanism involved in the photon detection, approximations involved in the implementation are explained.

#### *Radioactive tracer particle*

For tracking the phase of interest suitable radioactive particle (gamma-ray source) is chosen based on the criteria given by Roy et al. (2002) and Upadhyay (2010). In literature, different ways are followed to make a tracer particle for RPT experiments. For liquid tracking, small amount of radiotracer, mostly Scandium-46, is enfolded by hollow polypropylene or polystyrene balls. The density of this polymeric ball is matched by keeping some air gap inside the ball before sealing (Devanathan, 1991; Degaleensan, 1997; Upadhyay, 2010). For solid tracking, size and density difference between the solids and tracer is adjusted by

coating with polypropylene or encapsulating the tracer particle in suitable material like polypropylene or aluminum beads. Roy (2000) and Bhusarapu (2005) have implemented RPT technique in liquid-solids and gas-solids circulating fluidized bed respectively to track the motion of the solid. Roy (2000) has packed Scandium-46 isotope granules in an aluminum bead of same size as of the solids used in the experiments. Density of the prepared tracer particle is matched with solids used in experiment by maintaining the air gap before sealing the aluminum bead. Bhusarapu (2005) has used Scandium-46 metal particle as a tracer but in order to match the density of Scandium-46 particle with glass beads used in experiment, a thin layer of neoprene was coated on the tracer particle. However, in case of solid tracking ideally, material of construction of tracer particle and solids present in the system should also be matched for better prediction of solid-solid interactions and solid fluctuation. Hence, in current work small amount of scandium powder is doped in the glass beads (explained in detail later). The prepared particle is sent to the nuclear reactor (situated in BARC, Mumbai) for irradiation to make it radioactive. The tracer particle prepared in this way not only ensures similar size and density as of the other solids (glass beads) used in the experiment but also maintain the material of construction same as of the other solids. Hence, a better prediction of solid-solid interactions and solid fluctuations can be expected.

### ***Photon detection and counting***

A basic pulse detection system and schematic are shown in the Figure 2.7. It consists of scintillation detector, high voltage supplier, amplifier, single channel analyzer/discriminator and data acquisition system. Tracer particle may emit single or multiple energy gamma rays e.g. Caesium-137 emits single gamma-ray with energy peak at 669 keV, scandium-46 emits two gamma rays with 100% probability with energy peak at 889 keV and 1120 keV. Detector crystal material absorbs gamma ray and emits light flash. This

light flash is converted to the electric pulse by photocathode. Electric pulse is amplified and sent to the discriminator. According to the voltage received, the signals are discriminated and counted. The number of photopeak counts recorded in a sampling time is given by Larachi et al. (1994), which is shown in equation 2.1

$$C = \frac{T\nu A\varepsilon_{abs}\phi}{(1 + \tau\nu A\varepsilon_{abs}\phi)} \quad (2.1)$$

Where,  $T$  = Sampling time (s)

$\nu$  = Number of gamma ray photons emitted per disintegration

$A$  = Source strength (Ci)

$\phi$  = Photo peak fraction

$\tau$  = Detector dead time (s)

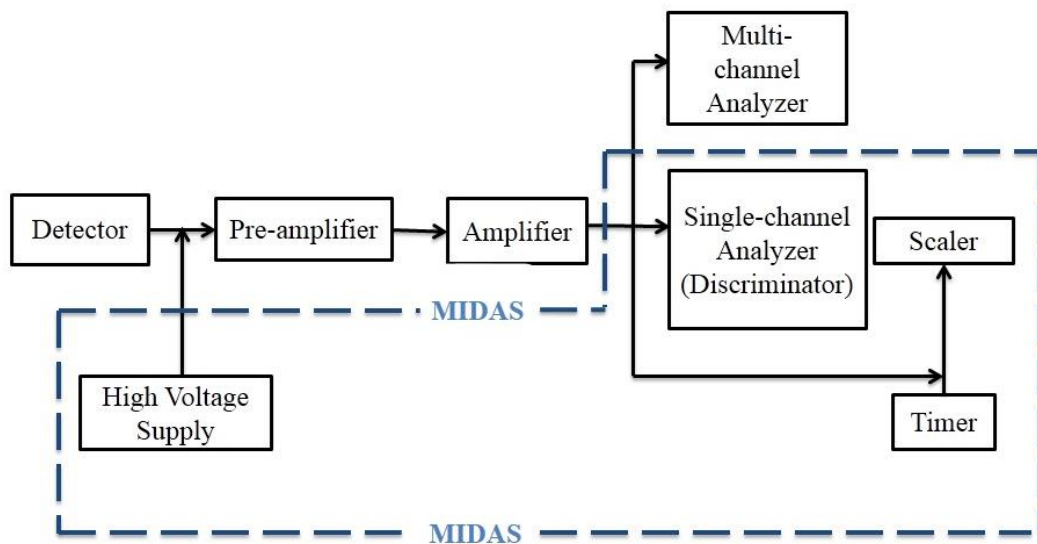


**Figure 2.7 Schematic diagram of data acquisition system**

### *Scintillation detectors*

Scintillation means “light flash”. Scintillation detector consists of scintillating crystal intimately attached with photomultiplier tube as shown in the Figure 2.8. When gamma ray falls on the crystal material, it transfers its energy to the metal present in the crystal, which excites the crystal material. While returning to normal state it releases light, this light is detected by photocathode. This photocathode emits electrons when it detects light. PMT consists of series of dynodes maintained in higher potential than the previous dynode to attract the electrons. When the electrons hits dynode, secondary electrons are emitted, thereby gets multiplied. Finally, once electrons reach anode of PMT an electric signal is produced. NaI (TI) is the commonly used detector for gamma ray detection.

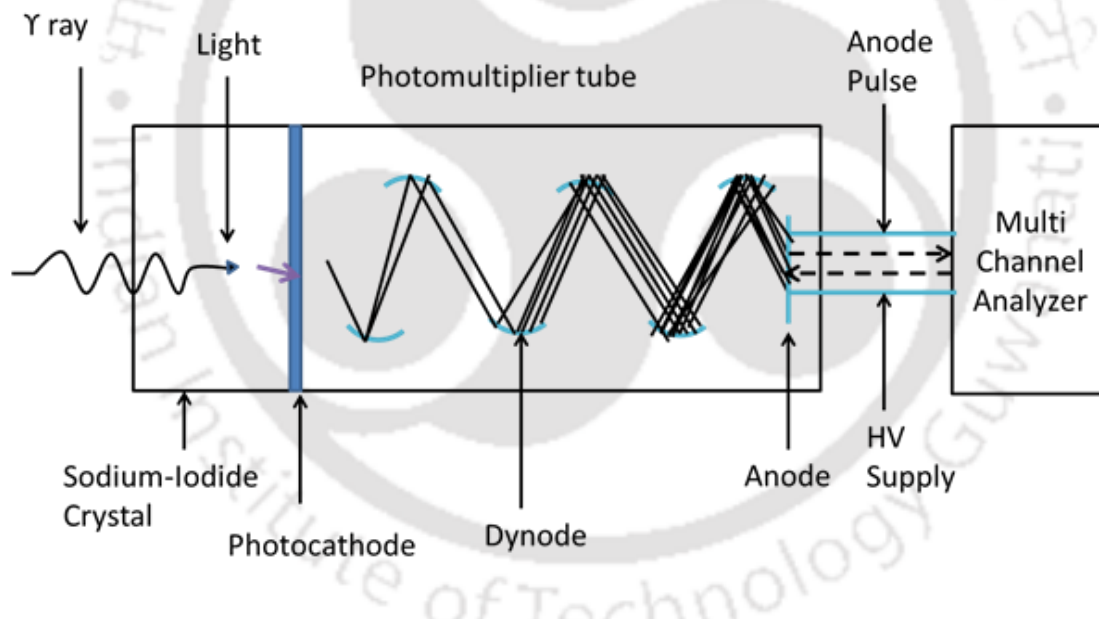


**Figure 2.8 Schematic diagram of NaI(Tl) detector**

### *Multichannel analyzer*

Multichannel analyzer (MCA) separates the incident photons according to their energy level. It converts analog signal to digital and bins according to their energy level. Each channel corresponds to the range of energy level to be binned. Increasing the number of

channels increase the resolution of spectra. Figure 2.9 shows the energy spectra of scandium-46 with peak from MCA with 1024 channels.

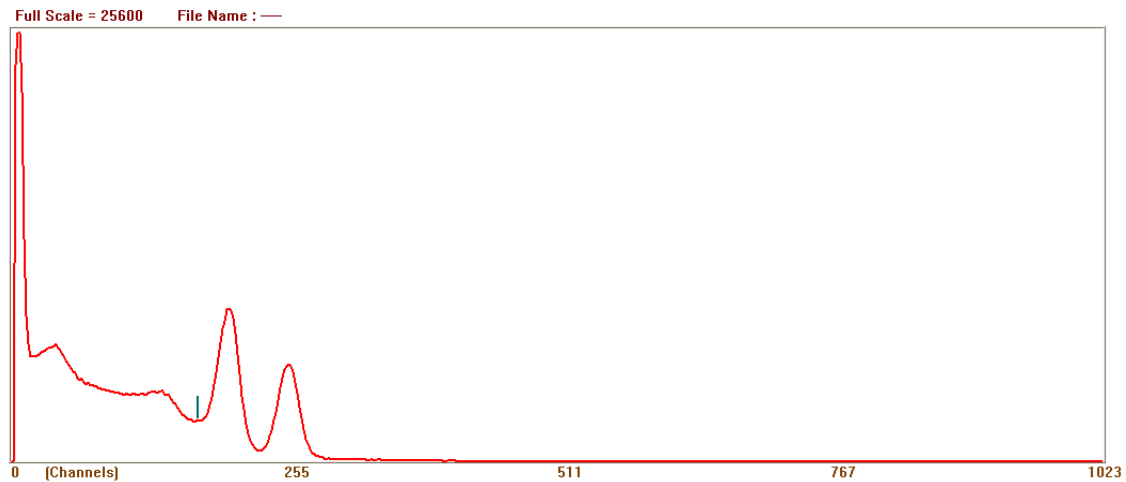


**Figure 2.9 Energy spectra of Scandium - 46**

### ***Single Channel Analyzer***

From the spectrum it can be inferred that it contains all the energy levels including Compton backscattered photons and electronic noise. These unwanted photons can be removed through a single channel analyzer (SCA) by using a threshold. A single channel analyzer (SCA) discriminates the incident photons between the LLD (Low level discriminator) threshold and the ULD (Upper level discriminator) threshold. SCA can be used for high frequency acquisition, as there are only threshold limits, it processes the data faster than MCA.

### **2.2.3 Calibration**

In RPT, a priori calibration at in-situ condition is needed for tracer particle position reconstruction. The accuracy of RPT experiment largely depends on the accuracy of calibration, which makes this step very critical. In calibration, a tracer particle is placed at a known location inside the vessel of interest at 'in-situ' condition with detectors, strategically placed around the column. The counts hereby recorded by the detectors are

noted down. Similarly, tracer particle is placed at different known locations inside the vessel and distance-count map is generated for all the detectors. Ideally, tracer particle should be placed at all the possible locations inside the vessel to achieve high accuracy. However, practically it is not possible to place the particle at all the locations. Further, it requires huge time and effort, which make the process tedious. To avoid this, Monte Carlo code for photon emission, transmission and detection developed by Larachi et al. (1994), later on modified by Upadhyay (2010) was applied, to mathematically generate the counts recorded on the detector for a known particle location. However to optimize the unknown fitting variables of Monte Carlo program, 'in – situ' calibration at few points is required (Upadhyay, 2010). In current work, Monte Carlo code is used to obtain the position – count map numerically using limited data of experimental calibration.

### ***Monte Carlo simulation***

An alternate way of constructing the distance - count map is by modeling the emission, transmission and subsequent detection of photons at the detector. While this is not intended to replace the real RPT calibration, however it provides a way of making the calibration part of the experiment more efficient. Also, it provides valuable information that can complement the experimentally acquired photon counts and allow for more accurate reconstruction. This modeling for gamma ray interaction is done by Monte Carlo simulation. In the Monte Carlo program, photon histories are tracked in their way from source, through the medium and their final detection at detector (Larachi et al., 1997; Beam et al., 1978). Both the geometry and radiation effects are accounted for estimation of detector efficiencies in capturing and recording the photons. To account the geometry effect, solid angle (angle created by the tracer particle to the detector) effect is accounted, which significantly affect the detector counting efficiency. Absolute efficiency can be evaluated with the equation 2.2 as given by Roy (2000). As most of the time tracer particle

is far from the detector axis the side face of the detector is more important than the front face.

$$\varepsilon_{abs} = \iint_{\Omega} \frac{\vec{r} \cdot \vec{n}}{r^3} \exp\left(-\sum_{j=1}^N \mu_j l_j\right) (1 - \exp(-\mu_D d)) d\Sigma \quad (2.2)$$

Where,  $\vec{n}$  the unit normal vector to the curved surface of the detector

$\vec{r}$  is the radius vector from source to detector

$\mu_D$  is the mass attenuation coefficient of the detector crystal material

$d$  is the penetration depth of photons in the detector crystal

$\mu_j$  is the mass attenuation coefficient of all the materials that comes in the path of photons between the source and the detector

In equation 2.2, mass attenuation, solid angle subtended by the detector disk and surface on the tracer particle and penetration depth of photons in the detector are unknowns. Penetration depth of photons can be obtained by geometrical arguments and explained in detail later. Solid angle is a complex function as particle emits photons in all the directions and each direction has different path length. It is calculated by tracking large number of photon histories in different direction through Monte Carlo method. Source strength, attenuation and dead time for each detector are evaluated using limited experimental values by suitable optimization algorithms.

In Monte Carlo method, domain is first chosen i.e. solid angle subtended. There are three possible type of particle position with respect to the detector location. As shown in Figure 2.10, if the particle is in position S<sub>1</sub>, photon can enter through both the flat and curved surface of the detector. If the particle in position S<sub>2</sub>, photon can enter only through the curved surface and if it is in position in S<sub>3</sub>, photon can enter only through the flat surface.

Depending on the particle position, solid angle subtended is different. The angular extremities  $\alpha_{\max}$ ,  $\alpha_{\min}$ ,  $\theta_{\max}$ ,  $\theta_{\min}$  and  $\theta_{\text{cri}}$ , which define the boundary of the surface as shown in the Figure 2.10 and arrived by the arguments as given by Beam et al. (1978). Different photon histories where each photon defined by  $\theta$  and  $\alpha$  in between the angular extremities are generated by using random generators (Beam et al., 1978). Depending on the exact orientation of the detector, all directions in the solid angle given by the  $(\alpha, \theta)$  combination are not equivalent. Appropriate statistical weights  $\omega(\alpha, \theta)$  according to the sampled direction is assigned to each photon sample. Beam et al., (1978) calculated individual directional weights  $\zeta(\alpha)$ ,  $\zeta(\theta)$  by geometrical arguments. So, the averaged value of solid angle is given by,

$$\tilde{\Omega} = \frac{1}{N} \sum_{j=1}^N \zeta(\alpha_j) \zeta(\theta_j) \quad (2.3)$$

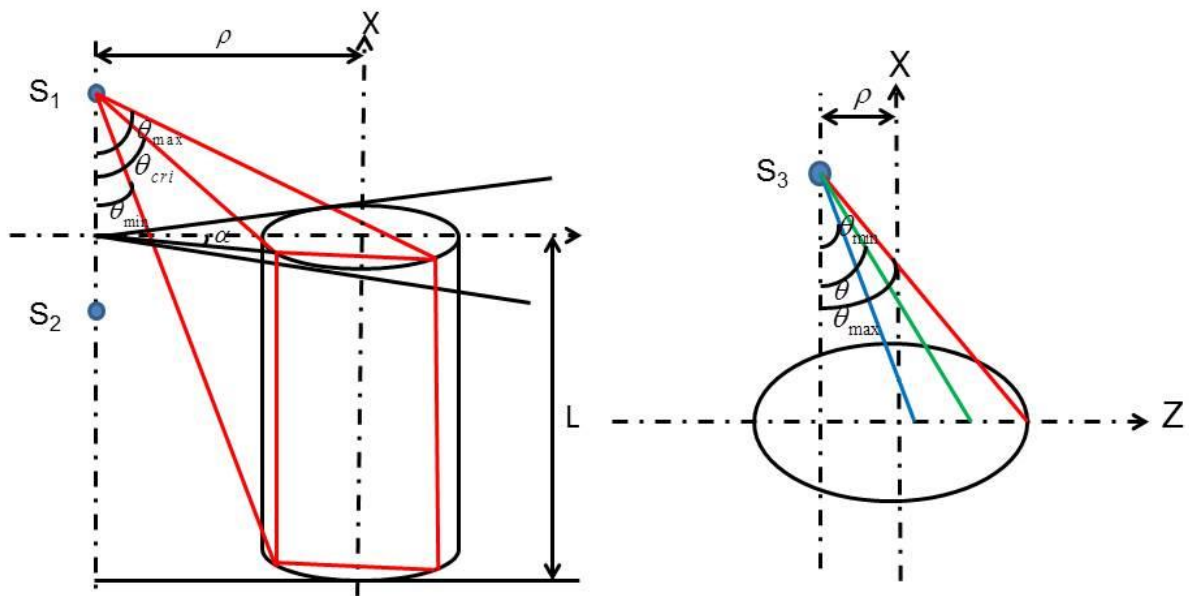


**Figure 2.10 Schematic diagram for relative positioning of source and detector**

Penetration depth of the photon in the crystal depends on the point of entry and exit. There are four possible ways in which the photon can enter and pass through the crystal, viz.,

Lateral entrance, bottom exit

Lateral entrance, lateral exit

Top entrance, bottom exit

Top entrance, lateral exit

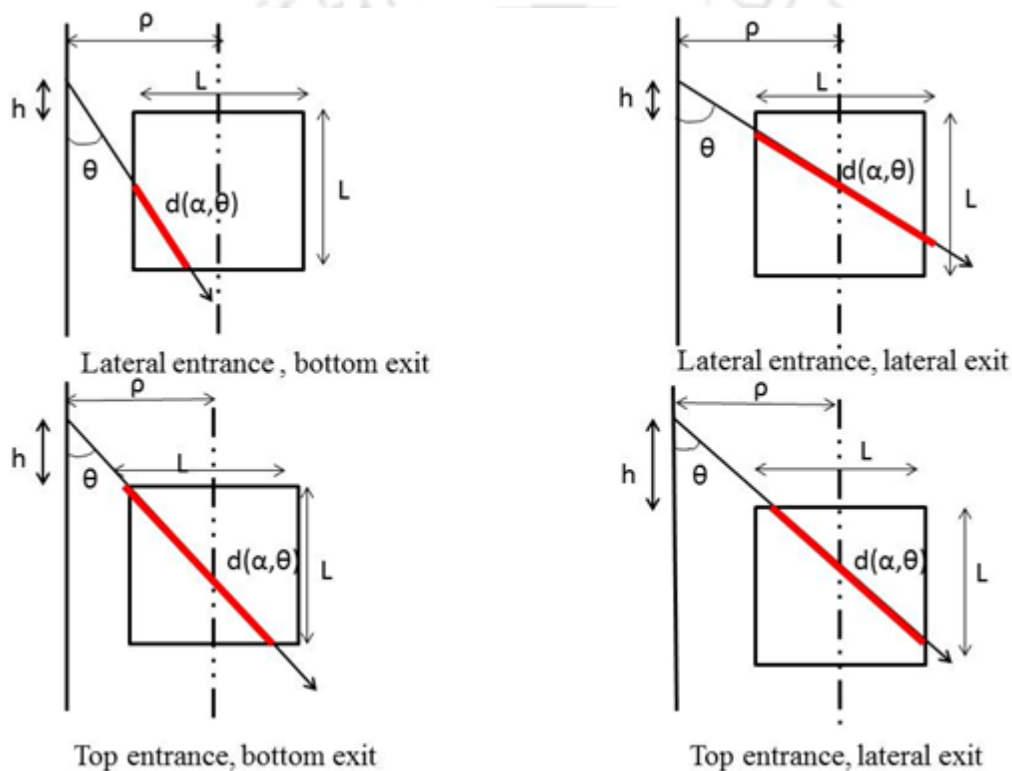


**Figure 2.11 Four possible cases in which photon can travel through a cylindrical detector**

Entry point is determined through angle,  $\theta$  and using geometrical arguments penetration depth is arrived (Figure 2.11). If depth of penetration is greater than chord length of detector, it is not consider as a count. Only the photons having depth of penetration less than the length of detector i.e. photon which will absorb by the detector crystal is considered as a count.

#### 2.2.4 Reconstruction algorithm

In RPT technique, a tracer particle that moves freely inside the vessel of interest tracks the phases of interest. During its sojourn through the vessel, the tracer particle emits photons, which are absorbed by scintillation detectors that are strategically placed around the vessel. The path of the tracer particle is reconstructed with the help of counts recorded by the scintillation detectors. In literature, mainly four type of reconstruction algorithm are used to reconstruct the tracer particle position. These are:

- Weighted Least Square Regression Method
- Monte Carlo Method
- Feed Forward Neural Network Method
- Cross Correlation Method

These methods have already been explained in detail by Upadhyay (2010). In the present work, Monte Carlo method is used for reconstructing the particle position. In Monte Carlo reconstruction method, two steps approach is used to reconstruct the unknown particle position. The first step is experimental calibration step. In experimental calibration step, tracer particle is placed at several known positions (on a coarse grid) and the counts of the photons are recorded at each detector. These counts are subsequently used to calculate the model parameter like dead time ( $\tau$ ) and medium attenuation coefficient ( $\mu$ ). Thereafter, equation 2.1 is used to generate an estimated count for every position of the tracer particle with respect to the detector. With the help of this model simulated calibration data is generated for all the possible location inside the vessel and stored in form of lookup table. The lookup table stores the co-ordinates of tracer particle and counts recorded by each detector as shown in Table 2.2.

**Table 2.2 Look up table showing calibration data**

| X | Y   | Z | C1  | C2  | C3  | C4  | C5  | C6  | C7 | C8 | C9 |
|---|-----|---|-----|-----|-----|-----|-----|-----|----|----|----|
| 0 | 0   | 0 | 400 | 385 | 400 | 150 | 125 | 150 | 40 | 30 | 40 |
| 0 | 0.2 | 0 |     |     |     |     |     |     |    |    |    |
|   |     |   |     |     |     |     |     |     |    |    |    |

Where X, Y and Z are the co-ordinate of tracer particle and C1, C2,.....C9 are the counts recorded by 1<sup>st</sup>, 2<sup>nd</sup>,....., 9th detectors. The second setup is experiments, where time – count map is obtained. To reconstruct an unknown particle position a chi ( $\chi$ ) square test (equation 2.4) is performed at every node point for which simulated calibration data is recorded in look up table. In other words, counts from the experiments and simulated calibration data are compared. The particle position is allotted to that node point for which chi square value is minimum. Similarly all the unknown positions of the tracer particle with time are reconstructed. To get satisfactory result, the value of chi square must be less than  $10^{-5}$ .

$$\chi^2(j) = \sum_{i=1}^{N_d} \frac{(C_i - M_i)^2}{\sigma_i^2} \quad (2.4)$$

Where j is the j<sup>th</sup> calibration node,  $C_i$  is the counts registered by the i<sup>th</sup> detector for the tracer particle at j<sup>th</sup> node (from the look up table),  $M_i$  is the counts measured by the i<sup>th</sup> detector for unknown particle position,  $N_d$  is the number of detector and  $\sigma_i^2 = C_i^2$ .

### 2.2.5 Optimal design of RPT experiments

Ideally, only four detectors are required to reconstruct the position of the tracer particle. However, more than four detectors are used to improve the accuracy of RPT measurement. As the electronics involved in RPT experiment is not very cheap, one needs to properly justify the use of each extra detector and electronics associated with it. Roy et al. (2002) has defined two parameters viz., resolution and sensitivity to quantify the performance of the RPT experiments. They have used Monte Carlo simulation to prepare distance count map in one dimensional and two dimensional geometry and have tried to numerically optimize the hardware involved in RPT experiments. Later, Upadhyay (2010) has used the same parameters, resolution and sensitivity, to quantify the goodness of the RPT measurements experimentally. He has optimized the optimal source strength, detector crystal material and detector size for different energy source. Further, he has found the optimal way of detector arrangement for a given column geometry. Though the results are limited to a particular column geometry and system type, the same approach can be used to optimize the detector arrangement prior to RPT experiment, to enhance the accuracy of the measurement. In current work, same approach is used to optimize the RPT measurement. The resolution and sensitivity are calculated for different possible detector arrangements for each column and only the arrangement that provide high resolution and sensitivity, is used for the measurement. Resolution is defined as the minimum distance between two neighboring position that can be discriminated. Sensitivity is defined as the fractional change in the counts with small change in the position. For the tracer particle moving in Z direction resolution and sensitivity can be calculated by using the equations 2.5 and 2.6, respectively (Roy, 2000).

$$R(z) = \sigma_c \frac{dz}{dC} \quad (2.5)$$

$$S(z) = \frac{1}{C} \frac{dC}{dz} = \frac{d \ln C}{dz} \quad (2.6)$$

Where,  $\sigma_c$  denotes the variance in counts due to the source fluctuation.

Further, it has been shown by Roy et al. (2002) that for a scenario of multiple detectors, the composite resolution and sensitivity functions for  $N$  detectors distributed in space can be represented by equation 2.7 and 2.8, respectively.

$$\frac{1}{\sigma_r(x, y, z)} = \frac{\cos \alpha}{\sigma_x(x, y, z)} + \frac{\cos \beta}{\sigma_y(x, y, z)} + \frac{\cos \gamma}{\sigma_z(x, y, z)} \quad (2.7)$$

$$S_r(x, y, z) = S_x(x, y, z) \cdot \cos \alpha + S_y(x, y, z) \cdot \cos \beta + S_z(x, y, z) \cdot \cos \gamma \quad (2.8)$$

In the above equations,  $\alpha$ ,  $\beta$  and  $\gamma$  are the direction cosines of the point  $(x, y, z)$  where the tracer particle is located in the domain of interest.

In any experimental setup, it is desirable to maximize sensitivity and resolution, i.e., maximize the value of  $S(z)$  and minimize the value of  $R(z)$ . The tracer particle source strength can drastically change the optimal configuration (Upadhyay, 2010). Further, dead time is also a function of source strength. Hence, arbitrary chosen source strength value to optimize the detector assembly may lead to wrong arrangement. Therefore, in the present study, to improve the accuracy of the RPT, resolution and sensitivity are calculated from the counts of calibration data itself. That is, count map generated from the Monte carlo program, where the unknown variables of the Monte Carlo codes are found by using calibration data points.

### 2.3 Implementation of RPT technique for high velocity system

RPT has been successfully implemented on variety of multiphase flow systems which are gas-liquid (Devenathan, 1991; Degaleesan, 1997; Upadhyay et al., 2013 etc.), gas-solids (Lin et al., 1985; Larachi et al., 1995; Mostoufi and Chaouki, 2001; Bhusarapu, 2005; Upadhyay and Roy, 2010 etc.), Liquid-solids (Limtrakul et al., 2005; Roy et al., 2005; Jain et al., 2014 etc.) and gas-liquid-solids systems (Kiared et al., 1997; Fraguio et al., 2006, 2007; Lefebvre et al., 2007 etc.). Most of the RPT investigations were carried out at relatively low velocity systems. There is only one study reported in literature where RPT is implemented on a high velocity gas-solids circulating fluidized bed system (Bhusarapu, 2005). However, Bhusarapu (2005) has reported an uncertainty of 5 mm in reconstructing the position of the tracer particle when data was acquired at a frequency of 200 Hz which corresponds to an uncertainty of 1 m/s in velocity prediction.

The accuracy of RPT measurement depends on the ability of the system to detect the path and position of the tracer particle with time in the phase of interest. The ability of the tracer particles to follow the phase of interest can be addressed by carefully designing the tracer particle, which is already presented by various researchers (Degaleesan, 1997; Roy, 2000; Upadhyay, 2010 etc.). The factors, which affect the ability to reconstruct the position of tracer particle, are:

- *Statistical fluctuation of gamma emission*
- *Fluctuation in medium attenuation with time*
- *Accuracy of reconstruction algorithm*
- *Dynamic bias*

Error due to the first two factors can be minimized by using the time averaged count (recorded at in situ conditions in the calibration step) for reconstruction. Time averaged

count ensures that maximum difference is within the standard deviation of Poisson distribution rather than twice of it. Upadhyay (2010) studied the accuracy of different reconstruction algorithms (weighted least square regression method, Monte Carlo method, feed forward neural network method and cross correlation method) used in RPT technique. It was found out that both Monte Carlo method and cross correlation method is able to locate the path of tracer particle with high fidelity.

In RPT, tracer particle is kept stationary during calibration and counts are recorded on the detectors at a particular frequency. However, during experiments, tracer particle moves freely inside the system of interest and data is recorded with the same frequency at which calibration was performed. Hence, the recorded count is an integral of counts for different positions which tracer particle has travelled between acquisition time intervals. For reconstruction of the tracer particle position, this integral of counts is compared with the stationary position counts from the calibration. This error is called dynamic bias. Figure 2.12 shows the schematic representation of source of dynamic bias error.

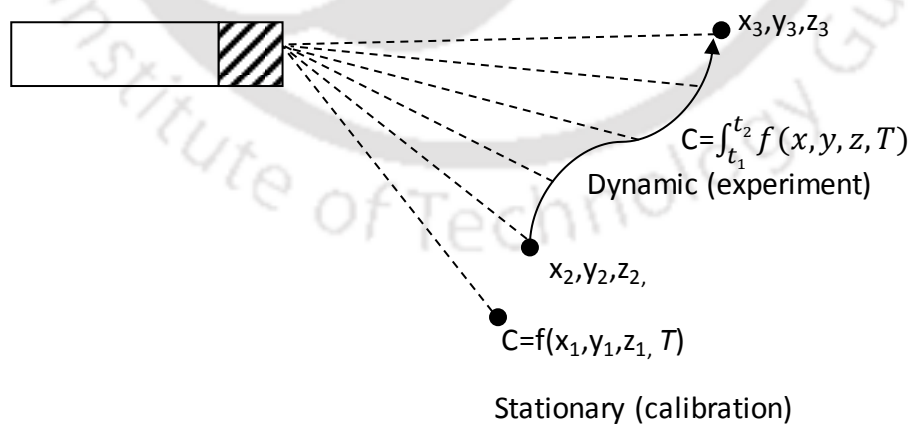


**Figure 2.12 Representaion of dynamic bias**

Though some effort has been made to determine the accuracy of RPT experiments by comparing the RPT results with an independent measurement technique (Chen et al., 1999; Upadhyay et al., 2012). However, it is not possible to determine the effect of dynamic bias on locating the exact position of the tracer particle during typical RPT experiments. Hence, a dedicated specially designed experimental setup is needed to determine the effect of dynamic bias on accuracy of RPT measurement. Few authors have tried to conduct accuracy studies under dynamic condition in a specially designed setup. The details of which are given below:

#### **Degaleesan (1997)**

In this work, two motors, screw conveyor and gears were used to generate the spiraling 3D motion. One motor was used to generate vertical motion using screw conveyor, which was connected to the vertical frame. On top of the vertical frame, another motor was fixed. Shaft of the motor is connected to the circular disc. Tracer particle was fixed at the tip of the plexiglass rod attached to the circular disc. Thus circular motion was generated by the second motor. Simultaneous operation of both motors gives the spiraling 3D motion. With these arrangements maximum displacement of 6.4 cm was achieved in vertical direction with 25.132 cm path circumference. Motion of tracer particle was tracked by using 16 detectors arranged around this assembly. Experiments were conducted and reported for different angular velocities at the same vertical velocity. Maximum angular velocity operated was 17.3 rad/s (3 Hz) and vertical velocity is 0.02 m/s. Data was acquired with 50 Hz frequency. Reconstructed position shows that tracer trajectory had precisely followed the trajectory of motion. The maximum, minimum, and RMS error was found to be -0.9, 0.66, 0.9 cm, respectively for maximum operating velocity. RMS error in velocity was reported as 5.4 cm/s in the x- direction. It is to be noted that the velocity was not constant

in the Cartesian co-ordinates. Further in this work, tracer movement was confined to the small distance and velocity at which experiments were performed was quite low.

### **Rammohan (2002)**

In this work, accuracy study was conducted in the stirred tank reactor (STR). Cylindrical tank of diameter 200 mm and L/D ratio of 1 was used in experiment with 6 blades Rushton turbine impeller. Impeller was driven by the motor placed at the top of the vessel. Four baffles were also present to give better mixing. However accuracy studies are conducted at the quiescent condition. Tracer was fixed at the tip of the turbine blade. Tachometers were used to monitor the impeller speed. Data was acquired at the frequency of 200 Hz and post processed to obtain the data corresponding to the acquisition rates of 25, 50 and 100 Hz. 16 NaI (TI) detectors were used to track the tracer particle. Experiments were conducted by varying impeller speeds from 60 rpm – 800 rpm equivalent to the tangential velocities 0.21 m/s - 2.79 m/s respectively.

Reconstructed radial position shows that RPT technique always underestimates the position of tracer particle compared to actual value (distance of the tracer from the axis of impeller). It was reported that with increase in velocity, minimum bias shifts towards the data acquired with higher frequency. For example: for the tangential velocity of 0.26 – 0.52 m/s, minimum bias lies in the frequency range of 25 – 50 Hz, while for the case of 1.05 – 2.79 m/s, it lies at 75- 125 Hz. It was also reported that at the frequency of 200 Hz, all the velocities give the same error. Tangential velocity predictions also follows similar trend as the radial position. However, it is important to note that in these experiments, for all the acquisition frequencies, RPT measurements always under predict the velocity compared to actual value with a minimum error of 20%. Further, it was reported that for all the velocity an optimal acquisition frequency window exists where the bias/error is minimum. For a

velocity range of 1.05 m/ to 2.79 m/s an acquisition frequency of 100 Hz was found to be optimal. Finally, contribution of dynamic bias error was found to be 14-30% of total error. It is to be noted that baffles used in the STR gives more attenuation compared with other places. Thus reconstruction at the dynamic conditions gives more error as evident from the reported results, which always under predict the velocity values.

### **Fraguio (2010)**

Piston - cylinder arrangement was used to generate the controlled motion. Pneumatic valves were used to control the cylinder pressure, thereby piston movement. Piston was operated at different speed from 0.1 – 1 m/s and overall it travels 20 cm. Aluminum rod was connected to the piston. Aluminum rod travels in the two phase mixture of the liquid and gas contained in the cylindrical column. Experiments were carried out at homogenous (no air input) and heterogeneous condition (at different air inlet velocities,  $U_g < 0.12$  m/s). Tracer particle was glued at the tip of the aluminum rod. Data was acquired at the rate of 50 Hz. Piston movement was photographically recorded. Processing of image provided the actual velocity of piston, which was evaluated from the positions by

- i. Time differentiating the successive positions
- ii. Time differentiating the position four time intervals apart
- iii. Time differentiating the entire transit (ascending / descending) by evaluating slope of the linear least square estimate of the reconstructed positions (LS)

PDF of the velocity showed that distribution is narrow for LS method and increased with decreasing time interval. It was also reported that the velocity calculated with LS method matches closely with imposed velocity value. Further, it was reported that with increase in the air velocity (heterogeneity) distribution increases in all the methods. However, it decreased with decrease in imposed velocity.

It can be observed that all these experiments were conducted below 2 m/s. In the above discussed studies, Degaleesan, 1997 and Rammohan, 2002 recommended to acquire the data at higher frequency while Fraguio (2010) suggested in opposite way. Hence, data reported in literature is inconclusive and fresh investigation is needed to resolve the issue. Further, there is no data available for a velocity more than 2 m/s, which is critically important for circulating fluidized bed.

### 2.3.1 Experimental setup

Figure 2.13 shows the photograph and schematic of specially designed experimental setup to study the ability of RPT experiments to locate the position of tracer particle. Two motors of similar power (1.5 kW) and dimensions, which are connected with a 1.02 m long belt, are used in the experiment. However, power is supplied to only one motor, which is connected with variable frequency drive (VFD) for precise control of motor RPM. Glass bead of 500 micron impregnated with Scandium - 46 is irradiated and used as tracer. The particle is glued on the belt to ensure one-dimensional motion. It also helps in locating the exact position of the tracer particle. Fourteen NaI(Tl) scintillation detectors are strategically placed around the belt as shown in Figure 2.13. Detectors are firmly fixed on a stand, which is grounded and is independent of the motor stand. This arrangement is made to avoid any vibration caused by the motor movement. To measure the RPM of the motor a high precision tachometer is used. Experiments are performed for different motor RPM to vary the speed of the belt and hence the velocity of the tracer particle. However, calibration is performed at stationary condition by placing the particle at different known locations on the belt. Data is acquired at different frequencies varying from 20 Hz to 100 Hz. A detailed experimental matrix is shown in Table 2.3.

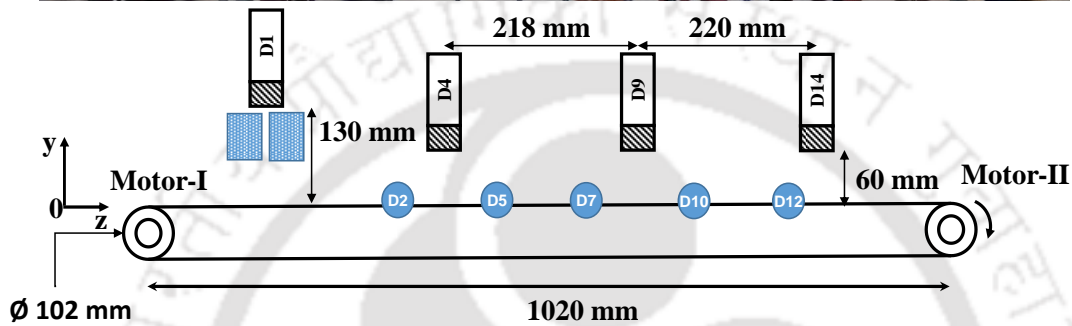


Figure 2.13 Photograph and schematic of experimental setup

Table 2.3 Experimental conditions

| Data Acquisition Frequency (Hz) | Velocity of the belt/tracer particle (m/s) |
|---------------------------------|--|
| 100                             | 0.851, 2.686, 4.852, 8.203                 |
| 83                              |  |
| 50                              |  |
| 33                              |  |
| 20                              | 0.851, 2.686, 4.852                        |

### 2.3.2 Resolution and sensitivity

Resolution and sensitivity are calculated for different detector arrangements for the current experimental setup. The arrangement, which provides maximum resolution and sensitivity, is used for further studies to achieve maximum accuracy. Figure 2.14 shows the resolution and sensitivity plots. Resolution is around 2 mm at the axis of the belt where tracer particle is placed. It should be noted that these experiments are performed in the air, which offer

almost no attenuation. Hence, counts recorded on detectors only depend on the distance between tracer particle and detector and solid angle formed by tracer particle on detector crystal. Therefore, the change in count with distance ( $dC/dz$ ) is low and hence a larger resolution is observed compared to the resolution, which will be observed in the presence of attenuation. Therefore, it can be concluded that these experiments are performed in severe condition and one will achieve better results in case of actual RPT experiments.

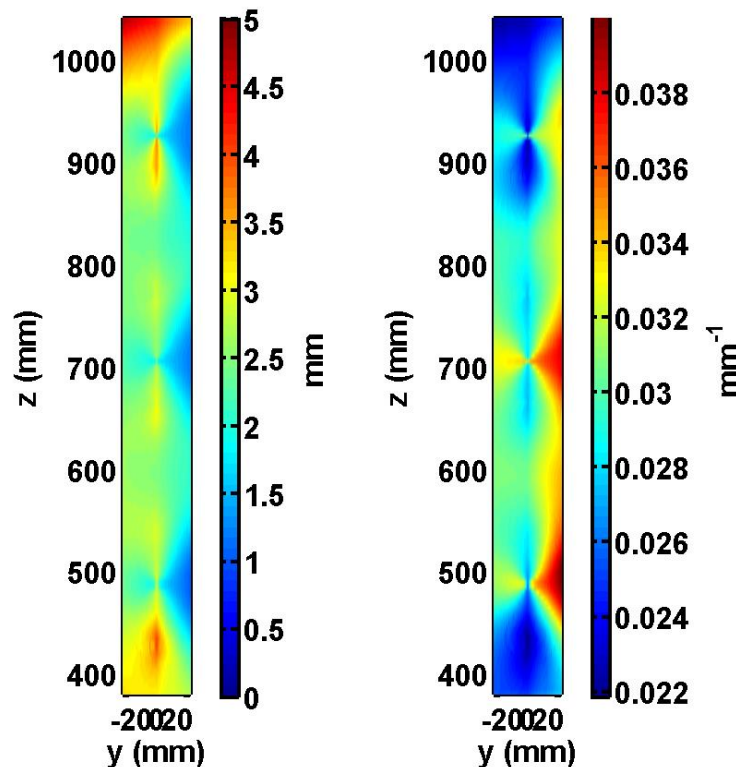


Figure 2.14 Resolution and sensitivity of the accuracy experiment

### 2.3.3 Results and discussions

#### *Stationary bias*

The ability of RPT measurement to accurately locate the position of the tracer particle is majorly affected due to the statistical nature of gamma emission, accuracy of reconstruction algorithm and data acquisition frequency. Upadhyay (2010) has studied the effect of

reconstruction algorithms on position reconstruction of the stationary tracer particle. However, the effect of data acquisition frequency on the ability of RPT measurement to locate the stationary position of the tracer particle has not been studied. Therefore, in the current work, with the same detector arrangement, the effect of data acquisition frequency on the ability of the RPT technique to locate the position of stationary tracer particle is studied. Experiments are performed by keeping the tracer particle at different positions distributed along the length of the belt. For each location data are acquired with different frequencies for long time (500 events/data points for each location at each frequency). To account the error due to statistical fluctuation, each event is treated as different data point and position of tracer particle is reconstructed by using the counts recorded on each detector for these individual events. This exercise is repeated at different positions and for different acquisition frequencies. It is to be noted that all these stationary positions, where accuracy of RPT measurement is tested, are not included in training of reconstruction algorithm. Figure 2.15 shows the reconstructed position of tracer particles at different locations for different data acquisition frequency. It is observed that for all the locations, deviation in reconstructed particle position increases with the increase in data acquisition frequency. Gamma emission and detection is a Poisson distribution process. The count recorded on detector is an integral of the count (area under the curve) between the time differences ( $\Delta t$ ) for which data is acquired. The probability of this integral count predicting the mean of the Poisson distribution increases with the increase in data acquisition time. Thus, with decreasing data acquisition frequency, error reduces. Table 2.4 shows the standard error obtained in position reconstruction at different frequency for different locations. It clearly shows that standard error in position reconstruction decreases with decrease in data acquisition frequency.

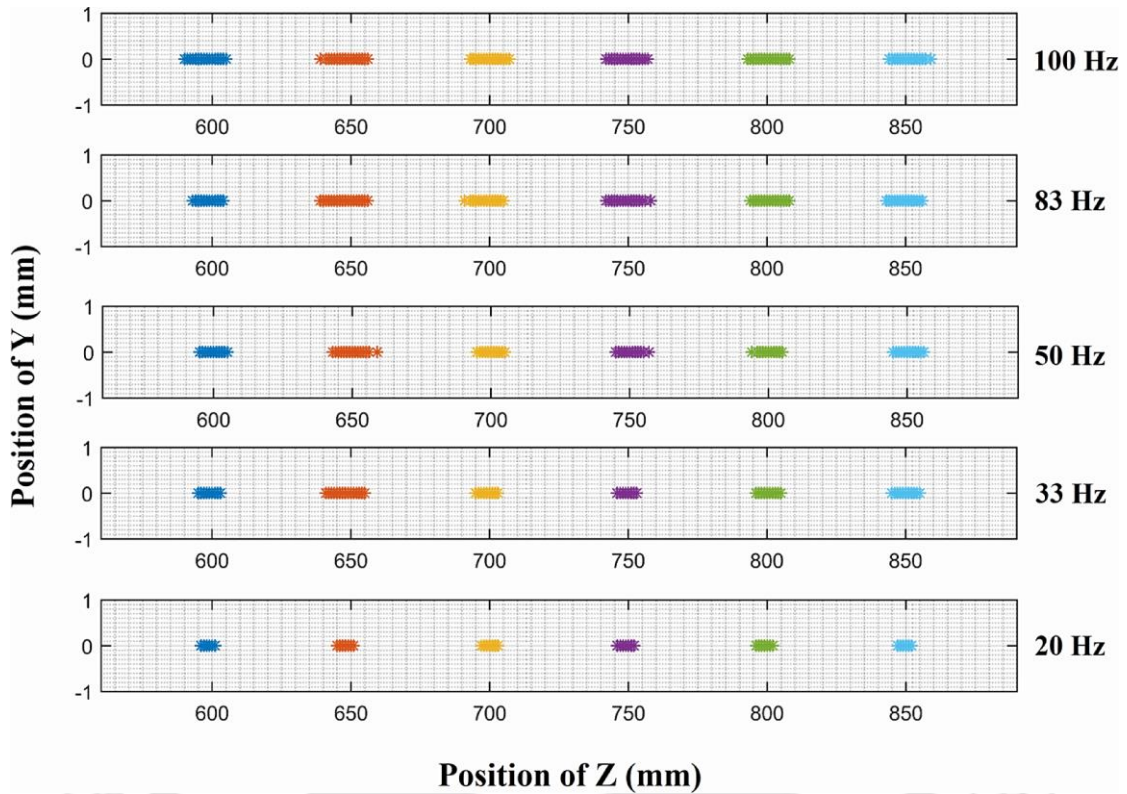


**Figure 2.15 Stationary bias**

**Table 2.4 Standard error in position reconstruction for stationary tracer position**

| Position | RMS error in position (mm) |        |        |        |        |
|----------|----------------------------|--------|--------|--------|--------|
|          | 100 Hz                     | 83 Hz  | 50 Hz  | 33 Hz  | 20 Hz  |
| 600      | 2.6514                     | 2.4645 | 1.7158 | 1.9824 | 1.6522 |
| 700      | 2.5071                     | 2.4029 | 1.7589 | 1.5716 | 1.2609 |
| 750      | 2.7085                     | 2.5079 | 1.8439 | 1.6124 | 1.4422 |
| 800      | 2.3164                     | 2.2108 | 1.7314 | 1.4463 | 1.1180 |
| 850      | 2.4694                     | 2.2436 | 1.7251 | 1.5073 | 1.1225 |

**Dynamic bias**

As previously explained, the dynamic condition of the tracer increases uncertainty (Figure 2.12). To quantify the error due to dynamic bias, experiments are conducted for different acquisition frequency and different velocity (given in Table 2.4). In these experiments

particle is in a dynamic condition. Hence, it is necessary to determine the accuracy of RPT experiments in terms of position reconstruction and velocity measurement. However, it is difficult to measure the actual position of the tracer particle with an independent measurement when the particle is moving. Hence, displacement is compared instead of the position of the tracer particle. To compare the displacement, error in displacement ( $\delta_m - \delta_a$ ) is plotted where the actual displacement ( $\delta_a$ ) is calculated through tachometer reading. Figure 2.16a shows the PDF of error in displacement for 0.85 m/s velocity of the tracer particle at different data acquisition frequencies. PDF is comprised of displacement calculated at all the locations under investigated length. Results show that standard deviation of the error in displacement increases with decrease in data acquisition frequency. It should be noted that error observed in these experiments is a combined effect of error due to statistical fluctuation, reconstruction and dynamic bias. Though it is difficult in current methodology to decouple the error caused due to stationary bias and dynamic bias, but it has been observed that error in dynamic condition has always been higher than error in a stationary condition. Further, it has been already established that the error due to stationary bias approximately remains same for a particular data acquisition frequency. Hence, the error above the stationary bias (mentioned in Table 2.4) for a particular data acquisition frequency can be seen as a contribution of dynamic bias, which reduces with increase in data acquisition frequency. Therefore, from these results it can be concluded that higher data acquisition frequency minimizes the error, in measured displacement, caused due to dynamic bias.

Instantaneous velocity in RPT experiment is calculated by time differencing of two successive particle positions ( $\Delta x / \Delta t$ ). Figure 2.16b shows the PDF of instantaneous velocity calculated through RPT measurement. The red line shows the velocity

measurement by a high precision tachometer and  $\langle v \rangle$  shows the mean velocity calculated through RPT experiments. Similar to displacement, PDF of instantaneous velocity is comprised of velocity calculated at all the locations under investigated length. Results indicate that though the error in displacement increases, the standard deviation of velocity prediction (calculated by using the mean velocity measured by tachometer) decreases with decrease in data acquisition frequency, Therefore, velocity prediction is better for lower data acquisition frequency compared to the higher data acquisition frequency. This is mainly because of  $\Delta x / \Delta t$ , which is used to calculate the velocity. Though the error in displacement is low at higher frequency, relatively lower value of  $\Delta t$  escalates the error in velocity measurement. Hence, acquiring the data at higher frequency to minimize the effect of dynamic bias, as suggested in literature, is not of much help particularly for velocity measurement. Therefore, one has to trade-off between accuracy in position reconstruction and accuracy in velocity measurement.

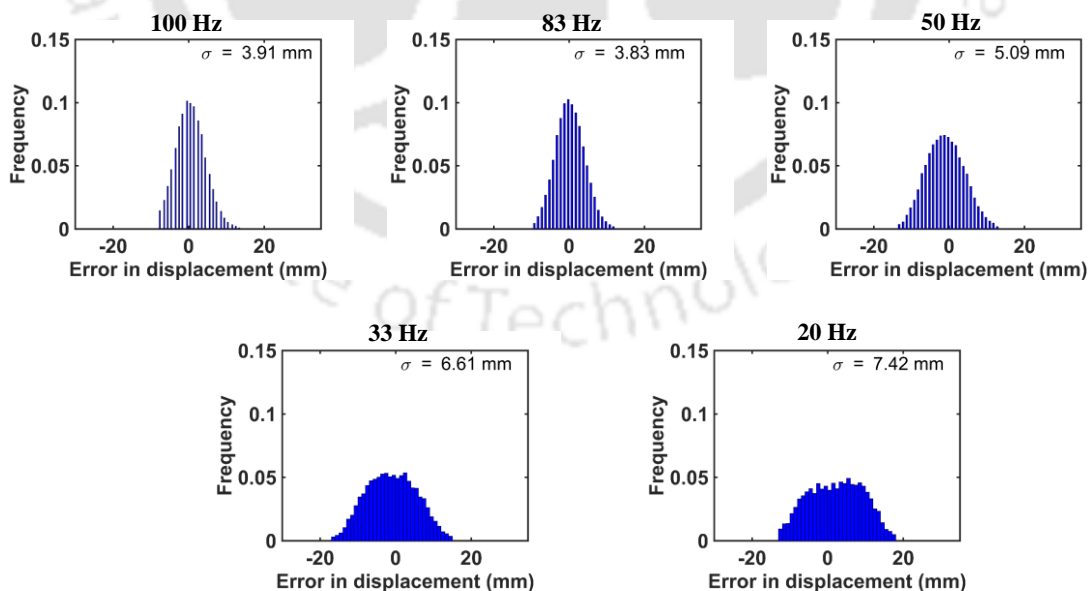


**Figure 2.16a** PDF of error in displacement at different acquisition frequency for tracer particle velocity of 0.85 m/s

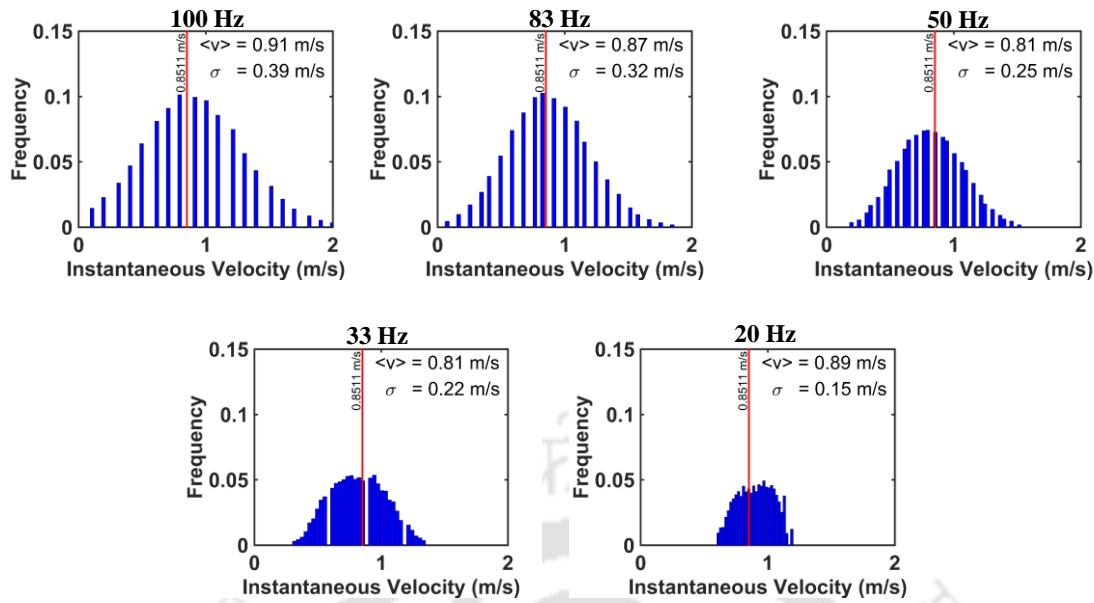


**Figure 2.16b PDF of instantaneous velocity at different acquisition frequency for tracer particle velocity of 0.85 m/s**

To find the optimal frequency range, experiments are performed for different velocity of the tracer particle. Figure 2.17 to Figure 2.19 shows the PDF of error in displacement and instantaneous velocity of the tracer particle for belt velocity of 2.686m/s, 4.81 m/s and 8.208 m/s respectively. Results clearly indicate that with the increase in tracer particle velocity standard deviation of the error in displacement and velocity are increasing for all the data acquisition frequencies. Further, it is observed that the mean error in displacement at 20 Hz frequency for 2.686 m/s velocity is negative at all the instances. This indicates that RPT predicts less displacement compared to actual displacement. For the same condition, velocity prediction is also lower at all the instances compared to the actual velocity of the tracer particle. Similar observation has been made by Rammohan (2002). This phenomenon can be inferred as the dominance of dynamic bias. Similarly, for 4.81 m/s tracer velocity, 20 Hz is found to be critical where the dynamic bias error dominates the accuracy of RPT measurement. However, for 8.208 m/s tracer velocity the critical frequency, at which dynamic bias error dominates is increased to 33 Hz. It is also observed that for any particular frequency, error in displacement increases with increase in tracer particle

velocity. Figure 2.15 shows that error caused due to statistical fluctuation of gamma emission and reconstruction is a function of data acquisition frequency only. Hence, increase in error in displacement with velocity is mainly due to the dynamic bias.

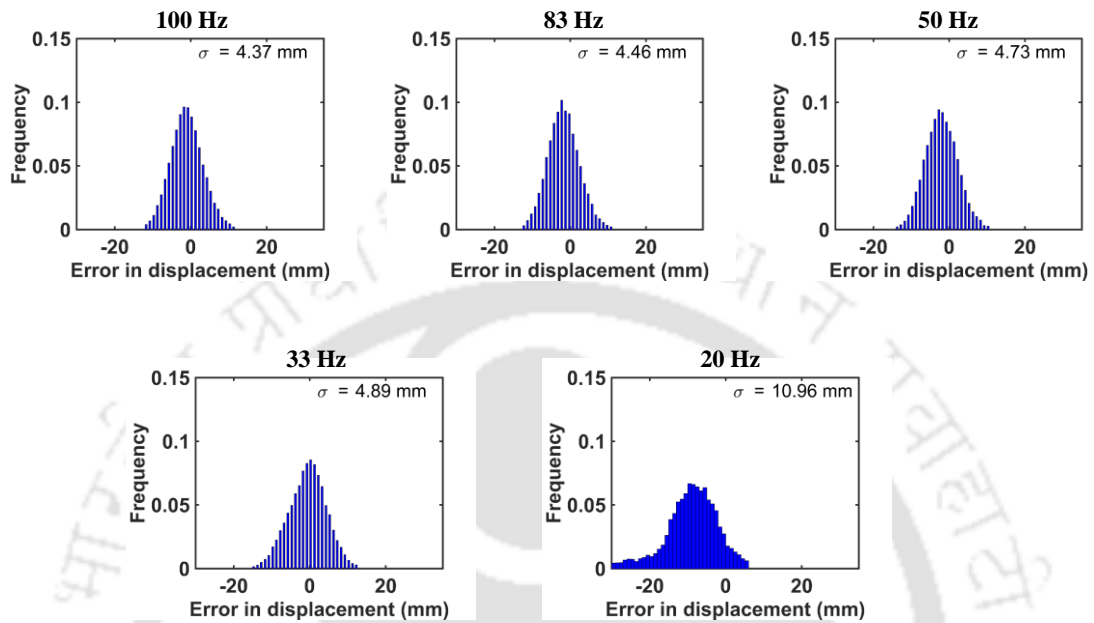


**Figure 2.17a PDF of error in displacement at different acquisition frequency for tracer particle velocity of 2.686 m/s**

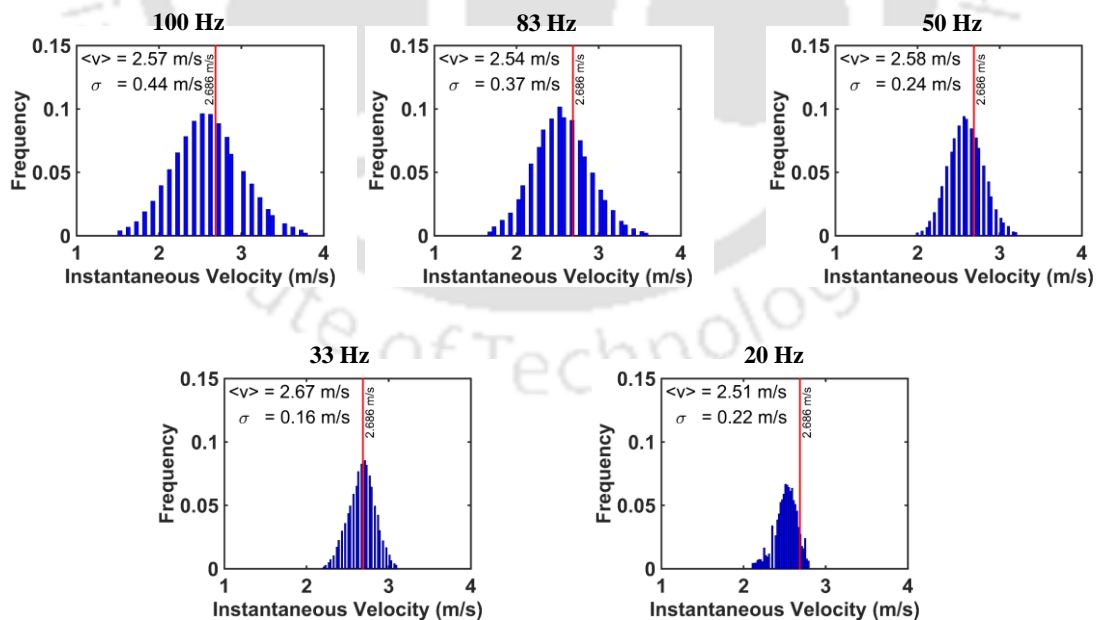


**Figure 2.17b PDF of instantaneous velocity at different acquisition frequency for tracer particle velocity of 2.686 m/s**

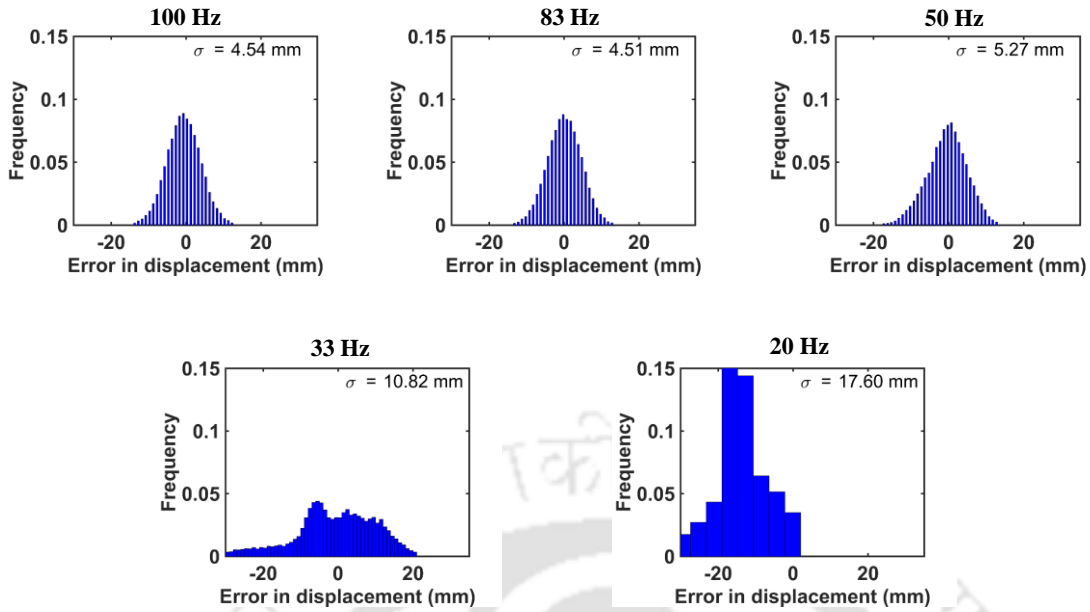


Figure 2.18a PDF of error in displacement at different acquisition frequency for tracer particle velocity of 4.852 m/s

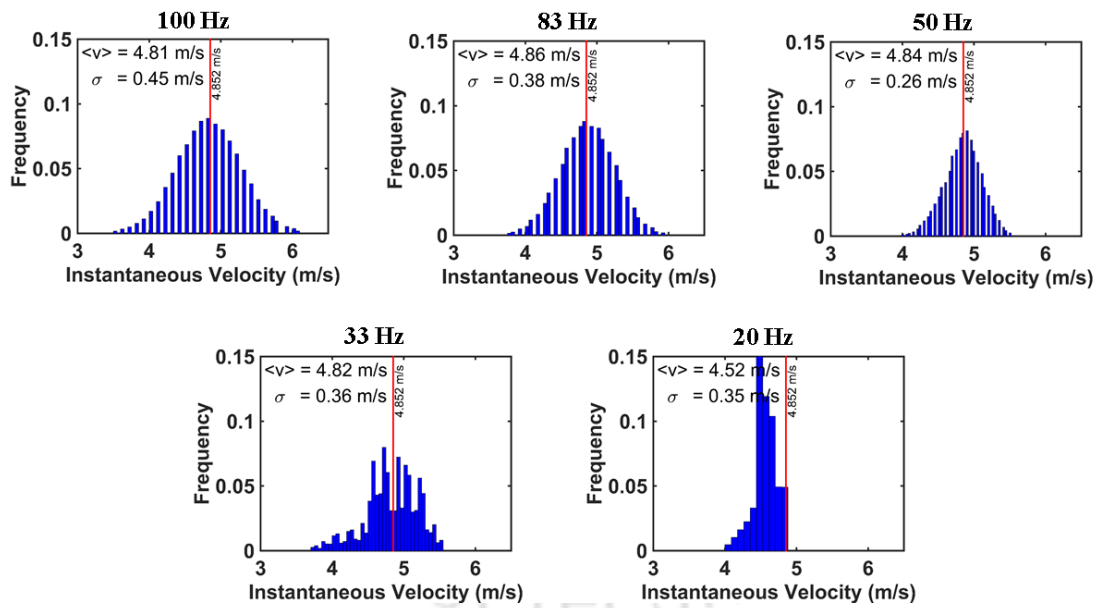
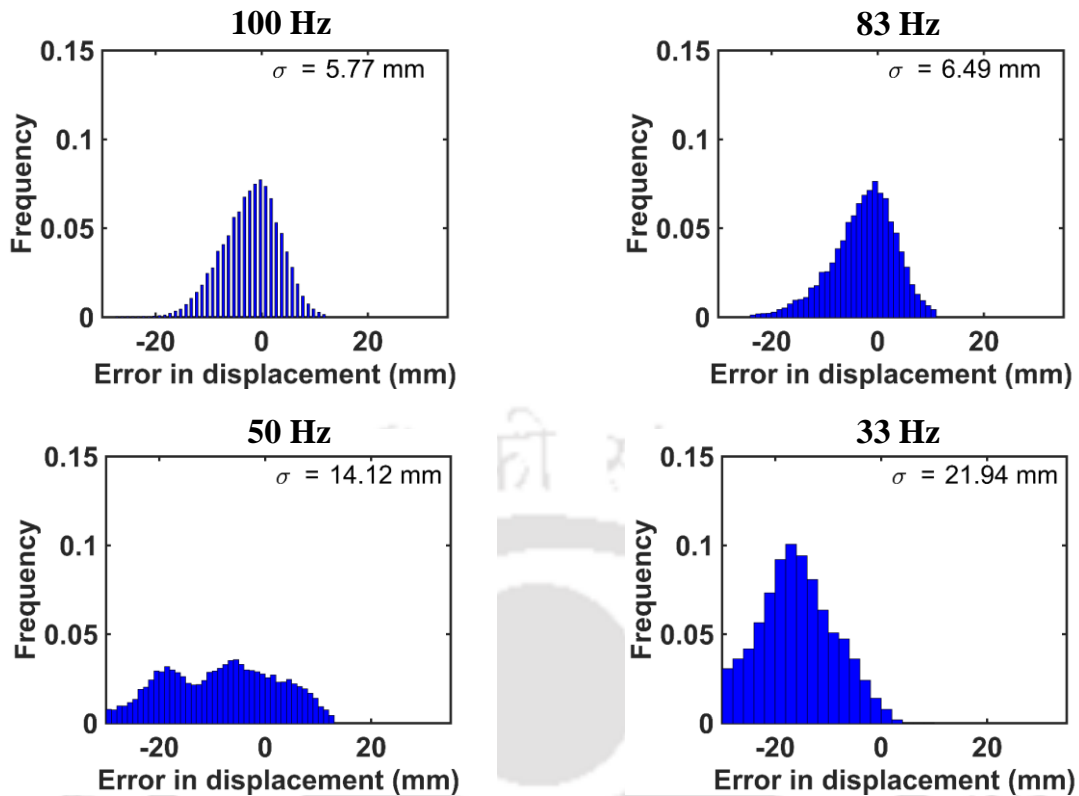


Figure 2.18b PDF of instantaneous velocity at different acquisition frequency for tracer particle velocity of 4.852 m/s



**Figure 2.19a PDF of error in displacement at different acquisition frequency for tracer particle velocity of 8.203 m/s**

Figure 2.20 shows the head to head comparison of standard deviation in the prediction of displacement and instantaneous velocity for different tracer velocities at different data acquisition frequencies. Results indicate that standard deviation in the prediction of displacement increases with decrease in data acquisition frequency. Standard deviation of velocity prediction decreases with decrease in data acquisition frequency. However, with small change in data acquisition frequency, increase in standard deviation of displacement is marginal compared to decrease in standard deviation of velocity prediction. Hence, an optimal window for data acquisition frequency can be obtained for each velocity of the tracer particle where both position and velocity can be predicted with minimum error.

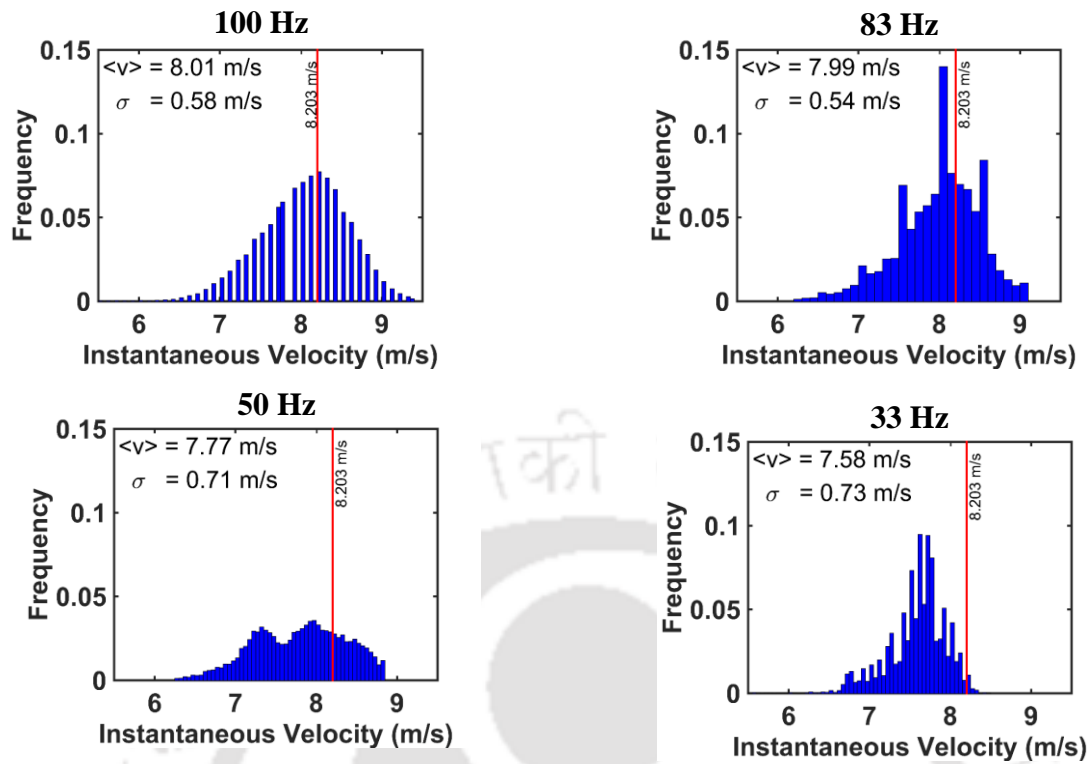


Figure 2.19b PDF of instantaneous velocity at different acquisition frequency for tracer particle velocity of 8.203 m/s

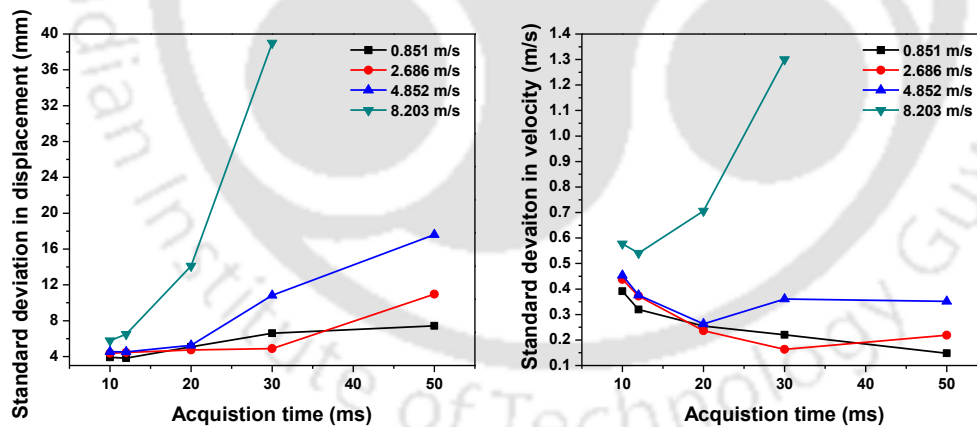


Figure 2.20 Comparison of standard deviation in displacement and velocity prediction for different value of tracer velocity at different frequencies

### 2.3.4 Conclusions

In the current work, experiments are performed to quantify the accuracy of RPT experiment in terms of ability to reconstruct the exact location of the tracer particle and velocity

prediction. To achieve this, experiments are performed in a specially designed setup, where particle motion can be precisely controlled. It is found that for stationary location of tracer particle, RPT measurements are able to locate the particle position with high accuracy which is in order of particle diameter. However, it is found that accuracy of particle position reconstruction, even at stationary condition, depends on data acquisition time. It is observed that accuracy of particle position reconstruction increases with decrease in acquisition frequency. This is mainly because of reduction in statistical fluctuation of gamma emission at lower data acquisition frequency. The experiments are also performed at dynamic conditions. It is observed that error in particle position reconstruction is higher at dynamic condition compared to stationary condition. This clearly indicates the existence of dynamic bias which affects the accuracy of RPT measurement. Further it is observed that the error in particle position reconstruction increases with increase in velocity of the tracer particle for the same frequency. However, it decreases with increase in data acquisition frequency for the same velocity of the tracer particle. These results indicate that error due to dynamic bias can be reduced by increasing the data acquisition frequency. Hence, RPT measurement will be more accurate at the higher frequency. To check this hypothesis, velocity of tracer particle is measured through RPT experiment for all the experimental conditions. It is observed that error in velocity prediction increases with increase in data acquisition frequency. This is mainly because the way velocity is calculated in RPT, through  $\Delta x / \Delta t$ , or in any other flow measurement technique. Therefore, at high frequency (very low value of  $\Delta t$ ) small error in position reconstruction will greatly affect the accuracy of velocity prediction. In RPT measurement it lower value of  $\Delta t$  is more critical as it is almost impossible to accurately locate the exact location of tracer particle, even if the particle is stationary, due to statistical nature of gamma-emission. Therefore, it is important to find an optimal data acquisition frequency for each velocity condition where error in position

reconstruction and velocity prediction is minimum. However, one has to keep hydrodynamic requirement of the system in consideration (minimum length and time scale of the system) before selecting the data acquisition frequency. Though, lower data acquisition frequency will provide better accuracy in terms of velocity prediction, it can skip several meta stable structures which exist at a time scale lower than the data acquisition frequency.

## 2.4 Summary

In this chapter, different velocity measurement techniques are discussed in detail and advantage of RPT technique over other velocity measurement techniques is specified. Further, RPT is discussed in detail and hardware involved in RPT measurement is discussed. Resolution and sensitivity of RPT measurement is deduced through the counts recorded during the calibration. Accuracy of RPT experiments are measured for stationary and dynamic condition of tracer particle. It is found that ability of RPT experiment to exactly locate the position of tracer particle strongly depends on data acquisition frequency even at stationary condition. Further, accuracy of RPT measurement is determined in terms of position reconstruction and velocity prediction at dynamic condition of tracer particle. It is found that at dynamic condition error in position reconstruction is higher compared to stationary condition due to dynamic bias which can be minimized by acquiring the data at higher frequency. However, at higher frequency, error in velocity prediction increases as velocity is calculated through  $\Delta x / \Delta t$ . Hence, small error in position reconstruction can significantly increase the error in velocity prediction. Therefore, a methodology has been developed to find the optimal data acquisition frequency to achieve the maximum accuracy in position reconstruction and velocity prediction for different velocity of the tracer particle. 10 and 12 ms are found to be optimal data acquisition time if the velocity varies between 1 to 5 m/s, which is the case in circulating fluidized bed. Hence, during implementation of

RPT technique in laboratory and pilot plant scale system, data is acquired at an interval of 10 or 12 ms based on the system velocity.

## Notations

|              |   |                     |
|--------------|---|---------------------|
| $A$          | Source strength   | [Ci]                |
| $C$          | Photo peak count  | [-]                 |
| $C_i$        | Counts registered by the $i^{\text{th}}$ detector for the tracer particle at $j^{\text{th}}$ node | [-]                 |
| $d$          | Penetration depth of photons in the detector crystal  | [m]                 |
| $i$          | Index of radial component   | [-]                 |
| $j$          | Index of azimuthal component  | [-]                 |
| $k$          | Index for axial component   | [-]                 |
| $KE$         | Fluctuating kinetic energy per unit volume  | [m <sup>2</sup> /s] |
| $l_j$        | Length of intervening medium between source and detector  | [m]                 |
| $M_i$        | Counts measured by the $i^{\text{th}}$ detector for unknown particle position                     | [-]                 |
| $N$          | Total number of photon trajectories tracked   | [-]                 |
| $N_D$        | Number of detector  | [-]                 |
| $N(i, j, k)$ | Number of occurrence in compartment index by $(i, j, k)$  | [-]                 |
| $q$          | Index for co-ordinate (r, $\theta$ , z direction)   | [-]                 |
| $R(z)$       | Resolution  | [mm]                |
| $S(z)$       | Sensitivity   | [mm <sup>-1</sup> ] |
| $t$          | Time of acquisition   | [s]                 |

|                             |   |                    |
|-----------------------------|---|--------------------|
| $T$                         | Sampling time   | [s]                |
| $v_r, v_z, v_\theta$        | Velocity in $r, \theta, z$ direction respectively   | [m/s]              |
| $v_q$                       | $q^{\text{th}}$ component of instantaneous velocity   | [m/s]              |
| $v_q'$                      | $q^{\text{th}}$ component of fluctuating velocity   | [m/s]              |
| $\langle v_q \rangle$       | $q^{\text{th}}$ component of ensemble average velocity  | [m/s]              |
| $\langle v_q \rangle^{az}$  | $q^{\text{th}}$ component of azimuthal average velocity   | [m/s]              |
| $\langle v_q \rangle^{RMS}$ | $q^{\text{th}}$ component of RMS velocity   | [m/s]              |
| $\langle v \rangle$         | Mean velocity calculated through RPT experiments  | [m/s]              |
| $z$                         | Axial level in the column   | [m]                |
| <b>Greek letters</b>        |   |                    |
| $\alpha$                    | angle formed by line connecting tracer particle and detector center, and the x-axis                                     | [radian]           |
| $(\alpha, \beta, \gamma)$   | The direction cosines of the point $(x, y, z)$  | [-]                |
| $\varepsilon_{abs}$         | Absolute efficiency of detector   | [-]                |
| $\phi$                      | Photo peak fraction   | [-]                |
| $\mu$                       | Medium attenuation coefficient  | [m <sup>-1</sup> ] |
| $\mu_j$                     | Mass attenuation coefficient of all the materials that comes in the path of photons between the source and the detector | [m <sup>-1</sup> ] |
| $\mu_D$                     | Mass attenuation coefficient of the detector crystal material   | [m <sup>-1</sup> ] |
| $\nu$                       | Number of gamma ray photons emitted per disintegration  | [-]                |
| $\Omega$                    | Solid angle   | [steradian]        |

|                         |   |                           |
|-------------------------|---|---------------------------|
| $\rho_p$                | Particle density  | [kg/m <sup>3</sup> ]      |
| $\tau_{qs}$             | Reynolds stress   | [kg/m.s <sup>2</sup><br>] |
| $\tau$                  | Detector dead time  | [s]                       |
| $\theta$                | Angle in osculating plane formed by source and detector<br>curved surface | [radian]                  |
| $\zeta(\cdot)$          | Weighting function in each sampled direction                              | [-]                       |
| $(\delta_m - \delta_a)$ | Error in displacement   | [m]                       |
| $(\delta_a)$            | Actual displacement   | [m]                       |
| <b>Subscript</b>        |   |                           |
| cri                     | critical  |                           |
| max                     | maximum   |                           |
| min                     | minimum   |                           |
| $r, \theta, z$          | Cylindrical co-ordinate   |                           |
| $x, y, z$               | Cartesian co-ordinate   |                           |

## References

- Beam, G.B., Wielopolski, L., Gardner, R.P., Verghese, K., 1978. Monte Carlo calculation of efficiencies of right-circular cylindrical NaI detectors for arbitrarily located point sources. Nucl. Instruments Methods 154, 501–508.
- Bhusarapu, S., 2005. Solid Flow Mapping in Gas-Solid Risers (D.Sc. Thesis). Washington University, USA.
- Bhusarapu, S., Al-Dahhan, M.H., Duduković, M.P., 2006. Solids flow mapping in a gas–solid riser: Mean holdup and velocity fields. Powder Technol. 163, 98–123.

- Boyer, C., Duquenne, A.M., Wild, G., 2002. Measuring techniques in gas-liquid and gas-liquid-solid reactors. *Chem. Eng. Sci.* 57, 3185–3215.
- Caloz, Y.P., 2000. Experimental investigation of local solids Fluid dynamics in different industrial-scale circulating fluidized beds with optical probes (Ph.D. Thesis). Swiss Federal Institute of Technology, Zurich.
- Cassanello, M., Larachi, F., Kemoun, A., Al-Dahhan, M.H., Dudukovic, M.P., 2001. Inferring liquid chaotic dynamics in bubble columns using CARPT. *Chem. Eng. Sci.* 56, 6125–6134.
- Chan, C.W., Seville, J., Yang, Z., Baeyens, J., 2009. Particle motion in the CFB riser with special emphasis on PEPT-imaging of the bottom section. *Powder Technol.* 196, 318–325.
- Chaouki, J., Larachi, F., Dudukovic, M.P., 1997. Noninvasive Tomographic and Velocimetric Monitoring of Multiphase Flows. *Ind. Eng. Chem. Res.* 5885, 4476–4503.
- Chen, J., Kemoun, A., Al-dahhan, M.H., Dudukovic, M.P., Lee, D.J., Fan, L., 1999. Comparative hydrodynamics study in a bubble column using computer-automated radioactive particle tracking (CARPT)/ computed tomography (CT) and particle image velocimetry (PIV). *Chem. Eng. Sci.* 54, 2199–2207.
- Degaleesan, S., 1997. Fluid dynamic measurements and modeling of liquid mixing in bubble columns (D. Sc. thesis). Washington University St. Louis.
- Devanathan, N., 1991. Investigation of Liquid Hydrodynamics in Bubble Columns via Computer Automated Radioactive Particle Tracking (CARPT) (D.Sc. Thesis). Washington University in St. Louis, USA.
- Fraguío, M.S., Cassanello, M.C., Larachi, F., Chaouki, J., 2006. Flow regime transition pointers in three-phase fluidized beds inferred from a solid tracer trajectory. *Chem. Eng. Process. Process Intensif.* 45, 350–358.
- Fraguío, M.S., Cassanello, M.C., Larachi, F., Limtrakul, S., Dudukovic, M., 2007. Classifying flow regimes in three-phase fluidized beds from CARPT experiments. *Chem. Eng. Sci.* 62, 7523–7529.

- Fraguio, M.S., 2010. Study of Multiphase Systems Using Noninvasive Techniques of Analysis (Ph.D. thesis). Universidad de Buenos Aires, Argentina.
- Godfroy, L., Larachi, F., Kennedy, G., Grandjean, B., Chaouki, J., 1997. On-line flow visualization in multiphase reactors using neural networks. *Appl. Radiat. Isot.* 48, 225–235.
- Gopalan, B., Shaffer, F., 2013. Higher order statistical analysis of Eulerian particle velocity data in CFB risers as measured with high speed particle imaging. *Powder Technol.* 242, 13–26.
- Jain, S., Saraswat, P., Jain, V., Pant, H.J., Upadhyay, R.K., 2014. Investigation of liquid–solids fluidized bed of different particle size through radioactive particle tracking techniques. *J. Radioanal. Nucl. Chem.* 302, 1309–1313.
- Kiared, K., Larachi, F., Cassanello, M., Chaouki, J., 1997. Flow Structure of the Solids in a Three-Dimensional Liquid Fluidized Bed. *Ind. Eng. Chem. Res.* 36, 4695–4704.
- Kondukov, N.B., Kornilaev, A. N., Skachko, I. M., Akhromenkov, A.A., and Kruglov, A.S., 1964. An Investigation of the Parameters of Moving Particles in a Fluidized Bed by a Radioisotopic Method. *Int. Chem. Eng.* 4, 43–47.
- Larachi, F., Kennedy, G., Chaouki, J., 1994. A  $\gamma$ -ray detection system for 3-D particle tracking in multiphase reactors. *Nucl. Instrum. Methods Phys. Res. Sect. A* 338, 568–576.
- Larachi, F., Chaouki, J., Kennedy, G., 1995. 3 D Mapping of Solids Flow Fields in Multiphase Reactors with RPT. *AIChE J.* 41, 439–443.
- Larachi, F., Chaouki, J., Kennedy G., and Dudukovic, M.P., 1997, Radioactive Particle tracking in Multiphase Reactors: Principles and Applications. in *Non-Invasive Monitoring of Multiphase Flows*, eds., Chaouki, J., Larachi, F., and Dudukovic, M. P., 335- 406.
- Lefebvre, S., Guy, C., Chaouki, J., 2007. Solid phase hydrodynamics of three-phase fluidized beds-A convective/dispersive mixing model. *Chem. Eng. J.* 133, 85–95.
- Ligrani, P.M., Singer, B.A., Baun, L.R., 1989. Miniature five-hole pressure probe for measurement of three mean velocity components in low-speed flows. *J. Phys. E: Sci. Instrum.* 22, 868–876.

- Lin, J.S., Chen, M.M., Chao, B.T., 1985. A novel radioactive particle tracking facility for measurement of solids motion in gas fluidized beds. *AIChE J.* 31, 465–473.
- Limtrakul, S., Chen, J., Ramachandran, P.A., Dudukovic, M.P., 2005. Solids motion and holdup profiles in liquid fluidized beds. *Chem. Eng. Sci.* 60, 1889–1900.
- Meek, C.C., 1972. Statistical Characterization of Dilute Particulate Suspensions in Turbulent Fluid Field (Ph.D. thesis). University of Illinois, Urbana, IL.
- Mostoufi, N., Chaouki, J., 2001. Local solid mixing in gas-solid fluidized beds. *Powder Technol.* 114, 23–31.
- van Ommen, J.R., Mudde, R.F., 2008. Measuring the Gas-Solids Distribution in Fluidized Beds – A Review. *Int. J. Chem. React. Eng.* 6, 1-29.
- Nieuwland, J.J., Meijer, R., Kuiper, J.A.M., Van Swaaij, W.P.M, 1996. Measurements of solids concentration and axial solids velocity in gas-solid two-phase flows. *Powder Technol.* 87, 127-139.
- Parker, D.J., Forster, R.N., Fowles, P., Takhar, P.S., 2002. Positron emission particle tracking using the new Birmingham positron camera. *Nucl. Instrum. Meth. A* 477, 540–545.
- Parker, D.J., Fan, X., 2008. Positron emission particle tracking — Application and labelling techniques. *Particuology* 6, 16–23.
- Prasad, A.K., 2000. Particle image velocimetry. *Curr. Sci.* 79, 51–60.
- Rados, N., Shaikh, A., Al-Dahhan, M.H., 2005. Solids flow mapping in a high pressure slurry bubble column. *Chem. Eng. Sci.* 60, 6067–6072.
- Rammohan, A., 2002. Characterization of Single and Multiphase Flow in Stirred Tank Reactor (D.Sc. thesis). Washington University, USA.
- Roy, S., 2000. Quantification of Two-Phase Flow in Liquid-Solid Risers (Ph.D. thesis). Washington University, USA.
- Roy, S., Larachi, F., Al-Dahhan, M.H., Duduković, M.P., 2002. Optimal design of radioactive particle tracking experiments for flow mapping in opaque multiphase reactors. *Appl. Radiat. Isot.* 56, 485–503.

- Roy, S., Kemoun, A., Al-Dahhan, M.H. and Dudukovic, M.P., 2005. Experimental Investigation of the Hydrodynamics in a Liquid-Solid Riser, *AIChE J.* 51, 802-835.
- Sanaei, S., Mostoufi, N., Radmanesh, R., Sotudeh-Gharebagh, R., Guy, C., Chaouki, J., 2010. Hydrodynamic characteristics of gas-solid fluidization at high temperature. *Can. J. Chem. Eng.* 88, 1–11.
- Seville, J.P.K., Ingram, A., Parker, D.J., 2005. Probing Processes Using Positrons. *Chem. Eng. Res. Des.* 83, 788–793.
- Tartan, M., Gidaspow, D., 2004. Measurement of granular temperature and stresses in risers. *AIChE J.* 50, 1760–1775.
- Tebianian, S., Dubrawski, K., Ellis, N., Cocco, R. a., Hays, R., Reddy Karri, S.B., Leadbeater, T.W., Parker, D.J., Chaouki, J., Jafari, R., Garcia-Trinanes, P., Seville, J.P.K., Grace, J.R., 2015. Investigation of particle velocity in FCC gas-fluidized beds based on different measurement techniques. *Chem. Eng. Sci.* 127, 310–322.
- Upadhyay, R. K., 2010. Investigation of multiphase reactors using radioactive particle tracking (Ph.D. thesis). IIT Delhi, India.
- Upadhyay, R.K., Roy, S., 2010. Investigation of hydrodynamics of binary fluidized beds via radioactive particle tracking and dual-source densitometry. *Can. J. Chem. Eng.* 88, 601–610.
- Upadhyay, R.K., Roy, S., Pant, H.J., 2012. Benchmarking Radioactive Particle Tracking (RPT) with Laser Doppler Anemometry (LDA). *Int. J. Chem. React. Eng.* 10, 1-14.
- Upadhyay, R.K., Pant, H.J., Roy, S., 2013. Liquid flow patterns in rectangular air-water bubble column investigated with Radioactive Particle Tracking. *Chem. Eng. Sci.* 96, 152–164.
- Werther, J., Molerus, O., 1973. The local structure of gas fluidized beds. II: The spatial distribution of bubbles. *Int. J. Multiph. Flow* 1, 123-138.
- Zhu, J., Li, G., Qin, S., Li, F., Zhang, H., Yang, Y., 2001. Direct measurements of particle velocities in gas – solids suspension flow using a novel five-fiber optical probe. *Powder Technol.* 115, 184–192.



## Chapter 3

# Experimental Investigation of Laboratory Scale Circulating Fluidized Bed

### Scope

In this chapter, solid velocity field in laboratory scale CFB are investigated. Initially current state-of-the-art on solid velocity is presented. Solid flux and their fluctuations measured without disturbing the flow are presented. Implementation of RPT technique on CFB is outlined. Lagrangian and Eulerian velocity measurements are presented. Effects of solid flux and superficial gas velocity on local and fluctuation velocities are investigated. Residence time distribution (RTD) studies are investigated at different sections of riser and findings are complemented with micro-mixing studies from radioactive particle tracking (RPT).

### 3.1 Introduction

Efficient chemical kinetics is important for chemical reactor performance. In addition to the chemical kinetics, transport processes (momentum, heat and mass transfer) plays a major role. In fact, in case of many multiphase flow reactors these processes are rate controlling steps. Hence, governs the performance of these multiphase flow reactors. In words of Levenspiel (1999), “if we have a complete velocity distribution map for the fluid in the vessel, then we should, in principle, be able to predict the behavior of a vessel as a reactor.” Further, for the fast reaction, local velocity field is more critical compared to the time averaged velocity field due to the time scale of the reaction. However, local velocity measurements were difficult to obtain in 1950s, when chemical reactor engineering concept was developed. Residence time distribution (RTD) and micro-mixing concepts were

introduced by Danckwerts (1953) and Zwietering (1959) respectively to model the mixing, thus performance of reactor. RTD provides information about how long the various fluid elements have been in the reactor. Therefore, for the single species reaction, knowledge of RTD is sufficient to characterize the performance of the reactor. However, for multiphase systems, where two different phases need to interact with each other, quantification based on global mixing doesn't provide the necessary information required for complete characterization of the flow. For complete characterization of the flow in addition to time averaged velocity and distribution of phases, local phase fraction and velocity distribution is needed.

Though several development has been reported in multiphase flow measurement technique to map the complete flow field. It is still difficult to map the entire flow field in gas-solid circulating fluidized bed to capture all the interactions occurring at different length and time scales. Further, it is still difficult to map the flow field at different scales with same accuracy to match the phenomena happening at the different scales. Therefore, to understand the design and scale-up issues of these reactors, reliable experimental data is required which can characterize the entire flow domain.

### **3.2 Literature on velocity studies in CFB**

Gas-solids circulating fluidized beds are widely used in many industries mainly for mass transfer controlled reactions. Hence, contacting of the two phases (gas and solids) present in the reactor plays a critical role in determining the performance of the reactor. Thus, a detailed understanding of the complete flow field is vital for better design and scale-up of these reactors.

Several researches have studied the behavior of circulating fluidized bed at different scale to understand the flow behavior of solids in CFB. Core annulus flow structure has been

reported by most of the researchers, where dilute core and dense annular structure are observed (Bader et al., 1988; Rhodes et al., 1988; Bolton and Davidson, 1988; Brereton and Grace, 1993). In core annulus structure flow, solids flow upwards in the core and downwards near the wall. It is reported that the axial solid velocity is maximum at the center of the column and minimum at the wall. Many authors have reported that the mean solid axial velocity at the centre is 1 to 2 times of superficial gas velocity, resembling a parabolic function radially (Bader et al., 1988; Parssinen and Zhu, 2001; Bhusparau et al., 2005; Wang et al., 2014).

Despite having a considerable radial gradient in axial velocity, no downward motion of solid is observed at high flux condition ( $>200 \text{ kg/m}^2\text{s}$ ). This kind of CFB is commonly called as high density circulating fluidized bed (Issangya et al., 1997). It is reported in literature that solids flow downwards near the wall for solids flux below  $200 \text{ kg/m}^2\text{s}$  and  $U_g$  less than  $6.5 \text{ m/s}$  (Parssinen and Zhu, 2001). Further, in literature various radial profile of mean axial velocity of solid, like parabolic,  $1/7^{\text{th}}$  power law, Boltzmann function, linear, is reported (Zhang and Arastoopour, 1995; Wei et al., 1998; Ibsen et al., 2002). Very steep profiles are usually the characteristics of dense suspension upflow, where high density of solids is also present in the system (Wang et al., 2014). With change in the operating conditions and particle properties, different radial profiles are reported. Solid radial profiles also depend on the regime of CFB operation (Wei et al., 1998). However, it is not clear how and when the particular profile is prominent. For example, for dilute flow conditions, both parabolic and power law profiles are reported (Wei et al., 1998; Pantzali et al., 2013). It has been well understood that how the cross sectional averaged solid velocity (CSA) changes with the operating conditions but not the profile of mean solid velocity.

To understand the characteristics, it is imperative to have detailed data of the system, not only mean values. In last three decades, studies on solid velocity measurements have gained

momentum, mainly due to the development of advanced techniques which are able to disseminate the local solid velocity field. Table 3.1 gives the studies available on solid velocity in the open literature where invasive and noninvasive techniques are used to study the CFB. Most of the studies are focused on the axial velocities and reported 2D velocity only. Further, most of the techniques are not able to give the higher order moments of the velocity. It is indeed important to understand the full velocity field including turbulence to understand the system. Further, these studies which are vital for model development and understanding the system are required for wide range of operating conditions.

Very few studies reported full velocity field including turbulence (Pantzali et al., 2013; Bhasparau et al., 2006; Tartan and Gidaspow, 2004; He et al., 2009; Gopalan and Shaffer, 2013). Pantzali et al. (2013) and He et al. (2009) used LDA technique, thus limited with the low volume fraction of solids. Tartan and Gidaspow (2004), Gopalan and Shaffer (2013) used intrusive PIV techniques. Former work conducted the experiments at low flux only, latter's work gave detailed data at different regimes. Gopalan and Shaffer (2013) measured mean, RMS velocities and granular temperature with high speed PIV. Chan et al. (2010) reported particle position track, mean particle velocities and velocity distribution using PEPT technique. However, detailed Eulerian information is not reported. Godfroy et al. (1999) and Bhusarapu (2005) are the two studies so far reported on CFB using RPT. In Godfroy et al. (1999) study, tracer particle of 500  $\mu\text{m}$  is used to track the sand particle of size 150  $\mu\text{m}$ . They reported that solid velocities and solid dispersion coefficient are decreased with increase in solid circulation rate. However, due to higher inertia of tracer particle compared to solids present in the bed, reported particle fluctuations may be smaller. Bhusarapu (2005) reported mean velocity of solids, phase distribution, velocity fluctuations, turbulent kinetic energy, and solid dispersion at various operating conditions.

Tracer particle size of 150  $\mu\text{m}$  was used in the study which was similar to the size of solids used in the experiment. However, uncertainty of 1 m/s in velocity measurement is reported.

Literatures reported are still not sufficient to completely characterize the flow behavior of CFB, as most of the information are limited to mean velocity profile. Further, limited information are available on fluctuating component of velocity. Time averaged fluctuation velocity profiles or RMS velocity profiles are not well understood in CFB. Further, validation of computational models requires detailed measurements. In addition to the first order moments, fluctuating level measurements are required for wide range of operating conditions to have a better understanding of CFB. Modeling of CFB suffers from the lack of such a detailed data for validation and development (Godfroy et al., 1999; Tartan and Gidaspow, 2004; Bhusarapu et al., 2006; Pantzali et al., 2013). CFB offers unique features like efficient gas - solid contacting. However, considerable work is required to achieve a better understanding of these high velocity systems and to allow them to be optimized with respect to reactor geometry and operating conditions (Grace, 1990). The operating conditions, riser geometry, solids inventory, and particle properties have been found to influence the solids distribution in CFB risers.

It is clear that available literature on detailed study of solid velocity in CFB is not enough to characterize the flow due to the complex nature of the system. Hence, a systematic study on effect of operating conditions is required. In this work, experiments are performed in a laboratory scale CFB setup to find the effect of operating condition on the behavior of CFB. An array of systematic data is produced to understand the system in detail. Further the data can also be used for CFD validation and model development.

**Table 3.1 Literature review of experimental work on solid velocities in CFB**

| Reference                  | Measurement Technique    | Riser Geometry<br>Dia x Height<br>cm x m | Solids material / diameter              | Operating conditions<br>$U_g G_s$<br>$\text{ms}^{-1} \text{kgm}^{-2}\text{s}^{-1}$ | Measurement region<br>m | Measured solids velocity                             | Remarks   |
|----------------------------|--------------------------|--|---|--|-------------------------|--|---|
| <b>Invasive techniques</b> |                          |  |   |  |                         |  |   |
| Bader et al. (1988)        | Pitot tube               | 30.5 x 12.2                              | FCC 76 $\mu\text{m}$                    | 3.7; 98  | H = 4, 9.1              | Mean radial profile                                  | Core annulus flow structure with parabolic profile  |
| Horio et al. (1988)        | Optical fiber probe      | 5 x 2.79                                 | FCC 60 $\mu\text{m}$                    | 1.17, 1.29; 11.7, 11.25  | H = 0.36, 1.06, 1.63    | Mean radial profile                                  | Annular flow with clusters  |
| Zhou et al. (1995)         | Optical fiber probe      | 14.6 x 14.6 x 914 $\text{cm}^3$          | Sand 213 $\mu\text{m}$                  | 5.5, 7; 20, 40   | H = 5.13, 6.2, 8.98     | Vertical and lateral profiles of particle velocities | Core annulus flow structure. Thickness of the annulus layer increases with the height                                       |
| Herbert et al. (1999)      | Optical fiber probe      | 41 x 8.5                                 | FCC, Glass beads 42 - 300 $\mu\text{m}$ | $\leq 13$ ; $\leq 250$   | H = 4, 4.2              | Mean radial profile                                  | Core annulus with the influence of particle diameter  |
| Parssinen and Zhu (2001)   | Five fiber optical probe | 7.6 x 10                                 | FCC 67 $\mu\text{m}$                    | 5.5, 8, 10; 100, 300, 400, 550   | H = 1.53 – 9.42         | Mean radial and averaged axial profiles              | Dense, intermediate dense, dilute, exit section can be distinguished. Upward velocity near the wall in bottom dense region. |
| Yan et al. (2003)          | Five fiber optical probe | 7.6 x 10                                 | FCC 67 $\mu\text{m}$                    | 5.5, 8; 20, 100, 200, 300, 400, 550  | H = 0.98 – 9.42         | Mean radial profiles                                 | Exit and entrance effects are more pronounced in high solid flux  |

|                               |                          |                           |                                |  |                                     |  |   |
|-------------------------------|--------------------------|---------------------------|--------------------------------|--|-------------------------------------|--|---|
| Tartan and Gidaspow (2004)    | PIV                      | 7.62 x 6.99               | Glass beads, 530 $\mu\text{m}$ | 4.9, 5.1, 5.6, 6.0, 14.2, 14.9, 21.4, 28.7, 43.9 | H = 4.2 - 5                         | Mean velocity and granular temperature                         | Reynolds stresses increases with solid flux and also high near the wall   |
| Yan and zhu (2005)            | Five fiber optical probe | 7.6 x 10<br>20.3 x 10     | FCC 67 $\mu\text{m}$           | 3.5, 5.5, 8; 50, 75, 100, 200                    | H = 1.47 - 8.79<br>H = 1.53 - 9.42  | Mean radial profile  | No significant variation between the two risers in the center, otherwise particle velocity is higher in the smaller column. Flow development becomes faster with increasing $U_g$ and slower with increasing $G_s$ . Effect of L / D ratio on the acceleration and flow development has to be studied |
| Yan et al. (2008)             | Optical fiber probe      | 7.6 x 10<br>10 x 10       | FCC 67 $\mu\text{m}$           | 3.5 - 8; 50 - 200                                | H = 1.53 - 9.42<br>H = 0.95 - 14.08 | Mean radial profile  | Multitube distributor gives more uniform profiles than the orifice distributor  |
| Gopalan and Shaffer (2013)    | HSPIV                    | 30.5 x 15.5<br>0.203 x 22 | HDPE, 802<br>FCC, 81           | 5.71, 7.58; 76, 96, 195<br>18.3, 9.15; 49, 390   | H = 9.75<br>H = 20                  | Mean axial velocities, RMS velocities and Granular temperature | Flat RMS profiles are reported for HDPE. In case of FCC, peaking at the wall is reported. Granular temperature decreases towards the wall.  |
| Wang et al. (2014)            | Optical fiber probe      | 7.6 x 10                  | FCC 76 $\mu\text{m}$           | 5, 7, 9; 100, 200, 300, 400, 600, 700, 800, 1000 | H = 0.59 - 10                       | Mean axial and radial profile                                  | With increases in solid flux, axial distribution of particle velocity is more uniform, radial distribution becomes steeper and flow development becomes slower.   |
| <b>Non-invasive technique</b> |                          |                           |                                |  |                                     |  |   |
| Wang et al. (1998)            | LDV                      | 14 x 10.4                 | FCC 36 $\mu\text{m}$           | 3.49 - 4.78; 2.6 - 78.3                          | H = 4 - 6                           | Mean Radial profile  | Radial profiles obeys 1/7 power law of turbulent flow   |

|                         |                               |                          |                                 |  |                                  |   |  |
|-------------------------|-------------------------------|--------------------------|---------------------------------|--|----------------------------------|---|--|
| Godfroy et al. (1999)   | Radioactive particle tracking | 8.2 x 7                  | Sand 150 $\mu\text{m}$          | 4; 23 – 75                                     | H = 4 - 5 (above distributor)    | 3 D Eulerian and Lagrangian velocity field (of a large particle)                              | Clusters formation; dispersion coefficient variation   |
| Zhang et al. (2003)     | LDV                           | 41.8 x 18                | FCC 77 $\mu\text{m}$            | 2.7 – 3.7; 29.7 – 44                           | H = 6, 14                        | Instantaneous and time averaged radial profile, PDD curves of particle velocity               | Dispersed particle phase and dense cluster phase exists  |
| Bhusarapu et al. (2005) | RPT                           | 15.2 x 7.93<br>14 x 5.77 | Glass 150 $\mu\text{m}$         | 3.2 – 4.5; 26.6 – 36.8; 5.49 – 7.71; 102 - 119 | H = 5 to 5.7<br>H = 2.08 to 2.79 | Instantaneous velocity, ensemble averaged velocity, turbulent kinetic energy, Reynolds stress | Dilute and core annular flow profiles are different.   |
| Chan et al. (2010)      | PEPT                          | 4.6, 9, 16 x 6.5         | Sand 120 $\mu\text{m}$          | 1 – 10; 5 – 622                                | Whole column                     | Instantaneous and average velocity.   | Residence time distribution and solid mixing are reported. Velocity distribution is also reported. |
| Kashyap et al. (2011)   | PIV                           | 3.048 x 15.78            | Polypropylene 750 $\mu\text{m}$ | 7.6; 39.31, 19.50                              | H = 6.98                         | Granular temperature, Reynolds stress   | Solid dispersion coefficient is higher in the radial direction than axial direction                |
| Pantzali et al. (2013)  | LDA                           | 10 x 8.7                 | FCC, 77 $\mu\text{m}$           | 3.5 and 5.3; 1                                 | H = 0.9 -5.5                     | Mean axial velocities and RMS velocities and turbulence quantities                            | Operated at very low flux. RMS profile is contrary to the mean velocity profile.                   |

### 3.3 Experimental setup

Laboratory scale circulating fluidized bed is designed and fabricated for experiments in this work. The CFB setup is made of mild steel. A modular CFB setup is designed in such a way that each section can be individually replaced with a glass section for visual observations. The designed setup has enough flexibility to incorporate different inlet and outlet designs as per the need. Further, several predesigned ports were made to facilitate RPT calibration. Same ports were used to place pressure transducers to record zone wise pressure fluctuations.

Figure 3.2 shows the schematic of laboratory scale CFB setup used in current study. Riser of 0.052 m diameter and 3.2 m height is used in experiments. Riser has two inlets. One at the bottom is used to supply the air in the riser. The other inlet is at 5 cm above the primary air inlet which is used as a solid inlet. At the top of the riser, 90° elbow exit is provided. Elbow is connected to the series of cyclones through the mild steel pipe. Dimension of the cyclone are sized according to the geometry of stairmand type cyclones (Svarovsky, 1986). Gas and solids flow co-currently upward in the riser where solids are separated from air in the primary cyclone (mounted above the downer) and secondary cyclones. Solids from the secondary cyclones flow to the downer via flexi hose. Downer is designed to hold large amount of solids by increasing the diameter of the downer to 0.1 m. Large inventory of solids enable continuous feeding of solids in the riser without starving. Converging and diverging ends of the downer ensures the smooth flow of the solids. Motive air is provided to the dipleg to ensure smooth flow. Dipleg is connected to the riser at the angle of 30°. Bag filter is provided at the exit of the air to trap the solids carried over with the air, if any. It is ensured that solid inventory fluctuation is less than 5% of the total inventory for the entire run of experiments.

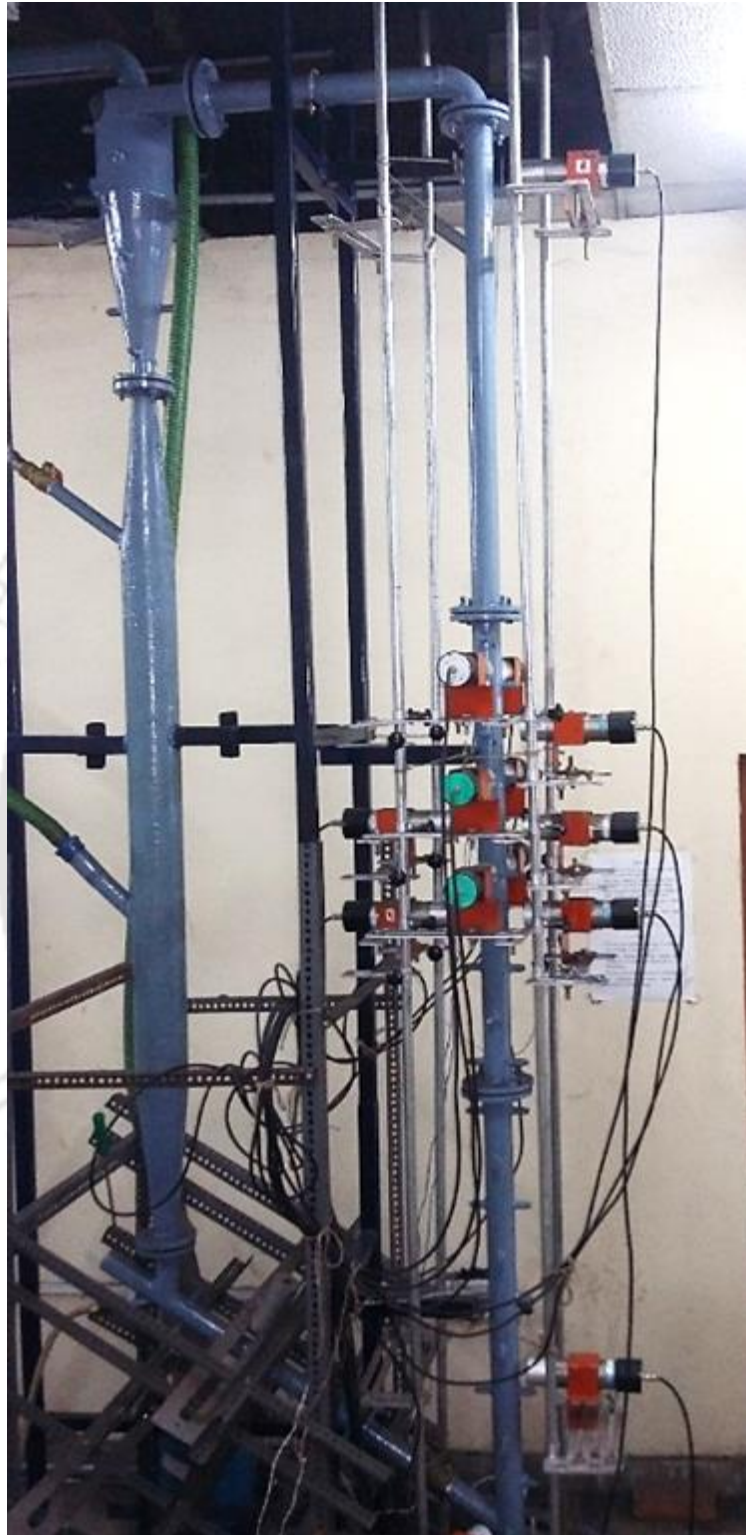


**Figure 3.1** Photograph of laboratory scale experimental setup

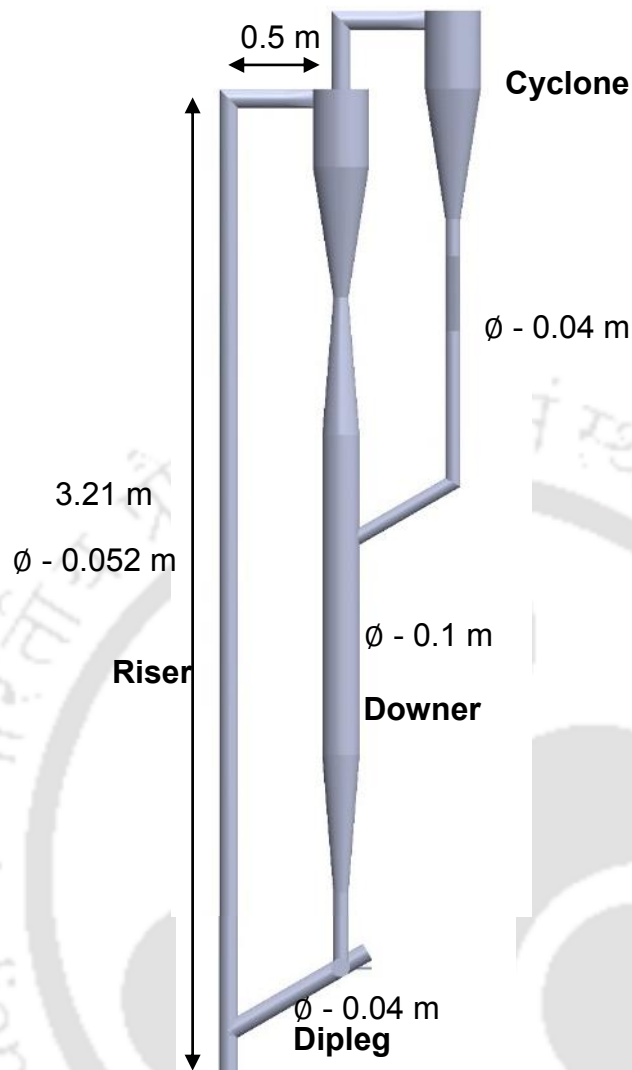


**Figure 3.2 Schematic of laboratory scale experimental setup**

Experiments are conducted at different solid flux and gas superficial velocity. Air blower and compressor are installed for supply of air. Reciprocating compressor is used for supply of motive air, which is supplied through secondary inlet. Twin lobe blower is used for primary air supply to the system. Blower can supply air upto 12000 LPM at 7000 mm WG (water gauge) pressure and compressor can supply air upto 950 LPM at 12 bar pressure. Standard metering device is used to measure the air flow rate. Experiments are conducted with glass beads of mean particle size of  $500 \mu\text{m}$  and density of  $2500 \text{ kg/m}^3$ . Minimum fluidization velocity of solids of  $0.2 \text{ m/s}$  and terminal settling velocity of  $4.13 \text{ m/s}$ .

### **3.4 Solid flux measurement**

To analyze the behavior of CFB, measuring 'accurate' solid flux in CFB is very essential. However, it is not very simple to measure the solid flux in CFB mainly because solids in CFB are in closed loop. The dynamic nature of CFB makes the measurement of solid flux more challenging. In literature, various invasive and non-invasive methods have been used for measuring the solid flux. Invasive methods like closing the permeable porous valve and then accumulating solids, an impact flow meter, a modified orifice meter, calorimetric method are examined by Burkell et al. (1988). Permeable porous valve placed in stand pipe is suitable for analyzing solid flux in CFB. However, the technique is intrusive and can interrupt the standpipe and CFB operation. Ludlow et al. (2008) have designed a device based on rotating spiral vane to measure the solid circulation rate. Though the electronics involved in measurement was placed outside of CFB, spiral vane was placed inside the stand pipe. Hence, this device can also alter the flow in standpipe.

Patience et al. (1991) have measured the pressure drop in a straight pipe line placed in between riser exit and cyclone inlet. The technique is online and do not interfere the flow in CFB. However, it requires pre calibration for measurement of solid mass flux. Roy et al. (2001) have used radioisotope based non-invasive technique to measure the solid flux. It is preferred that the solid mass flow measuring technique should be online, non-invasive and accurate. In contrary to most of the techniques reported in the literature which are either intrusive or require calibration, radiation based technique is non-invasive and does not require calibration. Hence, radiation based technique is used in current work to measure the solid flux.

#### **3.4.1 Velocity and volume fraction measurement methods**

In current work, velocity and volume fraction of the solids are measured to calculate the mass flux (Roy et al. 2001). Solid mass flux,  $G_s$  is expressed as,

$$G_s = \rho \int v_s \varepsilon_s dA \quad (3.1)$$

Thus, if the velocity  $v_s$  and volume fraction  $\varepsilon_s$  of solids is known then solid flux can be obtained. However, the fluctuation in solid flux majorly due to meta stable structures forms in CFB, which disturb the flow, is holy grail of accurate solid flux measurement. The issue becomes more critical for the techniques which is either invasive or require pre-calibration. Time averaged solid flux in CFB can be represented by equation (3.2) (Roy et al., 2001).

$$\langle G_s \rangle = \rho \left( \int \langle v_s \rangle \langle \varepsilon_s \rangle dA + \int \langle v_s' \varepsilon_s' \rangle dA \right) \quad (3.2)$$

The long-term time averaging of the fluctuation term in the equation (3.2) will be zero. Thus, in this work, measurements are taken for longer time. If the cross sectional variation of solid volume fraction is not significant then equation (3.2) can be approximated by equation (3.3) without possessing significant error (Roy et al., 2001). Hence, solid flux can be measured by measuring solid volume fraction and solid velocity individually.

$$\langle G_s \rangle = \rho \overline{\langle v_s \rangle} \cdot \overline{\langle \varepsilon_s \rangle} A \quad (3.3)$$

In current work, solid volume fraction is measured via densitometry technique. Mean velocity is measured by measuring the mean residence time solid spend between a particular section in standpipe. The details of both the techniques are explained in the subsequent sections. Measurements are performed at different sections of the stand pipe which are found to be with in  $\pm 2\%$  range. However, to have the exact knowledge of solid feed rate in to the riser, measurements reported in current work is performed at angled dipleg.

### Mean velocity measurement via Residence time distribution study

Residence time distribution between two planes is measured by positioning two scintillation detectors perpendicular to the angled standpipe as shown in Figure 3.3. Two detectors are placed 40 cm apart. Solid tracer preparation and electronics used are similar to the RPT experiments. Glass bead doped with Scandium-46 is used as radioactive tracer is allowed to move freely as solid phase. Whenever the particle comes near the detector, counts are recorded. However, maximum count (peak) is recorded at center plane of the detector. Time difference between the peaks of the two detector gives the time taken by the particle at each sojourn, as shown in Figure 3.4. Multiple such sojourns are recorded until statistically concurrent values are obtained. Mean residence time  $\bar{t}$  and variance of residence time curve can be calculated from multiple such sojourns, as given in equation (3.4) and (3.5)

$$\bar{t} = \frac{1}{N} \sum_{i=0}^N t_i \quad (3.4)$$

$$Var = \frac{1}{N} \sum_{i=0}^N (t_i - \bar{t})^2 \quad (3.5)$$

With the mean residence time, mean solid velocity  $\overline{\langle v_s \rangle}$  can be calculated by using equation (3.6), where  $L$  is center-to-center distance between the two detectors.

$$\overline{\langle v_s \rangle} = \frac{L}{\bar{t}} \quad (3.6)$$



Figure 3.3 Photograph showing the detector position for RTD measurements (Lead sheets are removed for the sake of clarity)

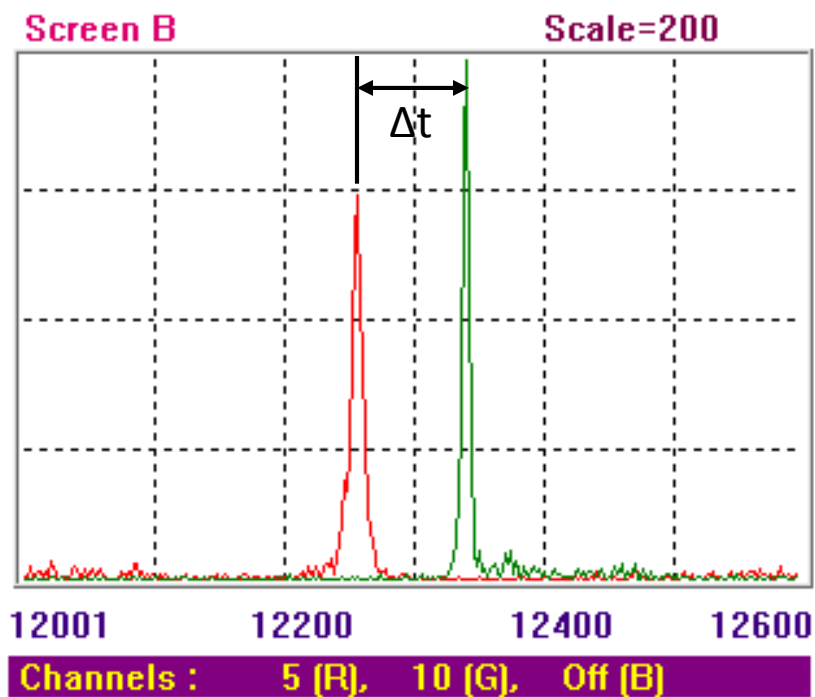


Figure 3.4 Count – time series for a single circulation

## Densitometry

The theory of densitometry technique emerges from the fundamental property of any matter to attenuate electromagnetic radiation (Kak and Slaney, 1988). The attenuation of any radiation beam depends upon the mass attenuation coefficient of the material and distance traveled by the beam in that material. According to Beer Lambert law, the intensity of collimated beam of radiation passing through any medium can be expressed by equation (3.7),

$$I = I_0 \exp \left[ - \int_L \mu(s) ds \right] \quad (3.7)$$

If the length of the medium and intensity recorded are known, mass attenuation coefficient of the medium can be obtained. In the case of gas - solid multiphase system, medium is mixture of gas and solids. From the average mass attenuation coefficient of mixture along the chord, time-averaged chordal averaged phase volume fractions of gas and solids system  $\varepsilon_g$  and  $\varepsilon_s$  can be calculated by using equation (3.8) and (3.9).

$$\mu = \mu_s \varepsilon_s + \mu_g \varepsilon_g \quad (3.8)$$

$$\varepsilon_g + \varepsilon_s = 1 \quad (3.9)$$

where  $\mu_g$  and  $\mu_s$  are the individual mass attenuation coefficients of the gas and solid. The air has negligible mass attenuation coefficient. To obtain the mass attenuation coefficients of solids, experiments are repeated at packed bed conditions of solids where packed bed volume fraction was known through bed height measurement.

Unlike RPT, in densitometry both source and detector are placed outside of the vessel. Detector and collimated source are placed in line in such a way that the detector centre and source centre are collinear as shown in Figure 3.5. Cesium-137 is used as radiation source.

Basic counting system, as explained in RPT is used to count the photons received. Only photon peaks are considered for counting to minimize the noise. Counts are recorded at the frequency of 50 Hz. At each point, data are acquired for 30 min so that random fluctuations will be phased out in the averaging. Experiments are conducted at 8 radial locations. It has been found that radial variation is not significant. Hence, chordal average and cross sectional average solid fraction will be same. Thus, chordal average solid fraction is used to calculate the solid mass flux. Experiments are also conducted at different planes between the two detectors positions where detectors are placed during the RTD measurement. It has been found that there is no significant change in the volume fraction between the two detectors positions.

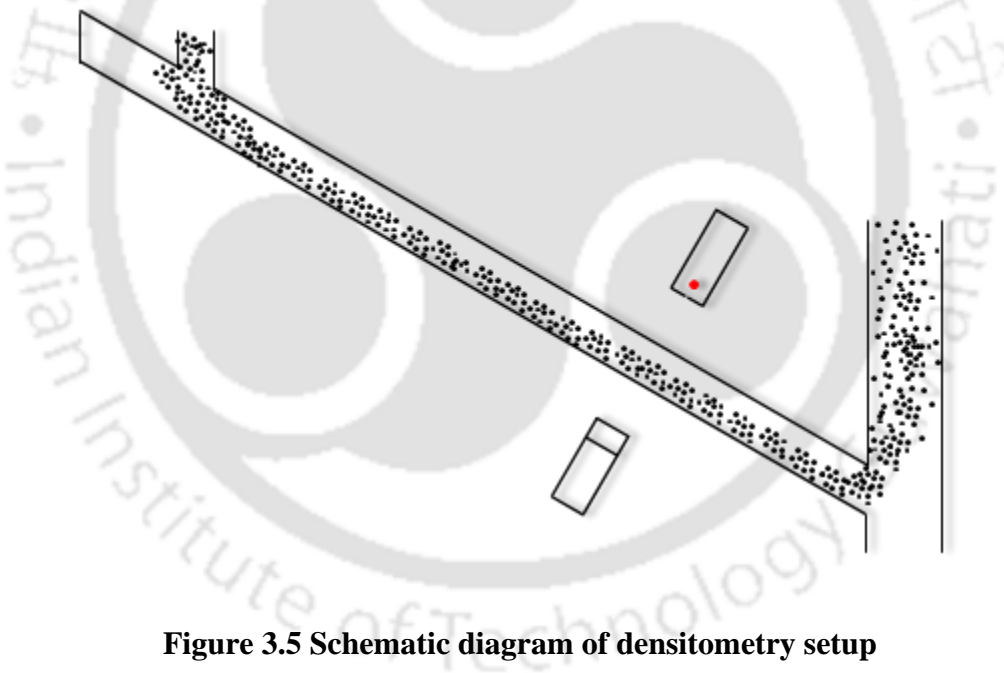


**Figure 3.5 Schematic diagram of densitometry setup**

Characteristic operating parameters of CFB, are solid flux and superficial gas velocity. Solid inventory is another independent variable, which defines the CFB characteristic. Solid flux can be altered either by changing the solid inventory in the system or changing the superficial gas velocity. One of the primary aims of this work is to study the effect of operating conditions on behavior of the CFB. Hence, it is critical to find the effect of gas

velocity and solid inventory on solid flux for stable operation of CFB. Therefore, solid flux measurements are conducted in riser for different solid inventories and air inlet velocities and few sample cases are given in Figure 3.6. Calibration curve were developed at fixed superficial gas velocity and at fixed solid flux. Figure 3.6 a shows the variation of solid flux with the solid inventory. It can be clearly observed that solid flux increases with increase in solid inventory in the system for a fixed velocity until it attains either the choking volume fraction or saturation carrying capacity of gas. It is also observed that the change in solid flux with the solid inventory for the fixed velocity is linear in the investigated range. Figure 3.6b shows the variation in gas velocities with increasing solid inventory for a particular solid flux. For a fixed solid flux, velocity and solid inventory change is not linear.

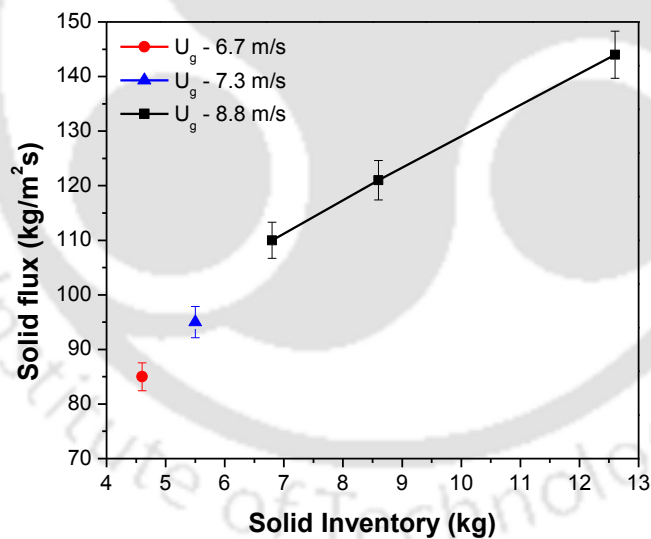


**Figure 3.6a Variation of solid flux with solid inventory**

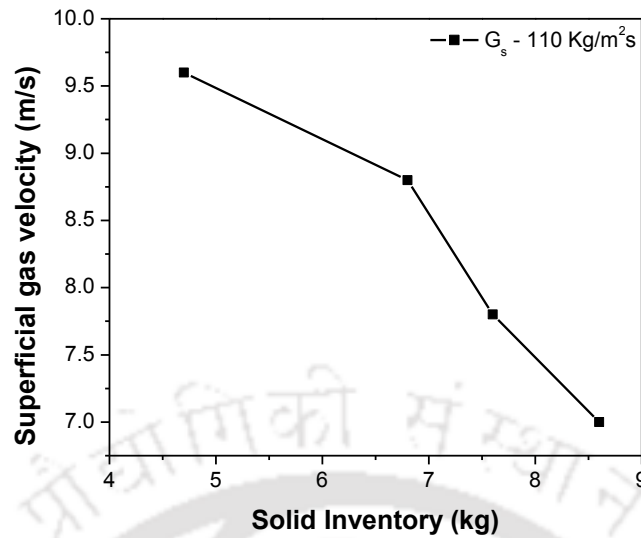


**Figure 3.6b Variation of superficial gas velocity with solid inventory for solid flux of 110 kg/m<sup>2</sup>s**

The above mentioned method accurately measures the solid flux by using densitometry and RTD techniques. However while doing RPT measurements, above method cannot be used. Since two different sources (one for densitometry and one for RPT) may affect the RPT measurements. Thus, for continuous monitoring of the solid flux during RPT measurements number of circulations method is used.

#### **Number of circulations method**

In this method, scintillation detector is fixed at a position. Radioactive tracer particle, which is similar to the solids present in the CFB, is allowed to move freely and each circulation is recorded. Data are acquired at a frequency of 83 Hz for different time intervals varying from 20 min to 6 hrs. It is found that 1 hour data is sufficient to get a steady solid flux value. This method assumes that no stagnation or dead volume is present in complete CFB loop, which is not a bad assumption to make for a long-term time average value. Solid flux is calculated from the number of circulation method by using the formula given in equation

(3.10)

$$G_s = \frac{N \times w}{A \times t} \quad (3.10)$$

where,  $G_s$  – Solid flux, kg/m<sup>2</sup>s

$N$  – Number of circulations, (-)

$w$  – Solid inventory, kg

$A$  – Cross sectional area of riser, m<sup>2</sup>

$t$  – Time, s

Table 3.2 compares the solid flux data from the two techniques. It is found that both the techniques differ within  $\pm 3.5\%$ . Thus, number of circulation method is used for monitoring the flux for entire duration of the experiment.

**Table 3.2 Comparison of solid flux by two methods**

| Operating conditions       | Velocity and volume fraction method (kg /m <sup>2</sup> s) | Number of circulations method (kg /m <sup>2</sup> s) |
|----------------------------|--|--|
| 4.6 kg, $U_g - 6.7$ m / s  | 85   | 82.3   |
| 5.5 kg, $U_g - 7.3$ m / s  | 95   | 96.9   |
| 6.8 kg, $U_g - 8.8$ m / s  | 110  | 113.1  |
| 8.6 kg, $U_g - 8.8$ m / s  | 121  | 121.3  |
| 12.6 kg, $U_g - 8.8$ m / s | 144  | 141.9  |
| 8.5 kg, $U_g - 7.0$ m / s  | 110  | 112.1  |
| 7.8 kg, $U_g - 7.8$ m / s  | 110  | 110.7  |
| 4.7 kg, $U_g - 9.6$ m / s  | 110  | 112.2  |

### 3.5 Radioactive particle tracking (RPT) measurements

Solid motion in the riser section of CFB is studied using RPT. Investigation is carried out at 1.2 m to 2.2 m from bottom of the riser. As explained earlier, RPT experiment is two-stage process. In the first stage, known as calibration, tracer particle is kept at a known position inside the riser and counts are recorded on the detectors, which are strategically placed around CFB. The counts recorded on the detectors depend on medium attenuation coefficient, which varies with solid fraction inside the riser. Therefore, 'in-situ' calibration is necessary and is conducted at the actual operating conditions to generate the position – count map. In the second stage, actual experiments are conducted and count-time map is obtained. Position-time series can be obtained by comparison of counts from the calibration and experiments. From the position – time series, instantaneous velocity time series, ensemble average velocities, velocity fluctuations and other turbulent quantities can be obtained. Detailed explanation of RPT technique is given in chapter 2. Here, specific information on the experimental setup, solid inventory, detector alignment and tracer preparation are detailed.

Calibration was done using threaded ports provided at the wall of the column. At a particular axis two calibration ports are provided which are 180° apart. Distance between two planes of ports is kept 10 cm. Ports are axially staggered to cover entire region. Tracer particle is glued at the tip of the threaded rod (calibration rod). Calibration rod is moved radially. At each plane, calibration is performed for 12 locations. Calibration is performed for 10 such planes. Using these few data points, counts at other locations are generated numerically using Monte Carlo method as explained in Upadhyay (2010).

Solid inventory was obtained from India glass beads, Mumbai, India. Density of the glass beads are 2500 kg/m<sup>3</sup>. Mean particle diameter is 500 μm (in the range of 410 μm - 600 μm).

Minimum fluidization velocity of solids is 0.2 m/s and terminal settling velocity is 4.13 m/s.

Due care is taken in tracer preparation for high velocity studies. Tracer particle is not adjusted with the conventional epoxy resin or aluminum ores (Roy, 2000; Bhusparau, 2005) which may lead to change in the surface properties and attrition of the particle due to irregular surface. Glass bead doped with scandium is prepared by heating as explained by Biswal et al. (2016). Glass cullet and scandium powder are kept in the microwave oven on the graphite surface. Temperature of 800° – 900°C is maintained in the microwave oven. Melted glass forms a spherical surface due to surface tension. Graphite bed is then cooled to form solids. Glass beads are then sieved and segregated. Due to practical difficulties exact match of size is not possible. However the selected particle size is in the range of 410  $\mu\text{m}$  – 500  $\mu\text{m}$ . Gravity settling experiments are conducted and settling time of tracer matches with the solids in the range of 410 – 510  $\mu\text{m}$ . Gravity settling experiments are conducted in 2 m height and 6 inch diameter cylindrical Perspex column. Glass bead doped with scandium is irradiated in the nuclear facility of Bhabha Atomic Research Center (BARC), Mumbai, India. Tracer particle of 500  $\mu\text{Ci}$  activity is used in all the experiments. Scandium 46 isotope has the half-life of 83 days. For each condition experiments are performed for 3 to 6 days continuously to obtain the sufficient statistics. Hence, decay in source strength is accounted as the first order reaction. Calibration and reconstruction program is modified accordingly to account the change in the strength.

Radioactive particle tracking (RPT) experiments require careful preparation of experimental setup and detectors arrangement. While positioning of detectors, saturation of detectors are taken into account for the closest possible position. Saturation occurs when the rate of photon reaching the crystal is higher than the photon counting rate of detector. If the detectors are positioned far away, detectors may not receive sufficient counts.

Detector face is mounted perpendicular to the riser wall. Detectors are strategically placed around the investigation zone as shown in the Figure 3.7. Array of 12 NaI (Tl) scintillation detectors are used to track the motion of the tracer particle. To have greater flexibility for positioning the detectors, detectors are mounted on the supports independent of experimental setup. At each plane, two detectors are mounted. Detectors at two successive planes are  $90^\circ$  apart. Two successive detector planes are kept at  $10\pm 1$  cm apart. Distance between the two axial levels of detectors is decided based on the resolution and sensitivity study. Outer disc of the detectors are kept at  $5\pm 1$  cm from the wall of riser.

As discussed in chapter 2, resolution and sensitivity are calculated for different detector positioning. The detector arrangement for which maximum resolution and sensitivity are found is used for the measurement. Figure 3.8 shows the resolution and sensitivity contours for the RPT experiments for the detector configuration and source strength used in the current study. Top and bottom regions have less resolution and sensitivity, as number of detectors available for tracking the tracer particle is less. Maximum resolution and sensitivity are observed at a length of 1.3 to 1.9 m from the bottom of the riser. Therefore, all the data for the current study are reported in this region only. It can be inferred from the contours that average resolution is 1.5 mm, for the acquisition frequency of 83 Hz. That is, if the tracer moves 1.5 mm or more within the data acquisition time, the position of the tracer particle can be discriminated as two different positions.

Some of the points, where calibration is performed, are not used in optimizing the Monte Carlo. These unused data is used for validation of reconstruction of position at stationary conditions as discussed in Chapter 2. From validation, standard error of 2.3 mm in z direction and 3.4 mm in r direction is obtained. It is to be noted that error is higher than the resolution. This is mainly due to the error contribution from statistical fluctuation in counts because of solid fraction fluctuations and error generated due to reconstruction algorithm.

During experiments, tracer particle moves in a closed loop and periodically passes through the zone of investigation. Each circulation is an independent separate event. In previous studies, two sentry detectors are used to found the tracer particle entry and exit through the investigation zone (Roy, 2000; Bhusarapu, 2005). However the sentry detectors are not used in the current work. Instead an algorithm is developed for finding the entry and exit of the detector based on the counts recorded in the four successive detectors placed at inlet and outlet respectively. From the calibration minimum counts recorded at 15 cm away from the entry of the detector plane are used as the basis of algorithm. Further, data from the height of 1.3 m – 1.85 m is considered for processing the results (based on resolution studies), thus entry and exit of the tracer will not affect the results. It is to be noted that the tracer stays only fraction of time of circulation in the investigation zone. Thus, requires long experimental time to obtain the sufficient statistics at all the locations in the investigation zone. Each experiments are carried out for 72 hours (3 days) - 144 hours (6 days) according to the operating conditions. Data are acquired at 83 Hz frequency. Each independent circulation between entry and exit section are reconstructed for position. From the position, velocity, fluctuation and other turbulent parameters are obtained as explained in section 2.2 and Table 2.1.



**Figure 3.7 Photograph of RPT test facility for laboratory scale CFB**

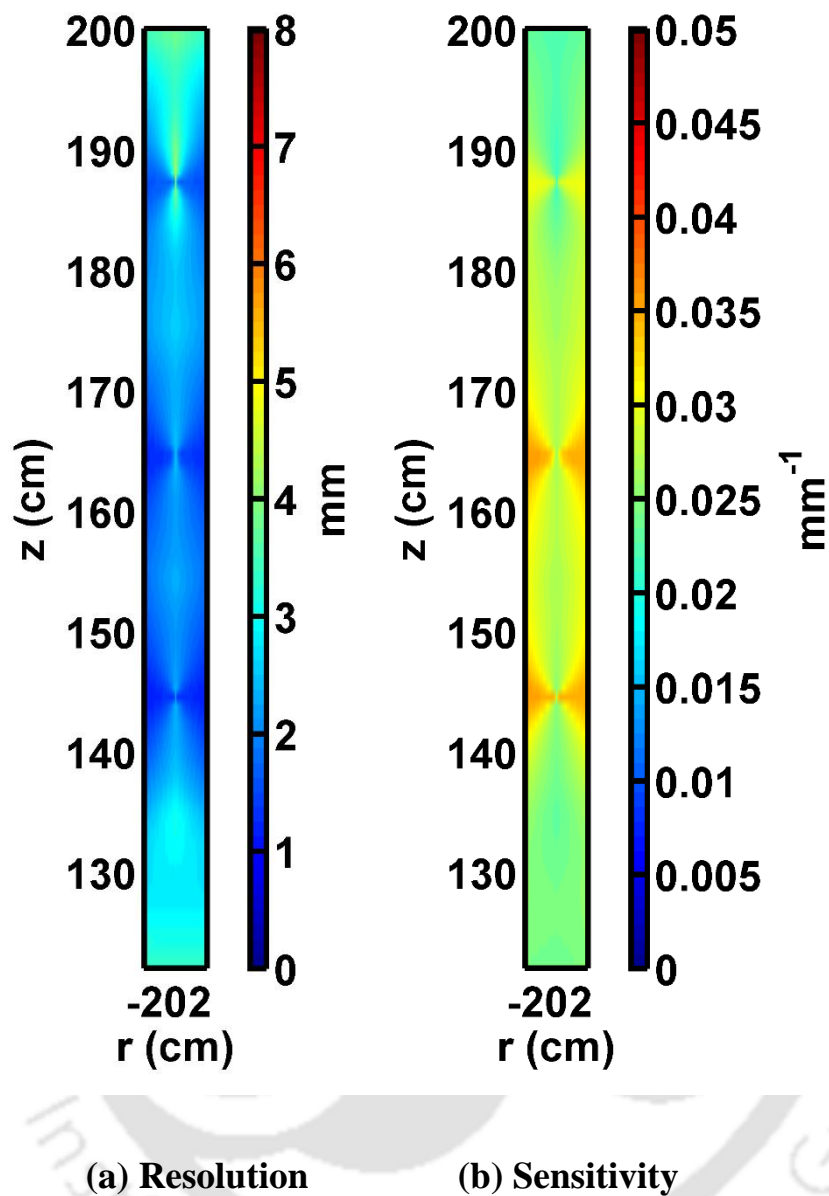


Figure 3.8 Contours of resolution and sensitivity for RPT experiments

### 3.6 Results and discussions

Solid flux studies detailed in the section 3.5 are used for the selection of operating conditions. Entire spectrum of study is not detailed here for brevity. Careful considerations are given for having enough margins from the choking conditions. Operating conditions chosen enables to have the systematic study of effect of flux and effect of superficial

velocity on behavior of laboratory scale CFB. Table 3.2 shows the detailed experimental matrix.

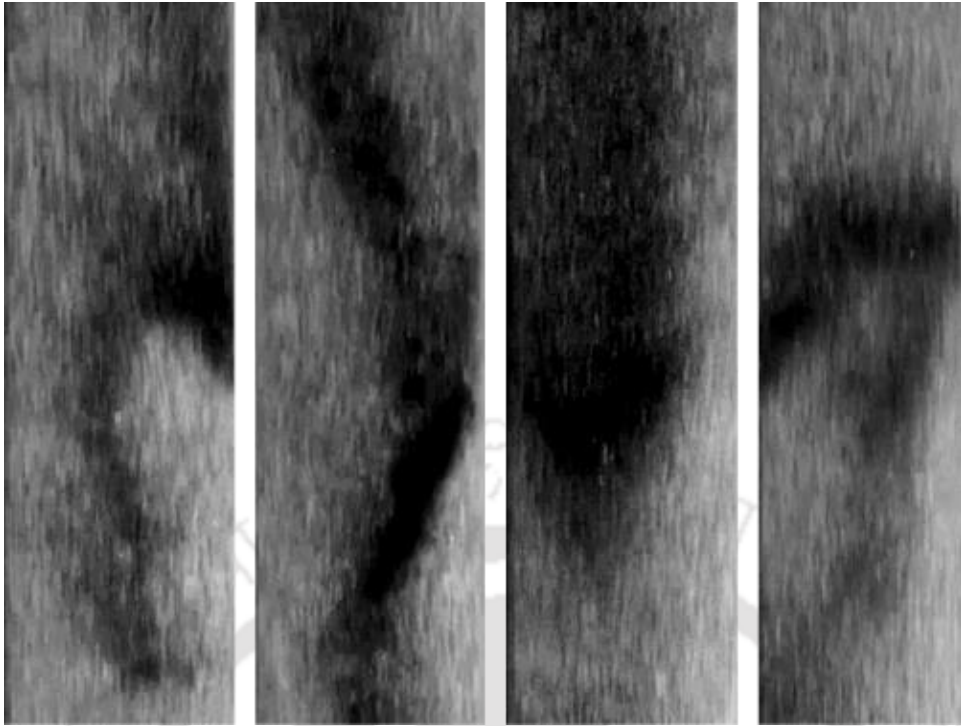
**Table 3.3 Operating conditions in laboratory scale experiment**

|   |     |     |     |     |               |     |
|---|-----|-----|-----|-----|---------------|-----|
| <b>Superficial velocity,<br/><math>U_g</math> (m/s)</b>     | 6.7 | 7   | 7.3 | 7.8 | 8.8           | 9.6 |
| <b>Solid flux, <math>G_s</math><br/>(kg/m<sup>2</sup>s)</b> | 85  | 110 | 95  | 110 | 110, 121, 144 | 110 |

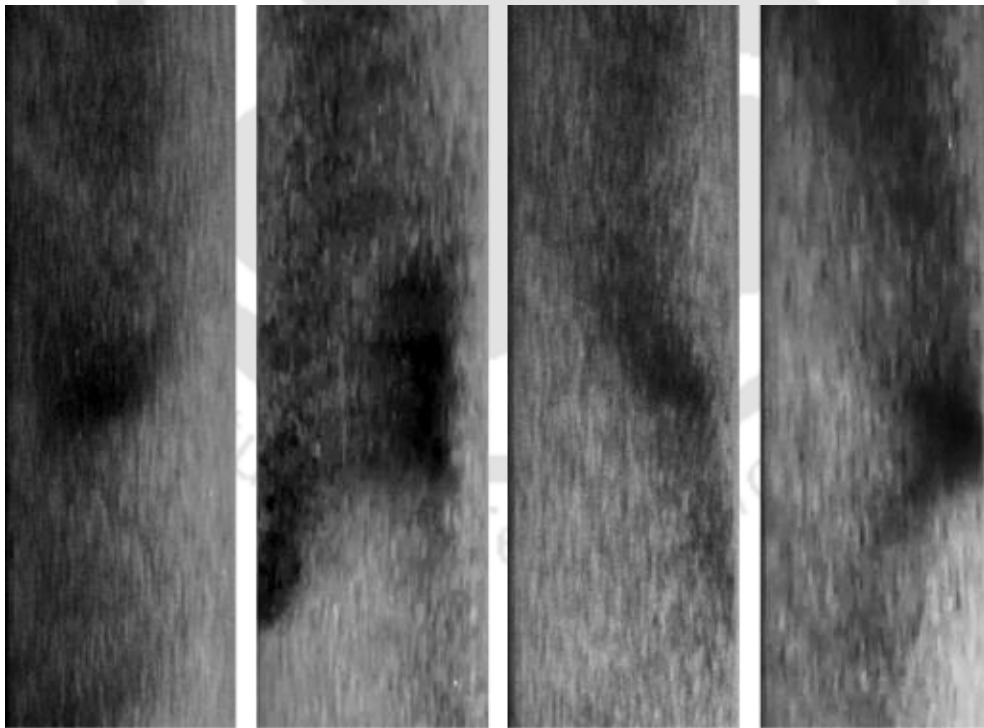
### 3.6.1 Visual observation of riser

Visual observation can give qualitative information about the characteristics of the system, so it would be beneficial to discuss before proceeding to RPT experiments. Since column is built of mild steel, it is not possible to have visual observation. To facilitate visual observation, mild steel section of investigation zone is replaced with glass section. Column is operated at all the operating conditions as in RPT investigation and observed for the distinguishable characteristics.

Solid motion is chaotic and it is not easy to characterize the solids behavior through visual observations. Fast moving, highly fluctuating turbulent motion of solids are observed. Cluster formation is prevalent in all the operating conditions. Frequency and size of clusters changes with the operating conditions. Shapes of the clusters are not easily identifiable. However, long strands and V – shaped clusters are recognizable. In case of  $U_g$  - 7 m/s and  $G_s$  - 110 kg/m<sup>2</sup>s, long strands of length of 20 cm – 30 cm is identifiable.



(a)



(b)

**Figure 3.9 Photographs of metastable structures (a)  $U_g - 7$  m/s and  $G_s - 110$  kg/m<sup>2</sup>s  
(b)  $U_g - 8.8$  m/s and  $G_s - 144$  kg/m<sup>2</sup>s**

Increase in the overall solid holdup is observed with decrease in the air velocity at the same solid flux and increase in the solid flux at the same velocity. Distribution of solids along the axial and radius location is not discernible. Qualitatively, almost all of the solids flow upwards. Most of the solids near the wall also flow upwards. Further, major change in velocities (fluctuations) is observed when the clusters are formed. Except at low velocity conditions (7 m/s and 7.8 m/s) change in the velocities are not distinguishable with the operating conditions.

### 3.6.2 Lagrangian track of particle position

In CFB, tracer particle along with solids are circulated continuously in the loop. Tracer motion is recorded whenever it passes through the interrogation zone. Hence, Lagrangian motion of a single solid particle is tracked. In each circulation, completely independent trajectories are followed. For an ergodic system, the individual trajectory of each single particle for long time represents single circulation trajectories of a large number of solids. Lagrangian track is used to characterize the system in detail and calculation of solid diffusivity which is discussed later on.

A typical trajectory of the tracer particle for single circulation is shown in the Figure 3.9 in the x-z, y-z, r-z and r- $\theta$  plane. It is observed with particle trajectories that predominantly solids move in axial direction. Radial and angular movements of solids are not significant. However, some random fluctuations are observed in the radial direction as shown in Figure 3.9. Internal circulations are also observed in some cases which may be characteristics of the cluster motion. Most of the tracks observed travel near the wall, reveals solid concentration is high near the wall.

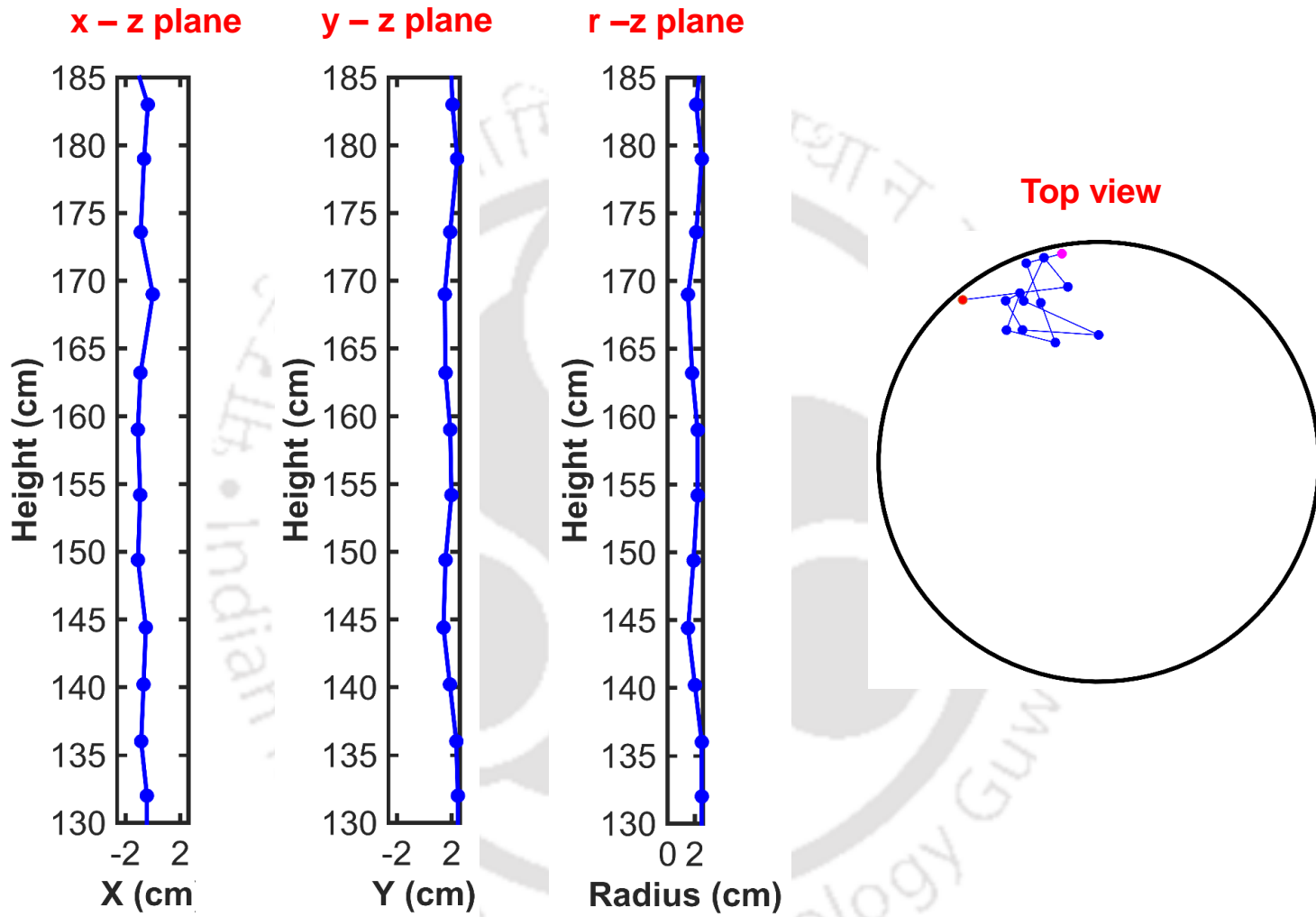


Figure 3.10 Typical position map of single trajectory in different planes ( $U_g = 8.8$  m/s,  $G_s = 110$  kg/m<sup>2</sup>s)

### 3.6.3 Lagrangian velocity of the solids

Instantaneous Lagrangian velocities of tracer particle are obtained by time differencing of the two successive positions of the tracer particle. Figure 3.11 shows the axial Lagrangian velocity of the solids with time. It can be seen that the trajectories of particle are accelerating during some of the instances and decelerating at some other instances. Deceleration of the solid particle is mainly due to the formation of cluster. Though the instantaneous velocity is able to provide the useful insight of the flow, our understanding of the classical fluid mechanics is for Eulerian references. Therefore, it is important to convert the Lagrangian data to Eulerian frame of reference. This can be achieved by integrating the entire tracer particle trajectories with space (ensemble average) over a control volume. If the system is ergodic, time average of a sample function is equal to the ensemble average (Bendat and Piersol, 2000). Almost all the natural processes are ergodic (Roy, 2000). In RPT experiments, instantaneous Lagrangian velocities are converted to the time averaged Eulerian velocities (ensemble averaged) invoking ergodicity (Roy, 2000; Bhusparau, 2005; Upadhyay, 2010). Stationarity is a necessary condition for ergodicity (Bendat and Piersol, 2000). Stationary condition is said to be satisfied if the moments of the distribution (mean, variance, etc.) do not differ over the time series. In other words, if the time series  $(t_1)$  satisfies the stationary condition, any more addition of data  $k$  such that series  $(N = t_1 + k)$ , do not change the moments of the distribution. In RPT experiments, with an increase in the data series (number of occurrences), moments of the distribution should not change to have a stationarity.

To obtain Eulerian velocities, virtual grid is formed. Velocity vector is assigned to the cell where the midpoint of line segment connecting the two position lies. The average velocity (ensemble) is calculated by summation of the instantaneous velocities in the cell and divided by the number of occurrence in the cell. Velocities at all the points can be obtained

if the experiments are carried out for sufficient long time, so that tracer particle visits all the locations multiple times. This will require a large amount of time. Hence, to reduce the experimental time finite volume grid is used in such a way that the stationary conditions are satisfied for each cell.

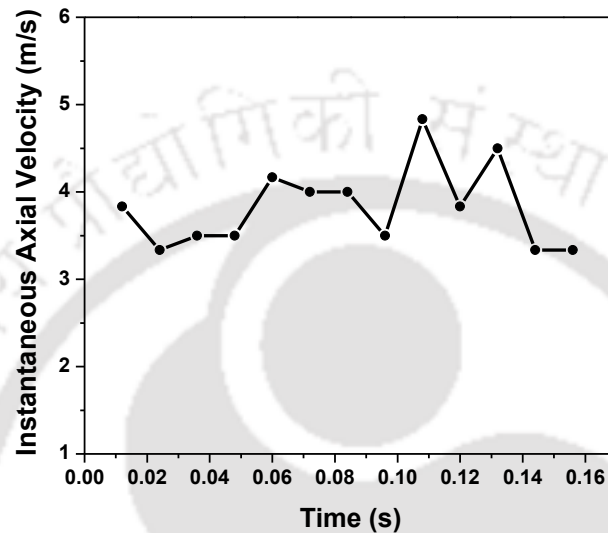


**Figure 3.11 Axial Lagrangian velocity of solids for a single trajectory ( $U_g = 8.8$  m/s and  $G_s = 110$  kg/m<sup>2</sup>s)**

Various discretization methods are followed in the literature with constant volume compartments, constant number of divisions in  $r$  and  $\theta$  directions and constant number of  $r$  and varying  $\theta$  divisions (Devanathan, 1991; Degaleesan, 1997). Basic underlying idea used in this work is to obtain equal volume of cells without comprising the statistics of the particle occurrences (Upadhyay et al., 2013). In this work,  $r$  and  $z$  directions are uniformly divided and  $\theta$  division is increased with  $r$ , as the annular area increases with radius. Figure 3.12 shows the comparison of two grids. Coarse grid ( $\Delta r = 6.5$  mm,  $\Delta z = 20$  mm) and fine grid ( $\Delta r = 5.2$  mm and  $\Delta z = 20$  mm) with  $\theta$  division varied to match the volume of the grid. No significant difference is observed for the two grids. In the present work fine grid was used, as it provided better resolution in the  $r$  direction. Therefore, the

radial direction has 5 divisions and z is divided into 28 divisions and each cell has a volume of 1.68 cm<sup>3</sup> approximately.

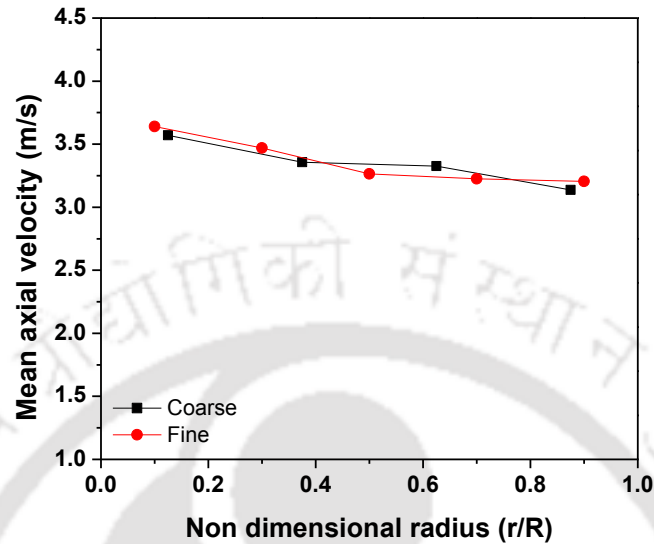
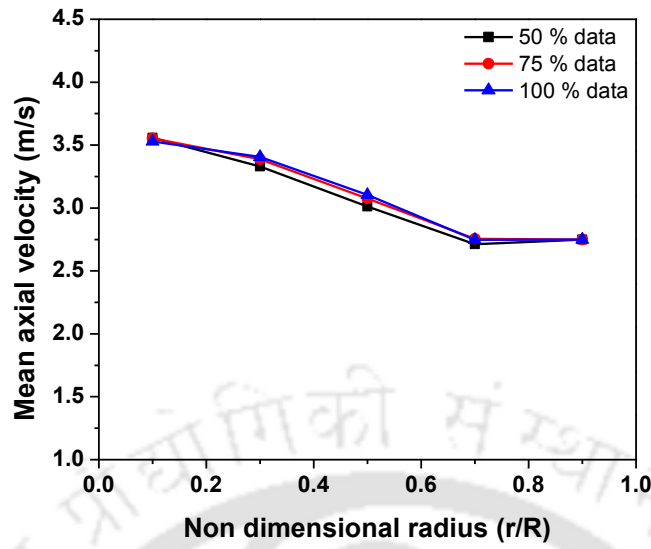
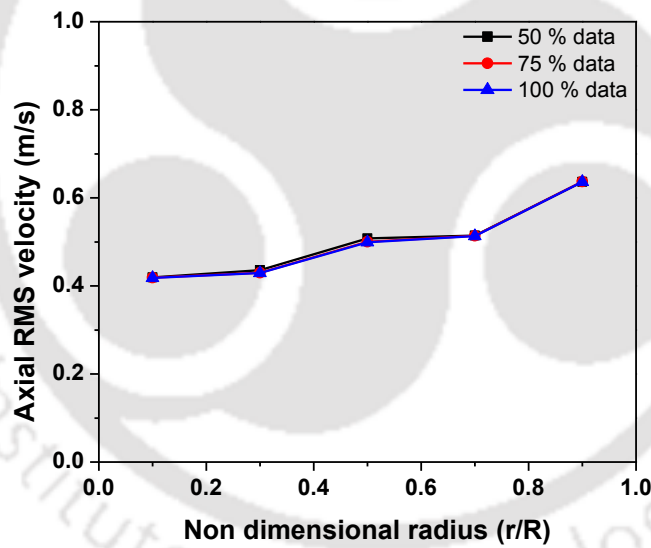


**Figure 3.12 Effect of grid on mean axial velocity at h - 1.65 m. ( $U_g - 8.8$  m/s,  $G_s - 110$  kg/m<sup>2</sup>s)**

Figure 3.13 shows the mean axial velocity and RMS velocity with 50%, 75% and 100% of total acquired data. Increase in the number of data points increases the occurrences of tracer particle in each cell. No significant change was observed in mean axial and RMS velocity. This validates the reproducibility and stationarity of the RPT experiments. It should be noted that stationarity changes with the grid size and operating conditions. Therefore, for all the operating conditions, stationarity is verified.



(a)



(b)

**Figure 3.13 Validation of stationarity (a) Axial mean velocity (b) Axial RMS velocity at  $h = 1.5$  m ( $U_g = 8.8$  m/s,  $G_s = 110$  kg/m<sup>2</sup>s)**

To present the outcome of the experiments effectively, results and discussions are initially presented only for one operating conditions ( $U_g = 8.8$  m/s,  $G_s = 110$  kg/m<sup>2</sup>s). This enables

us to understand the behavior of CFB at different height. Thereafter, comparative studies of the operating conditions are presented for volumetric averaged results

### 3.6.4 PDF of instantaneous velocity

If velocity at particular place in riser is monitored continuously, distribution of velocity is obtained. Such a velocity distribution is required for predicting the behavior of any reactor (Levenspiel, 1999). However, most of the available techniques do not provide such distribution. RPT is such a versatile technique, distribution of velocity at every point in space can be obtained. Due to the limitations of time, the size of space is limited to the size of the grid. Following approach can be used to obtain the velocity distribution. Lagrangian velocity vector can be obtained from the two successive reconstructed positions as explained previously. Velocity vector is assigned to the compartment in which the midpoint of the vector lies. With multiple occurrences in the compartment, distribution of velocities for a particular compartment is obtained. In the present study, the experiments are performed for the sufficiently long time to get enough statistics. It should be noted that stationarity condition ensures no further change of distribution.

Figure 3.14 shows the PDF of axial instantaneous velocity at three different axial and radial positions at zero degree theta for superficial air velocity 8.8 m/s and solid flux 110 kg/m<sup>2</sup>s. Results show that the velocity distribution at all the positions is unimodal, which clearly indicates there is a local maximum in each cell. This local maximum of the cell represents the mean velocity. Further, it has been observed that the distribution of solids velocity remains almost same with change in height for same radial locations. However, distribution changes with the change in radial position. The spread of PDF is higher near the wall compared to the center of the column. It is worthy to note that no negative velocity is observed at all the locations. Bhusarapu et al. (2006) stated that the negative velocities are the characteristics of clusters. No negative velocities was observed by Bhusarapu et al.

(2006) in the core region. However, in the current study we have clearly observed the presence of the clusters through photographic studies. Hence, it can be established that the presence of negative velocity alone cannot confirm the presence of the clusters. Since various sizes and shapes of clusters are observed, effect of clusters on velocity and type of distribution is not conclusive at this stage. Further, wide distribution of instantaneous velocity confirms the contribution of meso-scale meta-stable structures. Though, such structures can be observed at all the locations inside the riser, probability of occurrence is higher near the wall. This can be corroborated through higher velocity distribution observed near the wall of the riser. Figure 3.15 shows the PDF of radial instantaneous velocity. Results show that radial velocity at all the locations are negligible compared to the axial velocity of the solids. This affirms that in riser, solid motion is primarily in the axial direction. However, relatively larger distribution in radial velocity is observed near the center of the column compared to the wall.

### **3.6.5 Velocity vector plots**

Vector plot gives qualitative information on overall mixing pattern in riser. Figure 3.16 shows ensemble averaged velocity vector plots in  $r - z$  coordinate at different angular planes via 0, 45, 90 and 135 degree for  $U_g - 8.8$  m/s and  $G_s - 110$  kg/m<sup>2</sup>s. No negative velocities are observed in the time averaged sense. At all the places, flow is directed upwards which signifies dominant axial motion. No significant difference is observed between the velocity near the wall and at the center. All the planes show similar velocity profiles. This confirms the axi-symmetric flow. Finally, no significant difference is observed in axial velocity with the height of the riser. Hence, flow can be considered as ‘developed’ at least in axial direction. Even though in strict sense, fully developed flow requires radial and azimuthal velocities to be zero.

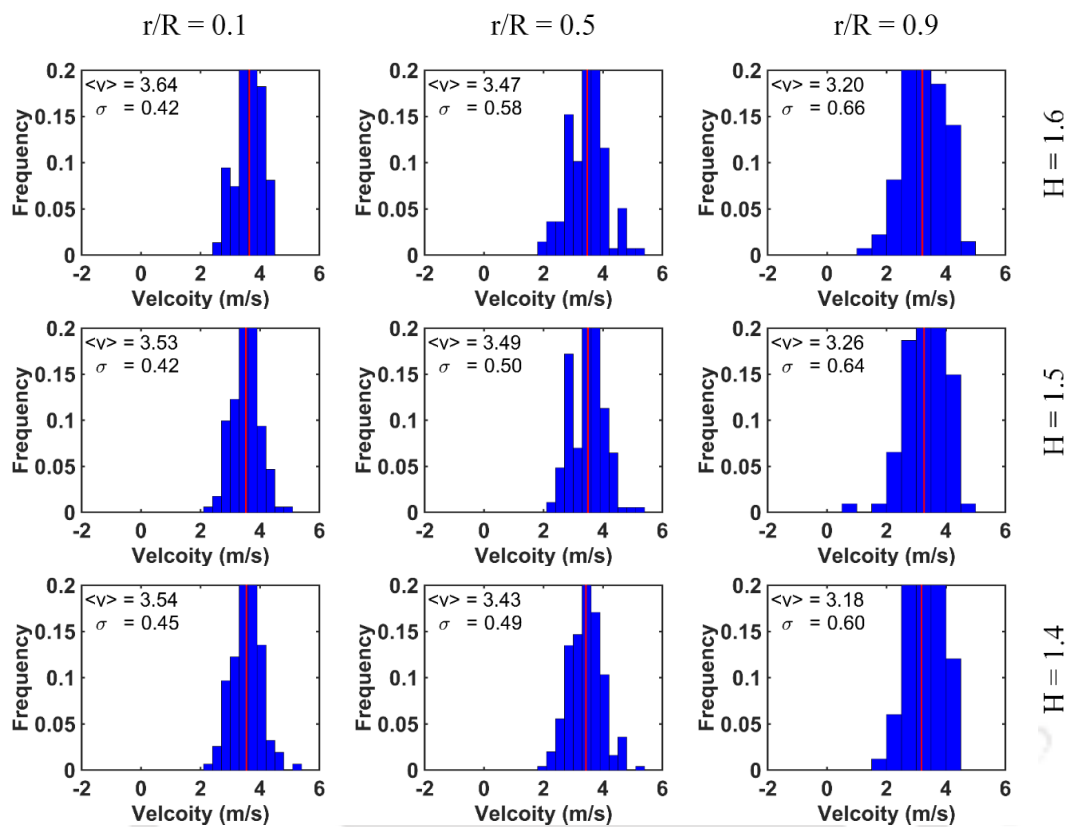


Figure 3.14 PDF of axial instantaneous velocities for the operating condition of  $U_g = 8.8 \text{ m/s}$  and  $G_s = 110 \text{ kg/m}^2\text{s}$  at  $\theta \text{ plane} = 0^\circ$

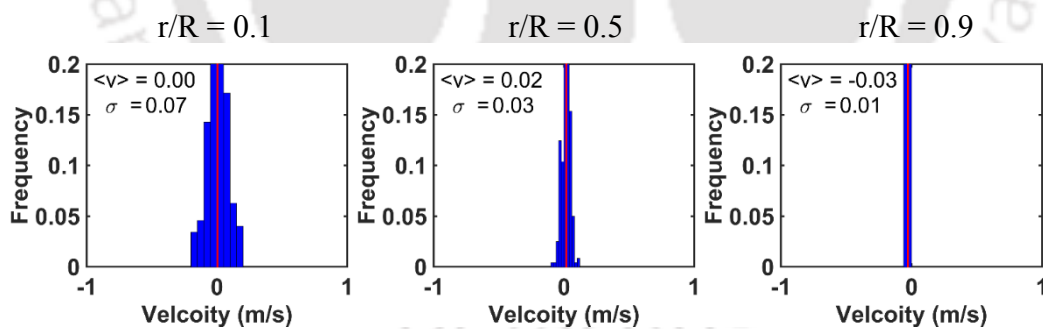
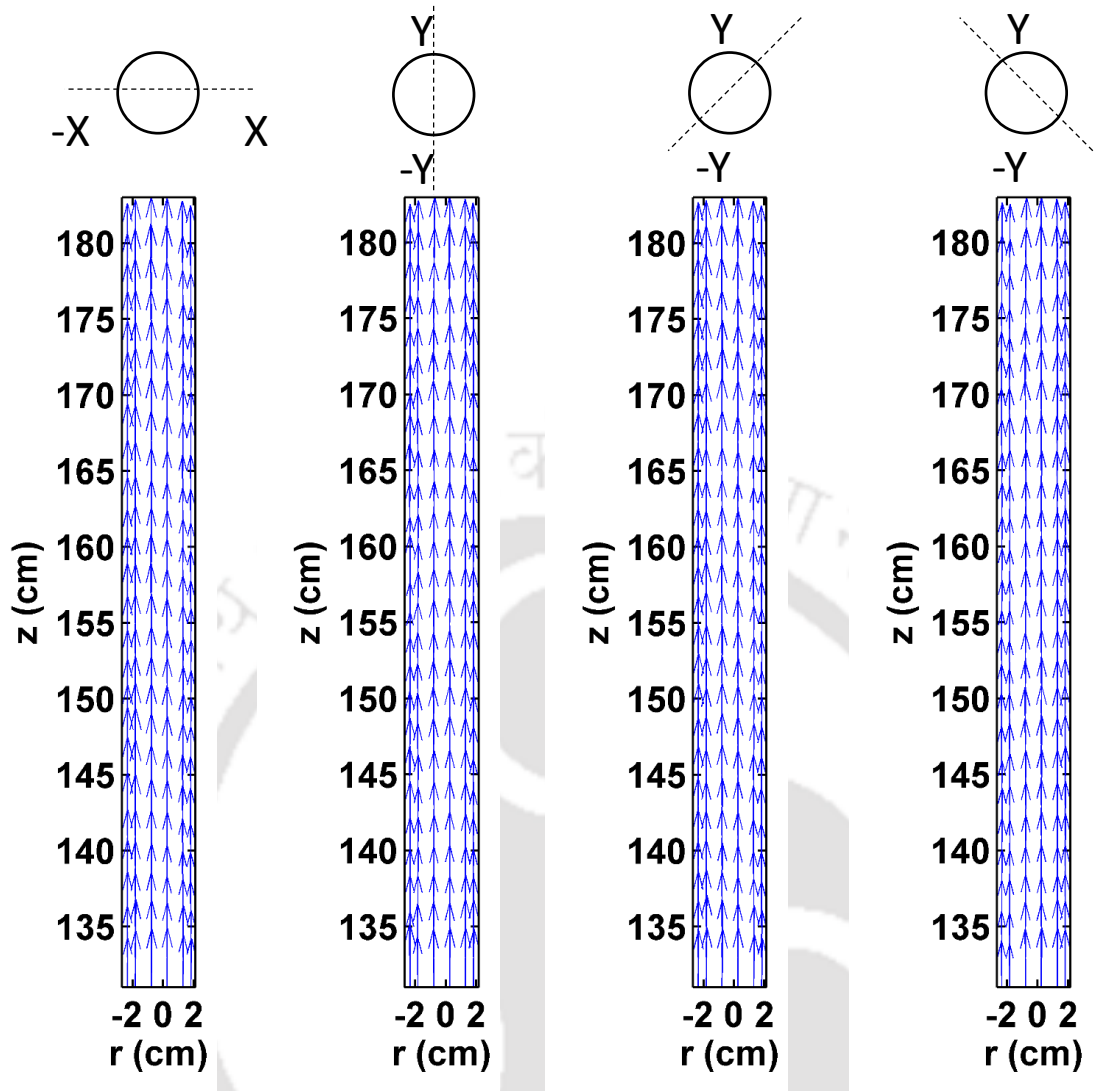


Figure 3.15 PDF of radial instantaneous velocities for the operating condition of  $U_g = 8.8 \text{ m/s}$  and  $G_s = 110 \text{ Kg/m}^2\text{s}$  at  $\theta \text{ plane} = 0^\circ$  at height of  $H = 1.5 \text{ m}$



**Figure 3.16** Vector plot at different planes for the operating condition of  $U_g - 8.8 \text{ m/s}$  and  $G_s - 110 \text{ kg/m}^2\text{s}$

Similar profiles are observed for all the operating conditions ascertain axi-symmetric flow is maintained. For comparative studies, azimuthally averaged values are used rather than individual planes, as two dimensional plots are easy for interpretation. Further at all the operating conditions axi-symmetric flows are ascertained, thus azimuthal average will not influence the comparison.

### 3.6.6 Number of occurrences

The total number of times tracer particle visits a particular location/cell volume is called number of occurrences. Tracer particle frequently visits those locations where solid fraction is high. Therefore, if velocity fields are known then these occurrences can provide a ‘good’ idea about the solid distribution. In the present work, occurrences plots are used to obtain the qualitative idea of solid distribution.

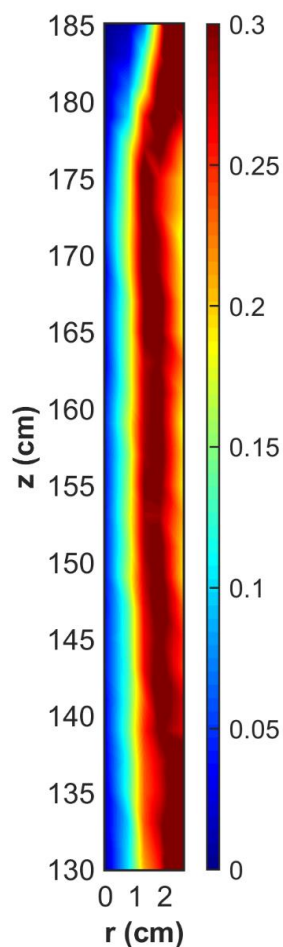


**Figure 3.17** Contour map showing the azimuthal averaged occurrence for the operating condition of  $U_g = 8.8$  m/s and  $G_s = 110$  kg/m<sup>2</sup>s

Figure 3.17 shows the contour of an azimuthally averaged normalized occurrence plot. Result shows that solid distribution is high near the wall and low at the center core region.

Occurrence increases steeply with radius. Most of the literature shows the wall peaking (Godfroy et al., 1999; Bhusarapu, 2005), however in this work, steep increase in occurrence has been observed from the center to the wall. So far qualitative analysis of the system is presented to find the overall flow pattern. However, quantitative analysis might give distinguishable characteristics of the system. Average velocities and other turbulent quantities at different axial position can throw light on the behavior of the riser in detail for the said operating conditions. These are discussed in detail in the following sections.

### 3.6.7 Ensemble averaged velocity

Figure 3.18 shows ensemble averaged velocity at three different heights for the operating condition of  $U_g - 8.8$  m/s and  $G_s - 110$  kg/m<sup>2</sup>s. Radial variation of mean axial velocity shows almost flat profile at all the heights. In fact, radial variation in the axial mean velocity is within 10% and the maximum velocity obtained is less than 0.5 times of the gas superficial gas velocity. Since the volume fraction of the solid phase is low, accumulation of solids near the wall has not significantly affected the solid flow profile. Similar profile has been reported by other researchers also (Tsuji et al., 1984; Mathisen et al., 2008; Gopalan and Shaffer, 2013). Typically in CFB, core annulus profile is reported, where solids flow downward near the wall. However, in current work negative mean axial solids velocity is not observed and solids moves upward both at center and near the wall in time average sense. Nevertheless, it does not mean that solids are not moving downward. Downward motions of the solids are observed in instantaneous velocity. However, occurrences of such events are relatively low and are mainly due to the meta-stable structures. Further, radial mean velocity of solids is close to zero. Thus it once again affirms that lateral motion is limited as reported in the instantaneous motion. Azimuthal mean velocity of solids also shows the similar profile as of radial mean velocity. Axial mean velocity variation with height is within 10%. This further validates that the flow is already

developed in the riser at investigated height. Further, it is noted that slip velocity is approximately 1.3 times of the terminal settling velocity of the solids, assuming gas velocity is same as the superficial gas velocity (plug flow). Such a slip velocity is usually observed either in dilute flow conditions or in dense suspension upflow conditions.

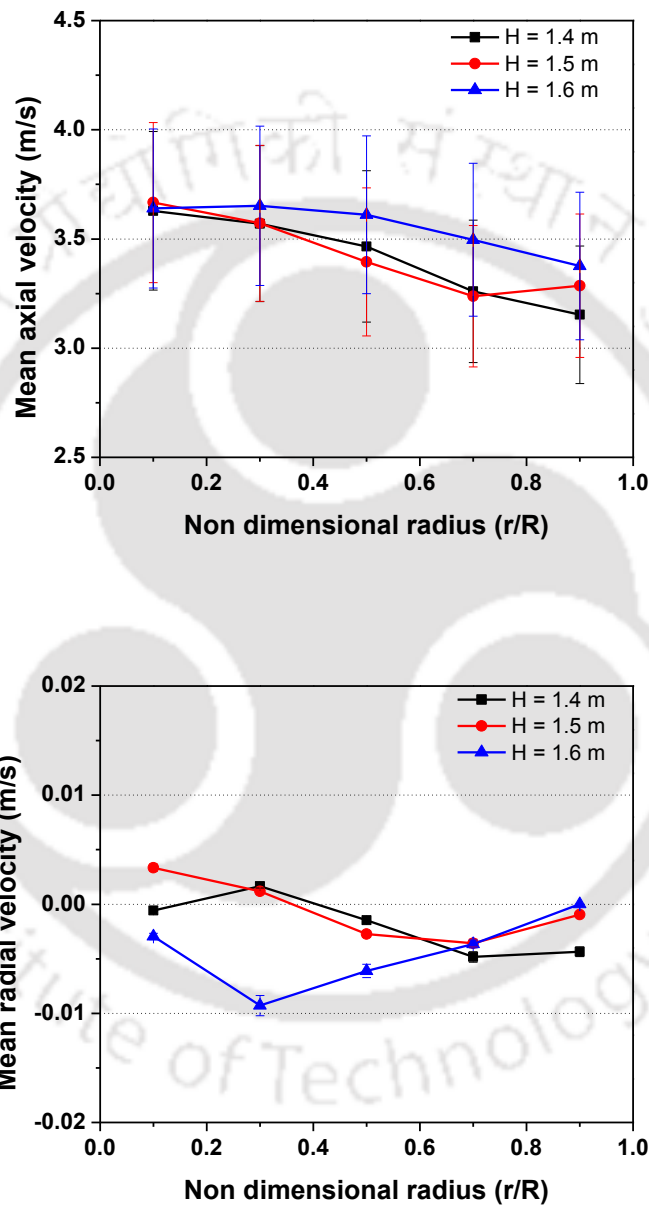


**Figure 3.18** Azimuthally averaged mean axial velocities at different heights for operating condition of  $U_g = 8.8$  m/s and  $G_s = 110$  kg/m<sup>2</sup>s

### 3.6.8 Solid velocity fluctuations

Visual observation of flow field in riser reveals large scale and meso-scale meta stable structures in axial and radial directions. Stationary nature of these snapshots cannot characterize the flow fluctuations. In order to characterize the fluctuating behavior of solids, second order moment of solid velocity (spatial correlation of fluctuation flow field  $\langle v' \rangle$ ) is studied (Tennekes and Lumley, 1972; Monin and yaglom, 1975). Spatial correlations of the second order moments are related to the Reynolds stresses,  $\langle v'_p v'_q \rangle$ , i.e. transport of momentum in q direction due to the fluctuation in p direction. It is to be noted that such an averaged way of representation leads to loss of information on scales of turbulences. Obtaining the averaged turbulence quantities are challenging for the multiphase flow systems and only limited data is available in the literature on CFB.

In the current work, solids turbulence is quantified following similar approach to the fluids. From the instantaneous velocities and ensemble average velocities in each grid, fluctuation velocities and root mean square velocities are calculated as,

$$v'_q(i, j, k) = v_q(i, j, k) - \langle v_q(i, j, k) \rangle \quad (3.11)$$

$$\langle v_q \rangle^{RMS} = \sqrt{\langle v_q'^2 \rangle} \quad (3.12)$$

Further, Reynolds stresses are obtained as,

$$\tau_{qs} = \rho_p \langle v'_q(i, j, k) v'_s(i, j, k) \rangle \quad (3.13)$$

From equation (3.11) and (3.13) six independent symmetric stress tensors are obtained.

Figure 3.19 shows the root mean square (RMS) fluctuations at three different heights for the operating conditions of  $U_g = 8.8$  m/s and  $G_s = 110$  kg/m<sup>2</sup>s. Radial variation of axial RMS velocities at different height show similar trend and almost remains same for all the heights.

Similarly, radial RMS velocities do not change with the height. Once again this proves that flow is fully developed.

Axial RMS velocities of solids are low at the center and gradually increase towards the wall. Similar kind of profile has been previously reported by Tsuji et al. (1984), Caloz (2000), Mathisen et al. (2008), He et al. (2009), Gopalan and Shaffer (2013), Pantzali et al. (2013) in CFB. Similar profile has also been reported for both Geldart Group A (Pantzali et al., 2013) and Group B (Caloz, 2000; He et al., 2009; Gopalan and Shaffer, 2013) particles. However, Caloz (2000) and He et al. (2009) reported axial RMS velocities attains the maximum value around  $r/R = 0.8$  and decreases towards the wall. In this work, such a maximum value is observed at the wall itself. Similarly, Mathiesen et al. (2000), Mathisen et al. (2008) and Pantzali et al. (2013) also reported maximum fluctuations at the wall only. The reason behind this phenomenon is not clear at this point. This might be due to the low volume fraction observed in these works which have not attained the critical volume fraction near the wall. In other words, fluctuations due to mean free path are still dominating and decrease in the mean free path is not critical enough to decrease the fluctuations. Further it is to be noted that radial RMS velocity and radial mean velocity is low near the wall. Thus, solid – wall interactions are not dominant. However, the wall shear due to the velocity gradient is not negligible. Further, as information on gas turbulence and effect of clusters on solid turbulence is not available, it is difficult to quantify the forces responsible for the solid fluctuations.

Axial RMS velocities are approximately five times higher than the radial RMS velocities. This confirms that fluctuations in axial and radial directions are not same. Therefore, the flow is anisotropic and fluctuations are dominant in the primary flow direction. Further, the radial variation of mean axial velocity and axial RMS velocity of solids are not same. This indicates that different mechanism/forces govern the mean velocity and fluctuations. Mean

velocity of solids is primarily due to the drag and majorly governed by the gas motion. However, the fluctuations are majorly governed by the solid interactions (both solids-solids and solids-wall) and metastable structures.

Figure 3.20 shows the normal and shear Reynolds stresses for the same operating conditions,  $U_g = 8.8$  m/s and  $G_s = 110$  kg/m<sup>2</sup>s. Results show that normal Reynolds stress per unit density in the axial direction is significant. However, in the radial and tangential directions (shear Reynolds stresses) the values are almost zero. This indicates that flow is anisotropic. Previously, anisotropic condition in CFB has been experimentally proved by lot of studies (Tartan and Gidaspow, 2004; Bhusarapu et al., 2006; Pantzali et al., 2013). Interesting observation is that shear stress  $\tau_{rz}$  is very less, almost negligible compared with  $\tau_{zz}$ . Similar kind of observation has been made by Tartan and Gidaspow (2004), with the particle size of 530 micron and density of 2460 kg/m<sup>3</sup>. However Bhusarapu et al. (2006), Pantzali et al. (2013) and Ibsen et al. (2002) reported significant values of  $\tau_{rz}$ , for the solids particles having lesser momentum. Insignificant values of  $\tau_{rz}$  might be due to the particle properties, as solids have high momentum, change in the direction of the motion is less likely to happen. From the present and previous studies, it can be concluded that particle properties play a major role in the radial motion of solids. Other kinetic and shear stresses are negligible.

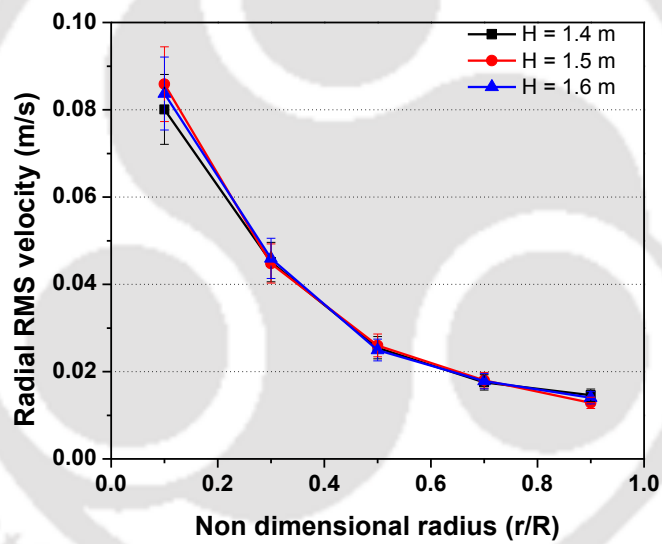
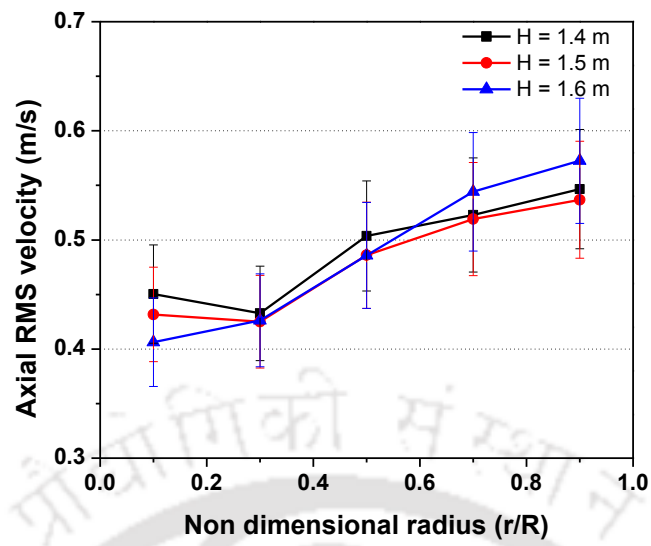
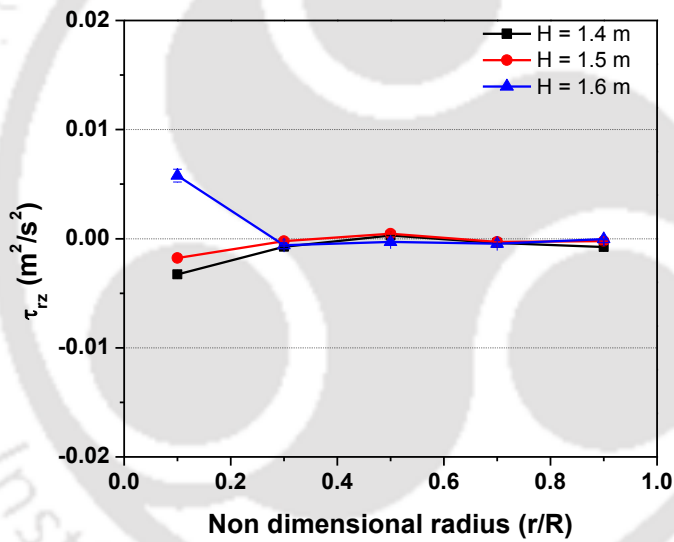
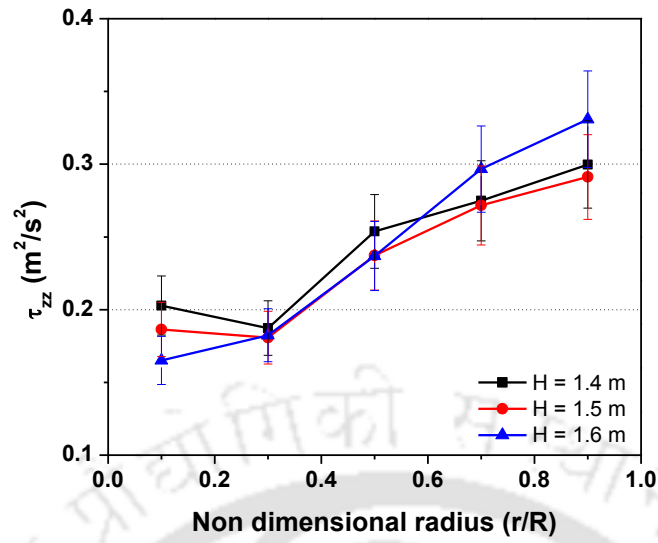


Figure 3.19 Azimuthally averaged RMS velocities at different heights for operating condition of  $U_g - 8.8 \text{ m/s}$  and  $G_s - 110 \text{ kg/m}^2\text{s}$



**Figure 3.20** Azimuthally averaged Reynolds stress at different heights for operating condition of  $U_g = 8.8 \text{ m/s}$  and  $G_s = 110 \text{ kg/m}^2\text{s}$

### 3.6.9 Turbulent kinetic energy

Normal components of the Reynolds stress give the fluctuating kinetic energy available. It can be expressed as,

$$KE = \frac{1}{2} \rho_p \left[ \langle v_r'^2 \rangle + \langle v_\theta'^2 \rangle + \langle v_z'^2 \rangle \right] \quad (3.14)$$

Kinetic theory of granular flow (KTGF) expresses the fluctuations in terms of granular temperature, similar to the thermodynamic temperature represented in kinetic theory of gases. Further discussion on KTGF can be obtained from Gidaspow (1994). Granular temperature is related to the turbulent kinetic energy as,

$$\frac{3}{2} \varphi = \frac{1}{2} \left( \langle v_r' \rangle + \langle v_\theta' \rangle + \langle v_z' \rangle \right) \quad (3.15)$$

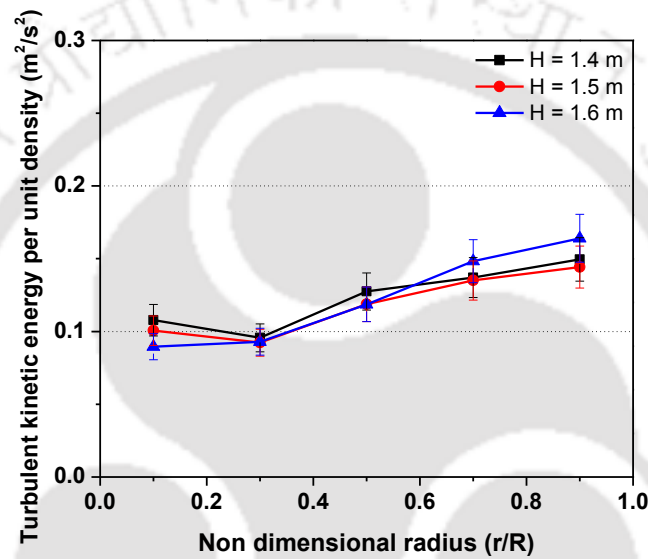


**Figure 3.21 Azimuthally averaged Turbulent kinetic energy at different heights for operating condition of  $U_g = 8.8$  m/s and  $G_s = 110$  kg/m<sup>2</sup>s**

Turbulent kinetic energy (TKE) per unit mass is given in the Figure 3.21 for  $U_g = 8.8$  m/s and  $G_s = 110$  kg/m<sup>2</sup>s. TKE is high near the wall and low at the center. TKE values are in the order of axial RMS fluctuations, in fact follows the similar trend. Similar to the previous results, with height, no significant change is observed for TKE. Trend and values of TKE is of the same order as in Tartan and Gidaspow (2004) and Pantzali et al. (2013), even though the superficial gas velocities and mass loading are higher in the current work. Turbulent kinetic energy can be interpreted as the energy available for dissipation. The

value of TKE for the operating condition of  $U_g = 8.8$  m/s and  $G_s = 110$  kg/m<sup>2</sup>s is relatively low, hence, energy available for dissipation is also comparatively low.

Discussion so far focused on the velocity characteristics and radial profiles of solid motion. Nevertheless, it does not give any information about the effect of operating conditions. In the following section, systematic studies on effect of operating conditions are given. Initially the effect of superficial gas velocity on behavior of solids flow in riser is discussed. Thereafter, the effects of solid flux are discussed. Finally, incremental change in both superficial velocity and solid flux on flow behavior of riser are discussed.

### **3.7 Effect of superficial gas velocity**

Riser is operated at different superficial gas velocities,  $U_g$  (7, 7.8, 8.8, 9.6 m/s) at the same solid flux of 110 kg/m<sup>2</sup>s. This is achieved by changing the mass of solids in the system as explained in section 3.4. Solids motion are turbulent and clusters are observed in all the operating conditions. Cluster size and frequency increases with decrease in gas velocity. Even though the profiles of solid holdup are difficult to characterize with the visual observation. Solid holdup is visibly increased for 7 and 7.8 m/s. Negative velocities are not observed in the mean velocity vector plots for all the conditions. Axi-symmetric motion is observed in all the conditions as evident from the vector plots (not given here for the sake of brevity). As discussed above, the PDF of instantaneous velocity reveals more insight of the flow. Hence, PDF of instantaneous velocities are compared for all the operating conditions. Figure 3.22 shows the PDF of axial instantaneous velocity at three different radial locations viz. at center, intermediate region and at the wall. Solid velocity distribution is provided here for the entire height (i.e 135 – 180 cm) under observation.

Unimodal peaks are observed for all the conditions at all the places. Negative axial velocities are observed near the wall for all the operating conditions. However, the

occurrences of negative velocities are reducing near the wall with an increase in gas velocities. In case of 8.8 and 9.6 m/s, the occurrence of negative velocities are almost negligible. This shows that the back mixing of the solids reduces with an increase in gas velocity. In case of 7 m/s and 7.8 m/s, negative velocities are observed all along the column. Further, it is observed that spread of instantaneous velocity distribution decreases with gas velocity. And also, spread increase while moving from center to the wall for all the conditions. The results show that at higher velocities solids movement is close to plug flow condition while at lower velocity, significant back mixing is observed even at the center of the column.

Since the overall mean velocity is positive, the solid back mixing at lower velocity (particularly at the center of the column) clearly indicates the presence of clusters which is also observed in photographic analysis. Further, more occurrences of negative velocity at lower superficial velocity of gas indicates that cluster formation rate is higher at lower velocity compared to higher velocity. However, it does not mean that no cluster formation take place at higher gas velocity. Photographic analysis shows that cluster formations at all the operating conditions. However, frequency of clusters, shape and size differs with operating conditions, typically decreases with increase in the velocity. Maximal size of clusters can be related with negative velocity. However, shape of clusters to be known to find the size of clusters. It is to be noted that the size distribution or size of clusters cannot be obtained from RPT.

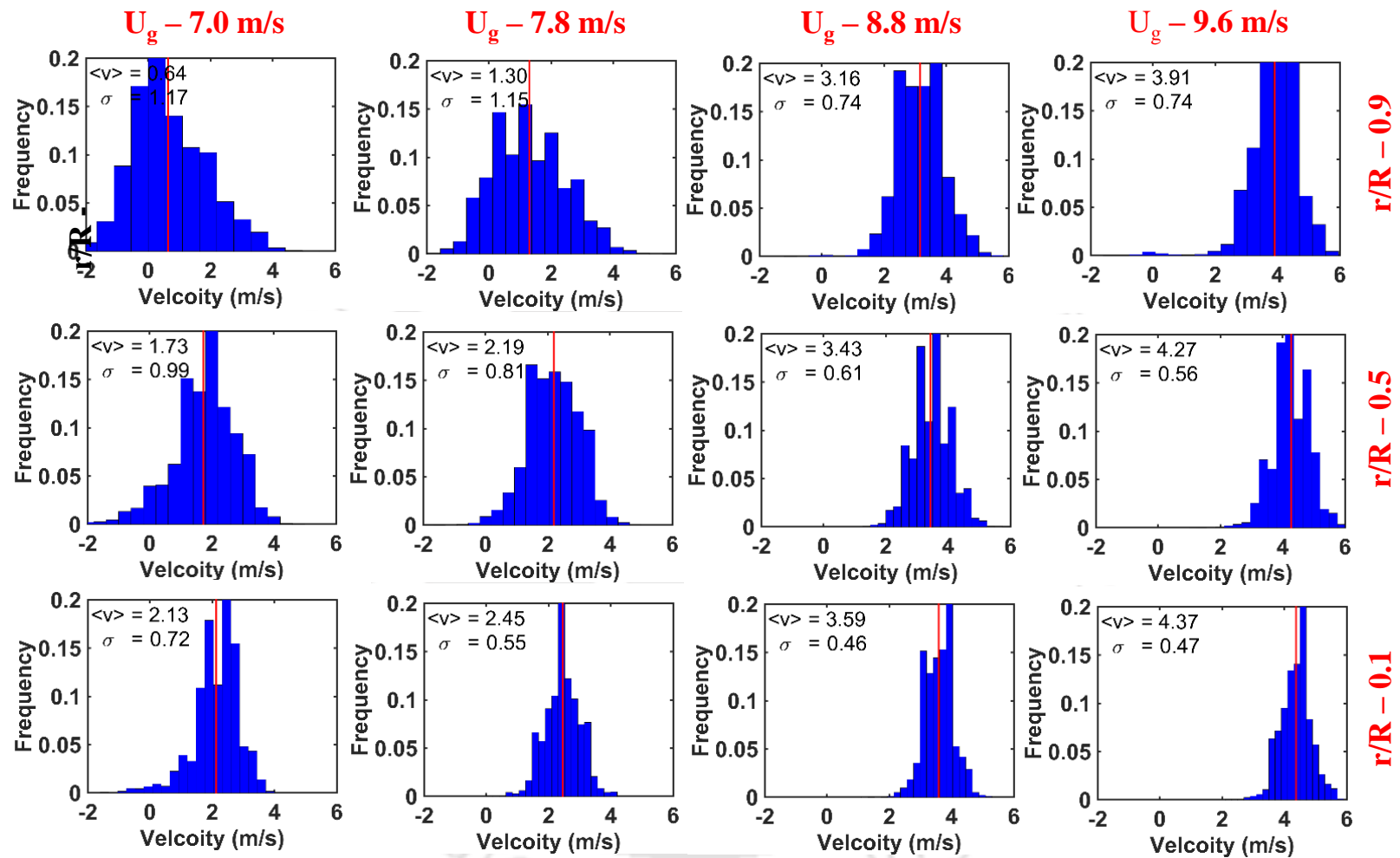


Figure 3.22 PDF of axial instantaneous velocity of solids for different gas velocity at the flux of  $110 \text{ kg/m}^2$

Since no significant difference is observed in mean solids velocity with the height (as shown in vector plot and section 3.6), all the plots presented hereafter are azimuthally and axially averaged for all the radial locations.

Figure 3.23 shows the mean axial and radial velocity profiles of the solids for different gas inlet velocities. It is observed that mean axial velocity of the solids increases with increase in inlet gas velocity. This is mainly due to the increased momentum of the gas which increases the solids velocity. This indicates that the mean motion of the solids predominantly depends on the drag and hence on the fluid-particle interaction. In the case of 7 m/s and 7.8 m/s flux, gradient in the  $r$  direction is comparatively higher, resembling parabolic profile. However, increasing the superficial gas velocity from 7.8 m/s to 8.8 m/s leads to almost flat profile of solids velocity. Actually, increase in the superficial gas velocity at the same flux decreases the volume fraction of solids in the riser and more uniform distribution of solids is achieved which leads to the flat profile.

Results indicate that change in the mean solid velocity with increase in the superficial gas velocity differs for each case depending upon the change in solids fraction and its distribution. When gas velocity is increased from 8.8 m/s to 9.6 m/s, change in the mean axial solid velocity is almost equal to the change in the gas velocity and there is no change in the profile. This indicates that after certain gas inlet velocity (8.8 m/s in this case), change in gas inlet velocity doesn't change the solid radial distribution significantly. This result indicates the existence of different regime.

For all the operating conditions, mean axial velocity of solids is positive, even near the wall. Figure 3.23b shows that mean radial velocity is very low, almost zero, for all the operating conditions. Similar profile has been observed for azimuthal mean velocity. This shows that the flow is predominantly in the axial direction for all the conditions.

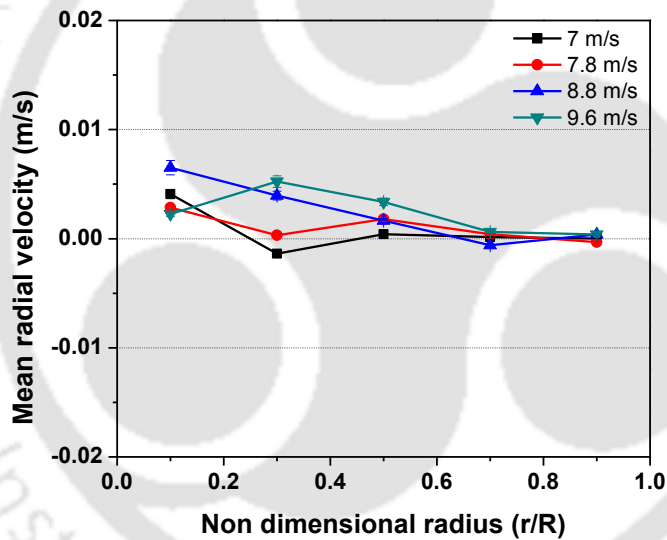
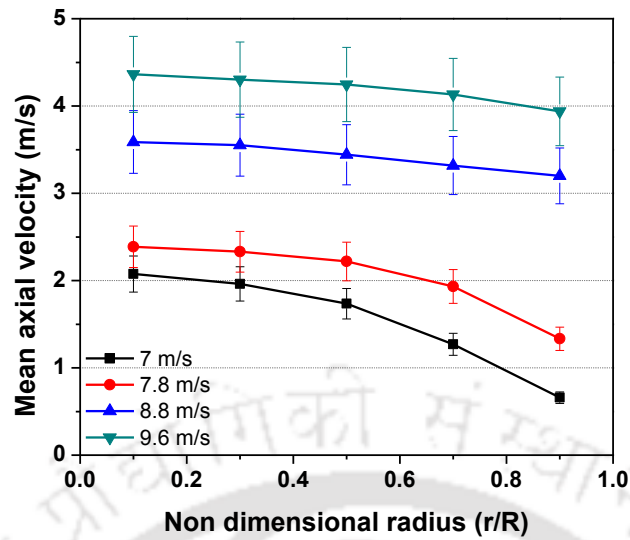


**Figure 3.23 Azimuthally and axially averaged mean velocities for different gas velocity for the flux of  $110 \text{ kg/m}^2\text{s}$**

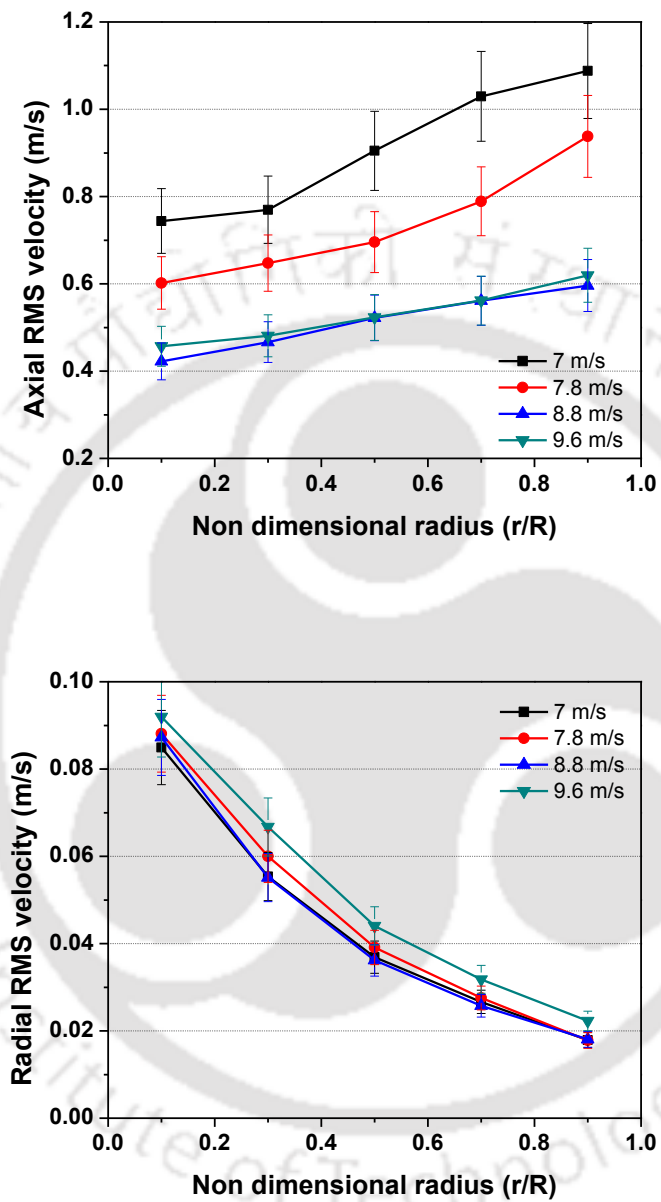
Figure 3.24 shows the radial variation of axial and radial RMS velocity at different superficial gas velocities. Axial RMS velocities are low in the center and high near the wall for all the conditions. However, shapes of the profiles are different. Similar to the mean axial velocity profile, gradient of mean axial RMS velocity is high along the radius for 7 m/s and 7.8 m/s conditions. However, in the case of 8.8 m/s and 9.6 m/s, almost a linear

profile is observed. With increase in the gas inlet velocity, axial RMS velocity decreases until 8.8 m/s and remains almost constant thereafter.

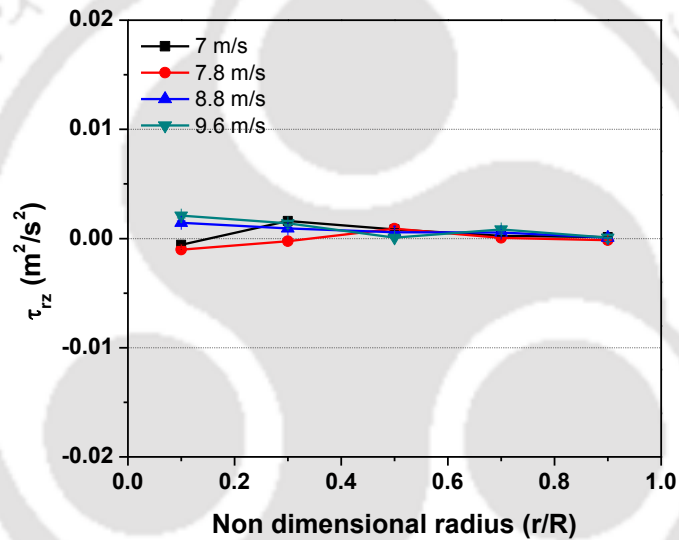
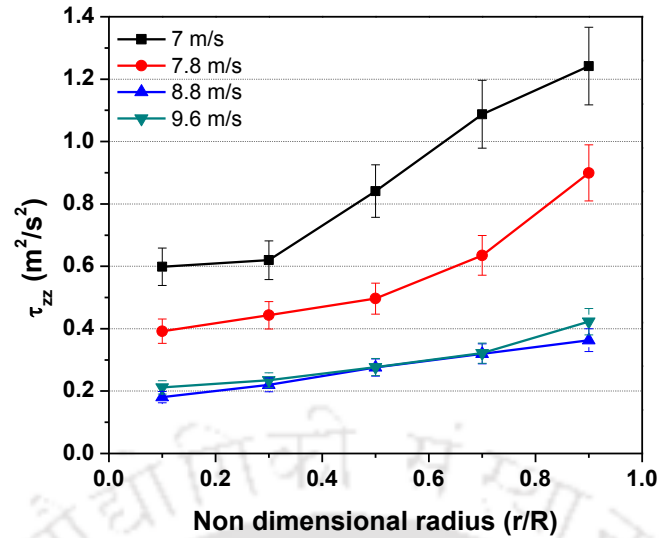
Fluctuations are low for high velocity condition, which is counter intuitive. Clearly indicates that fluid-solid interaction is not the only force which is responsible for the motion of the solids in riser. Fundamentally, solid fluctuations are due to the solid – solid interactions (solid – solid collisions and clusters) and gas – solid interactions (gas turbulence). With increase in the gas velocity, solid – solid interactions decreases and gas turbulence increases. Dominance of either of these two decides the increase or decrease in the solid fluctuations. With increase in the gas velocity, solid holdup is reduced, which minimizes the solids collisions. Further, with photographic analysis it has been found that the frequency of cluster (meso-scale meta-stable structure) formation reduces with increase in gas inlet velocity. Thus decrease of solid fluctuations with increase in gas velocity is due to the dominance of the solid – solid interactions over the gas turbulence. However, this general trend of decreases of solid fluctuations with increase in gas velocity is not observed for the case of 8.8 m/s to 9.6 m/s rather similar values are observed. Further, not much change in solid distribution, overall solid holdup and mean velocity profile is observed for these conditions. This might be due to the balancing of decrease in solids collision and increase in gas turbulence. Nevertheless, the contributions of gas-solids interaction for all the velocities are quite low on solid fluctuation and hence, higher axial RMS velocity is observed for low velocity system.

Figure 3.24 shows that radial RMS velocity is high at the center and low near the wall for all the conditions. This trend is opposite to the axial RMS velocity. Further, radial RMS velocities are one order magnitude lesser than the axial RMS velocities. However, no significant difference in the value of radial RMS velocity is observed for the different

operating conditions. These results further indicate that the motion is predominantly in axial direction.



**Figure 3.24** Azimuthally and axially averaged RMS velocities for different gas velocity for the flux of 110 kg/m<sup>2</sup>s



**Figure 3.25 Azimuthally and axially averaged turbulent stresses for different gas velocity for the flux of  $110 \text{ kg/m}^2\text{s}$**

Figure 3.25 shows the normal and shear component of Reynolds stresses for the solids. Similar to axial RMS velocity, with increase in the superficial gas velocity, axial normal Reynolds stress decreases and the value of normal Reynolds stress is lower at the center and higher near the wall. However, the increase in  $\tau_{zz}$  towards the wall is rapid for low velocity system compared to high velocity, where almost a linear increase is observed. Further, no significant difference in  $\tau_{zz}$  value is observed for 9.6 m/s and 8.8 m/s velocities. In the case of 7 m/s, axial normal Reynolds stresses near the wall is twice to that of the

center of the column. The values of normal Reynolds stresses are higher where the kinetic stresses are low. It has been observed that  $\tau_{rz}$  is close to zero for all the conditions. This further shows that the solids motion is mainly in axial direction.

Figure 3.26 shows the radial variation in turbulent kinetic energy for different gas inlet velocities. Turbulent kinetic energy of solids decreases with increase in the superficial gas velocity and follow the similar profile as of axial RMS velocity. For the case of 9.6 m/s, there is no significant change of TKE with respect to 8.8 m/s and profiles are flat. Since the values of axial RMS velocity are significantly higher than the radial RMS and azimuthal RMS, turbulent kinetic energy trends are very similar to the axial RMS velocity. It is to be noted that turbulent kinetic energy are strongly dependent on solid holdup (Bhuspararu, 2005; Gidaspow and Huilin, 1996). In the present study, the trend of the turbulent granular temperature is similar to that reported by Tartan and Gidaspow (2004), and Pantazali et al. (2013). The values are in the same order of magnitude, even though the superficial gas velocities are lower in those cases.

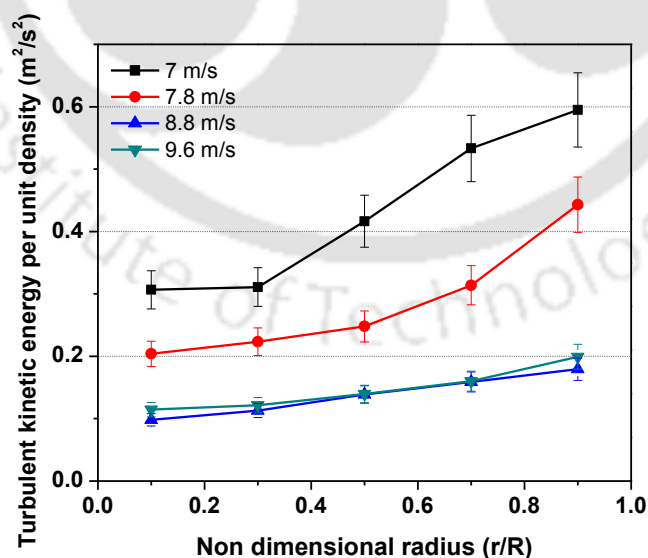


**Figure 3.26 Azimuthally and axially averaged turbulent kinetic energy for different gas velocity for the solid flux of 110 kg/m<sup>2</sup>s**

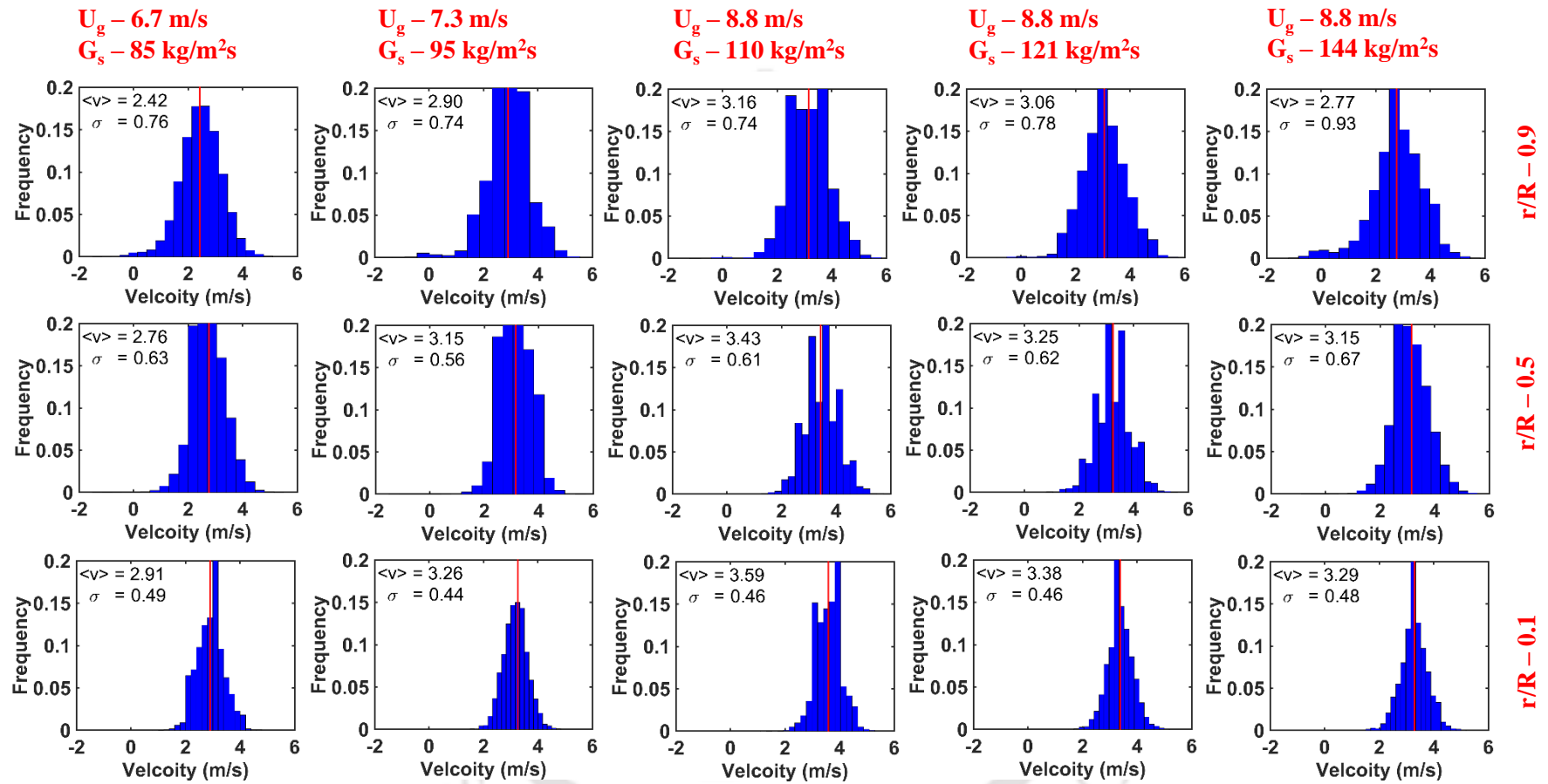


Figure 3.27 PDF of instantaneous velocity of different operating conditions

### 3.8 Effect of solid flux

So far discussion has been limited to the effect of superficial velocity at the same flux. In this section, effect of solid flux at the same gas velocity will be discussed. In addition to the effect of solid flux, combined effect of increase in the gas velocity and simultaneous increase in solid flux will also be discussed.

Figure 3.27 shows the PDF of instantaneous axial velocity at three radial positions, viz., centre, intermediate region and near the wall region for the entire height of the riser. While moving from the center to the wall, standard deviation in instantaneous axial velocity is increasing for all the conditions. For all the operating conditions, negative velocities are observed near the wall. Though the occurrences of the negative velocity are relatively low, increase in number of such occurrences observed increases with solid flux for the same gas inlet velocity. It can be concluded that solids back mixing near the wall increases with an increase in solid flux. Negative axial velocities are not observed at the center and intermediate region of the riser. Further, it is important to note that standard deviation in axial velocity remains almost same at the center and intermediate region for all the conditions. However, near the wall considerable change in standard deviation is observed with an increase in solid flux. Hence, it can be concluded that cluster formation frequency increases with the increase in solid flux and the probability of cluster formation is higher near the wall compared to the center of the riser.

Figure 3.28 shows the radial variation of mean axial and radial velocity for different operating conditions. At constant gas inlet velocity, increase in solid flux decreases the mean axial velocity of the solids. Increase in solid flux at a constant gas inlet velocity increases the solid holdup, resulting in decrease of solid velocity. It is interesting to

note that decrease in velocity is not uniform along the cross section. For increase in solid flux from 110 to 121 kg/m<sup>2</sup>s, decrease in solid velocity is more near the center of the column compared to the wall. However, for change in solid flux from 121 to 144 kg/m<sup>2</sup>s, change in velocity is more near the wall compared to the center of the riser. These results show that initial increase in solid flux uniformly increases the solid fraction across the cross-section. However, further increase in solid flux mostly increases the solid fraction near the wall. This results in increase of frequency of cluster formation near the wall and hence, reduces the mean axial velocity.

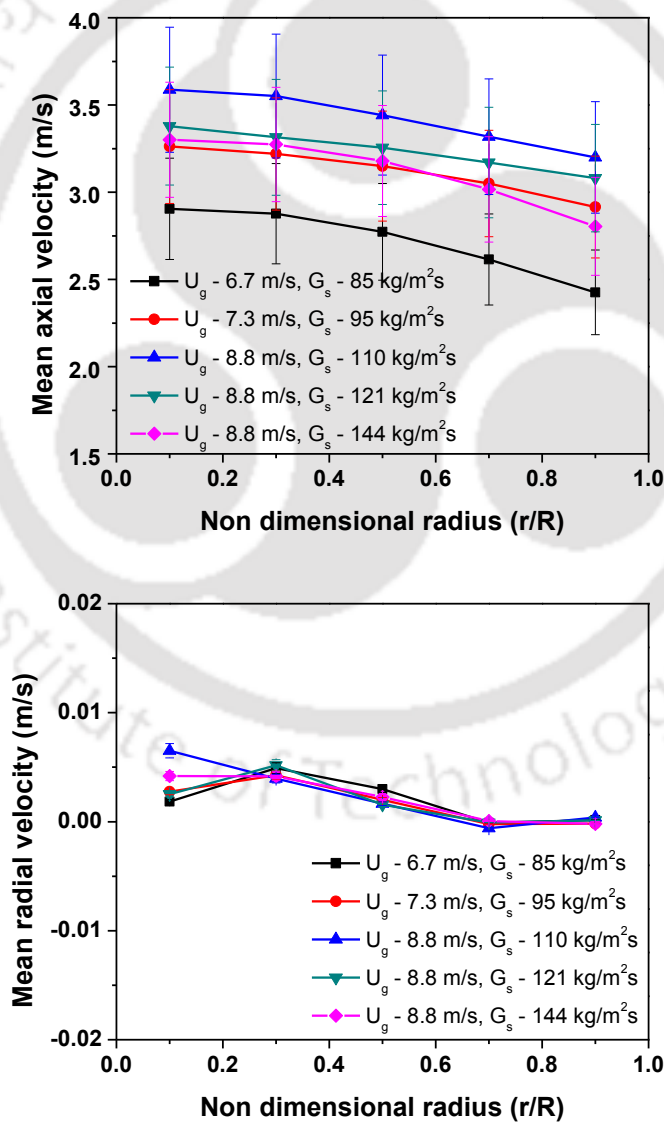


**Figure 3.28 Azimuthally and axially averaged mean velocities for different operating conditions**

It should be noted that, change in solid flux does not change the mean axial solid velocity significantly, as was the case with change in gas inlet velocity. Increase in the gas velocity and solid flux simultaneously increases the mean axial solid velocity considerably. Thus, once again it proves the dominance of the gas velocity over the solid flux. However increase of the mean axial solid velocity is not linear with the gas velocity neither with the solid flux. At low velocity, radial gradient is higher, however, at high velocity almost flat profile is observed. Radial mean velocity is close to zero for all the conditions. It can be concluded that axial direction motions are prominent for all the conditions and radial directed motions are negligible.

Figure 3.29 shows the radial variation of axial and radial RMS velocities for operated conditions. Results show that for all the conditions axial RMS velocity increases towards the wall while radial RMS velocity decreases towards the wall. It is observed that axial RMS velocity of solids increases with the increase in the solid flux. This is mainly due to the increase in solid hold-up with the increase in solid flux at constant gas inlet velocity, which increases the solids collisions. Hence, these results also confirm that particle-particle collision plays a crucial role in determining the solid fluctuations. It is to be noted that increase in axial RMS velocity is not significant in case of 110 to 121 kg/m<sup>2</sup>s. This further confirms our hypothesis that initial change in solid flux makes the solid distribution uniform throughout the cross-section. Hence, it does not significantly increase the solids collisions as change in volume fraction of the solids at any particular location is nominal. Axial RMS velocity for 6.7 m/s gas inlet velocity and 85 kg/m<sup>2</sup>s solid flux is relatively high. In fact, axial RMS velocity for this condition is higher than  $U_g$  - 8.8 m/s and  $G_s$  - 121 kg/m<sup>2</sup>s. This is mainly due to the formation of clusters at low velocity, as reported in section 3.7. This is evident from PDF of instantaneous velocity, which shows higher value of standard deviation

for  $U_g - 6.7 \text{ m/s}$  and  $G_s - 85 \text{ kg/m}^2\text{s}$  compared to  $U_g - 8.8 \text{ m/s}$  and  $G_s - 121 \text{ kg/m}^2\text{s}$ . Hence, it again proves that particle-particle interactions are more vital for solid fluctuations. Change in radial RMS velocity is insignificant for all the operating conditions. Further, radial RMS velocities are one order of magnitude lower than the axial RMS velocities for all the conditions.

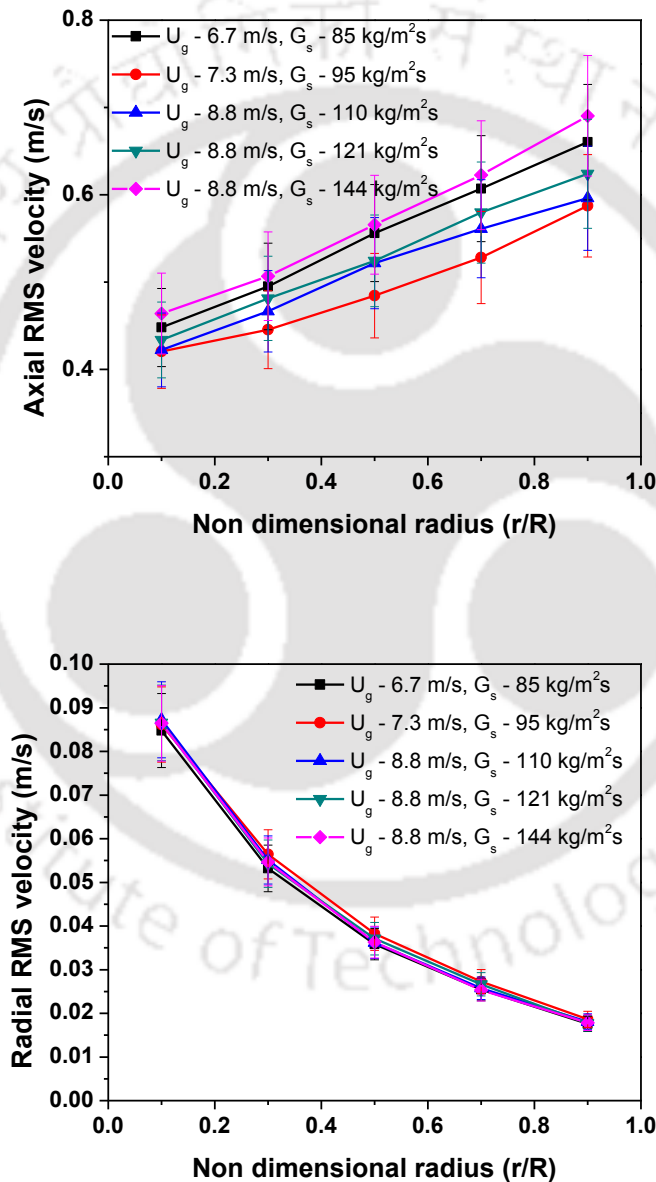
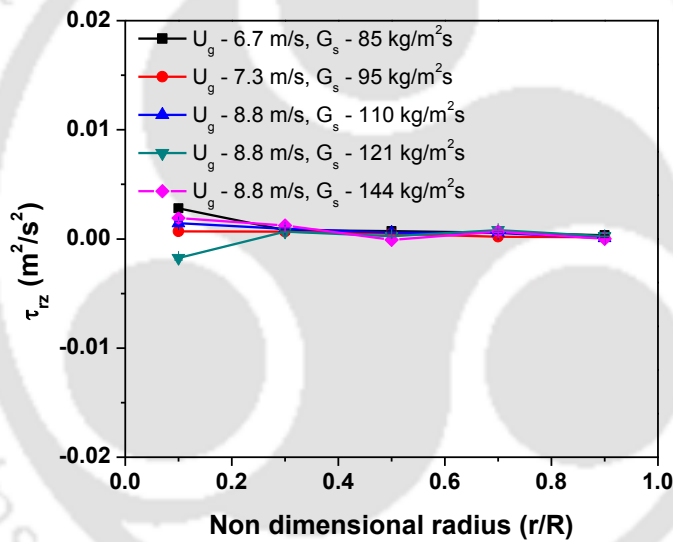
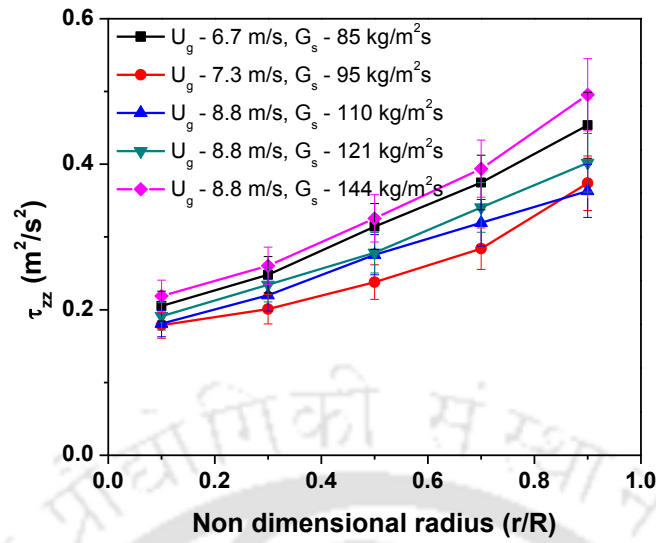
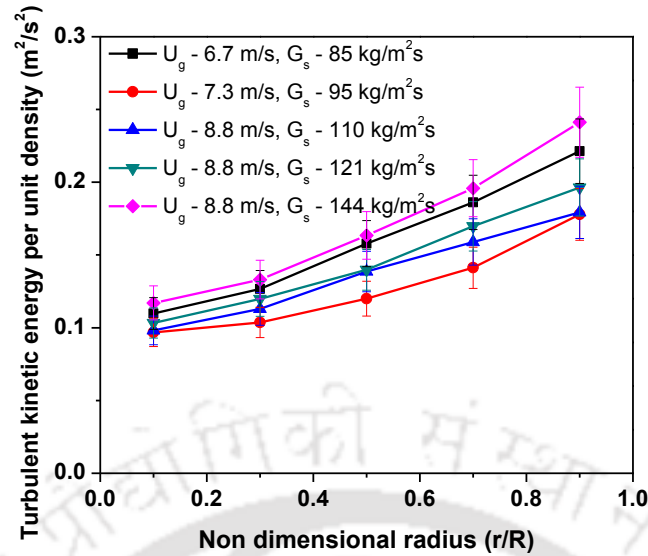


Figure 3.29 Azimuthally and axially averaged RMS velocities for different operating conditions



**Figure 3.30 Azimuthally and axially averaged turbulent stresses for different operating conditions**

Figure 3.30 and 3.31 show the Reynolds normal axial stresses and turbulent kinetic energy for different operating conditions. They show similar trend as of axial RMS velocities, which is expected. Since lateral RMS velocities are close to zero. Shear Reynolds stresses are insignificant compared to normal Reynolds stresses. Invariably, energy available for solid dissipation increases with the solid flux. However, increase is not uniform. This further confirms the existence of clusters.



**Figure 3.31 Azimuthally and axially averaged turbulent kinetic energy for different operating conditions**

### 3.9 Solid mixing studies

In the previous section, discussion was focused on the local velocity field. It gave insights about the riser characteristics. Conventionally for the industrial design and troubleshooting, residence time distribution is used to characterize the overall mixing of the solids. For fast reactions like in CFB, local mixing information is also important. In next section, residence time distribution for the different riser section is given. In addition to residence time distribution, degree of mixing of solids is also found by Macromixing index. Thereafter, local mixing information is also characterized in this work using RPT data.

#### 3.9.1 Residence time distribution

Residence time distribution (RTD) is widely studied phenomena across chemical engineering, biochemical and biological systems. Residence time distribution can be applied to any conserved entity in a flow system (Nauman, 2008). Residence time is defined as time spent by the inert entity in the system or any bounded region.

Temporary excursion out of the system is not included in the residence time (Nauman, 1981). Since entities follow different paths in the system, which may not be uniform (in terms of the length or velocity) to the other paths, thus distribution of residence time is obtained. RTD is a probability density function  $E(t)dt$  which gives the fraction of elements leaving the system that remained in the system for the time between  $t$  and  $t + dt$ . The idea of using RTD to analyze the chemical reactor performance was originally given by MacMullin and Weber (1935). However, the approach becomes more popular after Danckwerts (1953) defined most of the distribution which is required for detailed analysis of the reactor performance.

Experimental measurement techniques are critically reviewed by Harris et al. (2002). Similarly, models available to analyze the RTD data are reviewed by Naumann (2008) and Gao et al. (2012). Stimulus / Pulse response is the most widely used measurement technique. Different tracers are used for the measurement depending upon the system and measurement methods. In some cases chemical tracers are used to change the conductivity or pH of the flowing fluid. Some of the commonly used chemical tracer are NaCl, KCl, NaOH, BaCl<sub>2</sub> salt etc. (Bader et al., 1980; Zheng et al., 1992; Rhodes et al., 1991), Similarly phosphorescent tracer (Wei et al., 1994; Harris et al., 2003), radioisotope based tracer (Patience et al., 1990; Ambler et al., 1990), ferromagnetic tracer (Avidan and Yerushalmi, 1985) and colored tracer (Bi et al., 1995) are used for RTD studies. In the pulse response method, an amount of inert tracer is suddenly injected into the feed stream and response of the system is measured through the distribution of the tracer (typically in terms of concentration) at the downstream. Since RTD is defined in between the boundaries, defining the boundary is vital for the RTD measurement. Systems boundary can be closed – closed, open – open or mixed. In closed – closed boundary conditions, temporary excursions of tracer are not possible.

Under open – open boundary conditions or mixed boundary conditions, tracer may have temporary excursion outside of the system and re-enter the system. In such a system, most of the pulse response techniques fail to differentiate the temporary excursion of the system (Harris et al., 2002). Further injected tracer has difficulty in achieving flow profile of the system.

The above-mentioned problem can be solved to a great extent by using a single particle tracking technique instead of using a mass tracer. In case of single radioactive particle tracking technique the entry, exit and re-entry into the system can be unambiguously identified. Thus true RTD can be obtained. In the current work, radiation based technique is used where the trajectory of a single particle is tracked continuously for longer time to generate the RTD. It should be noted that except single particle tracking technique, all other techniques track in terms of concentration. While in single particle tracking, residence time is directly obtained, thus it is more primitive than the conventional techniques. Weinell et al. (1997), Bhusarapu et al. (2004), Godfroy (1999) and Mahmoudi (2011) used single particle technique for studying RTD in gas-solid CFB.

Harris et al. (2003) and Breault (2006) have reviewed the experimental studies on RTD measurement in gas-solid CFB. Recent studies can be found in the research work of van de Velden et al. (2007), Andreux et al. (2008), Yan et al. (2009) and Mahmoudi et al. (2011), (2012). Most of the authors reported single modal curves. However, some authors presented bimodal curves (Ambler et al., 1990; Wei and Zhu, 1996; Bhusarapu et al., 2004). Bhusarapu et al. (2004) segregates the second peak as a result of high back mixing in the fast fluidization regime. Residence time span is used to delineate operating regimes as a dilute riser or dense suspension flow and core annular flow

(Chan et al., 2010; Mahmoudi et al., 2011). However, no conclusive agreement is available on this.

Various researchers have reported different trends of axial dispersion for different operating conditions. Rhodes et al. (1991), Harris et al. (2003), Andreux et al. (2008) and Yan et al. (2009) reported that axial dispersion decreases with an increase in solid mass flux. Ambler et al. (1990) and Patience et al. (1990) have reported contrary observations where axial dispersion increases with an increase in solid mass flux. With increase in the gas velocity at the same mass flux of solid, increase in axial dispersion is reported by Ambler et al. (1990) while decrease in axial dispersion is reported by Harris et al. (2003) and Yan et al. (2009). For low density riser, increase in solid flux increases the axial dispersion, while in the high density riser (or dense suspension flow), axial dispersion decreases with increase in solid flux (Bi, 2004). Maximum value of the axial dispersion is reported for the transition from turbulent to fast fluidization regime by Avidan (1980). Further, studies (Amber et al., 1990; Patience et al., 1990; Brereton and Grace, 1993; Kruse and Werther, 1995; Harris et al., 2003) have also reported that the riser exit design also affect the solid mixing characteristics in riser. It is found that abrupt exit increases the solid mixing compared with the smooth exit.

Solids dispersion coefficients are varied of four orders of magnitude (Breault, 2006; Hua et al., 2014). Bhusarapu (2005) reported that dispersion coefficients varied from  $10^{-4}$  to  $30 \text{ m}^2/\text{s}$  in the literature. It is ascertained that such a huge difference in the reported values are mainly due to the different operating regimes and also different regions in CFB (bottom, transition and dilute zone) are not distinguished while reporting. Limited literatures are available where zone wise RTD is reported (Bader et al., 1988; Weinell et al., 1997). This is mainly because of the limitation of most of the methods used to find the RTD, which are not able to differentiate the boundary region.

So, it is difficult to find section wise true RTD, thus solid mixing in that region (Harris et al., 2002). Breault (2006) concluded that more systematic data are needed to understand the solid mixing. Further he emphasized that data should be available for different zones (bottom, transition and dilute zones) for complete characterization of the flow.

In current work, single radioactive particle method is used to study the solids RTD for different operating conditions. Further, zone wise solids RTD studies are carried out along the height of the riser. Finally, systematic studies are performed to understand the effect of solid flux and gas superficial gas velocity on solids RTD.

### **Measurement technique**

Figure 3.32 shows the schematic of experimental setup used in current work to find the zone wise RTD of solids. Detectors are placed along the riser height as shown in the Figure 3.32. Bottom region is 0.05 – 1.359 m from the distributor, middle (RPT) region is 0.5215 m and top region is 0.9985 m and overall length of the riser is 2.829 m. Detectors are shielded with lead except at the plane of measurement. Similar to RPT, a single radioactive tracer particle, which acts as a marker of phase, is introduced into the system. Counts are recorded whenever the tracer comes to the plane of the detector, which is also the boundary of the region. Time between the peaks of successive detectors gives the residence time for the closed – closed systems. For open – open system like CFB, particle may cross the boundary multiple times. Time between first entry at the inlet and final exit at the outlet excluding the temporary excursions are taken as the residence time. This provides the true RTD of the tracer (Nauman, 1981). Temporary excursions of tracer can be found by counting the peaks in pairs at the boundaries. In CFB, tracer circulates continuously as the solids, thus mapping flow path

of all the solids. Since system is ergodic (refer RPT section), the obtained RTD is representation of the entire solids in that volume. Further, limitation of achieving radial flow profile in the conventional injection are avoided.

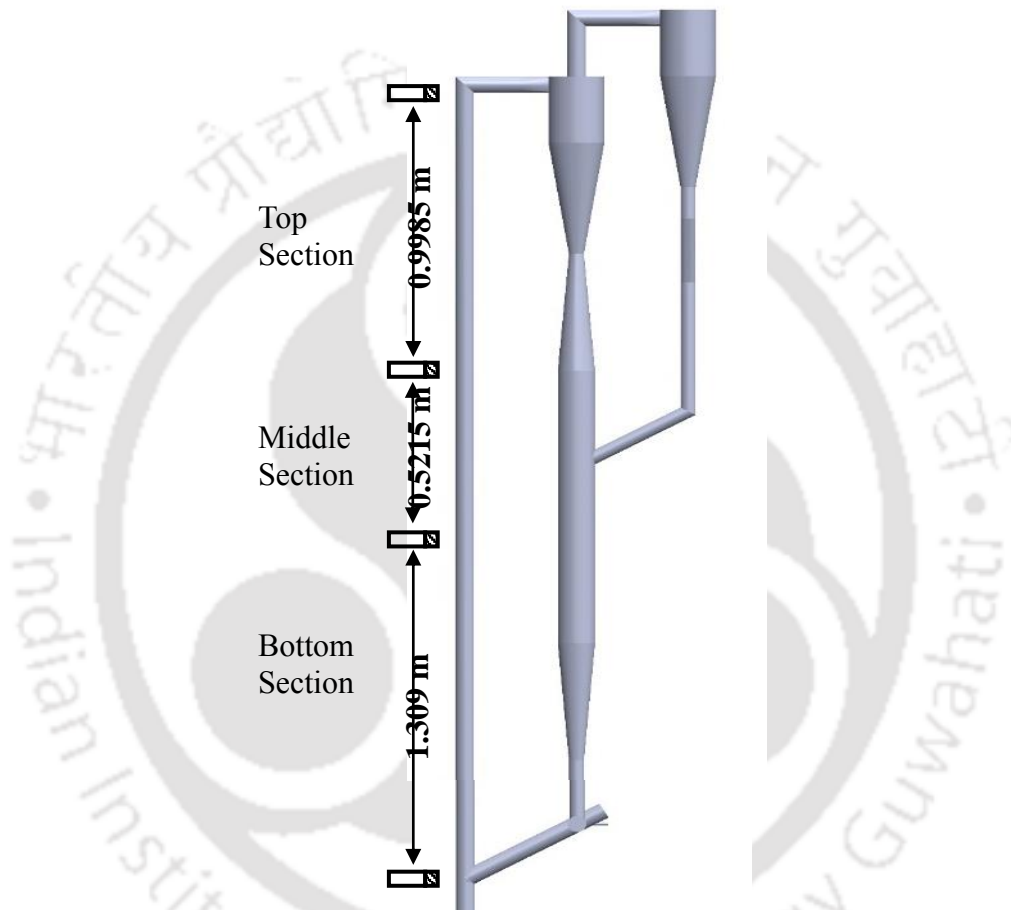


**Figure 3.32 Schematic of experimental setup showing different sections of RTD measurements**

### Results and discussion

Experiments were conducted for all the conditions in RPT. Each experiments was carried out for 24 – 48 hours depending upon the operating conditions until statistically sufficient data was obtained. Typical time frequency curve from single radioactive

particle technique is shown in the Figure 3.33. In this work, axial dispersion model is used to fit the data. Even though time distribution obtained from the experiments are more primitive to the definition of RTD, axial dispersion model requires mass conservation. In this work, it is assumed that the total numbers of samples are considered as the total mass injected and the frequency of each time interval as the mass fraction obtained in the interval. Thus, E – curve is obtained by normalizing the total samples and thus, area under the curve is 1. This E- curve is equivalent to the E – curve obtained from the conventional (mass) tracer injection methods. The E – curve obtained from the above experiment is used for regressive fitting of the axial dispersion model (ADM).

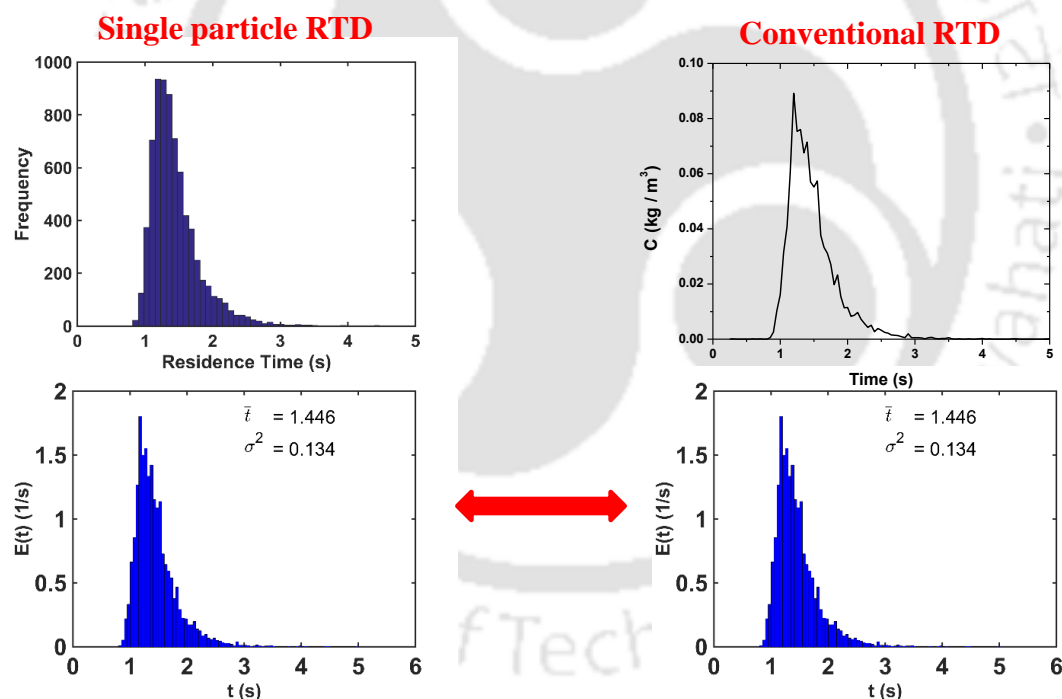


**Figure 3.33 Schematic explaining the equivalence of E – Curve from the single particle tracking and conventional tracer techniques**

Figure 3.34, 3.35, 3.36 and 3.37 shows the residence time distribution for all the operating conditions for bottom, middle, top and entire riser respectively. Corresponding dispersion number ( $D_{ax}/UL$ ) are given in Table 3.4, 3.5, 3.6 and 3.7.

Single modal curves are obtained for all the conditions for all the zones. Figure 3.34 shows the RTD curve for bottom region for different gas inlet velocity and solid flux. At all the operating conditions relatively longer tail is observed for the bottom zone which shows that back mixing at the bottom zone is relatively high. Hence, it can be concluded that independent of the operating condition bottom zone of CFB behaves like a mixed flow reactor. As there is no internal or dead volume available in the riser, the back mixing is mainly because of meso-scale meta-stable structures (clusters). Further, it is observed that with increase in gas inlet velocity both mean residence time and variance decreases at the bottom zone for constant solid flux. This clearly shows that mixing at bottom zone decreases with increase in gas inlet velocity. Results further indicate that increase in solid flux for a constant gas inlet velocity increases the mean residence time of solids and variance in bottom zone. Further, the dispersion number also increases with increase in solid flux. This clearly shows that increase in solid flux increases the back mixing due to increased solid-solid interaction which increases the frequency of cluster formation.

Figure 3.35 shows RTD curve for the middle region for different operating conditions. Significant change of the RTD curves can be observed in all the cases. Variance of all the curves is very low, further tail is not observed. This shows that back mixing is reduced in middle (RPT) zone. However, for the operating conditions of  $U_g = 7, 7.8$  m/s and  $G_s = 110$  kg/m<sup>2</sup>s, long tail is observed signifying solid back mixing is still high.

**Table 3.4 Axial dispersion number for the bottom region ( $\Delta L = 1.309$  m)**

| $U_g$ (m/s) | $G_s$ (kg/m <sup>2</sup> s) | $\bar{t}$ (s) | $\sigma^2$ (s) | Dispersion Number |
|-------------|-----------------------------|---------------|----------------|-------------------|
| 6.7         | 85                          | 0.9124        | 0.1229         | 0.0738            |
| 7.3         | 95                          | 0.9371        | 0.1202         | 0.0684            |
| 8.8         | 110                         | 0.8422        | 0.1218         | 0.0858            |
| 8.8         | 121                         | 0.9081        | 0.1569         | 0.0951            |
| 8.8         | 144                         | 0.9111        | 0.1701         | 0.1024            |
| 7           | 110                         | 1.5258        | 0.9519         | 0.2044            |
| 7.8         | 110                         | 1.1230        | 0.2340         | 0.0928            |
| 9.6         | 110                         | 0.6557        | 0.0370         | 0.0430            |

**Table 3.5 Axial dispersion number for the RPT region ( $\Delta L = 0.5215$  m)**

| $U_g$ (m/s) | $G_s$ (kg/m <sup>2</sup> s) | $\bar{t}$ (s) | $\sigma^2$ (s) | Dispersion Number |
|-------------|-----------------------------|---------------|----------------|-------------------|
| 6.7         | 85                          | 0.1951        | 0.0020         | 0.0267            |
| 7.3         | 95                          | 0.1706        | 0.0007         | 0.0114            |
| 8.8         | 110                         | 0.1539        | 0.0005         | 0.0114            |
| 8.8         | 121                         | 0.1667        | 0.0010         | 0.0179            |
| 8.8         | 144                         | 0.1734        | 0.0017         | 0.0279            |
| 7           | 110                         | 0.4459        | 0.2539         | 0.6385            |
| 7.8         | 110                         | 0.2973        | 0.0365         | 0.2067            |
| 9.6         | 110                         | 0.1236        | 0.0001         | 0.0044            |

**Table 3.6 Axial dispersion number for the top region ( $\Delta L = 0.9985$  m)**

| $U_g$ (m/s) | $G_s$ (kg/m <sup>2</sup> s) | $\bar{t}$ (s) | $\sigma^2$ (s) | Dispersion Number |
|-------------|-----------------------------|---------------|----------------|-------------------|
| 6.7         | 85                          | 0.3381        | 0.0021         | 0.0091            |
| 7.3         | 95                          | 0.3002        | 0.0005         | 0.0028            |
| 8.8         | 110                         | 0.2692        | 0.0006         | 0.0039            |
| 8.8         | 121                         | 0.2957        | 0.0016         | 0.0092            |
| 8.8         | 144                         | 0.3095        | 0.0034         | 0.0176            |
| 7           | 110                         | 0.7017        | 0.2782         | 0.2825            |
| 7.8         | 110                         | 0.4565        | 0.0267         | 0.0641            |
| 9.6         | 110                         | 0.2207        | 0.0002         | 0.0016            |

**Table 3.7 Axial dispersion number for the overall column**

| $U_g$ (m/s) | $G_s$ (kg/m <sup>2</sup> s) | $\bar{t}$ (s) | $\sigma^2$ (s) | Dispersion Number |
|-------------|-----------------------------|---------------|----------------|-------------------|
| 6.7         | 85                          | 1.4456        | 0.1343         | 0.0321            |
| 7.3         | 95                          | 1.4079        | 0.1228         | 0.0310            |
| 8.8         | 110                         | 1.2652        | 0.1247         | 0.0390            |
| 8.8         | 121                         | 1.3704        | 0.1627         | 0.0433            |
| 8.8         | 144                         | 1.4006        | 0.2387         | 0.0608            |
| 7           | 110                         | 2.6735        | 1.9983         | 0.1398            |
| 7.8         | 110                         | 1.8768        | 0.3526         | 0.0500            |
| 9.6         | 110                         | 1.0000        | 0.0374         | 0.0187            |

With increase in the superficial gas velocity at the same solid flux, mean residence time, variance and dispersion number decreases. While in case of increase in the solid flux at the same velocity, mean residence time, variance and dispersion increases. Dispersion number decreases from the bottom region to the middle region mainly because of increase in solid velocity when it moves from bottom to the top till flow is developing and thereafter it remains constant. However for the case of 7 and 7.8 m/s operating conditions, increase in the dispersion number is observed. It is to be noted that in those cases the velocity profile is parabolic, which offer additional mixing as the solids velocity are low near the wall. The 1D ADM model used is not accounting the flow profile in those conditions, thus discrepancies are observed.

Top region (Figure 3.36) also shows that increase in the dispersion number with increase in the solid flux at constant velocity and decrease in dispersion number with the increase in the superficial gas velocity at constant solid flux. Further decrease in dispersion number is observed from the middle region to the top region. Figure 3.37 shows the RTD curves for the entire riser. It also follows the similar trends with the operating condition as the other regions. Interesting observation is that entire region curve is more similar to the bottom region. That is, entire column RTD is dominated by the bottom region, as solid spend more time at the bottom zone compared to other zones. It should be noted that the length of the entire riser is 2.82 m out of which bottom region is 1.309 m. Above results, suggest that the solid – solid interactions and metastable structures play a major role in the dispersion.

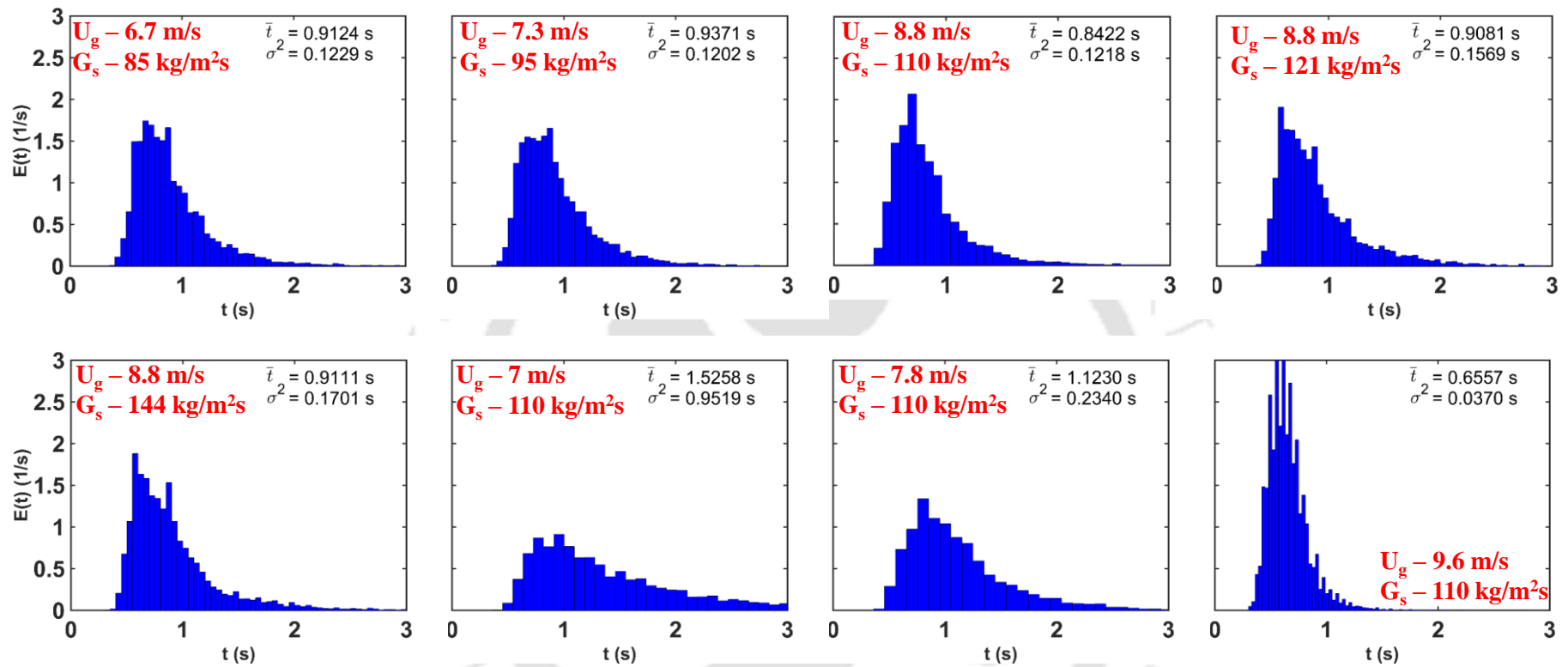


Figure 3.34 Residence time distribution for the bottom region

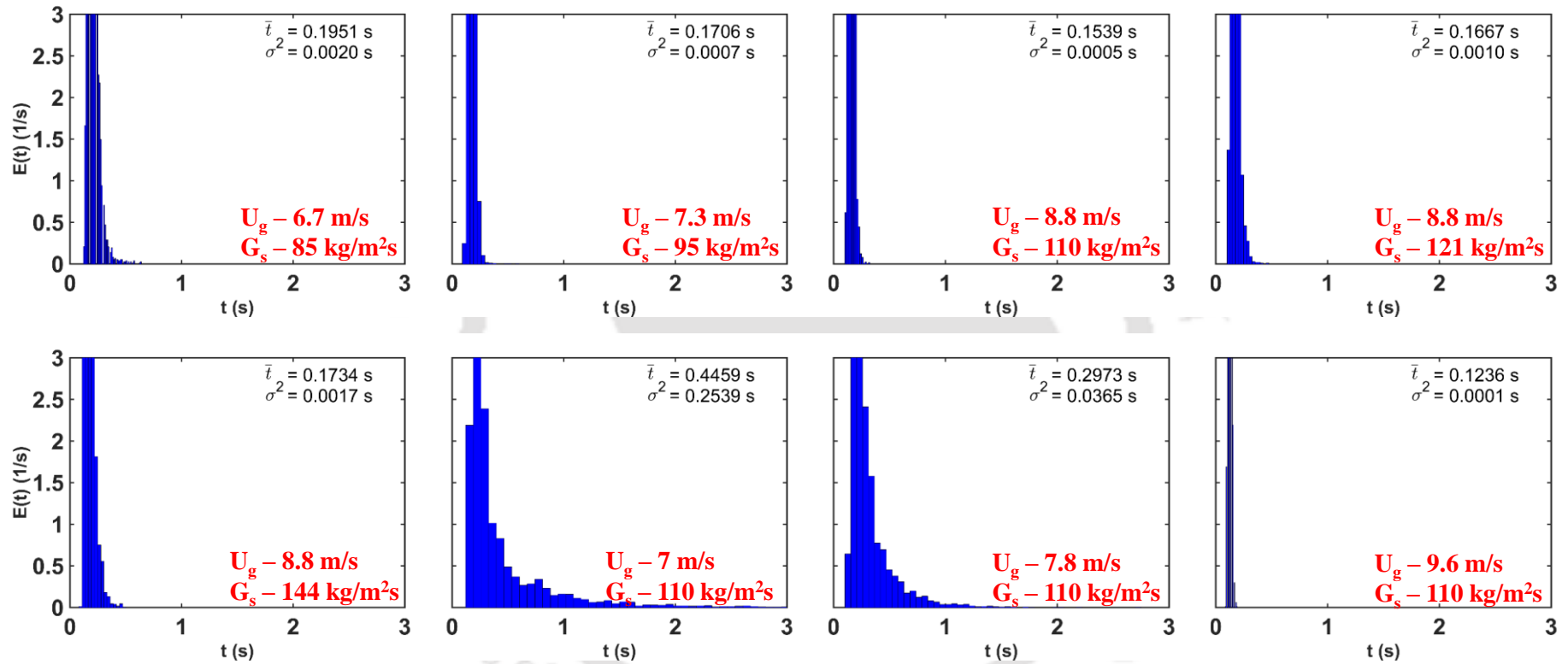


Figure 3.35 Residence time distribution for the middle (RPT) region

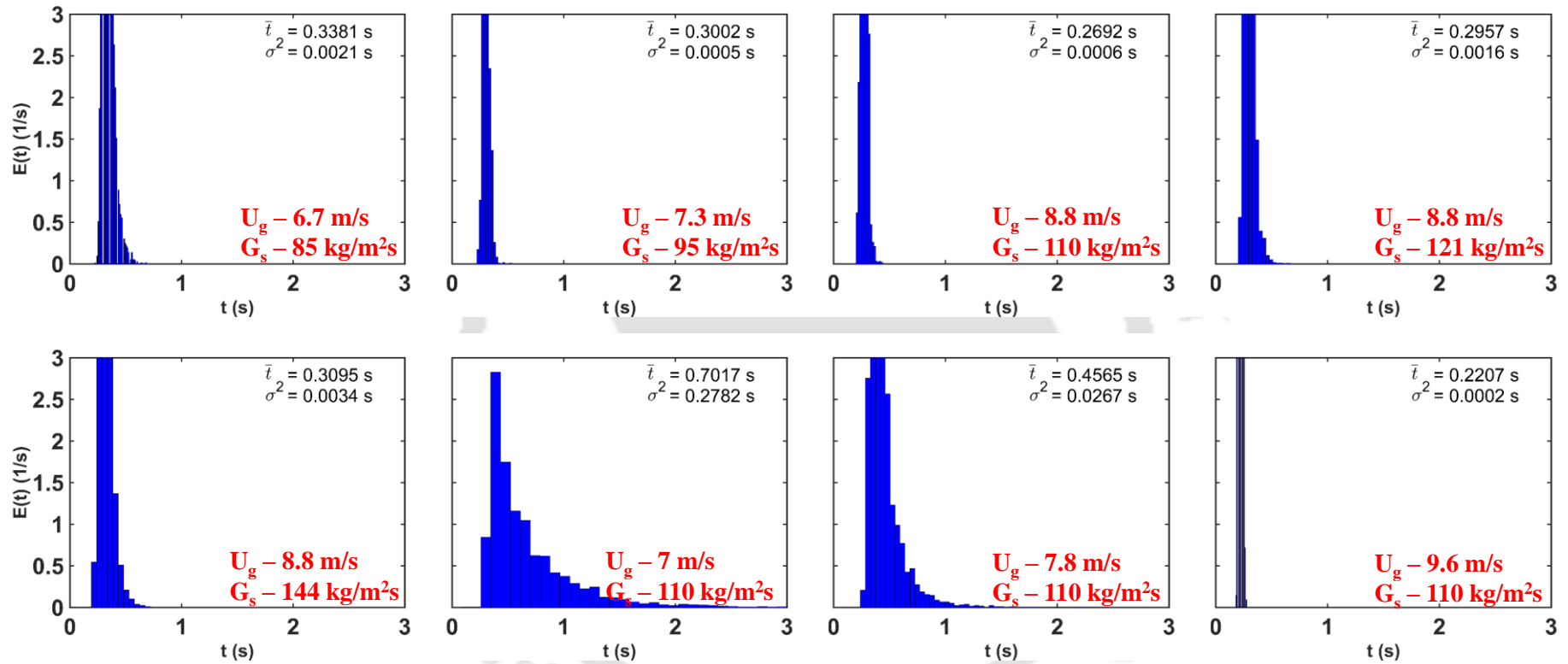


Figure 3.36 Residence time distribution for the top region

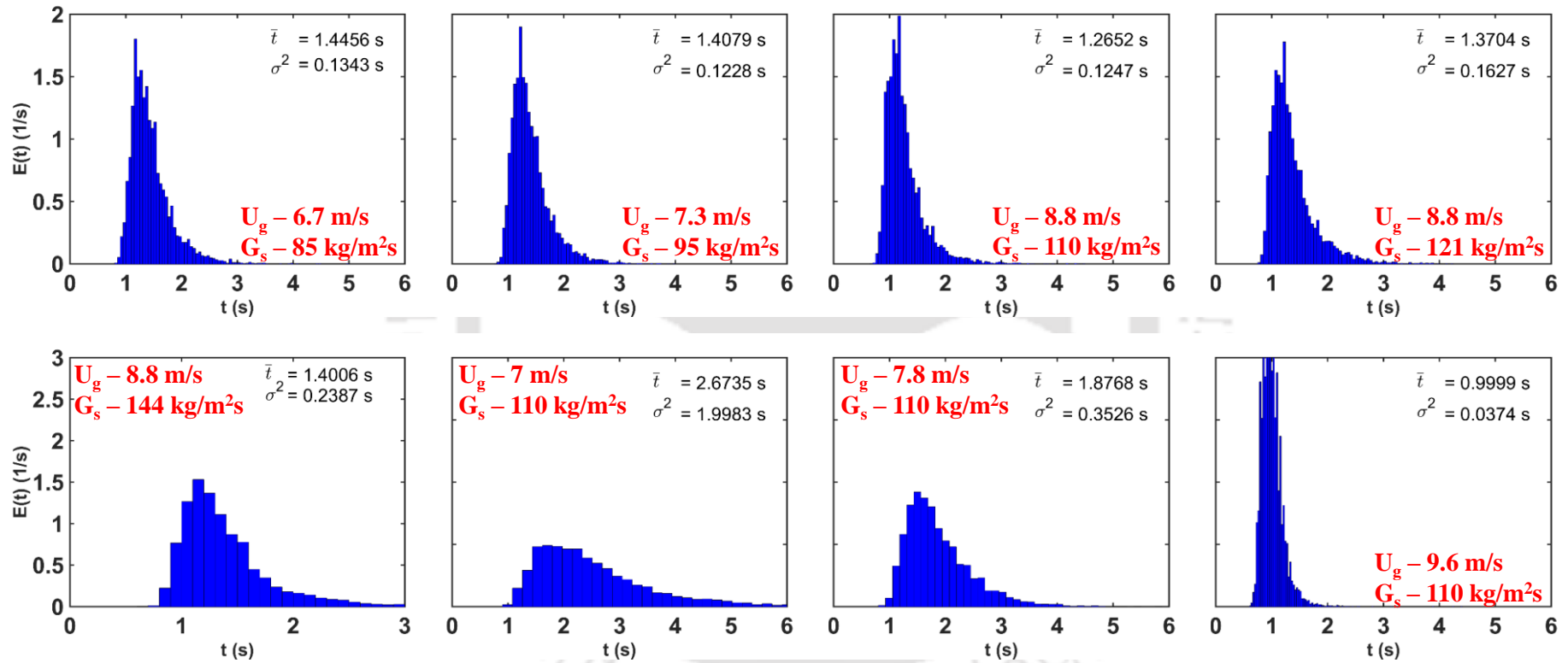


Figure 3.37 Residence time distribution for the entire riser

### 3.9.2 Trajectory length distribution (TLD)

Villermaux (1996) introduced the concept of quantifying the degree of mixing of solids based on the trajectory length distribution. Trajectory length distribution  $f(l)$  can be defined as the fraction,  $f(l)dl$ , of element that followed the trajectories between the length of  $l$  and  $l+dl$ . While the residence time distribution is based on volumetric approach, trajectory length distribution is Lagrangian approach. Videographic method using CCD camera (Villermaux, 1996) or particle tracking method (Bhusarapu, 2005) was used previously in the literature to obtain the TLD. Since particle tracking method is used for studying the particle motion in this work, this relatively new approach of studying the solids mixing is also used. Instantaneous positions are obtained for each trajectory. Distance travelled by such trajectories is calculated from their instantaneous position. Histograms of such trajectories gives distribution. Normalization of such trajectories gives the trajectory length distribution, presented as E – curve similar to RTD. Macromixing index introduced by Villermaux (1996) to quantify the degree of mixing, defined as,

$$M = \frac{\langle l \rangle}{L} \quad (3.16)$$

Where,  $\langle l \rangle$  is the mean length of the trajectories in the system and  $L$  is the distance between the two plane of measurements. If all the particle travels straight the between the plane of measurement without deviation from the path like plug flow,  $\langle l \rangle = L$ , thus  $M = 1$ . If the particles take tortuous path, then  $\langle l \rangle$  is greater than the  $L$ , for complete mixing like ideal MFR,  $M = \infty$ .

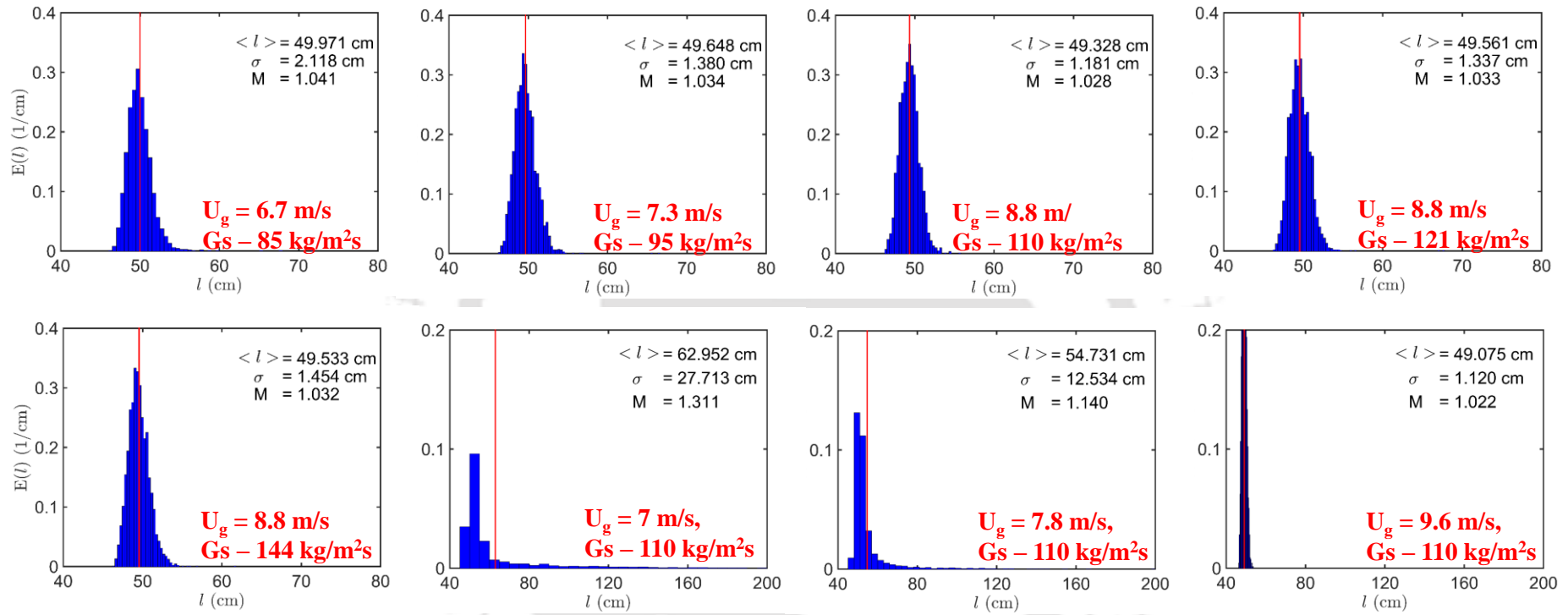


Figure 3.38 Trajectory time distribution for the middle region (RPT measurement section) for the length of  $L = 48$  cm

Figure 3.38 shows the TLD for the length of 48 cm, which is almost same region as the middle section reported in the RTD. It should be noted that scale is different for the operating conditions. Red line in the distribution denotes the mean length of the distribution,  $\langle l \rangle$ .  $M$  values for all the conditions are close to the 1, thus the flow is close to plug flow in RPT section. With increase in the solid flux, mixing increases evident from  $M$  values. Similarly, decreases in the superficial gas velocity, increases mixing. Mean length travelled and variance decreases with increase in the superficial gas velocity at the same solid flux. While it is increasing or almost remains same for increase in the solid flux at the same superficial gas velocity. Except 7 and 7.8 m/s, all the conditions shows that similar distribution around the mean. Further, mean values are also very close to the distance between the measurement planes. In the case of the 7 and 7.8 m/s, long tail is observed. This might be due to the internal recirculation or highly tortuous path of solids. It should be noted that RTD also gives the similar curve for 7 and 7.8 m/s. From the RTD, it is very difficult to conclude that internal circulation of solids are happening, because of slow moving clusters or decelerating clusters can also give similar values. However, length traveled highlights the path travelled by the solids, thus highlighting recirculation or highly tortuous path. Thus, RTD and TLD are complementary measurements.

### 3.9.3 Local solids mixing

RTD and TLD quantified global solids mixing. However, for fast reactions local mixing information is very important. For example, in fluid catalytic cracking (FCC) like partial reactions yield also varies with local mixing, thus decides the profitability of the plant. Global mixing is characterized as dispersive flow over the convective flow. Local mixing is characterized as the random motion. Rate of change of particle position ( $Z$ ) variance gives the spread of the particles (diffusion) released at the same time and at the same position. Taylor (1920) formulated the diffusion can be expressed as the autocorrelation

function and fluctuations of the velocity. It should be noted that Taylor (1920) equation formulated for continuous movements at isotropic conditions.

$$D_z = \frac{1}{2} \frac{d\bar{Z}^2}{d\tau} = \bar{v}^2 \int_0^\tau R(\tau) d\tau \quad (3.17)$$

Computation of Lagrangian correlation coefficients from RPT is elaborately discussed by Degeleesan (1997). To calculate Lagrangian correlation coefficients, Lagrangian tracks are identified in each cell. Particle which are entering after recirculation to the same cell are not considered in this work. Lagrangian mean and fluctuations of each tracks are computed. Correlation coefficients of fluctuation velocities of each tracks are computed. Ensembled average of all the tracks in that particular cell is considered as dispersion in that cell.

Figure 3.39 shows the azimuthally and axially averaged axial diffusivity. Almost a flat profile has been observed for all the conditions might be due to dilute conditions. However, diffusivity values differ by one order of magnitude between the operating conditions used in current work. In literature similar behavior is observed that diffusivity values are reported in the range of  $10^{-4}$  to  $1 \text{ m}^2/\text{s}$  depending upon operating condition, particle size and scale (Godfroy et al., 1999; Bhusarapu, 2005; Kashyap et al., 2011). Even though values are quite closer, increase in the diffusivity values with increase in the solid flux can be observed. Similar observations are made by Bhusupara (2005). With increase in the velocity, diffusivity decreases. Order of magnitude difference in the velocity might be due to the flow regime change. It is to be noted that order of magnitude difference has been observed between the local mixing (diffusivity) and global mixing parameters (dispersion number). However, both local mixing and global mixing changes in the same way with change in the operating conditions.

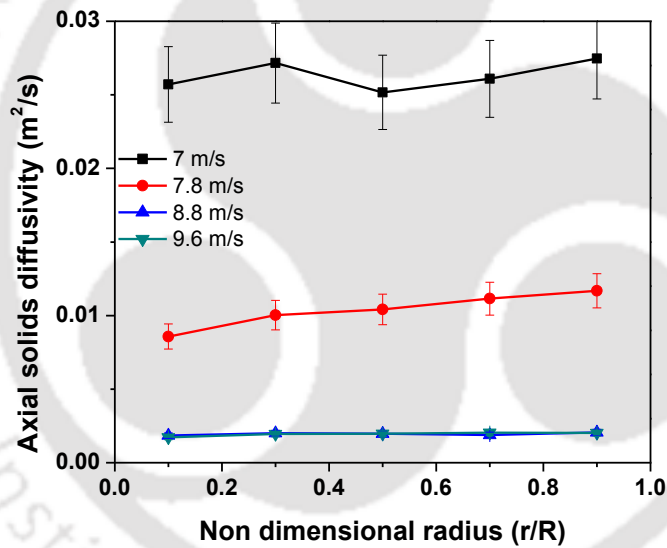
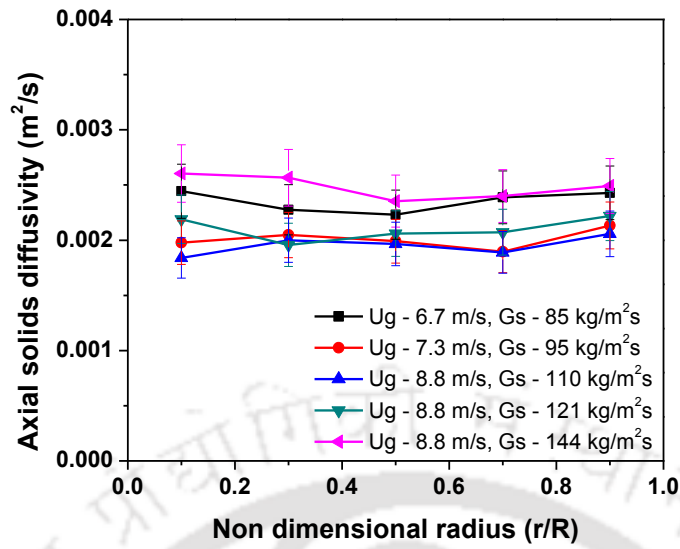


Figure 3.39 Axially and azimuthally averaged axial solids diffusivity

### 3.10 Summary

The results of this chapter are summarized in two parts, viz., Solid velocity field studies and solid mixing studies.

### ***Solid velocity studies***

The following major conclusions can be obtained from the Solid velocity field studies are as follows:

1. Clusters are observed in all the operating conditions. Different shapes and sizes of clusters are observed. Frequency of the clusters observed varies with the operating conditions.
2. Particle motion is predominantly in the axial direction and fine random fluctuations are observed.
3. Accelerating and decelerating motion of the solids are observed.
4. Spread of instantaneous velocity is high near the wall and low at the center. Further negative velocities are observed near the wall at all the operating conditions and their number occurrence is high for the low velocity and high flux conditions. With increase in the solid flux at the constant superficial gas velocity, spread increases along the column and spread decreases with increase in the gas velocity at constant flux.
5. No downward motion of solids is observed in the time averaged sense. Axial-symmetric flow of solids is ascertained.
6. Mean solid velocity of solids are high in the center and low near the wall. With increase in the gas velocity at constant flux, solid velocity increases. While solid velocity decreases with increase in the solid flux at constant gas velocity. However, gas velocity changes the solid velocity largely, small change has been observed for the solid flux change. Thus, mean velocity majorly governed by gas solid interaction. Radial and azimuthal mean velocities are negligible.
7. Axial RMS velocities are low in the center and high near the wall. With increase in the superficial gas velocity at constant flux, decrease in axial RMS velocities are

observed. While in the case of increasing solid flux at constant gas velocity, axial RMS velocity increases. Thus, it can be concluded that axial RMS velocity is governed by solid – solid interactions and metastable structures. Radial RMS velocities are one order of magnitude less than the axial RMS velocities and insignificant change is observed with the operating conditions. Reynolds normal stresses follows the similar trends as axial RMS velocities. Shear stresses components are negligible.

8. Turbulent kinetic energy values are order of magnitude lower than the normal kinetic stresses. Thus, energy available for dissipation is also very low.

#### ***Solid mixing studies***

1. Residence time distribution studies conducted in section wise. At bottom section mixing is high and behaves like a mixed flow reactor for all the conditions. With increase in the height, solid mixing decreases evident from the dispersion number. Solid mixing is governed by metastable structures and solid interactions. With increase in the gas velocity at constant solid flux decreases dispersion number and increase in the solid flux increases dispersion number.
2. Macromixing index from the trajectory length studies are close to one for all the conditions. Thus, all the operating conditions are close to plug flow behavior at the middle region (RPT) investigated.
3. Solids diffusivity values are in the order of magnitude  $10^{-3} - 10^{-2} \text{ m}^2/\text{s}$ . Solids diffusivity also follows similar trend as RTD with change in the operating conditions.

Overall, solid motion mean motion is governed by the gas velocity and fluctuations of solids are majorly governed by the solid interactions and metastable structures.

## Notations

|                       |  |              |
|-----------------------|--|--------------|
| $A$                   | Area of cross section                          | $[m^2]$      |
| $D_z$                 | Diffusivity                                    | $[m^2/s]$    |
| $G_s$                 | Solid mass flux                                | $[kg/m^2s]$  |
| $i$                   | Index of radial component                      | $[-]$        |
| $I$                   | Intensity of radiation at detector             | $[W/m^2]$    |
| $I_o$                 | Intensity of radiation at source               | $[W/m^2]$    |
| $j$                   | Index of azimuthal component                   | $[-]$        |
| $k$                   | Index for axial component                      | $[-]$        |
| $KE$                  | Fluctuating kinetic energy per unit volume     | $[kg/m.s^2]$ |
| $L$                   | Distance between the two plane of measurements | $[m]$        |
| $\langle l \rangle$   | Mean length of the trajectories in the system  | $[m]$        |
| $M$                   | Macromixing index                              | $[-]$        |
| $N$                   | Total number of photon trajectories tracked    | $[-]$        |
| $R(\tau)$             | Dimensionless autocorrelation function         | $[-]$        |
| $t$                   | Time   | $[s]$        |
| $U_g$                 | Superficial gas velocity                       | $[m/s]$      |
| $v_s$                 | Velocity                                       | $[m/s]$      |
| $v'$                  | Deviation in solids velocity from mean         | $[m/s]$      |
| $\langle v_s \rangle$ | Mean solid velocity                            | $[m/s]$      |
| $v_q$                 | qth component of instantaneous velocity        | $[m/s]$      |
| $v'_q$                | qth component of fluctuating velocity          | $[m/s]$      |
| $\langle v_q \rangle$ | qth component of ensembled average velocity    | $[m/s]$      |

|                             |   |       |
|-----------------------------|---|-------|
| $\langle v_q \rangle^{RMS}$ | qth component of RMS velocity                                 | [m/s] |
| $w$                         | Solid inventory   | [kg]  |
| $Z$                         | Instantaneous position of tracer particle in dispersion cloud | [m]   |

### Greek letters

|                  |   |                                   |
|------------------|---|-----------------------------------|
| $\varepsilon$    | Volume fraction   | [-]                               |
| $\varepsilon_s'$ | Deviation in solids volume fraction (holdup) from mean                        | [-]                               |
| $\mu$            | Medium attenuation coefficient  | [m <sup>-1</sup> ]                |
| $\rho$           | Density   | [kg/m <sup>3</sup> ]              |
| $\theta$         | Granular temperature  | [m <sup>2</sup> /s <sup>2</sup> ] |
| $\tau$           | Lag-time in diffusing cloud of particles                                      | [s]                               |
| $\bar{\tau}$     | Mean residence of time  | [s]                               |
| $\tau_{qs}$      | “Turbulent” stress due to cross-correlation of q and s components of velocity |                                   |

### Subscript

|                |                         |
|----------------|-------------------------|
| $g$            | Gas                     |
| $p$            | particle                |
| $r, \theta, z$ | Cylindrical co-ordinate |
| $s$            | Solids                  |

### References

Ambler, P.A., Milne, B.J., Berruti, F., Scott, D.S., 1990. Residence time distribution of solids in a circulating fluidized bed: experimental and modeling studies. Chem. Eng. Sci. 45(8), 2179–2188.

- Andreux, R., Petit, G., Hemati, M., Simonin, O., 2008. Hydrodynamic and solid residence time distribution in a Circulating Fluidized Bed: experimental and 3D computational study. *Chem. Eng. Process. Process Intensif.* 47, 463–473.
- Avidan, A.A., 1980. Bed expansion and solids mixing in high velocity fluidized beds (Ph.D Dissertation). The City College, New York, USA.
- Avidan, A.A., Yerushalmi, J., 1985. Solids mixing in an expanded top fluid bed. *AIChE. J.* 31, 835–841.
- Bader, R., Findlay, J., Knowlton, T. M., 1988. Gas/Solid Flow Patterns in a 30.5 cm diameter Circulating Fluidized Bed Riser. *Circulating Fluidized Bed Technology II*, P. Basu and J. F. Large, Eds., Pergamon Press, New York, 123–137.
- Bendat, J.S., Piersel, A.G., 2000. *Random Data: Analysis and Measurement Procedures*, 4th Edition, John Wiley & Sons, Inc., New York.
- Bhusarapu, S., Fongarland, P., Al-Dahhan, M.H., Duduković, M.P., 2004. Measurement of overall solids mass flux in a gas–solid Circulating Fluidized Bed. *Powder Technol.* 148, 158–171.
- Bhusarapu, S., 2005. *Solid Flow Mapping in Gas-Solid Risers* (D.Sc. Thesis). Washington University, USA.
- Bhusarapu, S., Al-Dahhan, M.H., Duduković, M.P., Trujillo, S., Hern, T.J.O., 2005. Experimental Study of the Solids Velocity Field in Gas - Solid Risers. *Ind. Eng. Chem. Res.* 44, 9739–9749.
- Bhusarapu, S., Al-Dahhan, M.H., Duduković, M.P., 2006. Solids flow mapping in a gas–solid riser: Mean holdup and velocity fields. *Powder Technol.* 163, 98–123.
- Bi, H.T., Grace, J.R., 1995. Flow regime diagrams for gas solids fluidization and upward transport. *Int. J. Multiph. Flow* 21, 1229–1236.
- Bi, J., Yang, G., Kojima, T., 1995 Lateral mixing of coarse particles in fluidized beds of fine particles. *Trans. Inst. Chem. Eng.* 73 (Part A), 162–167.
- Bi, H.T., 2004. Gas and solids mixing in high-density CFB risers. *Int. J. of Chem. Reactor Eng.* 2, 1–12.

- Biswal, J., Joseph, A., Shah, J.G., Pant, H.J., Dash, A., 2016. Preparation of <sup>46</sup>Sc glass microspheres by combined melt-quenching and microwave methods for applications in radioactive particle tracking experiments. *J. Radioanal. Nucl. Chem.* 308, 335–340.
- Bolton, L. W., Davidson, J, F., 1988. Recirculation of Particles in Fast Fluidized Risers. In *Circulating Fluidized Bed Technology II* (P. Basu and J. F. Large, eds.), Pergamon Press. New York, 501
- Breault, R.W., 2006. A review of gas-solid dispersion and mass transfer coefficient correlations in circulating fluidized beds. *Powder Technol.* 163, 9–17.
- Brereton, C., Grace, J.R., 1993. Microstructural Effects of the Behavior of Circulating Fluidized Beds. *Chem. Eng. Sci.* 48, 2565–2572.
- Burkell, J.J., Grace J.R., Zhao. J., Lim. C.J., 1988. Measurement of Solids Circulation Rates in Circulating Fluidized Beds', in *Circulating Fluidized Bed Technology II* (P. Basu and J. F. Large, eds.), Pergamon Press, New York, 501.
- Caloz, Y.P., 2000. Experimental investigation of local solids Fluid dynamics in different industrial-scale circulating fluidized beds with optical probes (Ph.D. Thesis). Swiss Federal Institute of Technology, Zurich.
- Chan, C.W., Brems, A., Mahmoudi, S., Baeyens, J., Seville, J., Parker, D., Leadbeater, T., Gargiuli, J., 2010. PEPT study of particle motion for different riser exit geometries. *Particuology* 8, 623–630.
- Dankwerts, P. V., 1953. Continuous Flow Systems: Distribution of Residence Times. *Chem. Eng. Sci.* 2, 1–13.
- Degaleesan, S. 1997. Fluid Dynamic Measurements and Modeling of Liquid Mixing in Bubble Columns (D. Sc. Thesis). Washington University St. Louis, USA.
- Devanathan, N., 1991. Investigation of liquid hydrodynamics in bubble columns via a computer automated radioactive particle tracking (CARPT) Facility (D.Sc. Thesis). Washington University Saint Louis, Missouri, USA.
- Gao, X., Wu, C., Cheng, Y., Wang, L., Li, X., 2012. Experimental and numerical investigation of solid behavior in a gas – solid turbulent fluidized bed. *Powder Technol.* 228, 1–13.

- Gidaspow, D., 1994. Multiphase flow and fluidization: continuum and kinetic theory descriptions. Academic Press Inc.: Boston.
- Gidaspow, D., Huilin, L., 1996. Collisional Viscosity of FCC Particles in a CFB AICHE J. 42, 2503–2510.
- Godfroy, L., Patience, G.S., Chaouki, J., 1999. Radial Hydrodynamics in Risers. Ind. Eng. Chem. Res. 38(1), 81–89.
- Gopalan, B., Shaffer, F., 2013. Higher order statistical analysis of Eulerian particle velocity data in CFB risers as measured with high speed particle imaging. Powder Technol. 242, 13–26.
- Grace, J.R., 1990. High-Velocity Fluidized Bed Reactors. Chem. Eng. Sci. 45(8), 1953–1966.
- Harris, A.T., Davidson, J.F., Thorpe, R.B., 2002. The prediction of particle cluster properties in the near wall region of a vertical riser (200157) 127, 128–143.
- Harris, A.T., Davidson, J.F., Thorpe, R.B., 2003. Particle residence time distributions in circulating fluidised beds. Chem. Eng. Sci. 58, 2181–2202.
- He, Y., Deen, N.G., Annaland, M.V.S., Kuipers, J.A.M., 2009. Gas - Solid Turbulent Flow in a Circulating Fluidized Bed Riser: Experimental and Numerical Study of Monodisperse Particle Systems. Ind. Eng. Chem. Res. 2009, 8091–8197.
- Herbert, P., Reh, L., Nicolai, R., 1999. The ETH experience: experimental database and results from past eight years, AICHE symposium series, 321 (95), 61–66.
- Horio, M., Morishita, K., Tachibana, O., Murata, M., 1998. Solids distribution and movement in circulating fluidized beds. In Circulating fluidized bed technology II (eds.P. Basu and J.F. Large), Pergamon Press, Toronto, 147–154.
- Hua, L., Wang, J., Li, J., 2014. CFD simulation of solids residence time distribution in a CFB riser. Chem. Eng. Sci. 117, 264–282.
- Ibsen, C.H., Solberg, T., Hjertager, B.H., Johnsson, F., 2002. Laser Doppler anemometry measurements in a circulating fluidized bed of metal particles. Exp. Therm. Fluid Sci. 26, 851–859.

- Issangya, A.S., Bai, D., Grace, J.R., Lim, K.S., Zhu, J., 1997. Flow behaviour in the riser of high-density circulating fluidized bed. *AIChE Symposium Series* 93, 25–30.
- Issangya, A.S., Grace, J.R., Bai, D., Zhu, J., 2001. Radial voidage variation in CFB risers. *Can. J. Chem. Eng.* 79, 279–286.
- Jung, J., Gidaspow, D., Gamwo, I.K., 2005. Measurement of Two Kinds of Granular Temperatures, Stresses, and Dispersion in Bubbling Beds. *Ind. Eng. Chem. Res.* 44, 1329–1341.
- Kak, A.C., Slaney, M., 1988. *Principles of computerized tomographic Imaging*, IEEE Press, New York.
- Kashyap, M., Chalermsoinsuwan, B., Gidaspow, D., 2011. Measuring turbulence in a circulating fluidized bed using PIV techniques. *Particuology* 9, 572–588.
- Kruse, M., Werther, J., 1995. 2D gas and solids flow prediction in circulating fluidized beds based on suction probe and pressure profile measurements. *Chem. Eng. Process.* 34, 185–203.
- Kunii, D., Levenspiel, O., 1991. *Fluidization Engineering*, 2nd Ed., Butterworth-Heinemann.
- Levenspiel, O., 1999. *Chemical Reaction Engineering*, 3rd Ed., John Wiley & Sons, New York, USA.
- Ludlow, J.C., Monazam, E.R., Shadle, L.J., 2008. Improvement of continuous solid circulation rate measurement in a cold flow circulating fluidized bed. *Powder Technol.* 182, 379–387.
- MacMullin, R.B., Weber, M., 1935. The theory of short-circuiting in continuous-flow mixing vessels in series and the kinetics of chemical reactions in such systems. *Trans. Am. Inst. Chem. Eng.* 31(2), 409–458.
- Mahmoudi, S., Baeyens, J., Seville, J., 2011. The solids flow in the CFB-riser quantified by single radioactive particle tracking. *Powder Technol.* 211, 135–143.
- Mahmoudi, S., Chan, C.W., Brems, A., Seville, J., Baeyens, J., 2012. Solids flow diagram of a CFB riser using Geldart B-type powders. *Particuology* 10, 51–61.

- Mathiesen, V., Solberg, T., Hjertager, B.H., 2000. An experimental and computational study of multiphase flow behavior in a circulating fluidized bed. *Int. J. Multiph. Flow* 26, 387–419.
- Mathisen, A., Halvorsen, B., Melaaen, M.C., 2008. Experimental studies of dilute vertical pneumatic transport. *Part. Sci. Technol.* 26, 235–246.
- Monin, A.S., Yaglom, A.M., 1975. *Statistical Fluid Mechanics*. MIT Press, New York.
- Nauman, E.B., 1981. Residence time distributions in systems governed by the dispersion equation. *Chem. Eng. Sci.* 36, 957–966.
- Nauman, E.B., 2008. Residence Time Theory. *Ind. Eng. Chem. Res.* 47, 3752–3766.
- Patience, G.S., Chaouki, J., Grandejean, B. P. A., 1990. Solids flow metering from pressure drop measurement in circulating fluidized beds. *Powder Technol.* 61, 95–99.
- Patience, G.S., Chaouki, J., Kennedy, G., 1991. Solids residence time distribution in CFB reactors. *Circulating Fluidized Bed Technology III*, P. Basu, M. Horio and M. Hasatani, Eds., Pergamon Press, New York, 627–632.
- Patience, G.S. Chaouki, J., 1991. Solids Circulation rate determined by pressure drop measurements. *Circulating Fluidized Bed Technology III*, P. Basu, M. Horio and M. Hasatani, Eds., Pergamon Press, New York, 599.
- Patience, G.S. and Chaouki, J., 1992, Solids hydrodynamics in the fully developed region of CFB risers. In O.E.Potter and D.J.Nicklin, *Fluidization VII*, New York: Engineering Foundation, 33–40.
- Pantzali, M.N., Lozano Bayón, N., Heynderickx, G.J., Marin, G.B., 2013. Three-component solids velocity measurements in the middle section of a riser. *Chem. Eng. Sci.* 101, 412–423.
- Parssinen, J.H., Zhu, J., 2001. Particle velocity and flow development in a long and high-flux circulating fluidized bed riser. *The 7th World Congress on Particle Technology* 56, 5295–5303.
- Rhodes, M.J., Laussmann, P., Vilain, F. and Geldart, D., 1988. Measurement of radial and axial solids flux variations in the riser of circulating fluidized bed in *Circulating*

- Fluidized Bed Technology II. P.Basu and J.F. Large Eds., Pergamon Press, New York, 155–164.
- Rhodes, M. J., Geldart. D., 1989. The Upward Flow of Gas/Solid Suspensions. Part 1. A Model for the Circulating Fluidized Bed Incorporating Dual Level Gas Entry into the Riser. *Chem. Eng. Res. Des.* 67(1), 20–29.
- Rhodes, M.J., Zhou, S., HIRAMA, T., Cheng, H., 1991. Effects of operating conditions on longitudinal solids mixing in a circulating fluidized bed riser. *AIChE J.* 37, 1450–1458.
- Roy, S., 2000 Quantification of Two-Phase Flow in Liquid-Solid Risers (Ph.D. Thesis). Washington University, USA.
- Roy, S., Kemoun, A., Al-Dahhan, M., Dudukovic, M., 2001. A method for estimating the solids circulation rate in a closed-loop circulating fluidized bed. *Powder Technol.* 121, 213–222.
- Shaffer, F., Gopalan, B., Breault, R.W., Cocco, R., Karri, S.B.R., Hays, R., Knowlton, T., 2013. High speed imaging of particle flow fields in CFB risers. *Powder Technol.* 242, 86–99.
- Smolders, K. Baeyens, J., 2000. Overall solids movement and solids residence time distribution in a CFB-riser. *Chem. Eng. Sci.* 55, 4101–4116.
- Sundaresan, S., 2013. Role of hydrodynamics on chemical reactor performance. *Curr. Opin. Chem. Eng.* 2, 325–330.
- Svarovsky, L., 1986. Solid-gas separation, Chapter 8 in *Gas Fluidization Technology*, D. Geldart, ed. John Wiley & Sons, New York, 197–210.
- Tartan, M., Gidaspow, D., 2004. Measurement of Granular Temperature and Stresses in Risers 50, 1760–1775.
- Taylor. G.I., 1920. Diffusion by Continuous Movements', *Proc. London Math. Soc.* 20, 196–212.
- Tennekes, H., Lumley, J.L., 1972. *A First Course in Turbulence*, MIT Press, London, England.

- Tsuji, Y., Morikawa, Y., 1982. LDV measurement of air-solid two-phase flow in a horizontal pipe. *J. Fluid Mech.* 120, 385–409.
- Tsuji, Y., Morikawa, Y., Shiomi, H., 1984. LDV Measurements of an Air-Solid Two-Phase Flow in a Vertical Pipe. *J. Fluid Mech.* 139, 417–434.
- Upadhyay, R. K., 2010. Investigation of multiphase reactors using radioactive particle tracking (Ph.D. thesis). IIT Delhi, India.
- Upadhyay, R.K., Roy, S., Pant, H.J., 2013. Liquid flow patterns in rectangular air-water bubble column investigated with Radioactive Particle Tracking. *Chem. Eng. Sci.* 96, 152–164.
- Van de Velden, M., Baeyens, J., Smolders, K., 2007. Solids mixing in the riser of a circulating fluidized bed. *Chem. Eng. Sci.* 62, 2139–2153.
- Villermaux, J., 1996. Trajectory Length Distribution (TLD), a Novel Concept to Characterize Mixing in Flow Systems. *Chem. Eng. Sci.* 51, 1939–1946.
- Wang, Y., Wei, F., Wang, Z., Jin, Y., Yu, Z., 1998. Radial profiles of solids concentration and velocity in a very fine particle ( $36\ \mu$ ) riser. *Powder Technol.* 96(1), 2–6.
- Wang, C., Zhu, J., Li, C., Barghi, S., 2014. Detailed measurements of particle velocity and solids flux in a high density circulating fluidized bed riser. *Chem. Eng. Sci.* 114, 9–20.
- Wei, F., Wang, Z., Jin, Y., Yu, Z., Chen, W., 1994. Dispersion of lateral and axial solids in a concurrent down flow circulating fluidization. *Powder Technol.* 81, 25–30.
- Wei, F., Zhu, J., 1996, Effect of flow direction on axial solid dispersion in gas-solids cocurrent upflow and downflow systems. *Chem. Eng. J.* 64, 345–352.
- Wei, F., Lin, H., Cheng, Y., Wang, Z., Jin, Y., 1998. Profiles of particle velocity and solids fraction in a high-density riser. *Powder Technol.* 100, 183–189.
- Weinell, C.E., Dam-Johansen, K., Johnsson, J.E., 1997. Single-particle behaviour in circulating fluidized beds. *Powder Technol.* 92, 241–252.
- Yan, A., Pa, J.H., Zhu, J., 2003. Flow properties in the entrance and exit regions of a high-flux circulating fluidized bed riser. *Powder Technol.* 131, 256–263.

- Yan, A., Zhu, J., 2005. Scale-up effect of riser reactors: Particle velocity and flow development. *AIChE J.* 51, 2956–2964.
- Yan, C., Fan, Y., Lu, C., Zhang, Y., Liu, Y., Cao, R., Gao, J., Xu, C., 2009. Solids mixing in a fluidized bed riser. *Powder Technol.* 193, 110–119.
- Zhang, Y. F., Arastoopour, H., 1995. Dilute fluidized cracking catalyst particles-gas flow behavior in the riser of a circulating fluidized bed. *Powder Technol.* 84, 221–229.
- Zhang, M., Qian, Z., Yu, H., Wei, F., 2003. The solid flow structure in a circulating fluidized bed riser / downer of 0.42-m diameter. *Powder Technol.* 129, 46–52.
- Zheng, C.G., Tung, Y.K., Li, H.Z., Kwauk, M., 1992. Characteristics of fast fluidized beds with internals. *Proceedings of the 7th engineering foundation conference on fluidization.* Australia: Brisbane 275–283.
- Zhou, J., Grace, J.R., Lim, C.J., Brereton, C.M.H., 1995. Particle velocity profiles in a circulating fluidized bed riser of square cross-section *Chem. Eng. Sci.* 50, 237–244.
- Zwietering, T.N., 1959. The Degree of Mixing in Continuous Flow Systems. *Chem. Eng. Sci.* 11(1), 1–15.

## Chapter 4

# Experimental Investigation of Pilot Scale Circulating Fluidized Bed

### Scope

In this chapter, solid velocity field in pilot scale CFB are investigated. Present state of the art on scale up studies of CFB is outlined. Lagrangian and Eulerian solid velocity fields in pilot scale setup are presented. Comparative studies with Lab scale experimental setup are also presented. Further hydrodynamic similarity studies are discussed. Then, empirical correlation developed in current work for the prediction of solid velocity is presented. Finally, solid mixing studies are presented.

### 4.1 Introduction

In own words of Matsen (1997), “*Scale up of CFB is still not an exact science, but is rather that mix of physics, mathematics, witchcraft, history and common sense that we call engineering*”. In fact the statement is well valid for most of the multiphase flow reactors where the interactions between the different phases or with in the phases are not well understood which take place at different length and time scale. It is well known that in CFB micro (solids), meso (metastable structures) and macroscale movements of the solids are causing complex interaction between gas – gas, solid – gas and solids – solids. This interaction also varies with reactor geometry, dimensions and operating conditions (Reh, 2003). Thus, depending upon the interactions, hydrodynamics can be different in large scale CFB compared to small scale CFB. In the era of partial reactions like gasification, chemical looping combustion, fluid catalytic cracking etc., hydrodynamic plays a vital role in prediction of performance of reactors.

Scaling laws are widely used for all the practical purpose. Glicksmann (1984) derived scaling law from the conservation equations of Anderson and Jackson (1967). So called full set of dimensionless scaling requires matching Reynolds number, Froude number, density ratio, length scale ratio, dimensionless particle size distribution and particle shape. Alternative forms of scaling laws are also available with limiting conditions of high and low Reynolds number (Horio et al., 1986; Chang and Louge, 1992; Glicksman, 1994; van der Meer et al., 1999; Kehlenbeck et al., 2001). Scaling laws does not account the inter-particle forces and coefficient of restitution (Berruti et al., 1995; Chang and Louge, 1992). Further, scaling law requires different particle size, in some cases different group of particle. However, metastable structures, solid – solid and solid – wall interactions differ for different particles sizes and particle groups. Unfortunately, these are not accounted in scaling laws.

Partial oxidation of n-butane to maleic anhydride commercial plant failed due to the scale issues even though pilot scale performed to the expectations (Duduvokic, 2010). Fundamental approach of scale up might had avoided such an expensive losses. However, due to the inherent complexity of CFB and it dependency on geometry and scale such approach is still missing. Development of such a fundamental approach requires detailed understanding of scale which requires reliable data at different scales with the same accuracy. However, such data are still largely missing. It is very tedious to obtain such a detailed data at the industrial scale. However, it is possible to compare the lab scale and pilot scale setups. In addition to the first order moments, second order moments (fluctuations) may be more helpful in revealing the flow behavior in the CFB with change in scale. Further, effect of scale in terms of fluctuations accelerates the development of fundamental approach of scale-up. This work and further studies in our group at IIT

Guwahati determined to provide such a data which might be useful for scaling and fundamental understanding of effect of scale.

## **4.2 Present state of the art of scale study**

CFB has been studied by various researchers with different solid particles, sizes, density, column diameter, column height, geometry, entrance and exit structures and operating conditions. Some conclusions can be inferred about effect of scale from their works. However, very few studies reported the effect of scale (Arena et al., 1985; Brereton and Stromberg, 1985; Bai et al., 1992; Xu et al., 2000; Yan and Zhu, 2004; Yan and Zhu, 2005). Experiments were also conducted to validate the scaling laws. Most of the scaling laws agree reasonably well for the solid hold up (Horio et al., 1989; Chang and Louge, 1992; Glicksman et al., 1993; Westphalen and Glicksman, 1993; Horio et al., 1993). However, solid fraction profiles and microscopic structures (clusters) formation are not similar for the scaled riser (Noymer et al., 2000).

Effect of diameter on solid concentration studies in the literature gives contrary results. Bai et al. (1992) reported that increasing diameter decreases the cross sectional solid concentration. Similar results were reported by Zhang et al. (1991), Rhodes et al. (1992). However, Brereton and Stromberg (1985), Xu et al. (2000) and Yan et al. (2004) reported that cross sectional solid concentration increases with increases in diameter of the riser.

As stated in the chapter 3, detailed velocity study itself is limited both at laboratory and pilot scales. Effect of scale on local velocity profiles of solids are further limited. Yan et al. (2005) conducted scale up investigation in 0.076 and 0.203 m diameter column using optical fiber probe. In their study, local particle velocity, local volume fraction and cross sectional velocity of solid were reported. They have reported that cross sectional particle velocity decreases with increase in the diameter. Dependency of solid velocity on solid

volume fraction was reported. Large diameter riser has steeper velocity profile, correspondingly solid volume fraction near the wall is also steeper. Flow development in the large diameter riser is slower compared to small diameter riser.

To the best of the author's knowledge, Caloz (2001) is the only study reported effect of scale on velocity fluctuations. Caloz (2001) reported the velocity fluctuation in the three different scales of CFB's. They have used two pilot (0.41 x 8.5 m, 0.83 x 11.2 m) scales and one industrial scale (11.5 x 37 m) setup for investigation. For pilot plant scales, glass beads of 62  $\mu\text{m}$  were used as a solids and temperature of the riser was maintained at 40  $^{\circ}\text{C}$ . However for industrial scale unit, ash particle of 180  $\mu\text{m}$  and 850  $^{\circ}\text{C}$  are used. It should be noted that industrial unit measurements were obtained at the real operating conditions. Measurements were compared at the similar hold up conditions. Optical fiber probe was used for measuring local solid velocity, volume fraction and velocity fluctuations. Mean solid velocity profiles are similar in all the units. However, the fluctuations profiles are different. Further for the same operating conditions in the pilot plant setups, axial solid velocity, axial solid velocity fluctuations and concentration are lower in the larger diameter pilot scale riser.

To the best of author's knowledge, no study is reported on effect of scale on velocity fluctuations using noninvasive techniques. Further there is only one study reported on the solid velocity fluctuations even using invasive techniques at different scales (Caloz, 2000). It is clear that there is dearth of data needed to understand the scale effect on velocity and its fluctuations. In fact, indirectly information about the effect of the scale on metastable structures is also obtained from the fluctuations. It should be noted that, all the techniques have limitations and accuracy of the technique differs at different scale. It is absolutely necessary to have similar accuracy technique or the same technique which gives the reliable data at all the scales. It is well reported in literature that change of scale doesn't affect the

accuracy of radioactive particle technique (RPT) technique. In this work, detailed investigation of pilot scale investigation is carried out to understand the effect of scale up on velocity and velocity fluctuations. Together with Laboratory scale results presented in Chapter 3, it provides detailed information on two scales. Further solid mixing studies are carried out to quantify the global mixing and local mixing and compared with laboratory scale setup.

### **4.3 Experimental setup**

Pilot scale circulating fluidized bed is designed by twice of the diameter and height of the riser of laboratory scale CFB. Diameter of the pilot scale riser is 0.102 m and height of the riser is 6 m. Photograph and schematic of the experimental setup is given in the Figure 4.1. Similar to the laboratory setup, pilot scale CFB setup is also fabricated of mild steel. Design is modular in nature so that each part can be replaced. Different types of exit and inlet structures are fabricated and fixed according to the need. Predesigned threaded ports are fabricated for calibration and pressure studies. Same blower as used in laboratory scale setup is used here. Rota meters are used to measure the air flow rate.

Air enters the riser from the bottom inlet. Solids enter the riser through the standpipe connected to the riser at 15 cm above the distributor. Ratio of diameter of standpipe to the riser is also maintained similar to the laboratory scale CFB. Wang et al. (2013) suggested that high inventory solid storage improves the solid flux. High inventory storage is used in this setup which can hold 100 kg of glass beads. The shape of the storage is conical at the bottom and cylindrical at the top. This storage is fluidized with air from the sides and bottom inlets. Standpipe is connected at the side of the conical section. Further, this solid storage avoids the starvation of solids in riser and ensures smooth flow of solids. Gas and solids flow upwards through the riser and separated through primary and secondary

cyclones provided at the top. Bag filter is provided at the outlet of the secondary cyclone to avoid the carryover of solids. In this work, 90° elbow is provided at the top of riser and standpipe is connected at 30° angle. Similar to the laboratory scale experiments, for the entire run of experiments solid inventory fluctuations is less than 5%.

Experiments are conducted with glass beads of mean particle size of 500  $\mu\text{m}$  and density of 2500  $\text{kg/m}^3$  as in the laboratory scale setup. Same tracer used in the laboratory setup is used in the pilot scale experiments too.

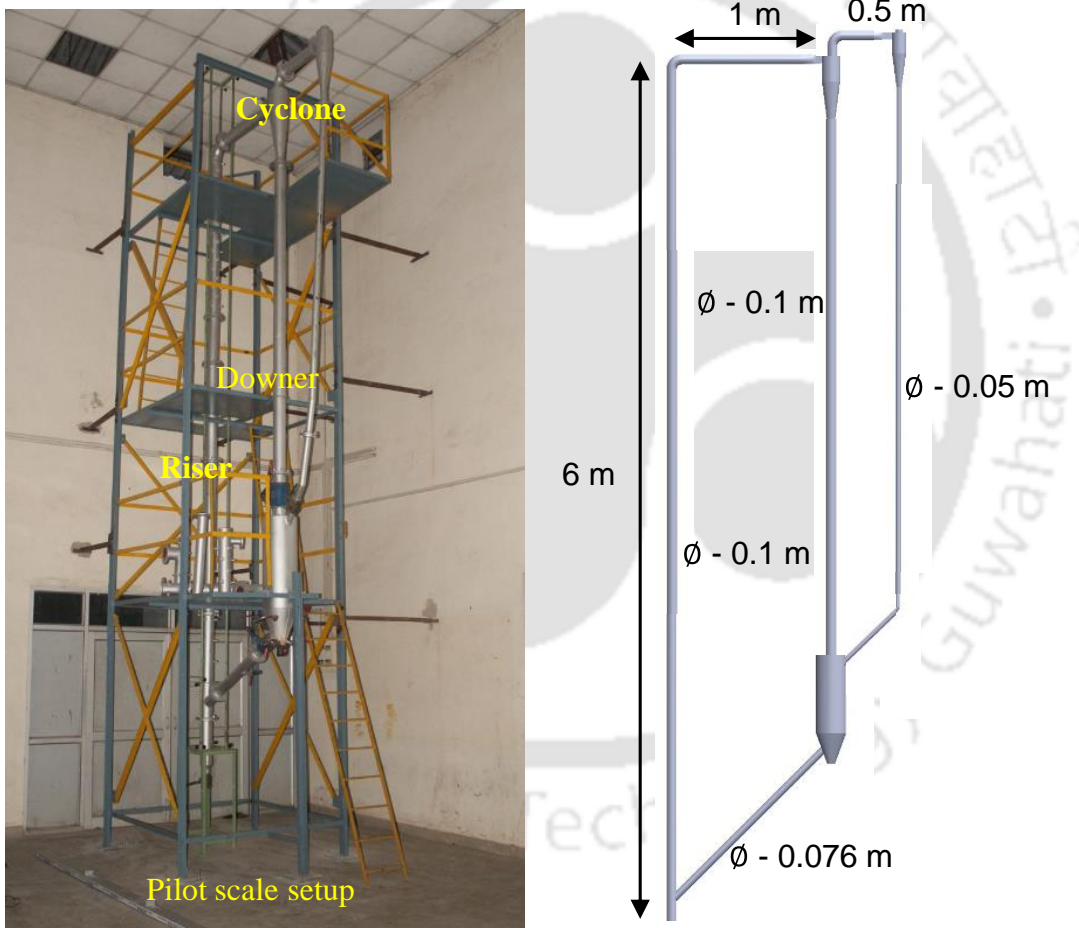


**Figure 4.1 Photograph and schematic of pilot scale experimental setup**

#### 4.4 Solid motion using radioactive particle tracking (RPT) technique

Investigation of solid motion was carried out in the riser section at the height of 3.5 – 4.3 m ( $h/D = 34.3 - 41.2$ ). Calibration and experimental procedure as explained in the section 3.5 and in section 2.2 were followed in pilot scale setup too. Experiments were conducted with same lot of glass beads as in the laboratory scale setup having mean particle size of 500  $\mu\text{m}$  and density of 2500  $\text{kg/m}^3$ . The tracer used in the laboratory setup is used in the pilot scale experiments too. Total 12 detectors were used for tracking the solid phase. In each plane, two detectors were placed at  $180^\circ$  apart. Detectors were positioned in such a way that the face of detectors was perpendicular to the wall. Detectors at successive planes are placed in staggered manner around the riser as shown in the Figure 4.2. Distance between the two detectors planes is kept approximately 10 cm. Face of the detectors were 3 – 4 cm from the wall.

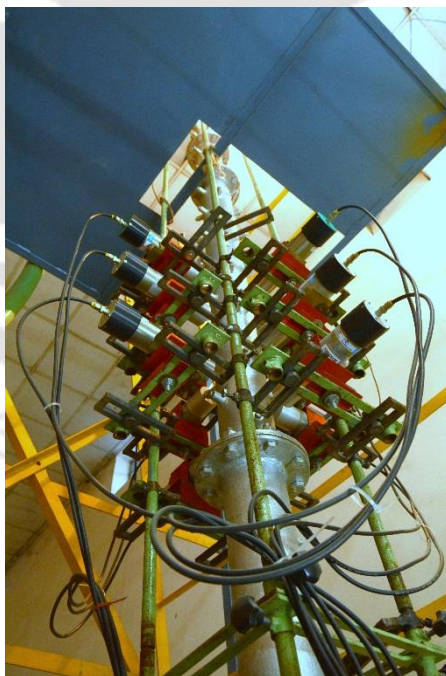


**Figure 4.2 Photograph detailing the detector arrangement in the investigation zone**

Calibration was done using tracer glued on the tip of the calibration rod and positioned in the riser using ports provided on the walls. In a plane, 3 ports are provided at 120° apart. Each plane of ports is 10 cm apart. In a plane, 18 positions were recorded. Calibration was done at in situ conditions. Calibration and reconstruction algorithm are appropriately accounted for the decay in source strength.

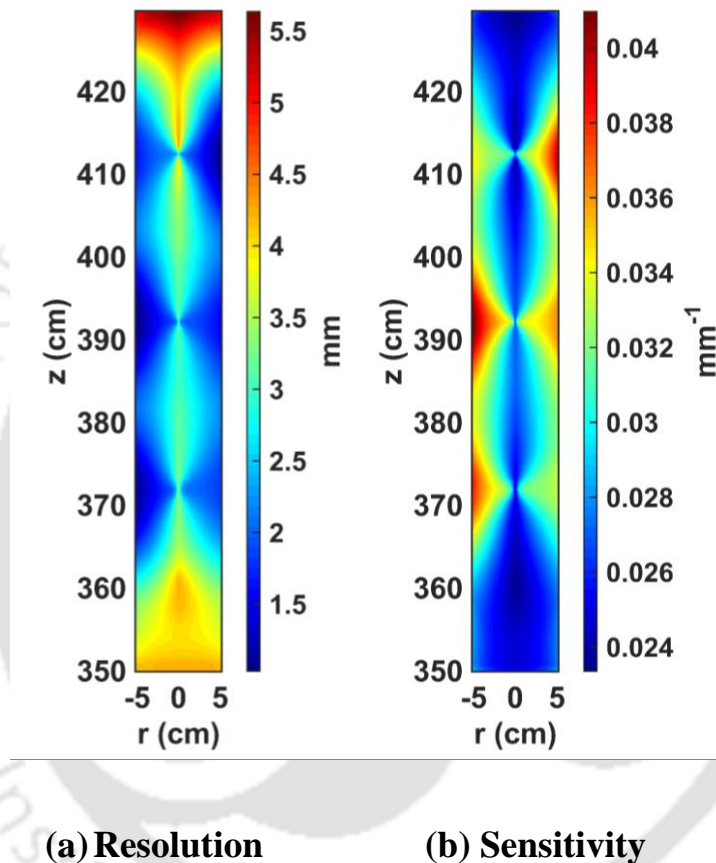


**Figure 4.3 Contours of resolution and sensitivity for RPT experiments used in current work**

Resolution and sensitivity are given in the Figure 4.3 for the configuration used in the experiments. Details on resolution and sensitivity and their use for selection of optimal design of RPT are already discussed in section 2.2.5. In the bottom and top region of investigation, less number of detectors is available, so resolution and sensitivity are low as shown in the Figure 4.3. So, all the results reported exclude that region and reported for the height between 3.6 – 4.2 m only. Average resolution of 2.5 mm and sensitivity of 25%/cm

change in the count was obtained for this configuration. That is, if the particle moves more than 2.5 mm, can be discriminated as the two separate positions.

**Table 4.1 Operating conditions of pilot scale setup**

| S.No. | Operating condition  |   | Study   |
|-------|--|---|---|
|       | Pilot scale  | Laboratory scale  |   |
| 1     | $U_g - 9.6 \text{ m/s}$ ,<br>$G_s - 90 \text{ kg/m}^2\text{s}$   | $U_g - 9.6 \text{ m/s}$ ,<br>$G_s - 110 \text{ kg/m}^2\text{s}$ | $Fr_D^{-0.3} G_s / \rho U_g - 0.00096$<br>Qi et al. (2008)        |
| 2     | $U_g - 10.5 \text{ m/s}$ ,<br>$G_s - 126 \text{ kg/m}^2\text{s}$ | -   | $Fr_D^{-0.3} G_s / \rho U_g - 0.0011$<br>Qi et al. (2008)         |
| 3     | $U_g - 9.6 \text{ m/s}$ ,<br>$G_s - 110 \text{ kg/m}^2\text{s}$  | $U_g - 9.6 \text{ m/s}$ ,<br>$G_s - 110 \text{ kg/m}^2\text{s}$ | Effect of scale<br>$Fr_D^{-0.3} G_s / \rho U_g - 0.0011$ (pilot ) |
| 4     | $U_g - 8.6 \text{ m/s}$ ,<br>$G_s - 70 \text{ kg/m}^2\text{s}$   | -   | Effect of operating conditions                                    |

Solid flux is measured by measuring volume fraction and time of flight of solids in the standpipe as explained in the section 3.4. Solid inventory of 50 – 70 kg was used according to the operating conditions. Data was acquired at the interval of 10 ms. Experiments were carried out anywhere between 240 - 288 hours (10 – 12 days) according to the operating conditions until the sufficient statistics were obtained. Operating conditions selected for the experiments are given in Table 4.1. The objective of the current work is to study the effect of the scale and effect of operating conditions. Hence, operating conditions are chosen judiciously. To understand the effect of scale, same operating conditions as laboratory scale is chosen and flow regime in both the scales are same (dilute flow) as per Bi and Grace (1996) criteria. In addition, operating conditions are chosen to understand the performance of hydrodynamic similarity law of Qi et al. (2008) at the fluctuations level. Hence, operating conditions are selected accordingly to obtain similarity condition in laboratory

and pilot scale setups. Further, other conditions were selected to understand the effect of operating conditions in pilot scale to find that whether the effects of change in operating conditions remains same or not.

Similar to the laboratory scale, velocity field of pilot scale operating conditions will be discussed first. Effect of operating conditions will be discussed in parallel. Thereafter, effect of scale and comparative studies will be discussed.

#### **4.4.1 Instantaneous position**

Solid tracer recirculates in loop mimicking other solid particles in the system. Counts recorded when the tracer passes through the investigation zone are reconstructed to obtain the time – position series. Inherently such a trajectory reveals Lagrangian motion of solids. Each circulation is an independent event. Tracking multiple such trajectories can decipher the solids motion in the investigation zone. Figure 4.4 shows one such trajectory of solid motion in the x-z, y-z, r-z and r- $\theta$  plane.

Most of the solid tracks observed have following characteristics. It should be noted that solid motion differs according to the operating conditions, following were observed in all the conditions. Most of the observations are similar to the laboratory scale setup. Interval between the two positions shows that solids motion is not uniform, sometimes accelerating and sometimes decelerating. Axial motion is predominant and lateral motion (radial and tangential) is not significant. Most of the cases, lateral direction has only fine random fluctuations. Trajectory reveals that solids motions are more towards the plug flow kind of the motion. Internal circulations are observed in some cases. However, those cases are very few. Solids travels near the wall in most of the cases observed. In case of the 8.6 m/s and 70 kg/m<sup>2</sup>s, some trajectories have significant difference in the number of positions recorded. This might be due to the slow moving long existing clusters.

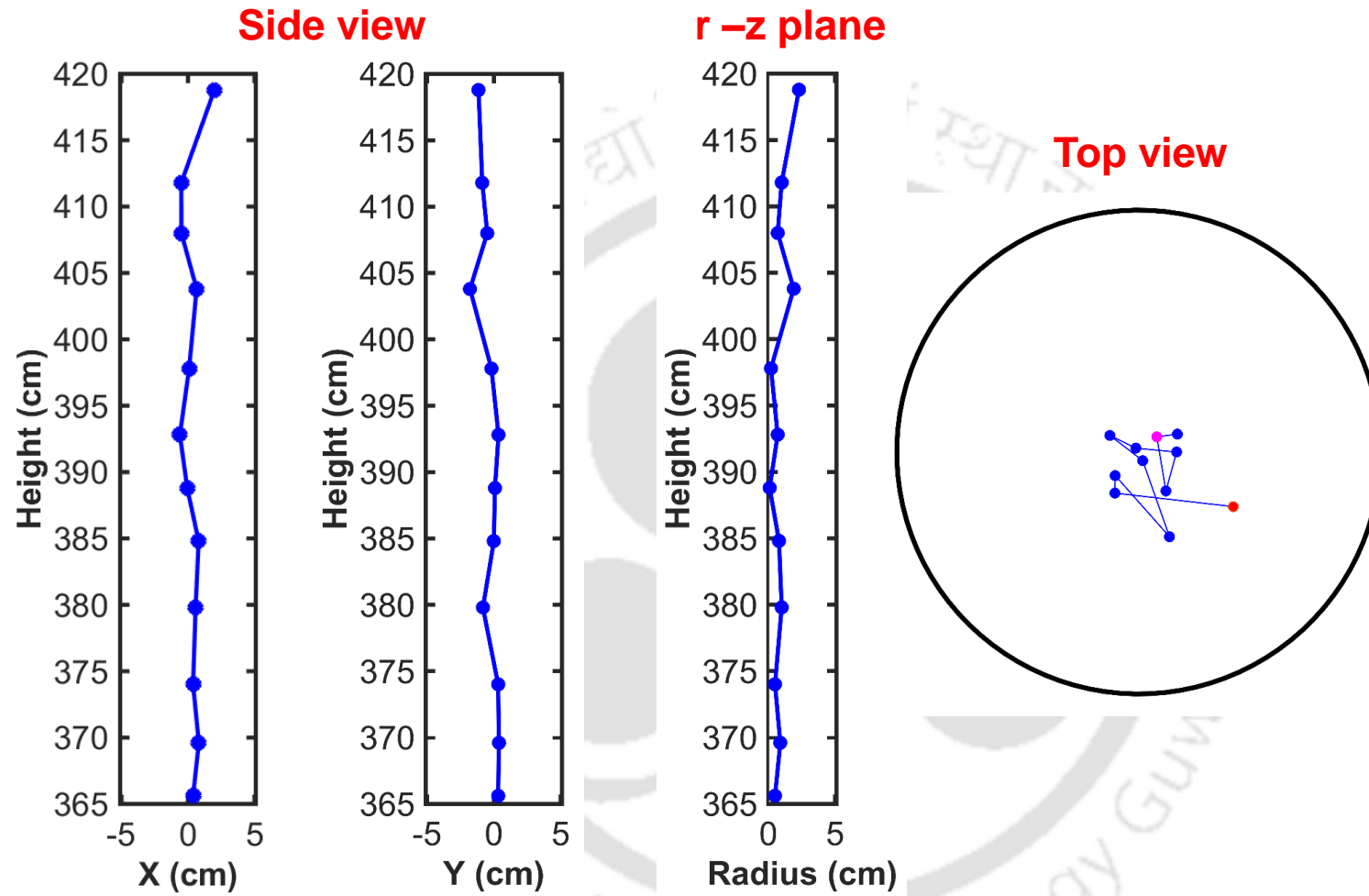
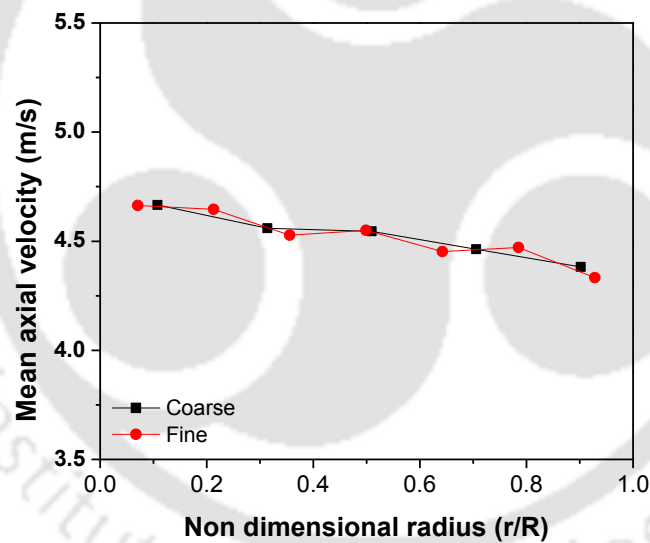


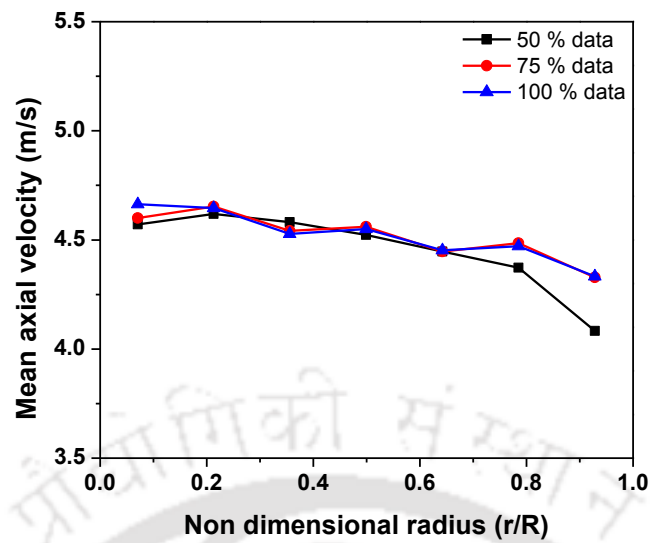
Figure 4.4 Typical position map of single trajectory in different planes ( $U_g = 9.6$  m/s,  $G_s = 110$  kg/m<sup>2</sup>s)

From the position time series, instantaneous Lagrangian velocities are obtained by time differentiation. Eulerian velocities are obtained by forming virtual grid and assigning the velocities according to the midpoint of velocity vector. Optimal grid is necessary as explained in the section 3.5. Different grids were tried. One such comparison is given in Figure 4.5 with coarse grid ( $\Delta r - 10 \text{ mm}$ ,  $\Delta z - 25 \text{ mm}$ ) and fine grid ( $\Delta r - 7.3 \text{ mm}$  and  $\Delta z - 25 \text{ mm}$ ) with theta division varied accordingly to match the volume of grid. Significant difference is not observed between these grids. It is observed that fine grid gives better resolution in the  $r -$  direction. Hence, in this work, fine grid with 7 divisions in the  $r -$  direction and 24 divisions in the  $z -$  direction are used. Volume of each cell is approximately kept constant at  $4.1 \text{ cm}^3$ .

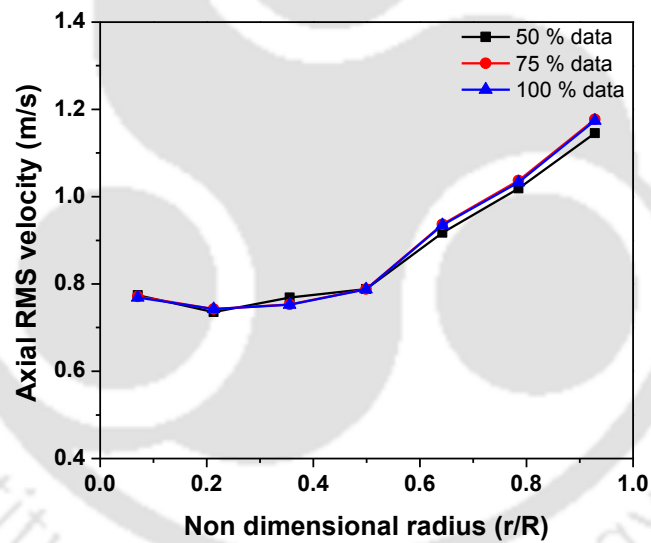


**Figure 4.5 Effect of grid on mean axial velocity at  $h - 3.75 \text{ m}$ . ( $U_g - 9.6 \text{ m/s}$ ,  $G_s - 110 \text{ kg/m}^2\text{s}$ )**

To check the reproducibility and stationary condition, 50%, 75% and 100%, mean and RMS of axial velocity are plotted in Figure 4.6. There is a small difference in the value for the sample of 50% data. However, with increase the sample size further, there is no change in the value is observed. This validates the reproducibility and stationary conditions.



(a)



(b)

**Figure 4.6 Validation of stationarity (a) Axial mean velocity (b) Axial RMS velocity at  $h = 3.75$  m ( $U_g = 9.6$  m/s,  $G_s = 110$  kg/m<sup>2</sup>s)**

#### 4.4.2 PDF of instantaneous velocity

Distribution of velocity can be obtained from the instantaneous velocity in each grid. To have a meaningful comparison between different operating conditions, instead of distribution in each grid, distribution along the column at three radial positions are plotted.

Figure 4.7 shows the PDF of instantaneous velocity at three radial positions, via centre, intermediate region and near the wall region for the entire height of investigation.

Distribution is single modal for all the operating conditions. Spread of the distribution increases from the center towards wall. Negative velocities are observed near the wall for all the conditions. However, negative velocities are more prominent in the case of  $U_g - 8.6$  m/s and  $G_s - 70$  kg/m<sup>2</sup>s. Further, distribution is also high, might be due to the high frequency of cluster. At the same velocity of 9.6 m/s, increase in the solid flux from 90 kg/m<sup>2</sup>s to 110 kg/m<sup>2</sup>s increases the distribution and decreases the mean velocity. At higher velocities,  $U_g - 10.5$  m/s and  $G_s - 126$  kg/m<sup>2</sup>s, negative velocities are observed even though gas velocity is twice of the terminal velocity of the solids. Negative velocity signifies the clusters formation, thus conforms the cluster formation in all the conditions. However, all the cluster formation may not lead to the negative velocities. Cluster size, shape and cluster existence time plays a significant role. From the instantaneous velocities, maximum size and frequency of clusters can be obtained. However, it doesn't give any information about the shape of clusters. Further, lower velocity and flux, spread of distribution is different. Other three conditions, even though distribution and velocity varies, it falls in the very close range. This difference might be due to the different regime of the operation.

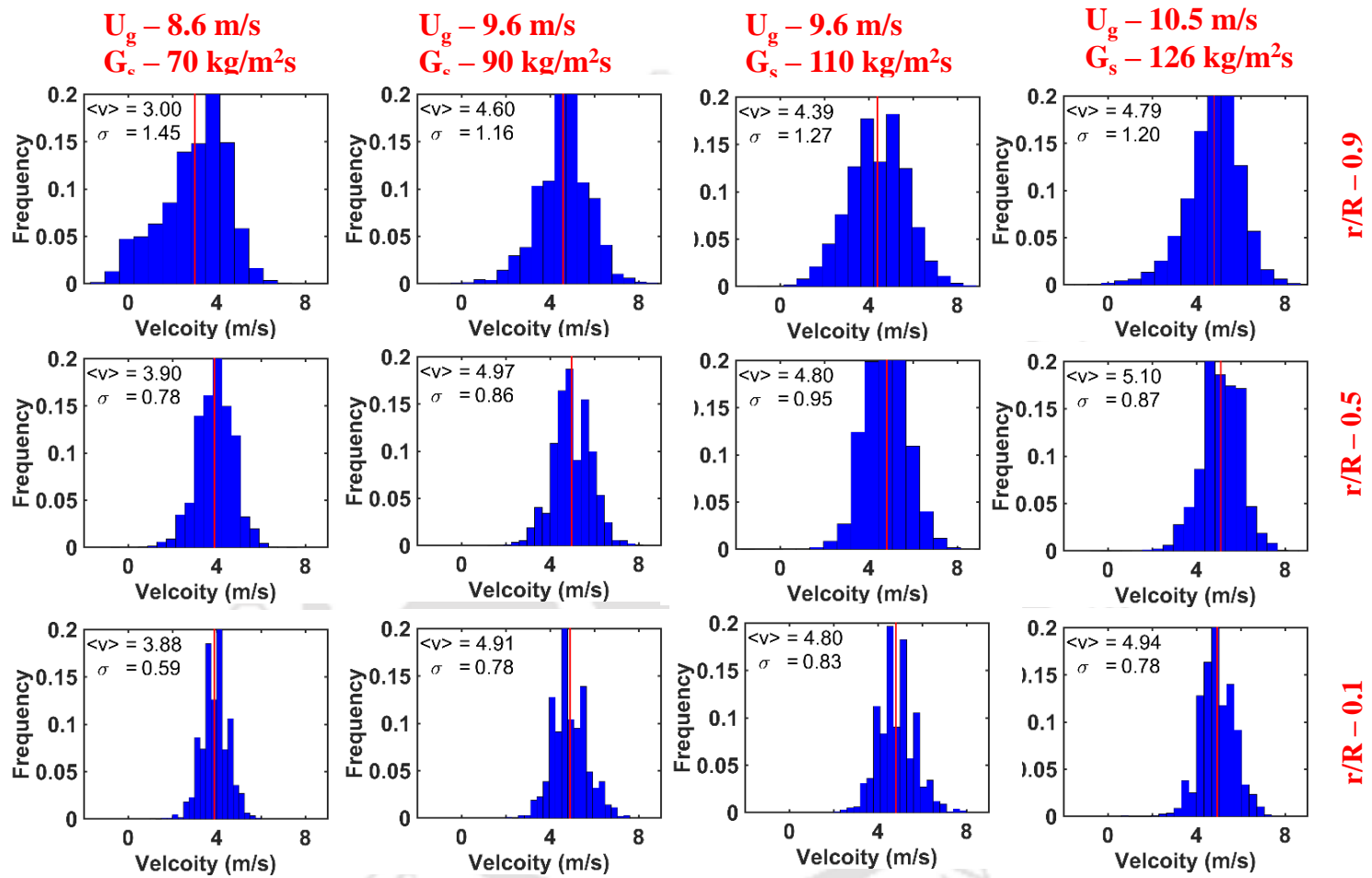
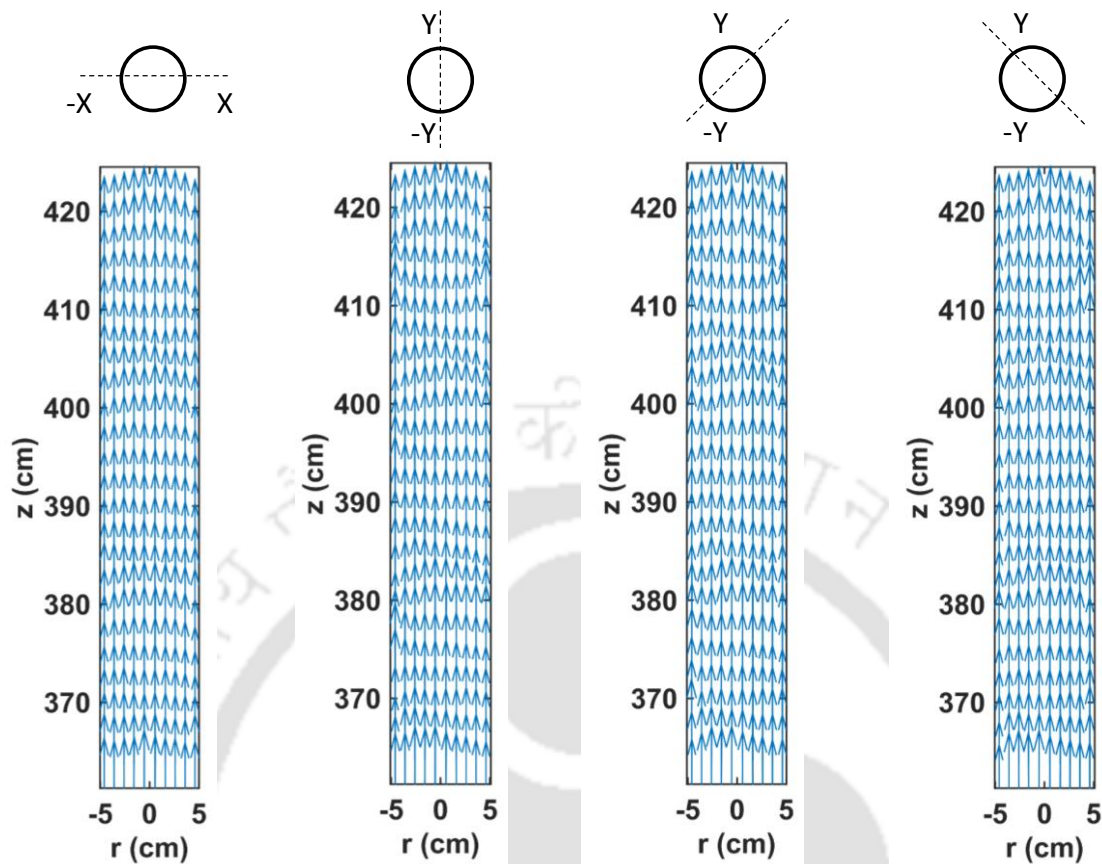


Figure 4.7 PDF of axial instantaneous velocity of solids for the operating condition of  $U_g = 9.6$  m/s and  $G_s = 110$  kg/m<sup>2</sup>s



**Figure 4.8** Vector plot at different planes for the operating condition of  $U_g = 9.6$  m/s and  $G_s = 110$  kg/m<sup>2</sup>s

#### 4.4.3 Velocity vector plots

Qualitative flow pattern in the riser can be obtained from the vector plots of ensemble averaged velocities. Figure 4.8 shows vector plots in x, y – z coordinates at different angular planes via 0, 45, 90 and 135° angle for the operating condition of  $U_g = 9.6$  m/s and  $G_s = 110$  kg/m<sup>2</sup>s. No downward directed motion is observed in ensemble averaged mean velocity confirms that in time averaged sense particles are only moving upward. Further, all the velocity vector pointing upwards which indicates that lateral direction velocities are negligible. Velocity vectors are almost uniform all along the column except very close to the wall. It is to be noted that velocity vectors in all the planes are similar conforming the axi-symmetric flow. Since, there is no significant flow in the radial and tangential

directions, flow can be considered as fully developed. All other operating conditions also have similar observations as it was made here. For the sake of brevity, it is not given here. Similar observation of axi-symmetry and fully developed flow was observed in the laboratory scale setup too.

#### **4.4.4 Contour of occurrences**

Solid fraction distribution can be obtained from the contour of occurrences as solid tracer mimics the solid flows. Occurrence distribution is directly proportional to the solid fraction. However, to obtain solid fraction from RPT, solid holdup is required (Godfroy et al., 1999; Bhusarapu, 2005). Since, solid holdup is not measured in this work; solid fraction distribution will be presented here. Figure 4.9 shows the contour of an azimuthally averaged normalized occurrence plot for all the operating conditions. It should be noted that even though color map has same scale, direct comparison between operating conditions is not correct as the normalization is based on the cross sectional occurrence and overall number of occurrence differs in each case. However relative distribution can be compared. For all the operating conditions, concentration increases towards the wall. Distinct three regions are found viz., dilute, intermediate and dense region. Even in the dense region, concentration increases towards the walls except in the case of 8.6 m/s and 70 kg/m<sup>2</sup>s. In case of 8.6 m/s and 70 kg/m<sup>2</sup>s, dense region is almost uniform except very close to wall.

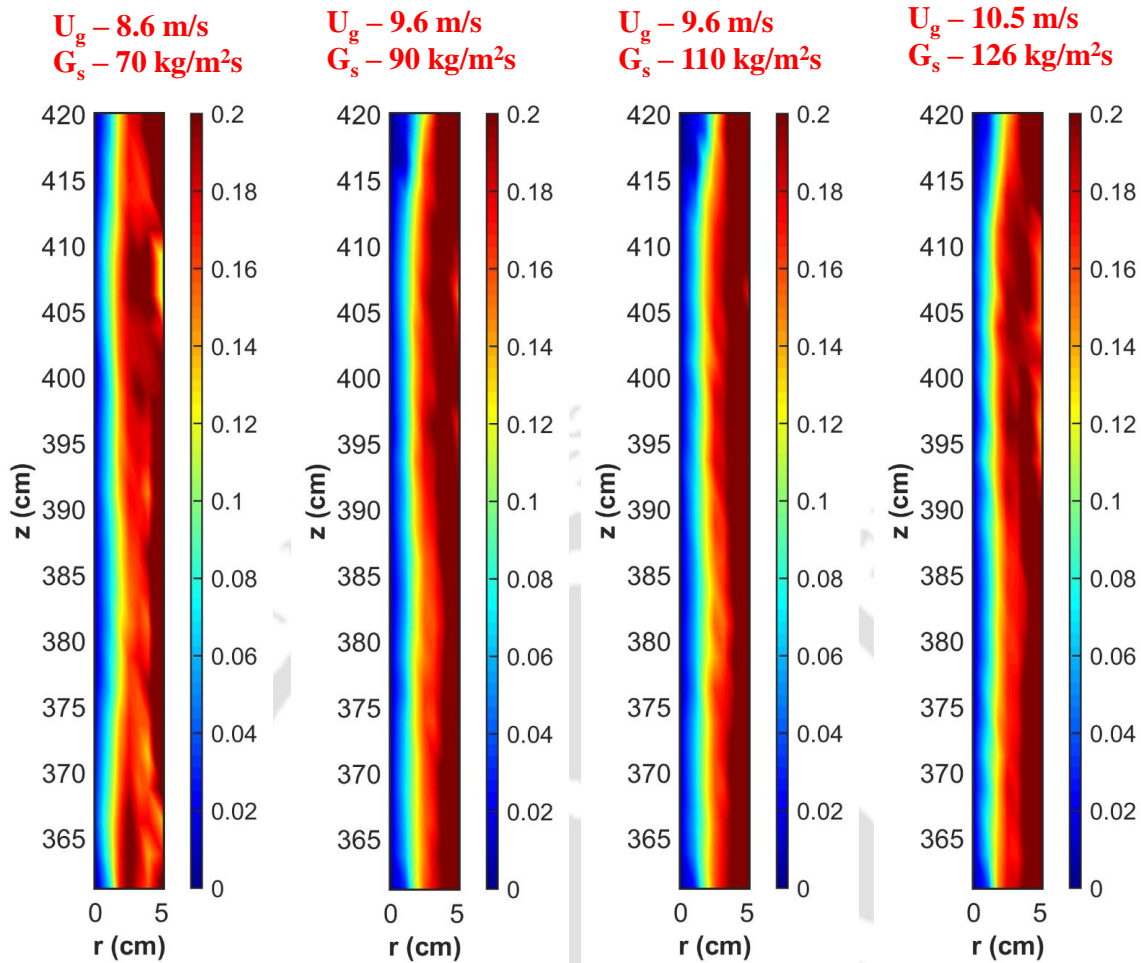


**Figure 4.9** Contour map showing the normalized occurrence for the all operating conditions

#### 4.4.5 Ensemble averaged velocity

Figure 4.10 shows axially and azimuthally averaged mean velocities for all the operating conditions in pilot scale setup. Mean axial velocity profiles are flat for all the cases except  $U_g = 8.6$  m/s and  $G_s = 70$  kg/m<sup>2</sup>s. Change in the velocity in radial direction is within 10%. Step change of around 5% is observed near the wall. While in case of  $U_g = 8.6$  m/s and  $G_s = 70$  kg/m<sup>2</sup>s, gradual change of velocity is observed along the radius resembling parabolic profile. Change of velocity from the centre to wall is almost 25%. It should be noted that even in laboratory scale setup, lower superficial gas velocity (7 and 7.8 m/s) conditions has similar kind of profiles. Mean velocity of solids are less than superficial gas velocity. In

fact, superficial gas velocity is twice of the solid velocity at most of the radial position. Negative axial mean velocity is not observed for any cases. Further, slip velocity (assuming gas velocity is equal to superficial gas velocity) is close to terminal settling velocity of a single particle thus conforms the dilute flow.

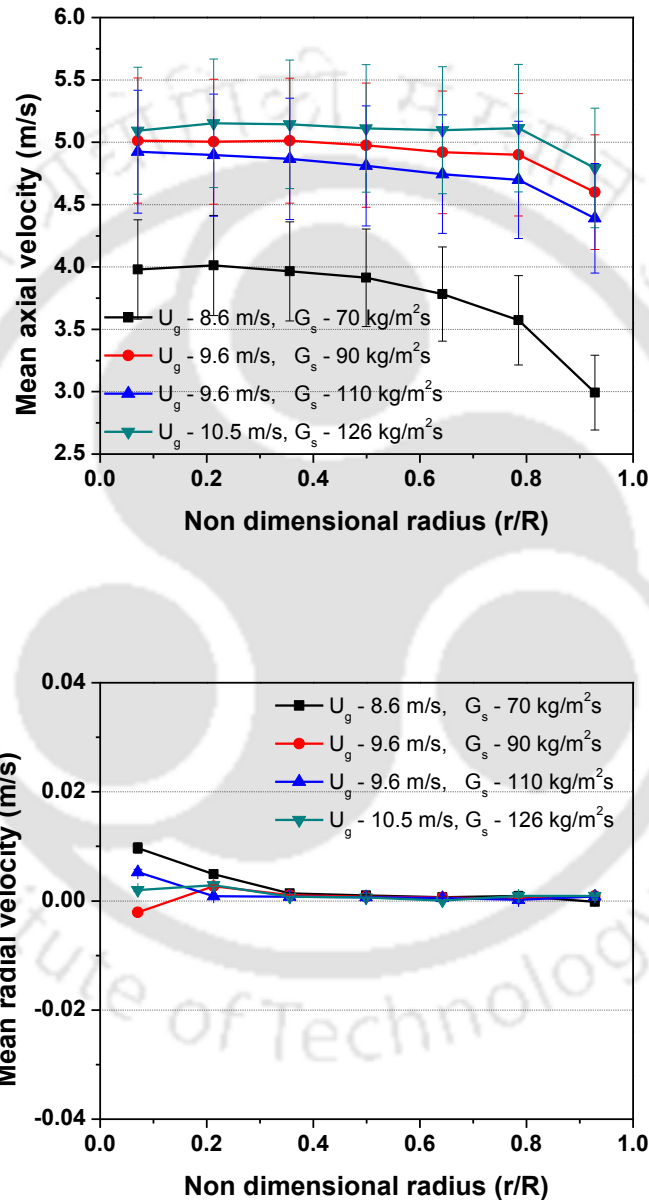


**Figure 4.10 Azimuthally and axially averaged mean velocities**

Radial mean velocities of the solids are close to zero which is similar to the laboratory scale setup. Thus, there is no mean radial directed motion ascertaining the fully developed flow

in the investigation zone. Azimuthal mean velocity also have similar profile as of the radial mean velocity. With increase in the flux at the same gas velocity, mean axial solid velocity decreases. Increase in the solid flux at the same superficial gas velocity, increases the solid hold up in the riser. Thus, now more solids distribute the same amount of energy leading to decrease in the mean axial solid velocity. Mean axial solid velocity increases with the increase in superficial gas velocity and solid flux. Mean axial velocity change with the operating conditions differs significantly for other cases and for the case of  $U_g = 8.6$  m/s and  $G_s = 70$  kg/m<sup>2</sup>s. This might be due to flow structure change however at this point it cannot be ascertained.

#### **4.4.6 Solid velocity fluctuations**

It is well known that solid motion in CFB is turbulent and metastable structures are present. However, mean velocity does not give any information on the turbulent motion. Solid fluctuations and Reynolds stress gives the turbulent information of solid motion. Figure 4.11 shows the azimuthally and axially averaged RMS velocities and Figure 4.12 shows the azimuthally and axially averaged Reynolds stresses. Axial RMS velocities are obtained from the instantaneous velocities and ensemble averaged velocities in each cell as given in equation 3.10 and 3.11. Reynolds stresses are obtained from the fluctuations velocities in each cell as given in equation in 3.12.

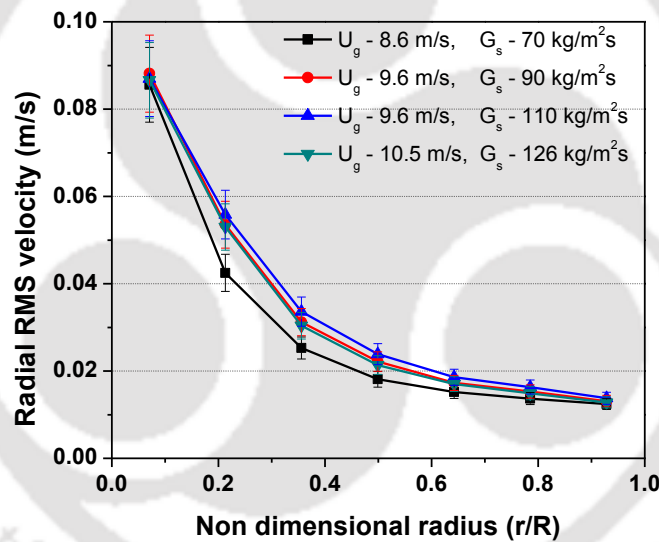
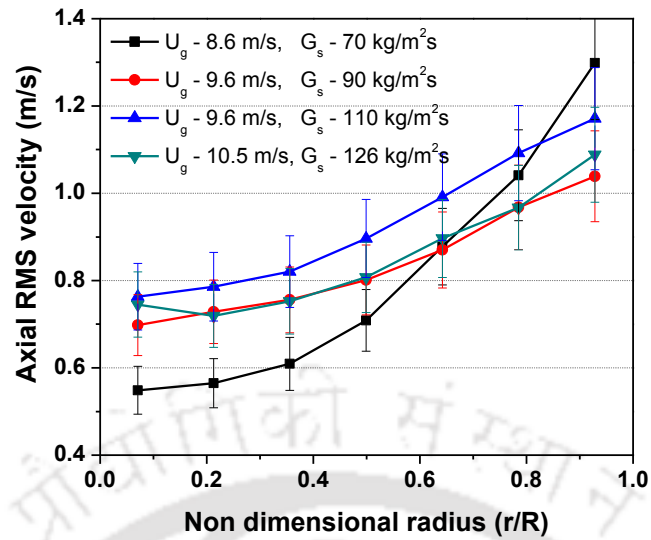


**Figure 4.11 Azimuthally and axially averaged RMS velocities**

Axial RMS velocity increases from the center of the riser to the wall. Similar kind of profile is reported by Mathisen et al. (2008), Pantzali et al. (2013). This kind of profile of solid fluctuations might be due to clusters which are high near the wall (He et al., 2009). However it is not ascertain at this point as further information on gas turbulence and other solid interactions are needed. Remarkable change in the profile of axial RMS is observed for the case of  $U_g = 8.6$  m/s and  $G_s = 70$  kg/m<sup>2</sup>s. Steep increase of axial RMS velocity is recorded

after  $r/R = 0.5$  the case of  $U_g = 8.6$  m/s and  $G_s = 70$  kg /m<sup>2</sup>s. While in other cases, gradual increase from the centre to the wall of axial RMS velocity is observed. It is to be noted that occurrence plot and mean velocity profile also shows the distinguishable profile for the case of  $U_g = 8.6$  m/s and  $G_s = 70$  Kg/m<sup>2</sup>s. This further confirms that solid distribution in this case is different from the other cases. It should be noted that similar observations has been made for the lower velocity cases in laboratory scale setup. At same superficial gas velocity increase in solid flux increases the axial RMS velocity. With increase in the solid holdup frequency of solid-solid collision increases, this results in increase in the axial RMS velocity. Even though axial RMS is lower in the center than the other cases, it is higher than all other conditions near the wall. It might be due to lower velocity of solids near the wall with the higher hold up may increase the collision frequency and cluster formation. Axial RMS is approximately same for the case of  $U_g = 9.6$  m/s and  $G_s = 110$  kg/m<sup>2</sup>s and  $U_g = 10.5$  m/s and  $G_s = 126$  kg/m<sup>2</sup>s. Radial RMS velocity decreases towards the wall. Axial RMS velocity is one order magnitude higher than the radial RMS velocity. Thus, confirming the flow is not isotropic and also axial fluctuations dominant as like axial mean velocity. Further axial mean velocity is more than 5 times of the axial RMS velocity. Thus, fluctuations are not dominating the flow and flow is more uniform. Trend of profiles of axial mean velocity and axial RMS velocity are opposite. May be due to different mechanism governing the mean and RMS, viz, mean velocity might be dominantly governed by drag and axial RMS might be due to the solid interactions and meta-stable structures.

Normal Reynolds stress per unit density profile is also similar to the axial RMS profile. Compared with normal Reynolds stresses, radial and tangential stresses are negligible. This kind of profile, where normal stresses are significant and shear stresses are negligible, are also reported by Tartan and Gidaspow (2004). This might be due to particle properties as

the Tartan and Gidaspow (2004) and this work has similar particle density and size. Further, different order of normal and shear stresses ascertains non – isotropic flow as previously reported by Tartan and Gidaspow (2004), Bhusarapu et al. (2006).

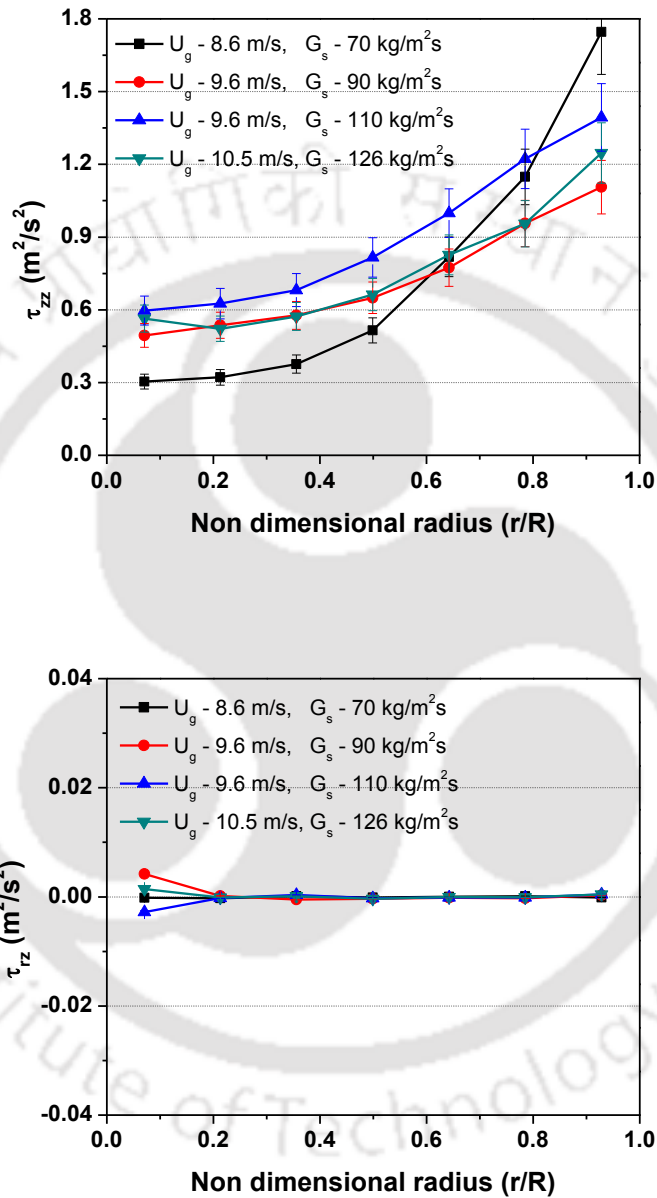


**Figure 4.12 Azimuthally and axially averaged turbulent stresses**

#### 4.4.7 Turbulent kinetic energy

Figure 4.13 shows the azimuthally and axially averaged turbulent kinetic energy per unit mass. Turbulent kinetic energy (TKE) increases towards the wall following the solid

fraction distribution. Similar trend and order of values are reported by Tartan and Gidaspow (2004) and Pantzali et al. (2013). For all the operating conditions, similar order of magnitude of values is obtained. It is to be noted that TKE strongly depends on the solid fraction (Tartan and Gidaspow, 2004; Bhusarapu et al., 2005). Thus, with increase in the flux at the same superficial gas velocity, TKE increases. Further, TKE is highest near the wall for the case of  $U_g = 8.6$  m/s and  $G_s = 70$  kg/m<sup>2</sup>s. Even though, solid loading and gas velocity are lowest, solid distribution and interactions plays great role in the TKE. TKE values are of fraction of kinetic energy available. Thus, energy available for the dissipation is very low.

As pointed out in the chapter 1, one of roadblock for development of CFD models is lack of detailed data. Greater emphasis is given here on the detailed data of solid velocity field in pilot scale. Another, major focus of the current chapter is on scale and similarity. Next section will detail on the effect of scale and thereafter effect of similarity. For comparative studies, data from the laboratory scale is used here.

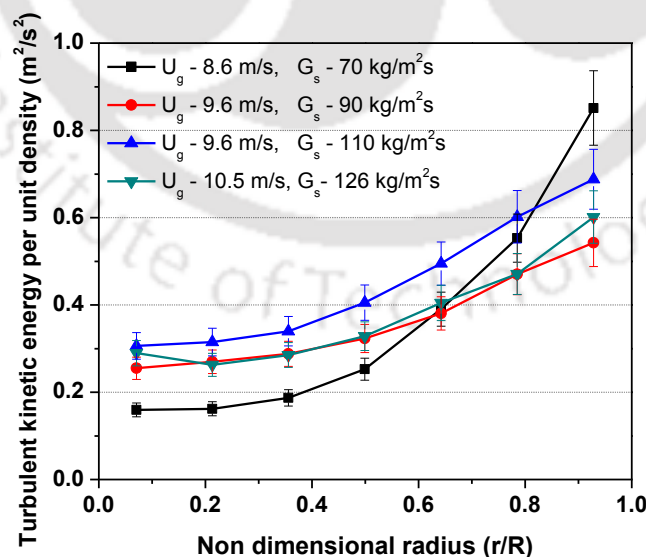


**Figure 4.13 Azimuthally and axially averaged turbulent kinetic energy**

#### 4.4.8 Effect of scale

To study the effect of scale, pilot and laboratory scale setup operated at the same ( $U_g = 9.6$  m/s,  $G_s = 110$  kg/m<sup>2</sup>s) condition as given in Table 4.1. Figure 4.14 shows the head to head comparison of laboratory and pilot scale setup. It is to be noted that reported values are fully developed profile and  $z/D$  of pilot and laboratory scale respectively are 35.78 – 41.17 and 25 - 35.57 and  $h/H$  of pilot and laboratory scale are 0.4 - 0.57 and 0.58 -0.7.

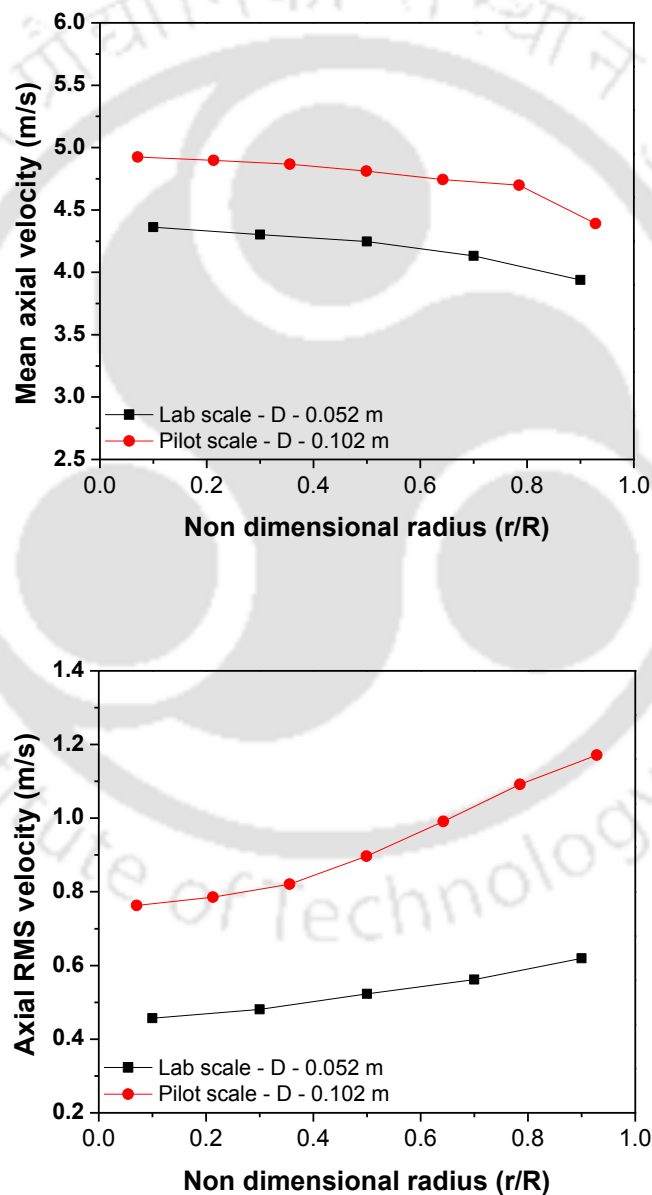


Figure 4.14 Azimuthally and axially averaged Mean axial velocity and Axial RMS velocity showing effect of scale

Axial mean velocity and axial RMS velocities of solids in both the scales have similar profile. Axial mean velocity increases with increase in the diameter. With increase in the diameter, solid concentration decreases for the same operating condition (Bai et al., 1999). Wall friction in the smaller diameter is higher, thus holding more solids than the larger diameter (Yan and Zhu, 2004). As the solid concentration decreases, solid velocity increases to maintain the flux. However, the velocity increase is marginal. Axial RMS velocity of solids also increases with increase in diameter. In fact, axial RMS velocity increased twice by doubling the diameter. With increase in the diameter, solid distribution also changes. Further, with reduction in the solid concentration and increase in the diameter, mean free path between the solids also increases. For dilute flow conditions, fluctuations also increase with the increases in mean free path (Huilin and Gidaspow, 2002; Bhusarapu et al., 2006).

#### 4.5 Hydrodynamic similarity

Qi et al. (2008) proposed hydrodynamic similarity law,  $Fr_D^{-0.3} G_s / \rho U_g$  and reported that for different operating conditions, local solid concentration, downward velocity, cluster concentration and frequency are same until,  $Fr_D^{-0.3} G_s / \rho U_g$  is maintained same. Further, they have reported that,  $Fr_D^{-0.3} G_s / \rho U_g$  is independent of gas – solid system. Solid holdup in different riser diameter and height for different particles is linearly related with  $Fr_D^{-0.3} G_s / \rho U_g$ . In other words, as long as  $Fr_D^{-0.3} G_s / \rho U_g$  is maintained, macro and microstructure hydrodynamics is not varying. Qi et al. (2008) similarity criteria being simplest, lot of interest has been shown as scaling law. This requires extensive experimental validation at the fluctuation level measurement. In the work of Qi et al. (2008), solid upward velocity is not reported. For different flux, solid concentration is same as per the empirical criteria so solid velocity should be changing. However this change in the velocity should

be linear with the solid flux. Further, solid RMS velocities represent fluctuations in the system including due to clusters. Macrostructure and microstructure similarity necessitates fluctuations in the system should be similar. In this work, Qi et al. (2008) similarity parameter is validated in terms of solid velocity and its fluctuations. Similarity conditions in the same column are validated in pilot and laboratory scale setups. Further, different riser at same  $Fr_D^{-0.3} G_s / \rho U_g$  is also compared for performance of the Qi et al. (2008) as scaling law. It should be noted that Qi et al. (2008) reported that solid holdup and similarity criteria is linearly related.

Figure 4.15 shows the mean and RMS axial velocities at laboratory scale of the operating conditions having same Qi et al. (2008) criteria. Figure 4.16 shows the mean and RMS axial velocities at pilot scale of the operating conditions having same Qi et al. (2008) criteria. Figure 4.17 shows the comparative plot of laboratory and pilot scale having same  $Fr_D^{-0.3} G_s / \rho U_g$ . In all the cases, mean axial velocity is not same for the same  $Fr_D^{-0.3} G_s / \rho U_g$  as expected. Since, with change in the flux, velocity should be changing linearly for the same solid concentration. However, such a linear change in the mean velocity is not observed. Change in the profile of the mean velocity is also observed in the laboratory condition. Axial RMS velocity change is observed for all the cases. Thus, Qi et al. (2008) similarity operating conditions is not giving macro and microstructure similarity for the operating conditions used in this work. It is clear that available scaling laws in the literature need more development with validation at the fluctuations level.

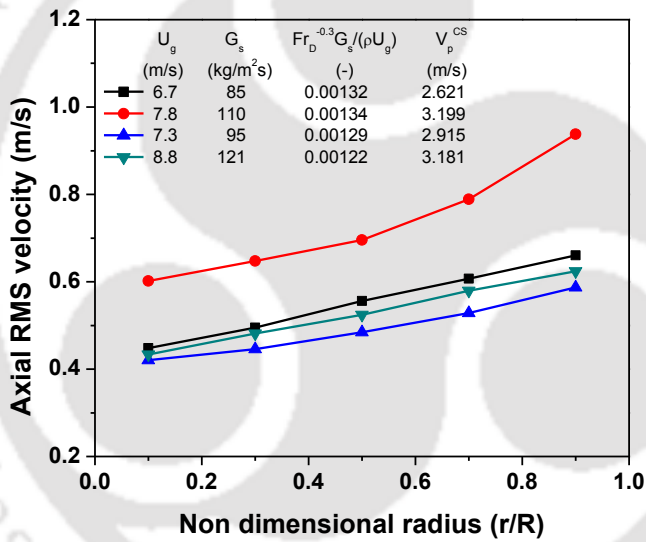
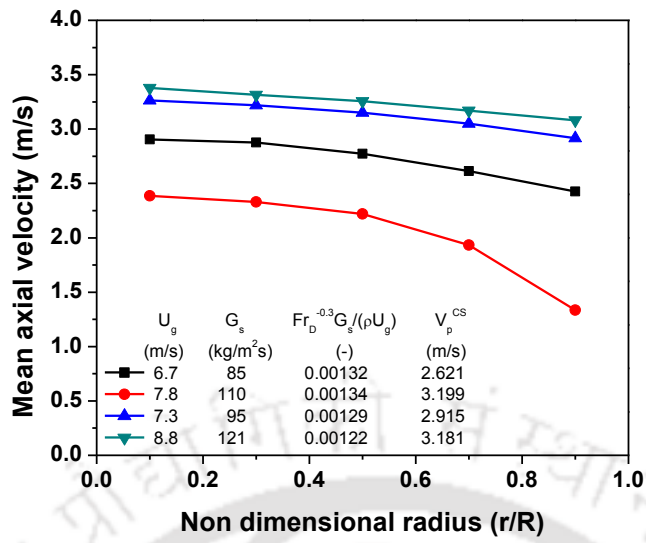


Figure 4.15 Azimuthally and axially averaged Mean axial velocity and Axial RMS velocity at the laboratory scale setup having same  $Fr_D^{-0.3} G_s / \rho U_g$

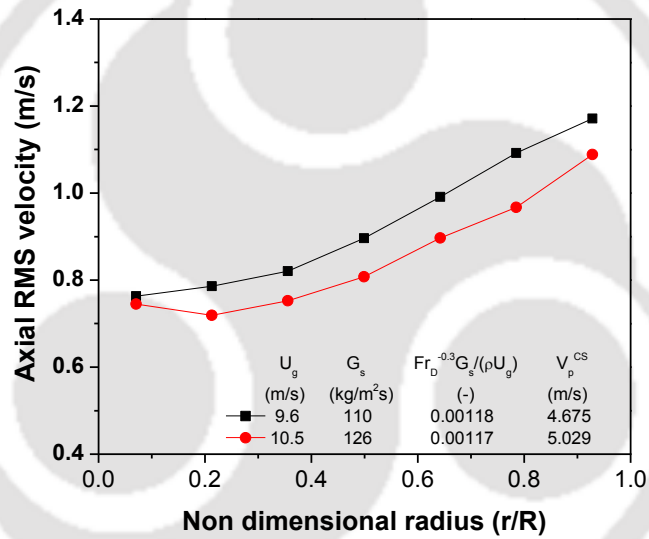
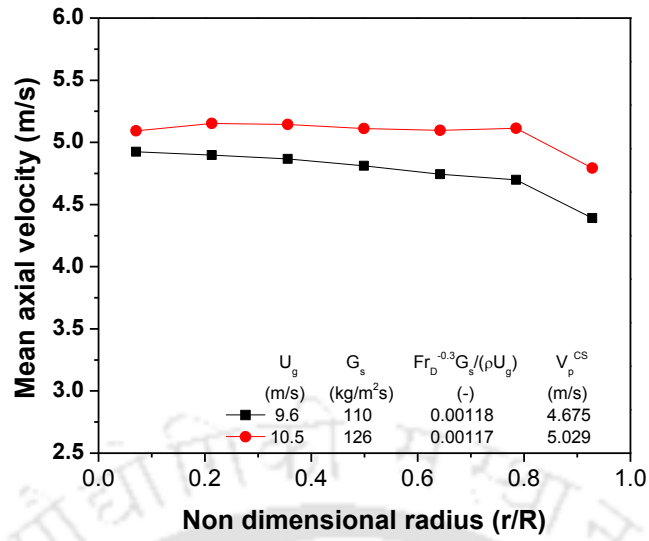


Figure 4.16 Azimuthally and axially averaged Mean axial velocity and Axial RMS velocity at the pilot scale setup having same  $Fr_D^{-0.3} G_s / \rho U_g$

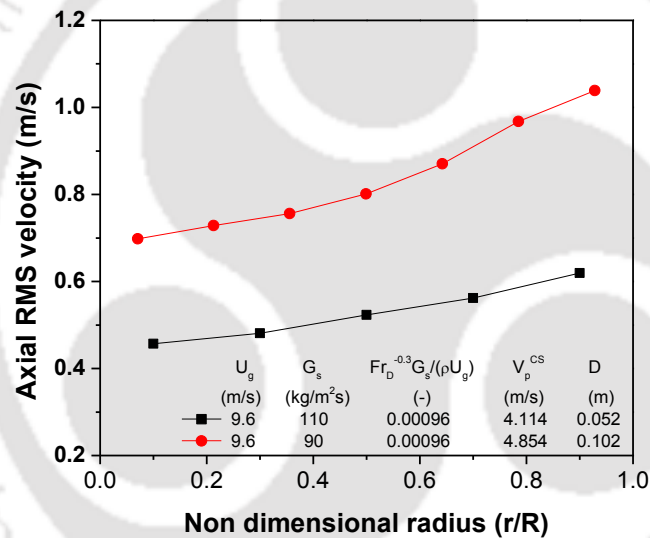
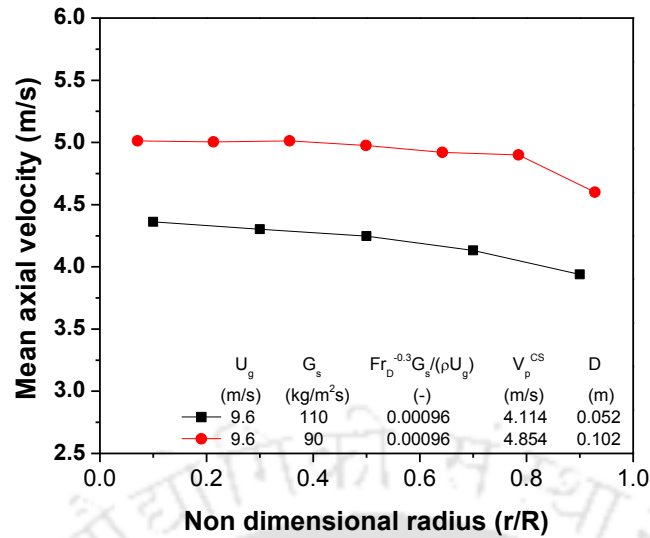


Figure 4.17 Azimuthally and axially averaged Mean axial velocity and Axial RMS velocity at laboratory and pilot scale setup having same  $Fr_D^{-0.3} G_s / \rho U_g$

#### 4.5.1 Development of the empirical equation for mean solid velocity

First approximation on the mean velocity would be of great help for designers. However from the previous results it is obvious that obtaining such information on the mean solid velocity is quite difficult due to the complex interactions. Previously attempts are made in literature to predict volume fraction and velocity. Patience et al. (1992) developed

correlation in terms of slip factor and Froude number as given in Equation 4.1. Slip factor is defined as the ratio of actual gas velocity to the solid velocity.

$$\varphi = 1 + \frac{5.6}{Fr} + 0.47 * Fr^{0.41} = \frac{U_g}{\varepsilon V_p} \quad (4.1)$$

However, solid holdup and solid velocities are unknown beforehand. Pressure drop is related with volume fraction and matched between the scales. Thus, mean velocity can be obtained. Due to its ease and applicability, Patience et al. (1992) correlation is widely used as the first approximation. However, Patience et al. (1992) correlation over predicts the slip factor in most of the cases in this work (both laboratory and pilot scale setups). Further, for initial design where no information is available on pressure drop, velocity prediction is difficult. In those cases, velocity prediction from the operating conditions and geometry would be of great help. In this work, efforts have been made to develop correlation for prediction of mean solid velocity from operating conditions and geometry parameter. Data from the literature and this work is used as shown in Table 4.2. Only Group B particles data are used. Further equation is developed for the dilute conditions where the mass loading is less than 15. Mean velocity of the solids depend on the solid concentration, gas velocity, diameter, metastable structures, wall friction, wall surface, solid properties, etc. It is not possible, to characterize all these parameters explicitly in terms of operating conditions, known solid properties and geometrical parameters at this stage. However, relationship between mean solid velocity and dominant forces in terms of known quantities can be found by optimization. For optimization, Powell's algorithm is used (Powell, 1964). Different combinations of known quantities in terms of dimensionless groups ( $G_s/\rho U_g$ ), Archimedes number, Reynolds number, Froude number, density ratio, diameter ratio, mass loading) are optimized to give mean solid velocity. Correlation obtained is validated with data which is not used for optimization with the current data and data reported in literature

$$4 < \left( \frac{\dot{m}_p}{\dot{m}_g} \right) < 15,$$

$$\left( \frac{\dot{m}_p}{\dot{m}_g} \right)^{-0.228} \left( \frac{U_g}{U_t} \right)^{-0.201} (Fr)^{-0.01} = \left( \frac{U_p}{U_g} \right) \quad 1.6 < \left( \frac{U_g}{U_t} \right) < 7 \quad (4.2)$$

$$10 < (Fr) < 180$$

**Table 4.2 Experimental and solid particles used for empirical correlation**

|                            | H(m)       | D(mm)    | Solid Material | $\rho_p$ (kg/m <sup>3</sup> ) | $d_p$ ( $\mu$ m) | $U_g$ (m/s)         | $G_s$ (kg/m <sup>2</sup> s) |
|----------------------------|------------|----------|----------------|-------------------------------|------------------|---------------------|-----------------------------|
| Godfroy et al. (1999)      | 7          | 82       | Sand           | 2600                          | 150              | 4                   | 23-75                       |
| Bhusarapu et al. (2005)    | 7.93, 5.77 | 152, 140 | Glass          | 2600                          | 150              | 3.2-4.5; 5.4-9-7.71 | 26.6-36.8; 102-109          |
| Gopalan and Shaffer (2013) | 15.5, 22   | 305, 203 | HDPE           | 863.3                         | 802              | 3.5-8               | 50-200                      |
| This Work                  | 3, 6.5     | 52, 102  | Glass          | 2500                          | 500              | 6.7-9.6; 8.6-10.5   | 85-144; 70-126              |

Correlation developed is given in equation 4.2. Figure 4.18 shows the comparison of mean velocity predicted from the equation and actual mean velocity. Most of the error is less than 30%. It is also observed that error is high for the cases where the mass loading is greater than 10 as well as  $U_g/U_t$  ratio is less than 2. So mean velocity prediction can be bounded as follows,

$$\left( \frac{\dot{m}_p}{\dot{m}_g} \right) < 10$$

$$\left( \frac{U_g}{U_t} \right) > 2$$

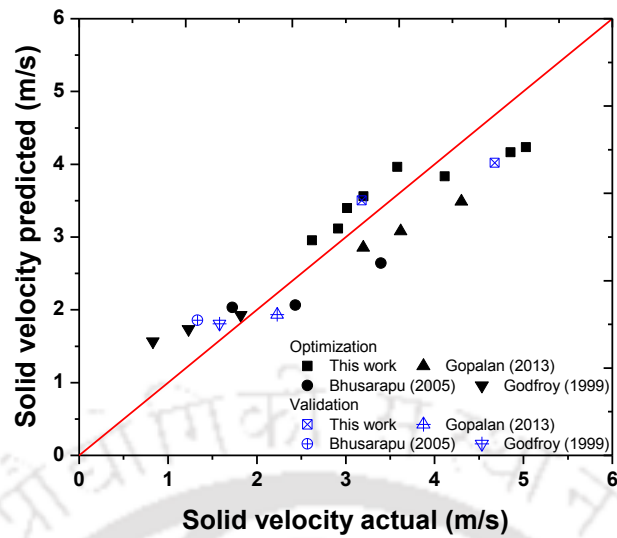


**Figure 4.18** Pox diagram for predicted Mean solid velocities from empirical correlation and measured solid velocity

## 4.6 Solid mixing studies

Overall and local mixing in the riser is investigated in this section. Similar to the laboratory scale setup, overall mixing is quantified using residence time distribution and trajectory length distribution and local mixing is quantified by axial diffusivity.

### 4.6.1 Residence time distribution

Literature on Residence time distribution (RTD) measurements of true residence time are explained in section 3.5. In the pilot scale system, residence time distribution measurement was carried out at 4 sections, viz. bottom, intermediate, middle (RPT), and top sections. Lengths of the sections are shown in the Figure 4.19. Detectors are shielded with lead. ‘True residence time’ is calculated from the peaks recorded at the two successive detectors. It should be noted that temporary excursions outside of the boundary is not accounted to compute true residence time (Nauman, 1981). Each experiment was carried out for 24 – 48 hours according to the operating conditions until sufficient statistics were obtained. Figure

4.20 – 4.23 gives residence time distribution for all the operating conditions at different sections. Figure 4.24 shows the residence time distribution for the entire riser for all the operating conditions. Table 4.3 shows the mean residence time and dispersion number for the different sections. Figure 4.20 shows that long tails are present, which is the characteristic of the back mixing. That is, bottom region of riser behaves like mixed flow reactor. Table 4.3 shows that at the bottom region dispersion number is one order magnitude higher than other sections and all the operating conditions have similar values. Still, with increase in the solid flux, increase in the dispersion number can be found, that is, with increase in the solid holdup, back mixing increases. Further, with increase in the height, tail of the curve disappears and reappears at the top region evident from the Figure 4.21 – 4.23. Solid back mixing reduces with the height until the top region, however at the top region due to the exit effect and high velocity, solid back mixing increases. This is also evident from the Table 4.3, variance decreases with the height until top region and increases once again at the top region. Since there is no mean negative velocity near the wall, solid back mixing is due to metastable structures and solid interactions. At all the heights, dispersion number of  $U_g - 8.6$  m/s and  $G_s - 110$  kg/m<sup>2</sup>s is high, even though all the operating conditions have close values. Once again it proves the dominance of gas velocity as like laboratory scale setup. Figure 4.24 and Table 4.4 shows the residence time distribution and dispersion number of the overall column respectively. Dispersion number is very close for all the conditions, revealing the fact that solid mixing at all the operating conditions is similar. However, still the dominance of velocity can be seen from the higher value for lower gas velocity conditions. Dispersion number of the laboratory scale and pilot scale setups are in the same order of magnitude. Further at the same operating conditions, pilot scale setup has slightly higher values. It is to be noted that axial RMS velocity is doubled in the pilot scale than the similar conditions in the laboratory scale conditions. This

signifies the fact that the solid mixing is governed by solid interactions and metastable structures.

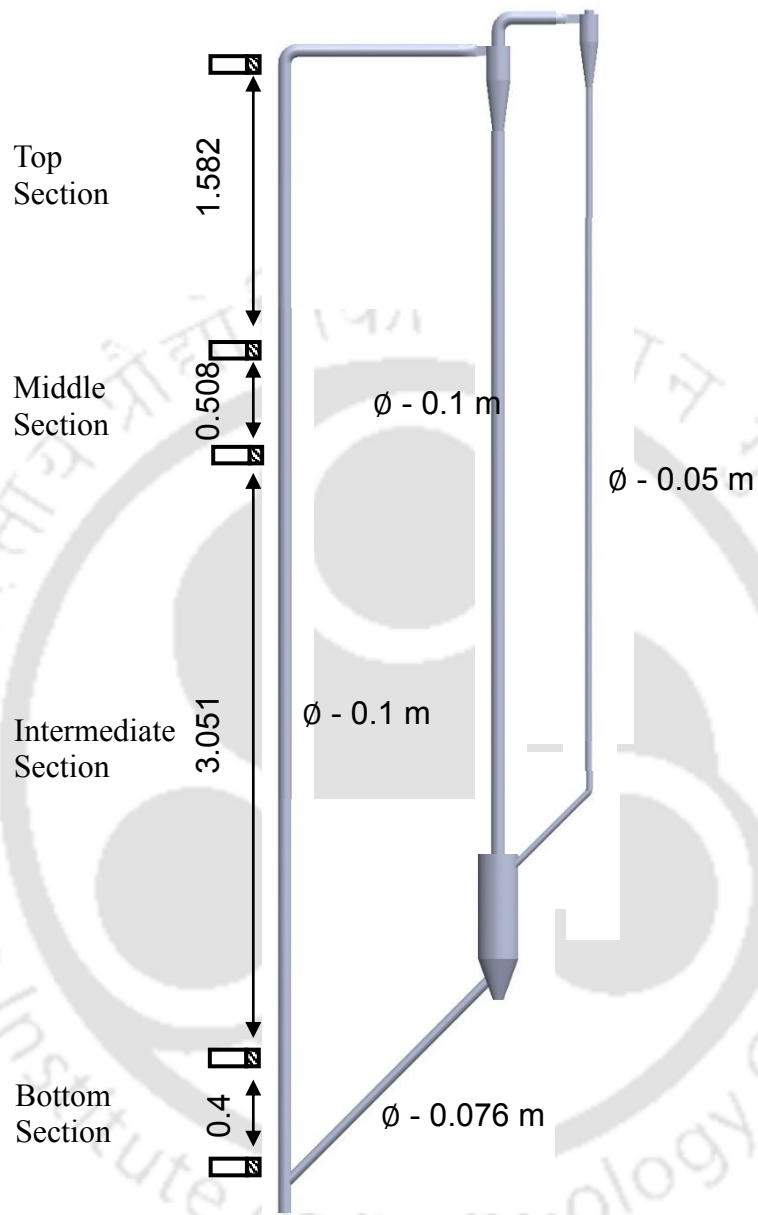


**Figure 4.19 Schematic showing different RTD sections in pilot scale setup**

**Table 4.3 Residence time distribution and dispersion number at different sections**

| $U_g$ (m/s)              | $G_s$ (kg/m <sup>2</sup> s) | $\bar{t}$ (s) | $\sigma^2$ (s) | Dispersion Number |
|--------------------------|-----------------------------|---------------|----------------|-------------------|
| Section 1 (Bottom)       |                             |               |                |                   |
| 8.6                      | 70                          | 0.3583        | 0.0907         | 0.3533            |
| 9.6                      | 90                          | 0.3305        | 0.0684         | 0.3130            |
| 9.6                      | 110                         | 0.3307        | 0.0808         | 0.3696            |
| 10.5                     | 126                         | 0.3044        | 0.0558         | 0.3011            |
| Section 2 (Intermediate) |                             |               |                |                   |
| 8.6                      | 70                          | 0.8595        | 0.0395         | 0.0267            |
| 9.6                      | 90                          | 0.7774        | 0.0266         | 0.0220            |
| 9.6                      | 110                         | 0.7872        | 0.0264         | 0.0213            |
| 10.5                     | 126                         | 0.7608        | 0.021          | 0.0181            |
| Section 3 (Middle)       |                             |               |                |                   |
| 8.6                      | 70                          | 0.1300        | 0.0024         | 0.0696            |
| 9.6                      | 90                          | 0.1101        | 0.0005         | 0.0198            |
| 9.6                      | 110                         | 0.1121        | 0.0006         | 0.0256            |
| 10.5                     | 126                         | 0.1101        | 0.0004         | 0.0152            |
| Section 4 (Top)          |                             |               |                |                   |
| 8.6                      | 70                          | 0.3995        | 0.0089         | 0.0277            |
| 9.6                      | 90                          | 0.3455        | 0.0043         | 0.0181            |
| 9.6                      | 110                         | 0.3533        | 0.0056         | 0.0223            |
| 10.5                     | 126                         | 0.3576        | 0.0068         | 0.0264            |

**Table 4.4 Residence time distribution and dispersion number for the entire riser**

| $U_g$ (m/s) | $G_s$ (kg/m <sup>2</sup> s) | $\bar{t}$ (s) | $\sigma^2$ (s) | Dispersion Number |
|-------------|-----------------------------|---------------|----------------|-------------------|
| 8.6         | 70                          | 1.7473        | 0.1707         | 0.0280            |
| 9.6         | 90                          | 1.5636        | 0.1275         | 0.0261            |
| 9.6         | 110                         | 1.5833        | 0.1357         | 0.0271            |
| 10.5        | 126                         | 1.5330        | 0.1052         | 0.0224            |

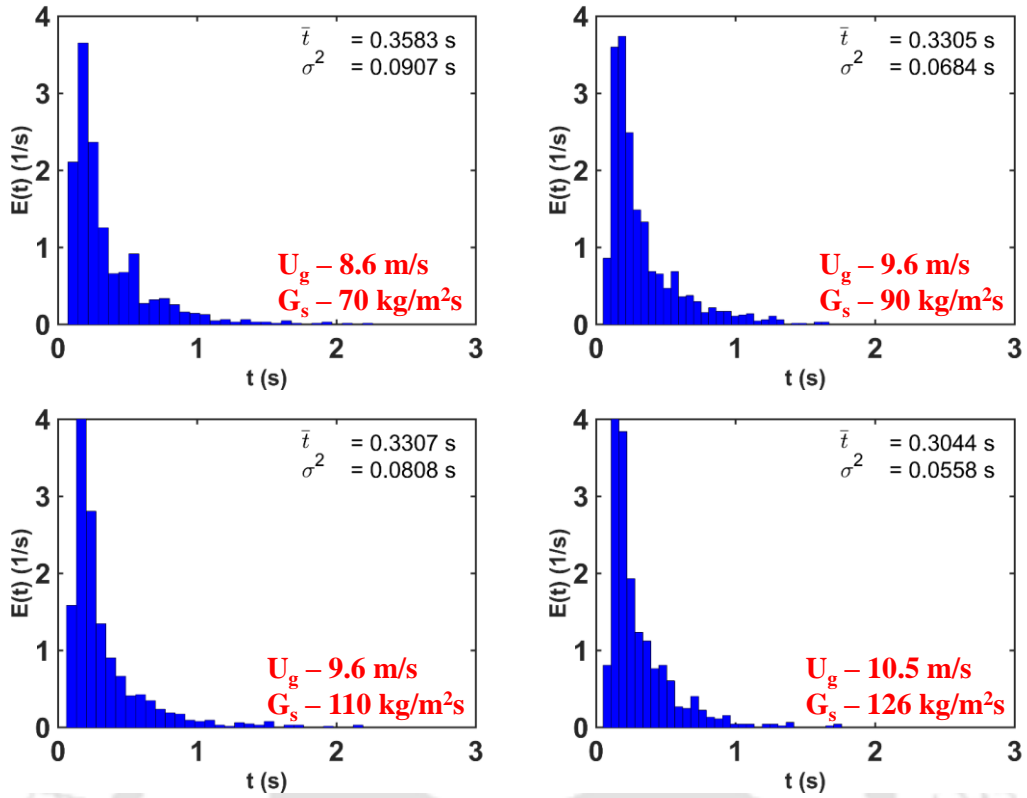


Figure 4.20 Residence time distribution for the section 1 (bottom)

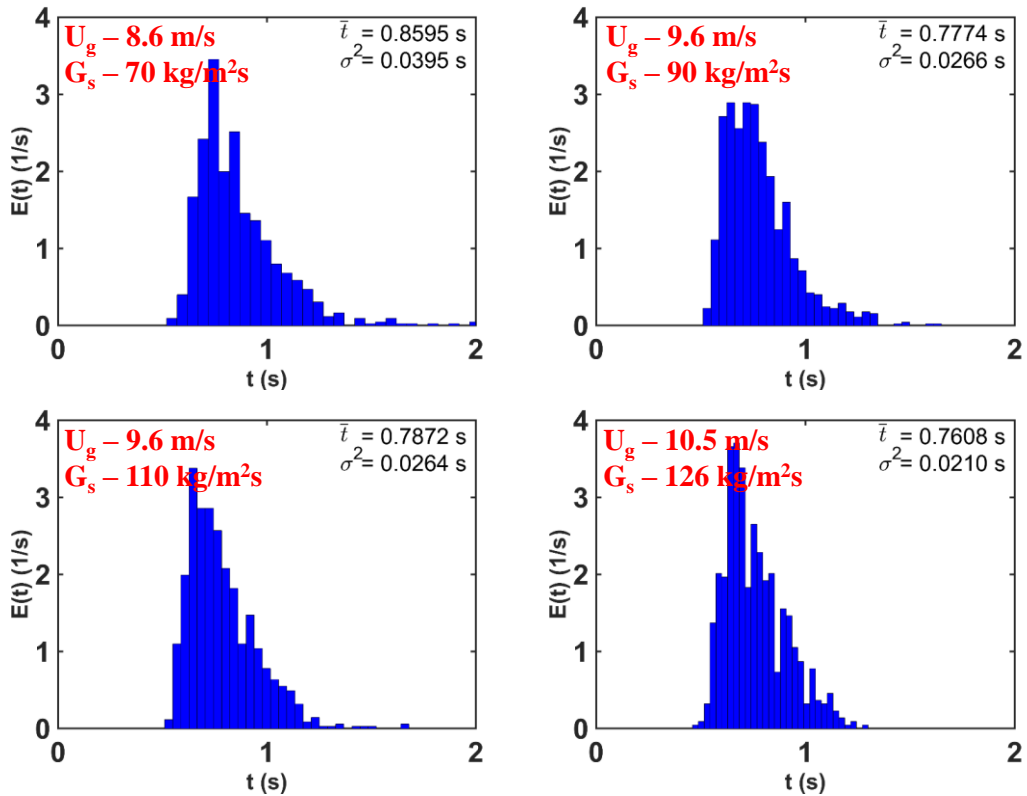


Figure 4.21 Residence time distribution for the section 2 (Intermediate)

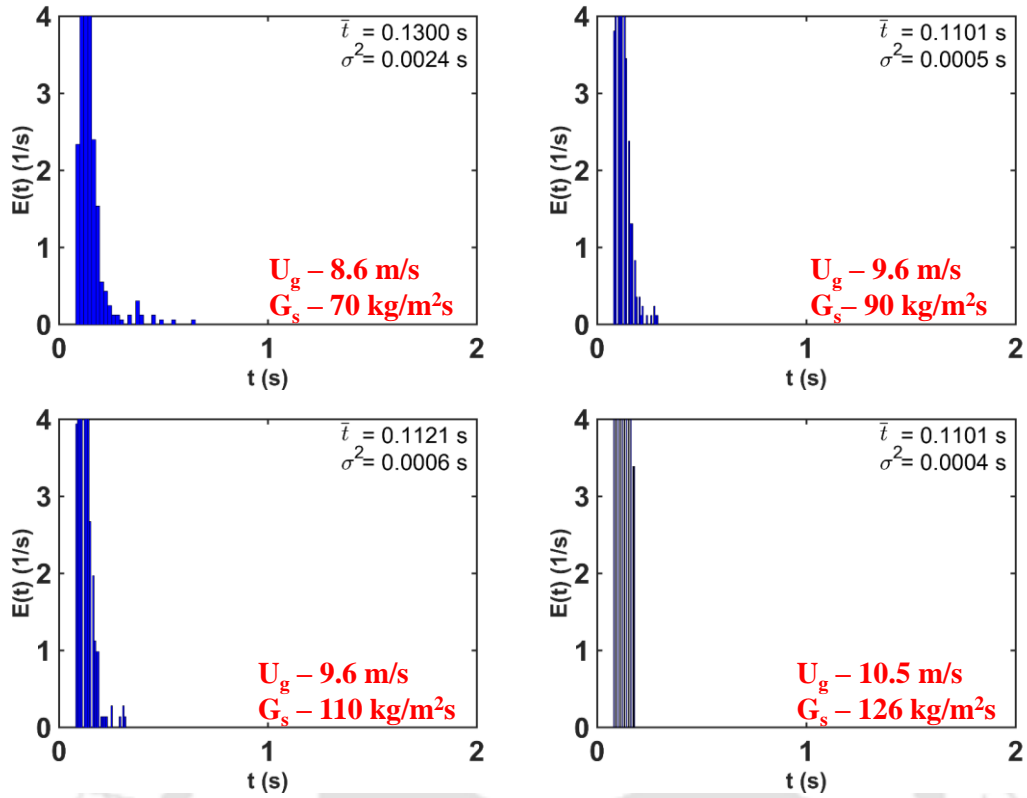


Figure 4.22 Residence time distribution for the section 3 (middle / RPT)

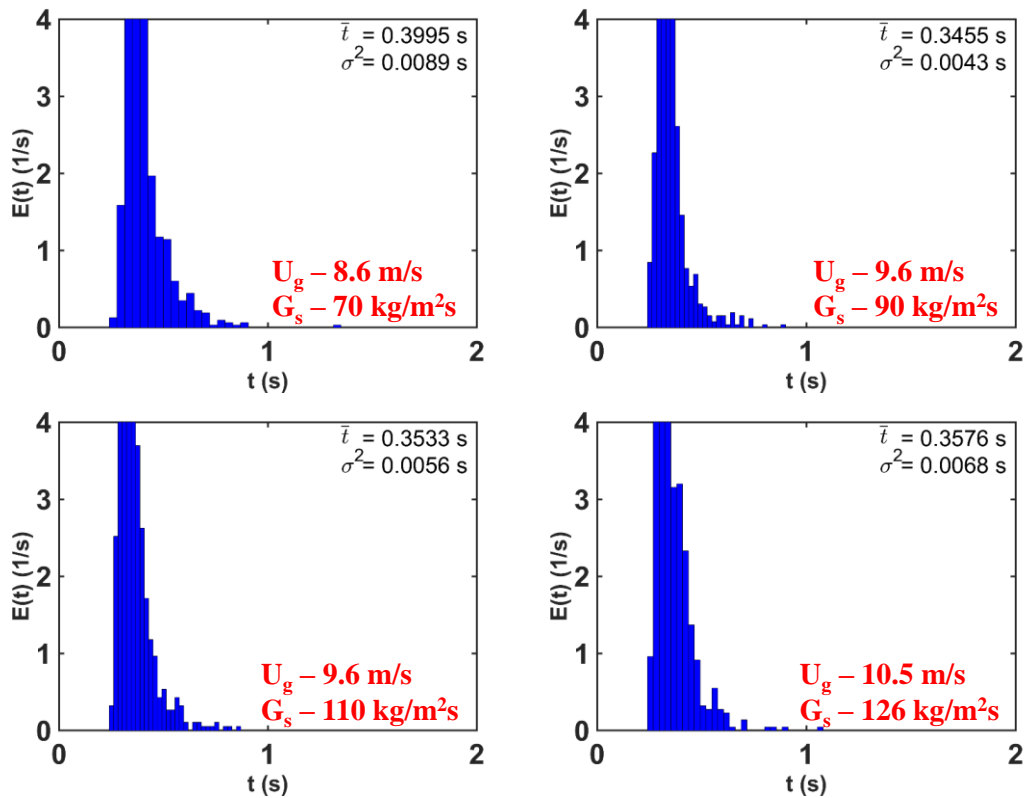


Figure 4.23 Residence time distribution for the section 4 (Top)

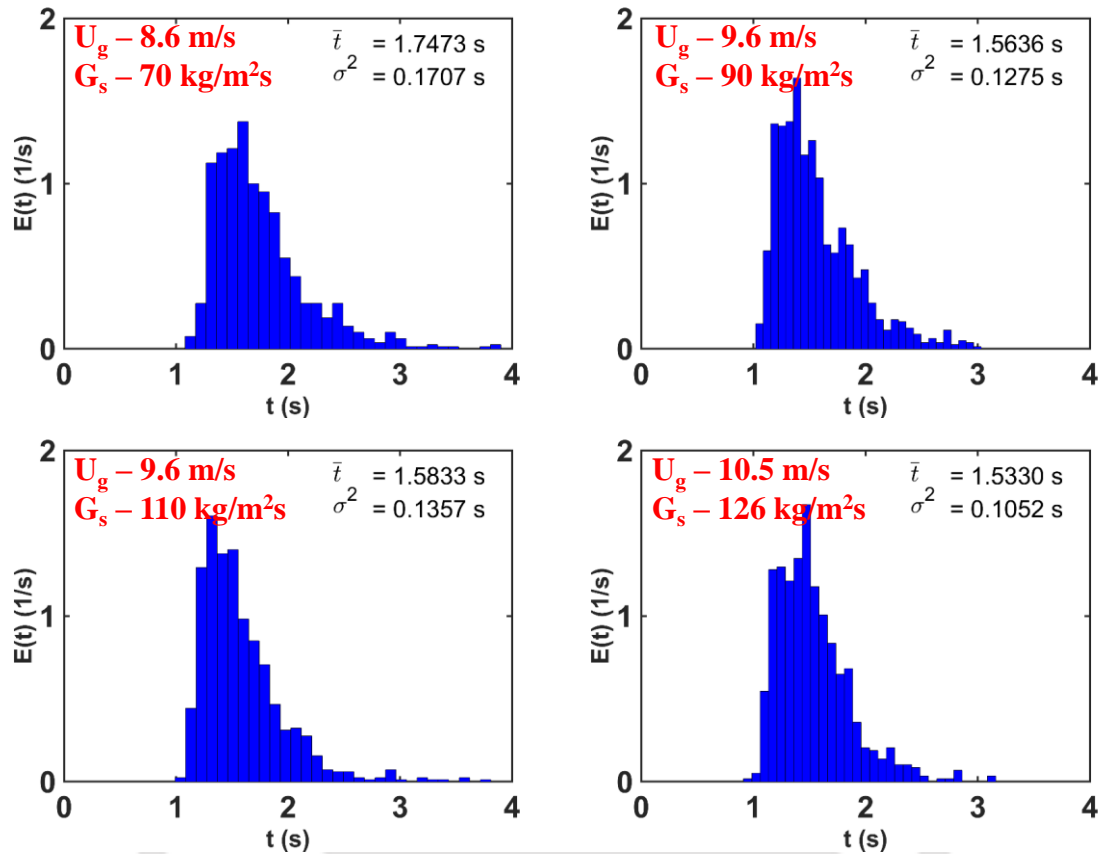
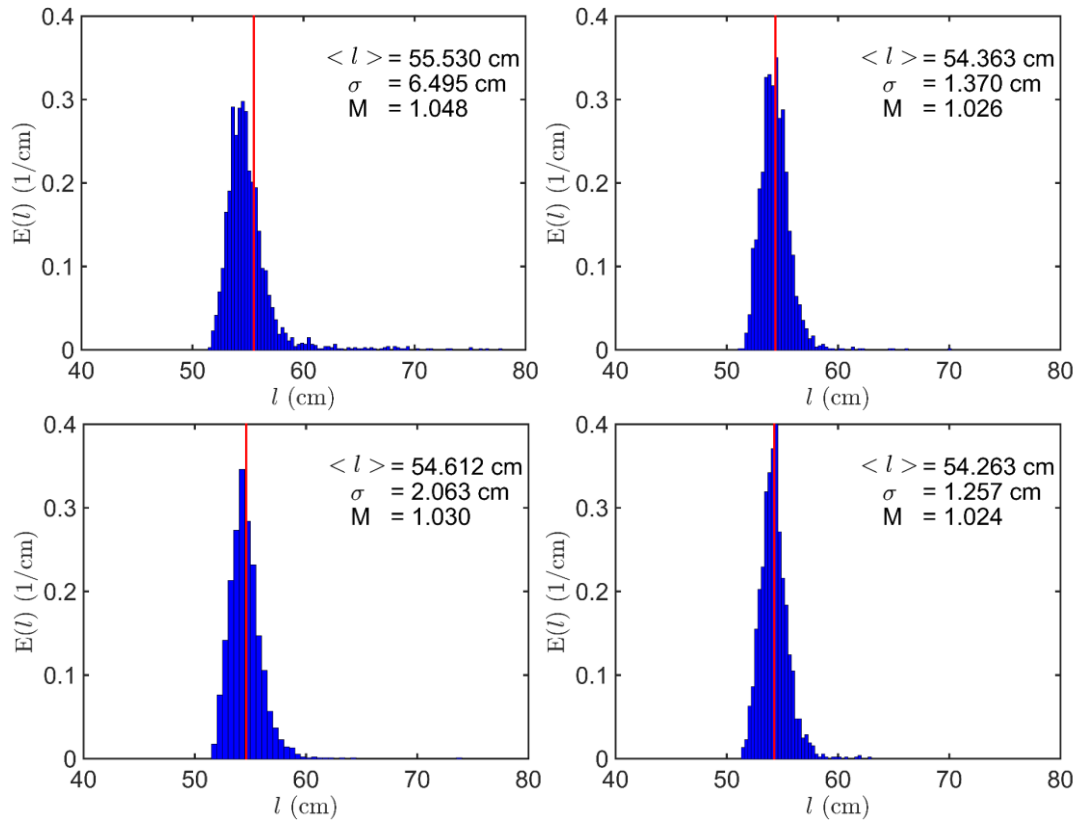


Figure 4.24 Residence time distribution for the overall column

#### 4.6.2 Trajectory length distribution (TLD)

Trajectory length distribution gives distribution of the distance travelled by solids in the system. Formally, trajectory length distribution  $f(l)$  can be defined as the fraction,  $f(l)dl$ , of element that followed the trajectories between the length of  $l$  and  $l + dl$ . Thus, quantifying mixing in terms of length of solids travelled. Distance travelled by each trajectory can be computed from the position vectors. Ratio of the mean of distribution to the distance between boundaries gives macro mixing index (M). For plug flow system, macro mixing index is 1, higher the macro mixing value higher the mixing. Figure 4.25 shows the TLD for all the conditions in the RPT section.



**Figure 4.25 Trajectory time distribution for the RPT region for the length of  $L = 53$  cm**

Macromixing index shows that flow in all the conditions close to the plug flow. Red line in the Figure 4.25 shows the mean of distribution. With increase in the solid flux, at the same superficial gas velocity, mixing increases evident from the macro mixing index and variance of the trajectory length. For the case of  $U_g = 8.6$  m/s and  $G_s = 70$  kg/m<sup>2</sup>s, long tail is observed, signifying internal circulations might be due to metastable structures. Further comparatively high variance is also observed, thus mixing is high than all the other operating conditions. For the case of  $U_g = 10.5$  m/s and  $G_s = 126$  kg/m<sup>2</sup>s, macromixing is close to  $U_g = 9.6$  m/s and  $G_s = 110$  kg/m<sup>2</sup>s, similar to the axial RMS velocities.

### 4.6.3 Local solids mixing

Diffusivity is computed as given in section 3.5. Figure 4.26 shows axial solid diffusivity for all the operating conditions. Axial solid diffusivity increases towards the wall for the

all the operating conditions. However, for the case of  $U_g = 8.6$  m/s and  $G_s = 70$  kg/m<sup>2</sup>s diffusivity values are twice of the other conditions. Magnitude of solid diffusivity is similar to the laboratory scale experiments. However, they are one order of magnitude less than the dispersion number. That is, global mixing is one order higher than the local mixing.

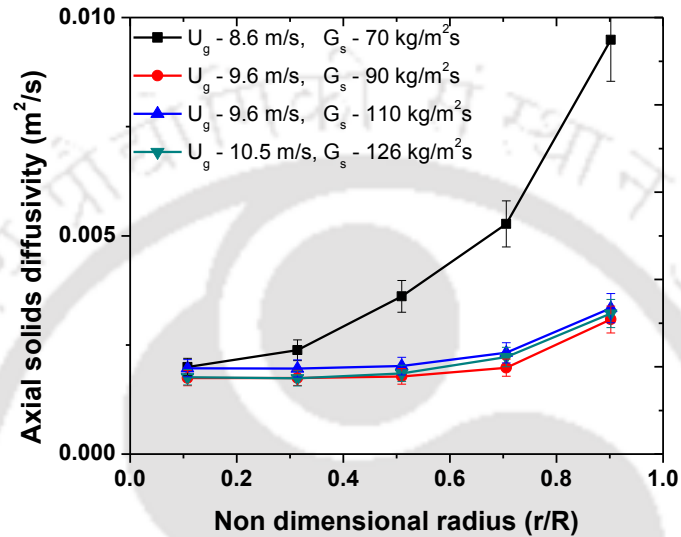


**Figure 4.26 Axially and azimuthally averaged axial solids diffusivity**

## 4.7 Summary

The results of this chapter are summarized in three aspects, viz, solid velocity field studies, scale studies and solid mixing studies.

### *Solid velocity field*

Solid velocity field studies using radioactive particle tracking shows that

1. Axial motion is predominant and very fine fluctuations are observed in the radial and azimuthal directions evident from the Lagrangian position maps.
2. Sometimes accelerating and sometimes decelerating motion of solids are observed.
3. Axisymmetric flow is confirmed from the velocity vector plots and there is no negative motion in the time averaged sense.

4. Spread of instantaneous velocity increases towards the wall and increases with increases in the solid flux along the riser.
5. Negative velocities are observed in the distribution of instantaneous velocity signifying the presence of clusters. However the occurrences of negative velocities differ with the operating conditions and increases towards the wall.
6. Number of occurrences profile signifies the solid distribution and shows the solid fraction increases towards the wall from the centre.
7. Mean solids velocities are flat for most of the observed conditions and high gradient near the wall is observed. However, in the case of  $U_g = 8.6$  m/s and  $G_s = 110$  kg/m<sup>2</sup>s parabolic profile is observed. Radial and azimuthal mean velocities are negligible.
8. Axial RMS velocities are high near the wall and low in the center and increases with the solid flux at the same gas velocity conditions. Radial RMS velocities are one order magnitude less than the axial RMS velocities. Further axial RMS velocities are also one order magnitude less than the mean solid velocities, signifies the fluctuations are lower compared with the kinetic normal stresses.
9. Turbulent kinetic energy follows the similar trend as the axial RMS velocities as other normal stresses are negligible.

### ***Scale up***

1. Higher mean axial velocities are observed with increase in the scale for the same operating conditions. Further, axial RMS velocities are increased by twice with increase in the scale.
2. Hydrodynamic similarity law of Qi et al. (2008) fails to give similar conditions in the laboratory scale as well as pilot scale setups evident from the different axial RMS (fluctuations) profiles.

- Empirical equation developed for prediction of velocity predicts within 30% for Geldart group B particles.

### ***Solid mixing***

- Residence time distribution studies in section wise shows the dominance of bottom section in mixing for all the conditions evident from the high dispersion number. Solid mixing increases with increase in the solid flux at the same superficial gas velocity.
- Macromixing index from trajectory length distribution shows that flow is approaching plug flow conditions at the middle region (RPT section).
- Solids diffusivity are one order magnitude less than the global mixing values and steep increase of solid diffusivity values near the wall is observed.

Overall, solid flow pattern is similar to the laboratory scale setup for the investigated conditions. With increase in the scale, significant increase in the fluctuations is observed.

### **Notations**

|             |                          |                       |
|-------------|--------------------------|-----------------------|
| $D$         | Diameter                 | [m]                   |
| $Fr_D$      | Froude number            | [-]                   |
| $G_s$       | Solid mass flux          | [kg/m <sup>2</sup> s] |
| $h$         | Height                   | [m]                   |
| $M$         | Macro mixing index       | [-]                   |
| $\dot{m}_p$ | Mass flow rate of solids | [kg/s]                |

|             |  |        |
|-------------|--|--------|
| $\dot{m}_g$ | Mass flow rate of gas                      | [kg/s] |
| $U_g$       | Superficial gas velocity                   | [m/s]  |
| $U_t$       | Terminal settling velocity                 | [m/s]  |
| $V_p$       | Cross sectional averaged particle velocity | [m/s]  |

#### Greek letters

|               |               |                      |
|---------------|---------------|----------------------|
| $\varepsilon$ | Void fraction | [-]                  |
| $\phi$        | Slip factor   | [-]                  |
| $\rho$        | Density       | [kg/m <sup>3</sup> ] |

#### Reference

- Anderson, T.B., Jackson, R., 1967. Fluid mechanical description of fluidized beds. Equations of motion. *Ind. Eng. Chem. Fundam.* 6(4), 527–539.
- Arena, U., Cammarota, A., Massimilla, L., Pirozzi, D., 1988. The hydrodynamic behaviour of two circulating fluidized bed units of different sizes. *Proceedings of the 2nd International Conference on Circulating Fluidized Bed*, 223—230.
- Bai, D., Jin, Y., Yu, Z., Zhu, J., 1992. The axial distribution of the cross-sectionally averaged voidage in fast fluidized beds. *Powder Technol.* 71(1), 51–58.
- Bai, D., Issangya, A.S, Grace, J.R., 1999. Characteristics of Gas-Fluidized Beds in Different Flow Regimes. *Ind. Eng. Chem. Res.* 38, 803–811.
- Berruti, F., Chaouki, J., Wdfroy, L., Pugsley, T.S., Patience, G.S., 1995. Hydrodynamics of Circulating Fluidized Bed Risers : A Review. *Can. J. Chem. Eng.* 73, 579–602.

- Bhusarapu, S., 2005. Solid Flow Mapping in Gas-Solid Risers (D.Sc. Thesis). Washington University, USA.
- Bhusarapu, S., Al-dahhan, M.H., Dudukovic, M.P., Trujillo, S., Hern, T.J.O., 2005. Experimental Study of the Solids Velocity Field in Gas - Solid Risers. *Ind. Eng. Chem. Res.* 44, 9739–9749.
- Bhusarapu, S., Al-Dahhan, M.H., Duduković, M.P., 2006. Solids flow mapping in a gas–solid riser: Mean holdup and velocity fields. *Powder Technol.* 163, 98–123.
- Brereton, C., Stromberg, L., 1985. Some aspects of the fluid dynamic behavior of fast fluidized beds. In *Circulating Fluidized Bed Technology I* ( Basu, P., Ed.), Pergamon Press. Oxford, U.K.
- Caloz, Y. Ph., 2001. Experimental Investigation of Local Solids Fluid Dynamics in Different Industrial Scale Circulating Fluidized Beds with Optical Probes. (PhD thesis). ETH Zürich,
- Chang, H., Louge, M., 1992. Fluid dynamic similarity of circulating fluidized beds. *Powder Technol.* 70, 259–270.
- Dudukovic, M.P., 2010. Reaction engineering: Status and future challenges. *Chem. Eng. Sci.* 65, 3–11.
- Gidaspow, D., Huilin, L., 1996. Collisional viscosity of FCC particles in a CFB. *AIChE J.* 42–49, 2503–2510.
- Glicksman L.R., 1984. Scaling relationships for fluidized beds, *Chem. Eng. Sci.* 39 (9), 1373–1379.
- Glicksman, R. L., Hyre. M., Farrell, P. A., 1994. Dynamic similarity in fluidization. *Int. J. Multiphase Flow* 20, 331-386.

- Glicksman, L.R., Hyre, M., Woloshun, K., 1993. Simplified scaling relationships for fluidized beds. *Powder Technol.* 77, 177–199.
- Godfroy, L., Larachi, F., Chaouki, J., 1999. Position and Velocity of a Large Particle in a Gas-Solid Riser using the Radioactive Particle Tracking Technique. *Can. J. Chem. Eng.* 77, 253–271.
- He, Y., Deen, N.G., 2009. Gas-solid turbulent flow in a circulating fluidized bed riser: numerical study of binary particle systems. *Ind. Eng. Chem. Res.* 48, 8098–8108.
- Horio, M., Nonaka, A., Sawa, Y., Muchi, I., 1986. A new similarity rule for fluidized bed scale-up. *AIChE J.* 32, 1466–1482.
- Horio, M., Hiroyuki, I., Kobukai, Y., Yamanishi, N., 1989. A scaling law for circulating fluidized beds. *J. Chem. Eng. Jpn.* 22, 587–592.
- Horio, M., Kuroki, H., Ogasawara, M., 1993. The flow structure of a three-dimensional circulating fluidized bed observed by the laser sheet technique. 4th Int. Conf. on CFB, Hidden Valley, PA, Aug 1-5, 86.
- Jiang, B., Dou, B., Song, Y., Zhang, C., Du, B., Chen, H., Wang, C., 2015. Hydrogen production from chemical looping steam reforming of glycerol by Ni-based oxygen carrier in a fixed-bed reactor. *Chem. Eng. J.* 280, 459–467.
- Kehlenbeck, R., Yates, J., Di Felice, R., Hofbauer, H., Rauch, R., 2001. Novel Scaling Parameter for Circulating Fluidized Beds. *AIChE J.* 47, 582–589.
- Mathisen, A., Halvorsen, B., Melaaen, M.C., 2008. Experimental studies of dilute vertical pneumatic transport. *Part. Sci. Technol.* 26, 235–246.

- Matsen, J.M., 1997. Design and scale-up of CFB catalytic reactors. In *Circulating Fluidized Beds*. ( eds Grace. J. R., Avidan, A. A., Knowlton, T. M.), Chapman & Hall, London, chap 14, 489–503.
- Nauman, E.B., 1981. Residence time distributions in systems governed by the dispersion equation. *Chem. Eng. Sci.* 36, 957–966.
- Noymer, P.D., Hyre, M.R., Glicksman, L.R., 2000. The effect of bed diameter on near-wall hydrodynamics in scale-model circulating fluidized beds. *Int. J. Heat Mass Transfer* 43, 3641–3649.
- Pantzali, M.N., Lozano Bayón, N., Heynderickx, G.J., Marin, G.B., 2013. Three-component solids velocity measurements in the middle section of a riser. *Chem. Eng. Sci.* 101, 412–423.
- Patience, G.S., Berruti, F., Chaouki, J., 1992. Scaling considerations for circulating fluidized bed risers. *Powder Technol.* 72, 31–37.
- Powell, M. J. D., 1964. An efficient method for finding the minimum of a function of several variables without calculating derivatives. *Comput. J.* 7(2), 155–162.
- Qi, X., Zhu, J., Huang, W., 2008. Hydrodynamic similarity in circulating fluidized bed risers 63, *Chem Eng Sci.*, 63, 5613–5625.
- Reh, L., 2003. Development potentials and research needs in circulating fluidized bed combustion. *China Particuology* 1, 185–200.
- Rhodes, M., Hideaki Mineo, H., Hiramata, T., 1992. Particle motion at the wall of a circulating fluidized bed. *Powder Technol.* 70 207–214.
- Tartan, M., Gidaspow, D., 2004. Measurement of Granular Temperature and Stresses in Risers. *AIChE J.* 50, 1760–1775.

- Van der Meer, E.H., Thorpe, R.B., Davidson, J.F., 1999. Dimensionless groups for practicable similarity of circulating fluidised beds. *Chem. Eng. Sci.* 54, 5369–5376.
- Wang, C., Zhu, J., Barghi, S., Li, C., 2014. Measurement of Granular Temperature and Stresses in Risers. *Chem. Eng. Sci.* 108, 233–243.
- Wang, C., Zhu, J., Li, C., Barghi, S., 2014. Detailed measurements of particle velocity and solids flux in a high density circulating fluidized bed riser. *Chem. Eng. Sci.* 114, 9-20.
- Westphalen, O., Glicksman, L. R., 1993. Experimental verification of scaling for a commercial - size CFB combustor. *Proc. 4th Int. Conf. on CFB*, Hidden Valley, Pa, 1-5 Aug.
- Xu, G., Nomura, K., Nakagawa, N., Kato, K., 2000. Hydrodynamic dependence on riser diameter for different particles in circulating fluidized beds. *Powder Technol.* 113, 80–87.
- Yan, A., Zhu, J.J., 2004. Scale-Up Effect of Riser Reactors (1): Axial and Radial Solids Concentration Distribution and Flow Development. *Ind. Eng. Chem. Res.* 43(18), 5810–5819.
- Yan, A., Ball, J.S., Zhu, J.X., 2005. Scale-up Effect of Riser Reactors (3) - Axial and Radial Solids Flux Distribution and Flow Development. *Chem. Eng. J.* 109(1-3), 97-106.
- Yan, A., Zhu, J., 2005. Scale-up effect of riser reactors: Particle velocity and flow development. *AIChE J.* 51, 2956–2964.
- Zhang, W., Tung, Y., Johnsson F., 1991. Radial voidage profiles in fast fluidized beds of different diameters. *Chem. Eng. Sci.* 46, 3045-3052.

## Chapter 5

### Numerical Investigation of Circulating Fluidized Bed

#### Scope

In this chapter, numerical investigation of circulating fluidized bed is carried out. Euler – Euler simulation is introduced wherein state of an art on numerical simulation of gas solid CFB using Euler – Euler model is discussed. Grid independence and model development studies are discussed. Simulation studies on effect of gas velocity, flux and scale are presented.

#### 5.1 Introduction

Scaling laws for fluidized beds are not universal and there is high level of uncertainty associated with the scaling laws (Knowlton et al., 2005; Dudukovic, 2010). Hence, a more fundamental approach is preferred. Computational fluid dynamics (CFD) is one such numerical technique that empowers scientists and engineers to have better insights into the flow, sometimes which is not achievable through the experiments. CFD is also an effective and least expensive approach for design, scale-up and trouble-shooting. In CFD, conservation laws of mass, momentum and energy from first principles are rigorously solved to yield results at high spatial and temporal resolution.

CFD is the preferred approach for process development in the risers (Dudukovic et al., 1999). As discussed in previous chapters, gas-solids risers are complex systems in which phenomena occur at different length and time scales. This large separation of scales, both in length and time, presents the prime challenge for modeling risers (van der Hoef et al., 2005). As explained in chapter 3, even in the dilute flows, metastable structures are present

with non-uniform shape and size. These large structures can be of the order of meters which are influenced by particle – particle interactions that take place in millimeter scale.

Euler – Euler and Euler – Lagrangian approach are the two widely used modeling approaches in gas – solid riser. In Euler – Lagrangian approach, continuous phase is solved by using continuum (mostly Navier-Stokes) equation and time history of each particle (discrete phase) is tracked by solving Newton's second law of motion (Tsuji et al., 1987; Deen et al., 2007). Particle – particle interactions are well represented in this approach (Deen et al., 2007). Euler – Lagrangian approach is widely used for meso-scale, micro-scale simulations, where identities of solid particles are preserved. Euler – Euler approach is used for macro scale simulation, where both the phases are considered as interpenetrating continua. Continuum equations (Continuity and Momentum equations) are solved for both the phases individually. The interactions between the phases are modeled by using drag. It is clear that, Euler – Lagrangian approach is an approach closer to the reality, as solid and fluid phases are correctly represented in the model. However, due to the practical limitations of computer resources, meso-scale and micro-scale simulations are difficult to achieve in engineering scales. For example, pilot scale used in the work, has 60 million solid particles. Tracking these many particles needs huge computational resource and impossible at industrial scale with the computational power available today. However, Euler – Euler simulations can simulate industrial scales without much difficulty with the current computational resource. Further, Euler – Euler approach can give reasonable engineering scale details for design and scale-up. Therefore, in this work, Euler – Euler approach is used for modeling the riser.

Euler – Euler approach has been used for modeling the riser for more than three decades. However, depending upon the model complexity various closures are required to solve the equations. The selection of suitable closures (mostly empirically developed) and tuning the

parameters of the closures pose the major challenge in modeling of gas-solid riser. Further, the closure selection is not universal and may change with change in solid properties, operating conditions and regimes in the riser (Vaishali, 2009). Further, most of the models developed in literature are not validated to the fluctuations level. For higher accuracy it is crucial in multiphase flow that CFD simulations should be validated to the fluctuations level (Kuipers and van Swaaij, 1997). In this work, Euler – Euler approach is used for developing model for simulating the riser used in the laboratory scale setup. Further, effect of operating conditions and scale is studied. Finally developed model is validated with mean and fluctuation velocities of the solids from RPT experiments.

## **5.2 Literature on Euler – Euler modeling of gas solid riser**

Arastoopour and Gidaspow (1979) are among the first researchers who applied two fluid (Euler - Euler) model for riser simulation, they formulated one dimensional steady state model equations. Further, the works of Wallis (1969), Leung (1980) has shown importance of solid phase rheology in two fluid model for gas – solid fluidization. Sinclair and Jackson (1989) adopted kinetic theory of granular flow for a steady two-dimensional model of the gas-solids riser. Lateral segregation of the solid phase is predicted successfully using this model. Kinetic theory of granular flow (KTGF) became popular after the works of Ding and Gidaspow (1990), and Gidaspow (1994). This theory is based on kinetic theory of non-uniform gases developed by Chapman and Cowling (1990).

Core annular flow in dense (10% volume fraction) and dilute (1% volume fraction) column are reported by Tsuo and Gidaspow (1990) using a two-dimensional unsteady state model where empirical equation for solid viscosity is used. They claimed that transient integration does not converge towards a steady state value; this is an evidence for flow never reaches a steady state. Pita and Sundaresan (1993) studied the effect of inlet configuration in

vertical riser using 2D model and reported that the inlet configurations greatly effects internal recirculation and radial segregation. Nieuwland et al. (1996) obtained better predictions of experimental data by modeling gas phase turbulence using mixing length model. Neri and Gidaspow (2000) compared granular temperature, solid viscosity and pressure with experimentally measured values. Benyahia et al. (2000) simulated high solid flux of  $489 \text{ kg/m}^2\text{s}$  in 2D column using KTGF and Arastoopour drag model and were able to predict qualitatively the solid fraction, solid flux and granular temperature.

Instabilities in the gas solid fluidized bed is mainly because of the particle – particle, wall – particle, gas – particle interactions, reported by various researchers (Sundaresan, 2003; Li, 2003). Due to these interactions, meso-scale meta-stable structures (clusters) are formed, size of which varies from particle diameter to diameter of the column. Agarwal et al. (2001) studied the effect of meso-scale structures. These meso-scale structures affect the solid viscosity, stress and drag force, must be accounted by suitable subgrid model. Yang et al. (2003) used structure dependent drag coefficient using Energy Minimization Multi Scale (EMMS) model to simulate the riser. They concluded that drag model based on EMMS is a very promising approach by comparing the conventional drag coefficients and EMMS based drag coefficients.

Most critical issue in Euler – Euler modeling is the development of the best suited closures (Nieuwland et al., 1994; Yang et al., 2004). Andrew et al. (2005) reported that a sufficiently fine grid (10 dp) is enough to resolve the mesoscale structures in Euler – Euler modeling of risers. Therefore with these major developments in the Euler – Euler modeling, a brief review is discussed hereafter for modeling in risers using Geldart's B particles.

Adamczyk et al. (2014) reported that comparable results are obtained from Dense Discrete Phase Model (DDPM) and Euler – Euler simulations. Further, they have reported that large

deviations are at the bottom section only. Panday et al. (2014) discussed the Euler – Euler (EE) and Euler – Lagrangian (EL) models. Both the models are able to give reasonable prediction with the experimental values of pressure and solid velocity. However, EE strongly depends on the resolution of the grid. Further, most of the models predict asymmetric solid flux profiles.

Wang et al. (2009) developed new drag model based on Energy Minimization Multi-Scale Model (EMMS) and reported that the solid volume fraction matches with the experimental values. Hartge et al. (2009) compared Syamlal O'Brien (1989), Gidaspow (1994) and EMMS drag model and reported that EMMS drag model is able to predict the bottom bed density. Lu et al. (2011) reported that difference between Gidaspow (1994) drag model and EMMS decreases when the Archimedes number of particle increases, since the slip velocity approaches the homogenous limit.

Gao et al. (2012) used steady state model for simulating CFB. They reported that influence of wall restitution and specular coefficient on the predictions is weak, while solid restitution has considerable influence. Further, gas – solid fluctuating velocity correlation dominates influence on the granular temperature. Li and Benyahia (2013) compared model for variable specular coefficient and constant specular coefficient. They concluded that constant specular coefficient can give reasonable predictions. Further, they reported that specular coefficient varies with the operating conditions.

**Table 5.1 Literature on Euler – Euler simulations using Geldart’s B particle**

| Author                        | Operating conditions  |  | Solids properties |                               | Validation |              |
|-------------------------------|-----------------------|--|-------------------|-------------------------------|------------|--------------|
|                               | $U_g$ (m/s)           | $G_s$ (kg/m <sup>2</sup> s)            | $d_p$ ( $\mu$ m)  | $\rho_p$ (kg/m <sup>3</sup> ) | Mean       | Fluctuations |
| Huilin and Gidaspow (2003)    | 0.8, 1.0              | NA<br>(fixed inventory of solids used) | 120, 185          | 2400                          | Yes        | Yes          |
| Ibsen et al. (2004)           | 1.0                   | NA                                     | 164               | 2400                          | Yes        |              |
| Tartan and Gidaspow (2004)    | 4.9, 5.1, 5.6, 6      | 14.2, 21.4, 28.7, 43.9                 | 530               | 2460                          |            | Yes          |
| Vaishali et al. (2007)        | 3.2                   | 26.6                                   | 150               | 2550                          | Yes        | Yes          |
| Wang et al. (2008)            | 1.1, 1.1              | 4.2, 8.3                               | 100               | 2650                          | yes        |              |
| Hartge et al. (2009)          | 3, 4                  | 7.8, 20                                | 190               | 2600                          | Yes        |              |
| Wang et al. (2009)            | 15.5                  | 140                                    | 330               | 2630                          | Yes        |              |
| Zhang (2010)                  | 6.32                  | NA                                     | 20                | 2000                          | Yes        |              |
| Lu et al. (2011)              | 1.17, 7.76            | 14.3, 151.6                            | 300               | 2500                          | Yes        |              |
| Shah et al. (2011)            | 4.5                   | 32.6, 35.7                             | 150               | 2550                          | Yes        |              |
| Wang et al. (2011)            | 11.7                  | 327                                    | 463               | 2630                          | Yes        |              |
| Gao et al. (2012)             | 4.9                   | 14.2                                   | 530               | 2460                          | Yes        |              |
| Li et al. (2012)              | 5.71, 7.58,           | 96, 190                                | 802               | 863                           | Yes        |              |
| Li and Benayahia (2013)       | 7.76                  | 50, 400                                | 300               | 2500                          | Yes        |              |
| Chalermsinsuwan et al. (2014) | 0.75, 1.25, 5         | 300                                    | 380               | 2650                          | Yes        |              |
| Li et al. (2014a)             | 0.6 scm               | 14                                     | 802               | 863                           | Yes        |              |
| Li et al. (2014b)             | 7.58                  | 193                                    | 213               | 2640                          | Yes        |              |
| Dai et al. (2015)             | 7.5                   | 151                                    | 300               | 2500                          |            |              |
| Liu et al. (2015)             | 1.52, 2.1, 4.28, 4.78 | 14.3, 24.1, 13.0, 22.0                 | 180               | 1420                          | Yes        |              |
| Upadhyay and Park (2015)      | 2                     | 39, 51, 73                             | 130               | 2525                          | Yes        |              |
| Zhang et al. (2015)           | 8.6                   | 485                                    | 89                | 2951                          | Yes        |              |

Upadhyay and Park (2015) studied the influence of restitution and specularly coefficients. They reported that particle – wall restitution coefficient does not vary the predictions if the specularly is 0.0001 to 0.00001 and that the particle – particle restitution values in the range of 0.8 to 0.9 gives better results.

Huilin and Gidaspow (2003) using separate granular temperature for each solid particle developed model for binary mixture simulation in riser. They reported that for inelastic solid particles, granular temperature can be lower in the center due to the low volume fraction and increases towards the wall. Further, fluctuating velocity of solid particles are higher than the experimental values. Tartan and Gidpasow (2004) reported that granular temperature and mean velocity are quantitatively matching with the experimental data. Also, they have obtained analytical solution assuming completely elastic particles. In the numerical solution, they have used restitution coefficient of 0.99, 0.98, 0.89 for particle – particle collision and 0.6 for particle – wall collision. Vaishali et al. (2007) reported that mean velocity profiles are matched with the experiments however the profile of the granular temperature are not matched (Vaishali et al., 2007). Further, Vaishali et al. (2007) reported that different drag models, Wen and Yu (1966) and Syamlal –O'Brien (1989), predicts the granular temperature by order of magnitude difference in fast fluidization regime.

Some of the key observations from the above review and Table 5.1 are,

1. Modeling parameters and drag are not universal. According to the operating conditions, particle properties and regime, influence of modeling parameters and drag varies
2. Developed models and effect of model parameter studies must be rigorously validated with experimental data. However, most of the studies validation is not satisfactory.
3. Most of the studies reported only first orders moments. Further, very few studies reported second order moments (fluctuations) and validated with the experiments.

In this work, attempt is made to formulate Euler – Euler model and validate with the experimental results detailed in the previous chapters. Further, effect of velocity, solid flux and scale are studied using formulated model. All the validations will be done at the fluctuation level. Such a validation is rarely available in the literature. Thus, it may help to improve the existing models. This work is a similar contribution as challenge problem of NETL / PSRI, USA, where they generate data and made available for model developers to validate.

### **5.3 Euler – Euler modeling approach**

Euler-Euler (E-E) modeling of gas solid riser assumes that both gas and solid phase as interpenetrating continuum. In other words, both solid and gas phases can exist at the same position in space at the same time. Further, volume fraction at any point is summation of the volume fraction of all the phases at that point (and equal to one). Formulation of the conservation equations can be done by ensemble averaging of the conserved local instantaneous quantities of each phase and discussed extensively by Anderson and Jackson (1967), Drew (1983). Here attempt is not made to present the derivation of Euler – Euler model rather formulation is discussed in terms of gas – solid riser application.

For each phase, mass and momentum conservation equations are solved. Both the phases are considered as incompressible. Interaction between the two phases is accounted by the momentum exchange coefficient (drag). Kinetic theory of granular flow (KTGF) is used to account for the solid phase fluctuations. Solid pressure and viscosity are related with the solid fluctuations. The above formulation is discussed in detail below. ANSYS® Fluent 15.0 commercial solver is used in this work.

### 5.3.1 Conservation equations

Governing conservation equations are

Continuity equation:

$$\frac{\partial}{\partial t}(\varepsilon_k \rho_k) + \Delta \cdot (\varepsilon_k \rho_k \vec{u}) = 0 \quad (5.1)$$

where,  $k = f, s$ . Equation 5.1, is solved for both fluid,  $f$  and solid phase,  $s$

Momentum equation:

*Gas phase*

$$\begin{aligned} \frac{\partial}{\partial t}(\varepsilon_f \rho_f \vec{u}_f) + \nabla \cdot (\varepsilon_f \rho_f \vec{u}_f \vec{u}_f) = \\ -\varepsilon_f \nabla p + \nabla \cdot \bar{\tau}_f + \varepsilon_f \rho_f \vec{g} + K_{sf}(\vec{u}_s - \vec{u}_f) + \vec{F}_f \end{aligned} \quad (5.2)$$

*Solid phase*

$$\frac{\partial}{\partial t}(\varepsilon_s \rho_s \vec{u}_s) + \nabla \cdot (\varepsilon_s \rho_s \vec{u}_s \vec{u}_s) = -\varepsilon_s \nabla p - \nabla p_s + \nabla \cdot \bar{\tau}_s + \varepsilon_s \rho_s \vec{g} + K_{sf}(\vec{u}_f - \vec{u}_s) + \vec{F}_s \quad (5.3)$$

$$\varepsilon_s + \varepsilon_f = 1 \quad (5.4)$$

Equation 5.1 gives continuity equation, where the first and second term on the left side represents the temporal and spatial gradients respectively. Since there is no mass generation or consumption due to the reaction and also, there is no mass exchange between the phases in this work, right term is zero.

Equation 5.2 and 5.3 are the momentum conservation equations for the gas and solid phase respectively. The left side of the equation 5.2 and 5.3 represents the local and convection acceleration. Right hand terms are source and sink terms. Hydrodynamic pressure is shared by both the phases. In other words, flow of both the phases contributes to the hydrodynamic pressure. In the case of solid phase one more pressure term, represents the solid pressure,

is added which is mainly due to the collision between the solids. Normal stress contribute to the solid pressure, while shear stresses due to the collision contribute solid shear stress term,  $\nabla \cdot \bar{\tau}_s$ . Viscous forces of the gas phase is represented by the shear stress,  $\nabla \cdot \bar{\tau}_f$ .

The terms  $\varepsilon_s \rho_s \vec{g}$  and  $\varepsilon_f \rho_f \vec{g}$  represents the body forces of solid phase and fluid phase respectively. Interphase momentum exchange terms ( $K_{sf}(\vec{u}_s - \vec{u}_f)$  and  $K_{sf}(\vec{u}_f - \vec{u}_s)$ ) represents the momentum exchange between the two phases. Momentum exchange terms in the two equations are equal but opposite in sign. Further  $K_{sf}$  is a momentum exchange coefficient and it is a function of slip velocity and volume fraction. Other external forces like magnetic, electrical forces are represented with  $\vec{F}_s$  and  $\vec{F}_f$ , in this work those terms are accounted as zero.

For solving the conservation equations 5.1 – 5.3 requires additional constraint since the number of unknowns exceeds the number of available equations. For two dimensional solution, available equations are 7 and number of unknowns are 15. Further, fundamental approach should represent all the interactions in the systems to obtain the convincing and acceptable solution. In the gas – solid riser, this requires the representation of the interactions of mean and fluctuation within and between the phases as follows,

1. Drag force: Interactions between the mean velocities of the gas and solid phases
2. Flux of kinetic energy: Interactions between the fluctuating motion of the gas and fluctuating motion of solids
3. Solid phase pressure and viscosity (KTGF): Interactions between the mean and fluctuating motion of solids
4. Turbulence: Interactions between the mean and fluctuating motion of gas

Mathematical formulation of the above interactions are explained below and used as closure equations in the momentum conservation equation 5.2 and 5.3. Interactions between the fluctuating motions are expected to be lower order than the other interactions, so they are not accounted in this work (Sinclair and Jackson, 1989).

### 5.3.2 Solid phase fluctuations

Solid phase interactions are quantified by kinetic theory of granular flow (KTGF) (Chapman and Cowling, 1990; Ding and Gidaspow, 1990). KTGF considers that the solid phase stresses are due to micro-scale mechanism of momentum transfer between the particles. The random motion of particle generates an effective pressure in the particle phase, together with an effective viscosity that resists shearing of the particle assembly. Motion of the particles resembles thermal motion of the molecules in a gas. Thus kinetic energy of fluctuating motion of the particles is characterized by granular temperature. Effective solid pressure and solid viscosity is expressed as a function of the granular temperature. Similar to the momentum equation, transport equation of granular temperature,  $\Theta_s$  can be expressed as,

$$\frac{3}{2} \left[ \frac{\partial}{\partial t} (\varepsilon_s \rho_s \Theta_s) + \nabla \cdot (\varepsilon_s \rho_s \vec{u}_s \Theta_s) \right] = \left( -p_s \bar{I} + \bar{\tau}_s \right) : \nabla \vec{u}_s + \nabla \cdot (k_{\Theta_s} \nabla \Theta_s) - \gamma_{\Theta_s} + \phi_{fs} \quad (5.5)$$

The first term in the right side accounts for generation of energy by solid stress tensor, second term for diffusion of energy, third term for collisional dissipation of energy and final term for interphase energy exchange. Each term on the right side solid pressure, solid viscosity, bulk viscosity has to be closed in terms of granular temperature.

Following, Ding and Gidaspow (1990), solids pressure,  $p_s$  is expressed as follows,

$$p_s = \rho_p \varepsilon_s \Theta_s + 2(1 + e_{ss}) \rho_s \Theta_s g_o \varepsilon_s^2 \quad (5.6)$$

The first term on the right side is a kinetic part and the second term represents the additional pressure due to the collisions. The first term will present even there is no collisions and it is linearly proportional to the volume fraction and the second term is proportional to the square of the volume fraction. The coefficient of restitution of particle – particle collision,  $e_{ss}$ , represents the reduction of pressure according to the nature of the collision. If the collision is inelastic,  $e_{ss} = 0$ , and if it is elastic,  $e_{ss} = 1$ . The radial distribution function,  $g_o$ , accounts for the steep increases of collision probability at high volume fraction (like clusters). Radial distribution bounded by the upper limit at packed bed conditions and lower limit at dilute conditions. Following Ding and Gidaspow (1990), radial distribution function,  $g_o$ , used in this work is,

$$g_o = \frac{1}{1 - \left( \frac{\varepsilon_s}{\varepsilon_{\max}} \right)^{\frac{1}{3}}} \quad (5.7)$$

### Solid shear stresses

The solid stress tensor contains bulk and shear viscosities. The shear viscosity contains the collisional and kinetic part, following Ding and Gidaspow (1990), expressed as:

$$\mu_s = \frac{4}{3} \varepsilon_s^2 \rho_s d_p g_o (1 + e_{ss}) \left( \frac{\Theta_s}{\pi} \right)^{\frac{1}{2}} + \frac{5 \rho_s d_p}{48 \varepsilon_s (1 + e_{ss}) g_o} \sqrt{\Theta_s \pi} \left[ 1 + \frac{4}{5} g_o \varepsilon_s (1 + e_{ss}) \right]^2 \quad (5.8)$$

The first term is the collision term and is a stronger function of the volume fraction. The second term represents the kinetic term. Both terms are function of the granular temperature. Resistance of the solid particles for compression and expansion is accounted by the bulk viscosity. In this work, expression of Lun et al. (1984) is used:

$$\lambda_s = \frac{4}{3} \varepsilon_s \rho_s d_s g_{0,ss} (1 + e_{ss}) \left( \frac{\Theta_s}{\pi} \right)^{1/2} \quad (5.9)$$

### Solids conductivity

The diffusive flux of the granular energy is accounted in the transport equation of the granular temperature (equation 5.5) as,

$$\vec{q} = k_s \nabla \Theta_s \quad (5.10)$$

This term is similar to the heat conduction. Fluctuation is transported to the low fluctuation region from the high fluctuation region by collision and translation. Granular conductivity or diffusion coefficient of granular energy,  $k_s$  is given by (Gidaspow et al., 1992),

$$k_s = \frac{15d_p \rho_s \varepsilon_s \sqrt{\Theta_s \pi}}{4(41 - 33\eta)} \left[ 1 + \frac{12}{5} \eta^2 (4\eta - 3) \varepsilon_s g_0 + \frac{16}{15\pi} (41 - 33\eta) \eta \varepsilon_s g_0 \right] \quad (5.11)$$

Similar to the solid viscosity, diffusion coefficient also have collision and kinetic term. At low solids holdup, kinetic term dominates and collisional terms has minor role. However, in the case of high solid holdup, both the terms plays significant role. It is to be noted that restitution coefficient has significant role in the solid viscosity and conductivity, as they require contact of solid particles.

### Dissipation of granular energy

The third term in the right hand side of the equation (5.5) accounts for the energy dissipation due to the collisions. Dissipation of granular energy term is accounted by (Lun et al., 1984),

$$\gamma_{\theta n} = \frac{12(1 - e_{ss}^2) g_{0,ss}}{d_s \sqrt{\pi}} \rho_s \alpha_s^2 \Theta_s^{\frac{3}{2}} \quad (5.12)$$

Solid holdup plays a dominant role, if the solid holdup is high, dissipation is high due to the frequency of collisions, provided the collisions are inelastic.

### Boundary conditions for granular temperature

For solving, transport equation of granular temperature (equation 5.5), initial and boundary conditions need to be specified. Inlet velocity and outlet pressure are provided. At the walls, for gas phase, no slip is specified. However solids have finite velocity at the wall. Solid velocity at the wall is calculated from the formulation of Johnson and Jackson (1987). Dissipation of fluctuating energy at the wall is equal to the sum of flux of granular temperature and the granular temperature generation at the wall (Johnson and Jackson, 1987) can be written as,

$$q_{w,\theta_s} + \frac{\pi\rho_p u_s^2 \phi \sqrt{\Theta_s}}{2\sqrt{3} \left( \frac{\varepsilon_{s,\max}}{\varepsilon_s} - \frac{\varepsilon_{s,\max}^{\frac{2}{3}}}{\varepsilon_s^{\frac{2}{3}}} \right)} - \frac{\sqrt{3}\pi\rho_p (1-e_{sw}^2) \Theta_s^{\frac{2}{3}}}{4 \left( \frac{\varepsilon_{s,\max}}{\varepsilon_s} - \frac{\varepsilon_{s,\max}^{\frac{2}{3}}}{\varepsilon_s^{\frac{2}{3}}} \right)} = 0 \quad (5.13)$$

The first term accounts for the flux of granular kinetic energy from the bulk flow, the second term represents the generation of granular kinetic term at the wall and the last term represents the dissipation of granular temperature due to the inelastic collision between the particle and wall, represented by the  $e_{sw}$ , restitution coefficient of particle – wall collision.

### 5.3.3 Drag closure

In the conservation equation (5.2) and (5.3), interaction between the two phase is accounted by the interphase momentum exchange (drag) term, with  $K_{sf}$ , being momentum exchange coefficient. Interphase momentum exchange coefficient is conventionally accounted by the empirical correlation as the numerical solution of stresses on the each particle is intractable at this stage. Most of the empirically developed correlation is a function of slip velocity and the volume fraction.

**Table 5.2 Interphase momentum exchange coefficients**

| Drag Model             | Equation   |
|------------------------|--|
| Wen & Yu (1966)        | $k_{s,f} = \frac{3 C_D \varepsilon_s \varepsilon_f  \vec{v}_s - \vec{v}_f  \varepsilon_f^{-2.65}}{4 d_p}$  |
| Syamlal-O'Brien (1989) | $K_{sf} = \frac{3 \varepsilon_s \varepsilon_g \rho_g}{4 v_{r,s}^2 d_s} C_D \left( \frac{Re_s}{v_{r,s}} \right)  \vec{v}_s - \vec{v}_g $ <p><math>v_{r,s}</math> is the terminal velocity correction for solid phase</p> $v_{r,s} = 0.5 \left( A - 0.06 Re_s + \sqrt{(0.06 Re_s)^2 + 0.12 Re_s (2B - A) + A^2} \right)$ $A = \varepsilon_g^{4.14}$ $B = 0.8 \varepsilon_g^{1.28} \quad \text{for} \quad \varepsilon_g \leq 0.85$ $B = \varepsilon_g^{2.65} \quad \text{for} \quad \varepsilon_g > 0.85$ |
| Gidaspow (1994)        | $k_{s,f} = \frac{3 C_D \varepsilon_s \varepsilon_f  \vec{v}_s - \vec{v}_f  \varepsilon_f^{-2.65}}{4 d_p} \quad \varepsilon_g > 0.8$ $k_{s,f} = 150 \frac{(1 - \varepsilon_f)^2 \mu_f}{\varepsilon_f d_p^2} + 1.75 \frac{\rho_g \varepsilon_s  \vec{v}_s - \vec{v}_f }{d_p} \quad \varepsilon_g \leq 0.8$ $C_D = \frac{24}{\varepsilon_f Re_p} \left[ 1 - 0.15 (\varepsilon_f Re_s)^{0.687} \right]$  |

---

|                              |   |
|------------------------------|---|
| Huilin &<br>Gidaspow<br>2003 | $K_{sf} = \psi \left( 150 \frac{(1 - \varepsilon_f)^2 \mu_f}{\varepsilon_f d_p^2} + 1.75 \frac{\rho_f \varepsilon_s  \vec{v}_s - \vec{v}_f }{d_p} \right) +$ $(1 - \psi) \left( \frac{3 C_D \varepsilon_s \varepsilon_f  \vec{v}_s - \vec{v}_f  \varepsilon_f^{-2.65}}{4 d_p} \right)$ $\psi = \frac{1}{2} + \frac{\arctan(262.5(\varepsilon_s - 0.2))}{\pi}$ |
|------------------------------|---|

---

Drag closures are conventionally derived from the bed expansion or pressure drop experiments (Richardson and Zaki, 1954; Wen and Yu, 1966; Ergun, 1952; Gibilaro et al., 1985). Various drag correlation were considered for this work, such as, Wen & Yu (1966), Syamlal -O'Brien (1989), Gidaspow (1994), Huilin and Gidaspow (2003). All these correlations are given in Table 5.2. As explained already, drag correlations are developed in the specific system and under specific set of flow conditions. In the gas solid riser, the conditions in which the correlation developed were rarely realized. Hence the correlations used are extrapolated for all the conditions attained in the system including clusters.

### 5.3.4 Gas phase turbulence

Closure for the second term of the momentum equation (equation 5.2) is discussed here. This closure represents the momentum transfer in the gas phase, both through the turbulent and molecular transport processes. Turbulence dominates where the Reynolds number is high. Particularly, in current work where the Reynolds number is more than 20000. It is important to account this contribution appropriately. Turbulence features energy cascading and dissipative process. Due to instabilities, kinetic energy of large scale eddies divided in to smaller eddies. This process is repeated to smaller scales until it dissipate energy at the molecular scales. Ideally all length and time scales of eddies should be accounted to solve the turbulence (e.g. Direct numerical simulation). However, this is not computationally tractable for high Reynolds number even for laboratory scale systems (Pope, 2000).

Moments (statistical) approach is the natural alternative. Time smoothing of the Euler – Euler equations, results in cross correlation (moments) terms of the form  $-\rho_f \langle u'_i u'_j \rangle$ , representing the momentum transport due to the fluctuating velocity. In equation (5.2), cross correlation terms have been lumped into the total shear stress,  $\vec{\tau}_f$  (Roy, 2000).

The total shear stress term can be expressed as,

$$\vec{\tau}_f = \mu_f^{turb} \nabla \vec{u}_f \quad (5.14)$$

where  $\vec{u}_f$  represents the ensemble averaged time smoothed velocity as in equation (5.2) and  $\mu_f^{turb}$  represents the effective turbulent viscosity.

The effective turbulent viscosity,  $\mu_f^{turb}$ , represents the diffusion of turbulent momentum and expressed in terms of the energy dissipation and turbulent kinetic energy (e.g. Tennekes and Lumley, 1972).  $\mu_f^{turb}$  scales as the square of the length scale of turbulent eddies and inversely as the time scale of turbulent kinetic energy dissipation (e.g. Tennekes and Lumley, 1972). Thus:

$$\mu_f^{turb} = \rho_f C_\mu \frac{k_{tf}^2}{\varepsilon_{tf}} \quad (5.15)$$

with length and time scales as,

$$l_f^{turb} = \sqrt{\frac{3}{2}} C_\mu \frac{k_{tf}^{\frac{3}{2}}}{\varepsilon_{tf}} \quad (5.16)$$

$$t_f^{turb} = \frac{3}{2} C_\mu \frac{k_{tf}}{\varepsilon_{tf}} \quad (5.17)$$

where  $k_{tf}$  and  $\varepsilon_{tf}$  is written as (repeated indices represent summation, following Einstein's notation),

$$k_{tf} = \frac{1}{2} \left( \langle u_i' u_i' \rangle \right) \quad (5.18)$$

$$\varepsilon_{tf} = \frac{\mu_f}{\rho_f} \left\langle \frac{\partial u_i'}{\partial x_k} \frac{\partial u_i'}{\partial x_k} \right\rangle \quad (5.19)$$

Turbulence models attempts to estimate the turbulent viscosity. The  $k - \varepsilon$  model is one such model widely and successfully used in the riser for turbulence modeling (Launder and Spadling, 1974). In this model, length scale of the turbulence is calculated by solving the transport equations for turbulent kinetic energy and dissipation. In this work, modified  $k - \varepsilon$  model accounting for the presence of solid particles is used (Elgobashi and Abou-Arab, 1983):

$$\frac{\partial}{\partial t} (\varepsilon_f \rho_f k_{tf}) + \nabla \cdot (\varepsilon_f \rho_f \vec{u}_f k_{tf}) = \nabla \cdot \left( \varepsilon_f \frac{\mu_f}{\sigma_k} \nabla k_{tf} \right) + \varepsilon_f \rho_f (p - \varepsilon_{tf}) \quad (5.20)$$

$$\frac{\partial}{\partial t} (\varepsilon_f \rho_f \varepsilon_{tf}) + \nabla \cdot (\varepsilon_f \rho_f \vec{u}_f \varepsilon_{tf}) = \nabla \cdot \left( \varepsilon_f \frac{\mu_f}{\sigma_\varepsilon} \nabla \varepsilon_{tf} \right) + \varepsilon_f \rho_f (C_{1\varepsilon} p - C_{2\varepsilon} \varepsilon_{tf}) \quad (5.21)$$

The above equation contains  $\varepsilon_f$  representing hold up of gas. Last term in the right hand side represent the source and sink (negative) terms. First term represents the diffusive transport. For solving the above transport equation requires initial and boundary conditions. Inlet velocity and outlet pressure are specified. It is assumed that normal flux of turbulent kinetic energy vanishes at the wall and production rate of kinetic energy and the dissipate rate are equal (Launder and Spalding, 1972). Thus, boundary conditions at the wall are,

$$\left. \frac{\partial k}{\partial r} \right|_w = 0 \quad (5.22)$$

$$\varepsilon_w = \frac{C_\mu^{\frac{3}{4}} k_w^{\frac{3}{2}}}{\kappa y_p} \quad (5.23)$$

Where  $\kappa$  is constant value of 0.42 and  $y_p$  is the distance from the wall where the bulk flow may be assumed. Typically, this is taken to be equal to grid dimension.

It should be noted that other closure models also available in the literature. Here, we have discussed only the closures used in this work.

#### 5.4 Base case formulation

In this work, 2-D simulations were conducted. 2-D Cartesian geometry of the laboratory and pilot scale setup (section 3.4 and 4.4) were used. Schematic of 2-D geometry is shown in the Figure 5.1. Two symmetric inlets and outlets were assumed for the entry and outlet of solids. It is to be noted that experimental setups are cylindrical column in which solids enter and exit from one inlet and one outlet respectively. This arrangement of two entry and exits are provided to achieve uniform mixing at the inlet as suggested by Benyahia et al. (2000). Since one entry at the inlet leads gas to flow opposite side of the solid inlet and results in asymmetric profiles throughout the column (Benyahia et al., 2000). Similar to experiments, air was fed from the bottom and solids were fed from the side inlets. Solids were fed at minimum fluidization conditions through side inlets. Initially, there were no solids in the system. For all the simulations in current work, ANSYS® Fluent 15 commercial solver was used.

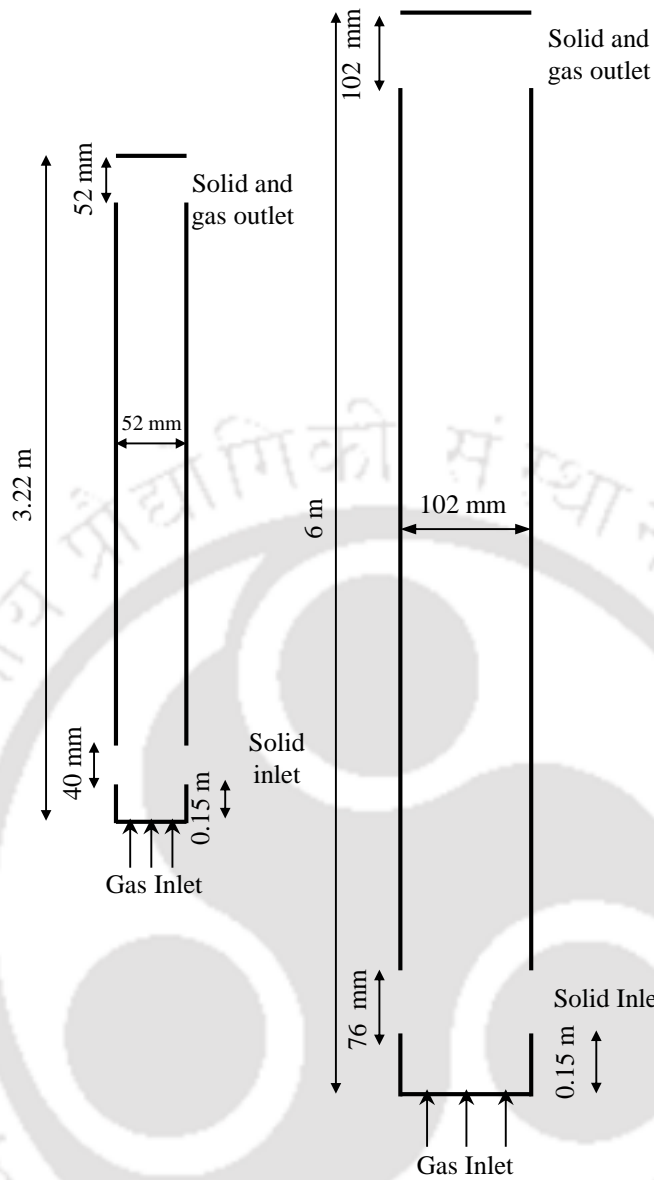


**Figure 5.1 Schematic of computational domain of laboratory and pilot scale setup**

**Table 5.3 Simulation conditions and parameters**

| <b>Parameters</b>              | <b>Model / Value</b> |
|--------------------------------|----------------------|
| Particle diameter              | 500 $\mu\text{m}$    |
| Density                        | 2500 $\text{kg/m}^3$ |
| Superficial gas velocity       | 8.8 m/s              |
| Solid and air inlet            | Velocity inlet       |
| Outlet                         | Pressure outlet      |
| Wall (air)                     | No slip              |
| Wall (solid)                   | Johnson and Jackson  |
| Restitution coefficient (p-p)  | 0.9                  |
| Viscous model                  | $k - \epsilon$       |
| Gas-solid drag                 | Wen and Yu (1966)    |
| Shear viscosity                | Gidaspow             |
| Bulk viscosity                 | Lun et al.           |
| Solid pressure                 | Lun et al. (1984)    |
| Radial distribution            | Lun et al. (1984)    |
| Specularity coefficient        | 0.1                  |
| Pressure velocity coupling     | SIMPLE               |
| Momentum Discretization        | Second order UPWIND  |
| Volume Fraction Discretization | QUICK                |
| Grid                           | Uniform grid         |
| Time step                      | 0.0005 sec           |

Initially, a base case model was developed using laboratory scale geometry. Closures available in the literature for gas-solid CFB were used for development of model. Further, empirical parameters were tuned to obtain the best match with the experimental data. Best suited model was selected based on the validation. Developed model is used for studying

the effect of operating conditions keeping the closure parameters same. Further, developed model was used to simulate the pilot scale geometry. Simulations were conducted and validated at the operating conditions used in the RPT experiments presented in chapter 3 and chapter 4.

For the base case model formulation, operating condition of  $U_g = 8.8$  m/s and  $G_s = 144$  kg/m<sup>2</sup>s is used. Table 5.3 shows the simulation parameters used. Base case is checked for the grid convergence. Best suited drag closure, specular coefficient and restitution coefficients are selected based on the validation with the experimental results. Time averaging of data is started after sufficient time when inlet and outlet flux is balanced. Typically, time averaging is started after 40 seconds of the simulation time. Each simulation is time averaged for 60 seconds.

### **Grid convergence**

Three grids of radial and axial division of  $10 \times 210$ ,  $20 \times 420$ ,  $40 \times 1134$  were checked. All the grids are having uniform divisions. Figure 5.2 shows the mean axial velocity and mean volume fraction of solids along the axis for the different grid sizes. No significant difference in the mean velocity plots are observed for all the grid sizes. However, small change in mean volume fraction of solids is observed at the bottom region for the fine mesh. It is to be noted that absolute mean volume fraction of solids is below 3% and change in the value for different grid size observed is minimal.

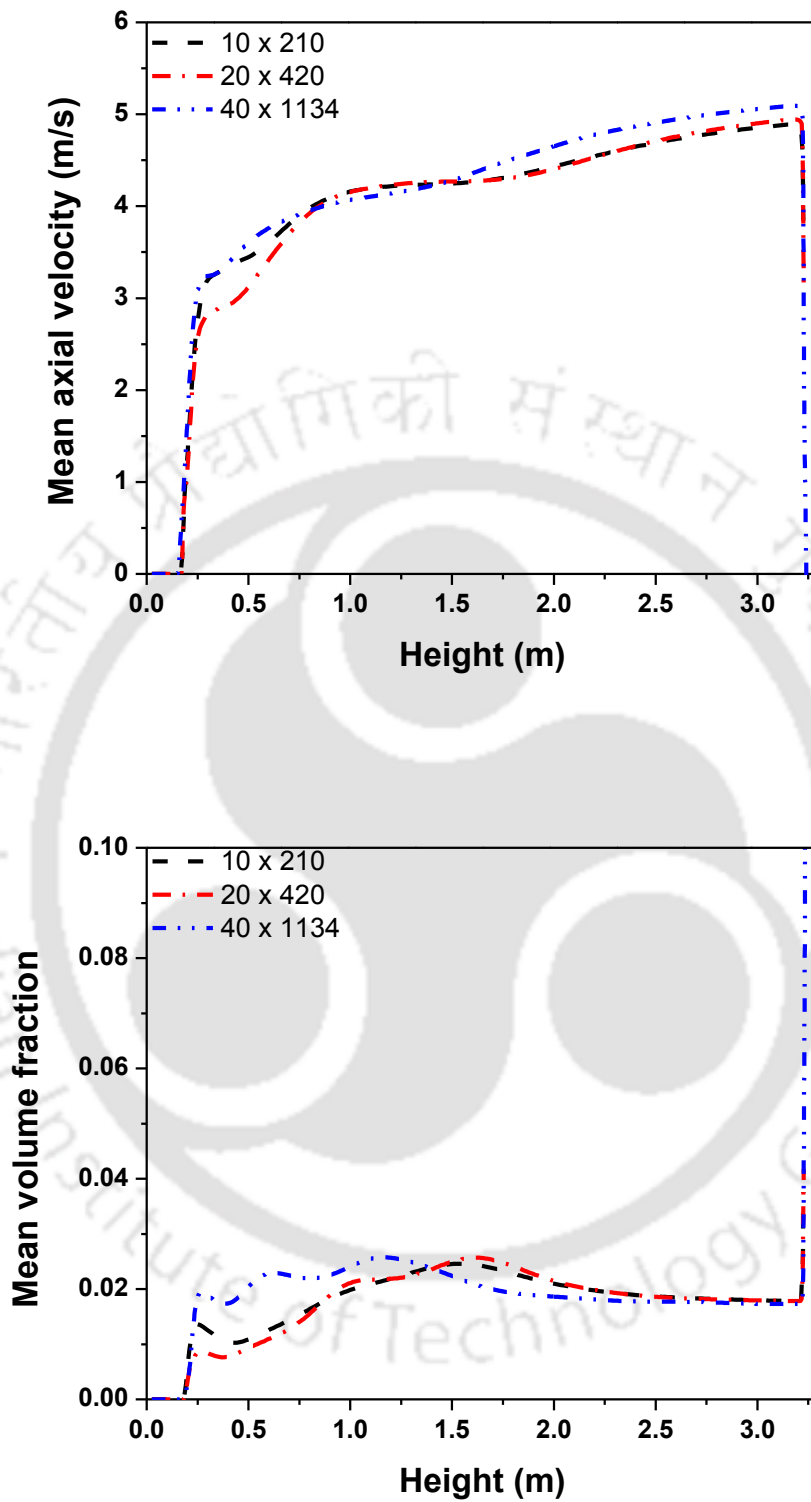
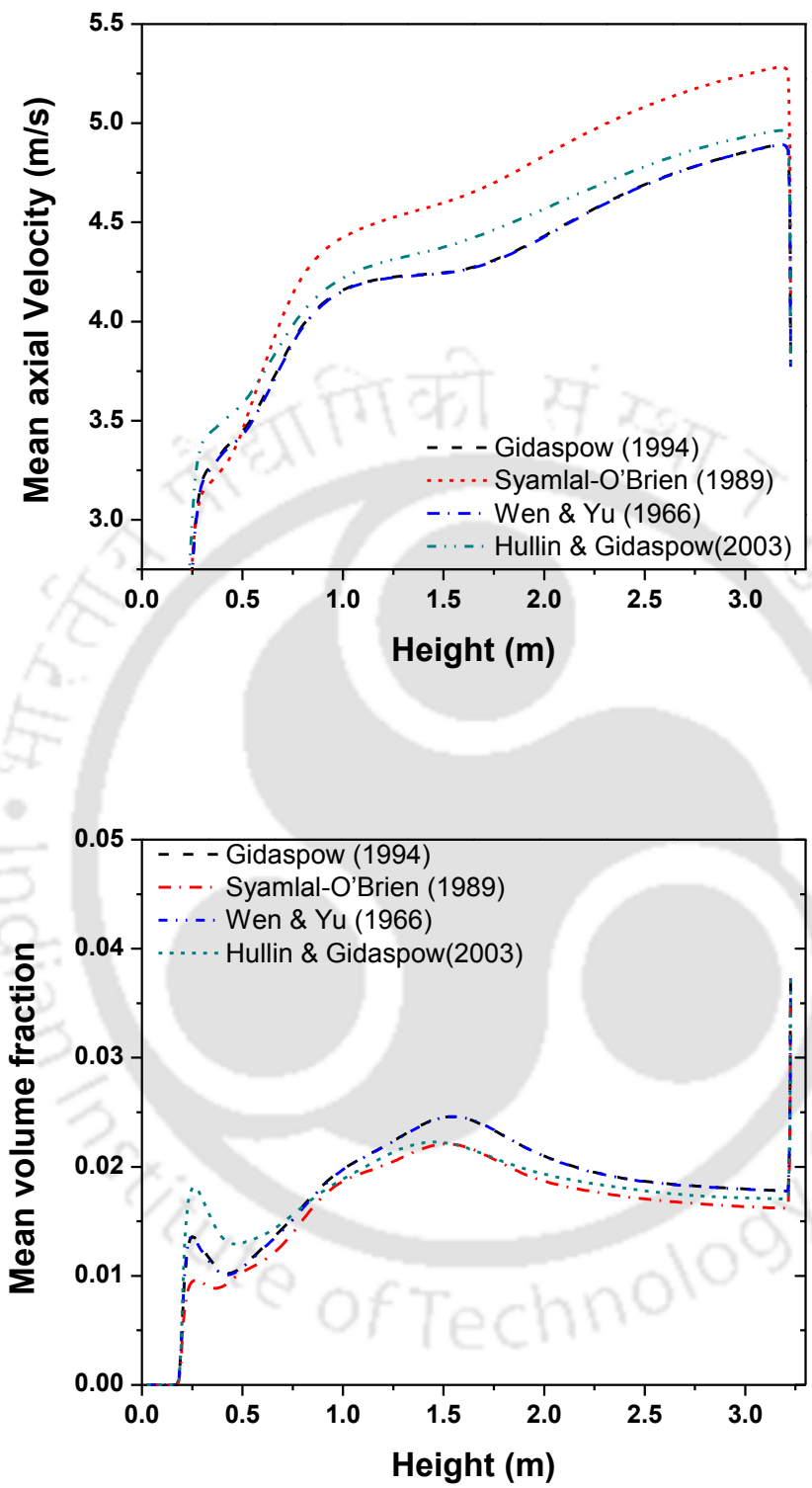


Figure 5.2 Axial profile of mean axial velocity and mean volume fraction for different grids at the axis of the riser ( $U_g = 8.8$  m/s and  $G_s = 144$  kg /m<sup>2</sup>s)



**Figure 5.3 Axial profile of mean axial velocity and mean volume fraction for different drag model at the axis of the riser ( $U_g = 8.8 \text{ m/s}$  and  $G_s = 144 \text{ kg/m}^2\text{s}$ )**

As the absolute value of velocity is dominating the flow profile, the convergence of grid should be viewed with velocity convergence or with solid flux for better accuracy (Vaishali, 2009). Further, in the literature it is reported that grid size of  $10 d_p$  is enough to resolve the flow structure in CFB (Andrew et al., 2005; Wang et al., 2009). Hence, in current work, coarse grid of  $10 \times 210$ , which gives similar values as of the other fine grids, are used for the simulations.

### **Drag closure**

Figure 5.3 shows the profile of mean axial velocity and mean volume fraction of solids along the height at the axis of the riser for different drag closures. Symalal – O'Brien (1989), Wen and Yu (1966), Gidaspow (1994) and Huilin & Gidaspow (2003) drag models which are commonly used for gas – solid CFB and given in Table 5.2 were tried. Wen and Yu (1966) and Gidaspow (1994) drag model gives similar results as the flow is very dilute and volume fraction is less than 2% in most of the places. Further, Wen and Yu (1966) and Gidaspow (1994) drag predicts lower velocity of the solids (higher slip velocity) compared to other drag models. It is to be noted that slip velocity are close to the terminal settling velocity of single solid in the experiments. Wen and Yu (1966) predicts the mean velocity similar to the single particle terminal velocity and successfully used for simulation in CFB (Vaishali, 2009; Shah et al., 2012). However, metastable structures are observed in the experiments. For predicting clusters, drag models which accounts for structures will be better option. Lu et al. (2011) reported that for high Archimedes number, EMMS and Gidaspow (1994) drag model predicts similarly. In this work, Archimedes number is 9226, hence, Wen and Yu (1966) drag model is used for all further simulations in this work.

## Specularity coefficient and restitution coefficient

Wall boundary condition of Johnson and Jackson (1987) has two empirical constants, specularity constant and restitution coefficient between wall and particle. Specularity coefficient represents the fraction of momentum exchange from particle to wall. It depends on the surface roughness of the wall, for perfectly specular collision specularity coefficient is zero and unity for perfectly diffusive collisions. In this work, specularity coefficient of 0.05, 0.1, 0.2, 0.5 and 1 (no slip) are investigated. Figure 5.4 shows the profiles of axial mean velocity and mean volume fraction of solids at the axis for different specularity coefficient. Clearly, specularity coefficient influences the flow development, mean axial velocity and mean volume fraction. At close to free slip condition (0.05), velocity of solids is higher while at no slip condition, volume fraction of solids is higher.

Velocity decreases (which means particle is decelerating) along the height of the riser for the specularity coefficient of 1 (close to no slip condition) and increases (which means particle is accelerating) along the height for free slip condition (specularity coefficient - 0.05). This has not been observed in experiment. Further, for the cases of specularity coefficient of 0.1 and 0.2, flow is developed at the height of 1.2 m. From the RTD experiments, it is known that flow development is achieved at this height. So, either of 0.1 and 0.2 might be best suited value of specularity coefficient. Further for specularity coefficient value of 0.2, mean axial velocity of solids predicted are lower than the experimental mean velocity range of 3 - 3.5 m/s while it is very close to experimental value for specularity coefficient of 0.1. Hence, specularity coefficient of 0.1 is used for all further simulations in this work.

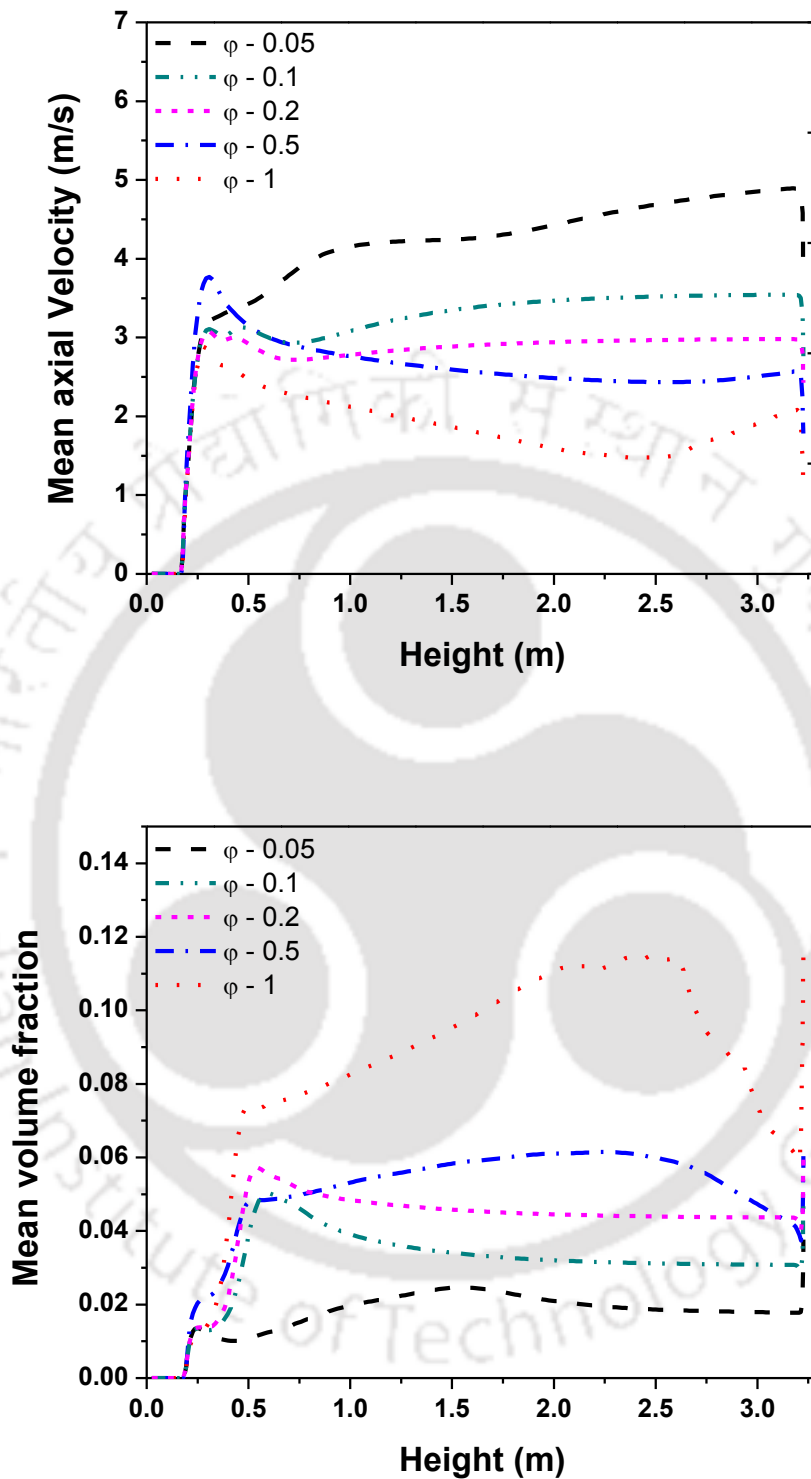


Figure 5.4 Axial profile of mean axial velocity and mean volume fraction for different specularities at the axis of the riser ( $U_g = 8.8$  m/s and  $G_s = 144$  kg /m<sup>2</sup>s)

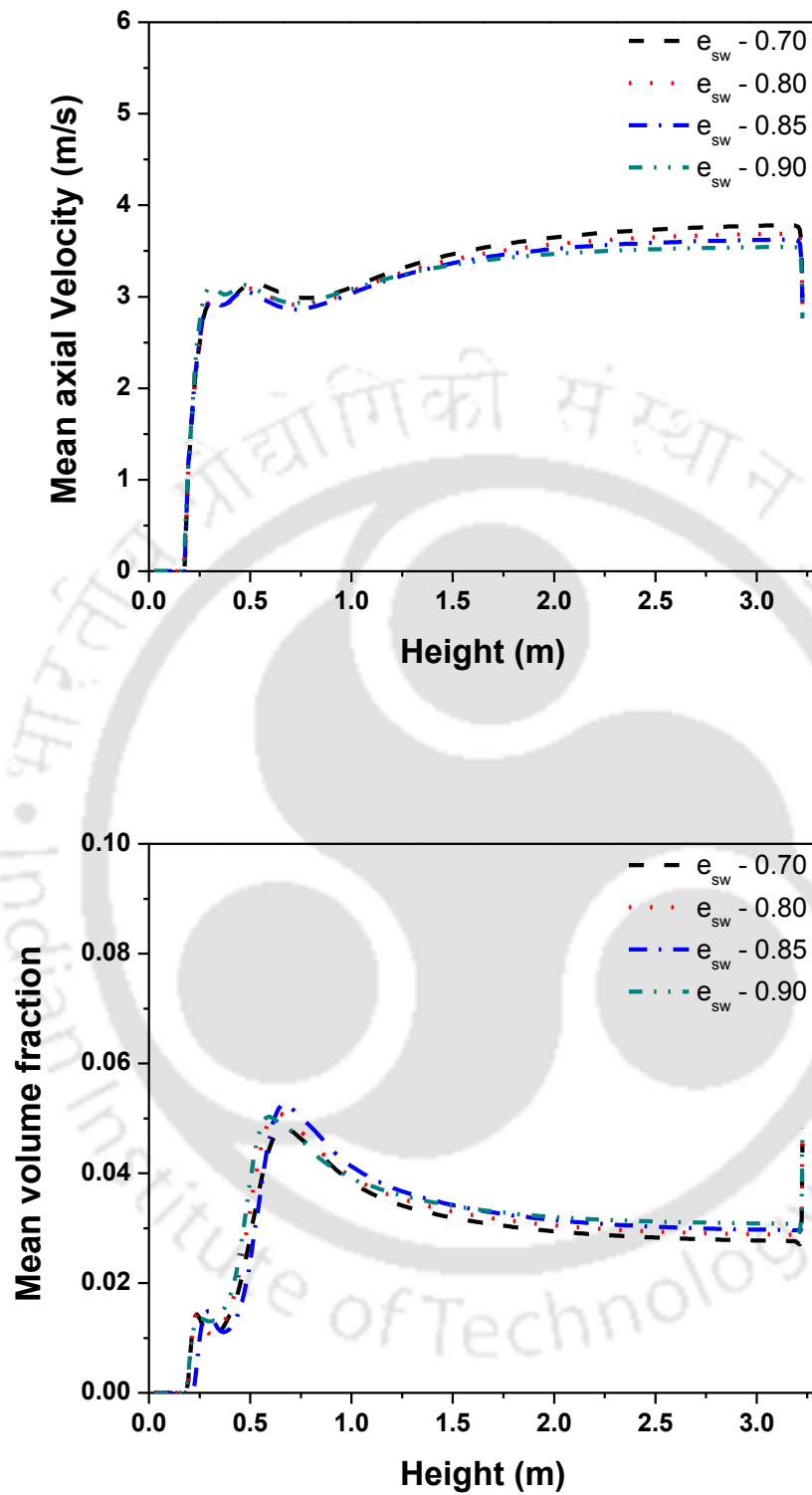


Figure 5.5 Axial profile of mean axial velocity and mean volume fraction for different restitution coefficient at the axis of the riser ( $U_g = 8.8$  m/s and  $G_s = 144$  kg /m<sup>2</sup>s)

Another empirical constant, restitution coefficient represents the elastic nature of collision between the particle and wall. If the collision is elastic,  $e_{sw} = 1$ , for inelastic collision,  $e_{sw} = 0$ . In this work, restitution coefficient of 0.7, 0.8, 0.85 and 0.9 were investigated. Figure 5.5 shows the axial profile of mean axial velocity and mean volume fraction for different restitution coefficient. No significant difference in the profiles was observed for all restitution coefficients. Therefore, in current work, restitution coefficient of 0.9 is used for further simulations.

### **Validation**

Figure 5.6 shows the axial mean velocity and granular temperature comparison of experimental and simulation data at different specularity coefficient. For specularity coefficient of 0.1, a 'good' match is observed, both qualitatively and quantitatively, between simulation and experimental data for mean axial velocity of the solids. However, granular temperature matches qualitatively but not quantitatively. Interesting observation is that at low specularity coefficient, CFD simulation predictions are closer for granular temperature values. However, opposite trends are observed in mean axial velocity prediction.

Huiln and Gidaspow (2003) reported that, due to the low concentration of particles in the centre, particle – particle interactions are also low which increases towards the wall due to increase in the concentration of particles. Thus, higher granular temperature is observed near the wall compared to the centre of the riser. Further, there are two kinds of granular temperature reported in literature, laminar granular temperature and turbulent granular temperature. Laminar granular temperature is due to the particle oscillations and turbulent granular temperature is due to the clusters which can be given by the Reynolds normal stresses (Gidaspow et al., 2004; Jung et al., 2005). Euler – Euler simulations using KTGF

model gives only laminar granular temperature (Chalermssinsuwan et al., 2009). In CFB, turbulent granular temperature is much lower than the laminar granular temperature (Tartan and Gidaspow, 2004; Gidaspow et al., 2004; Jung et al., 2005). It is to be noted that Tartan and Gidaspow (2004) have used similar solid size and density for their experiments and their laminar granular temperature is approximately thrice of the turbulent granular temperature. In this work, granular temperature values from experiments are calculated from the Reynolds normal stresses. So, reported experimental values are turbulent granular temperature. Hence, Euler-Euler CFD simulations predict much larger value compared to experimental prediction. In current work CFD simulation predicts the granular temperature (laminar) values approximately thrice of the experimental values. Thus, it can be concluded that developed model parameters are able to predict the mean axial velocity and granular temperature. Now, with this developed model parameters, effect of superficial gas velocity, solid flux and performance at the pilot plant (scale studies) were investigated.

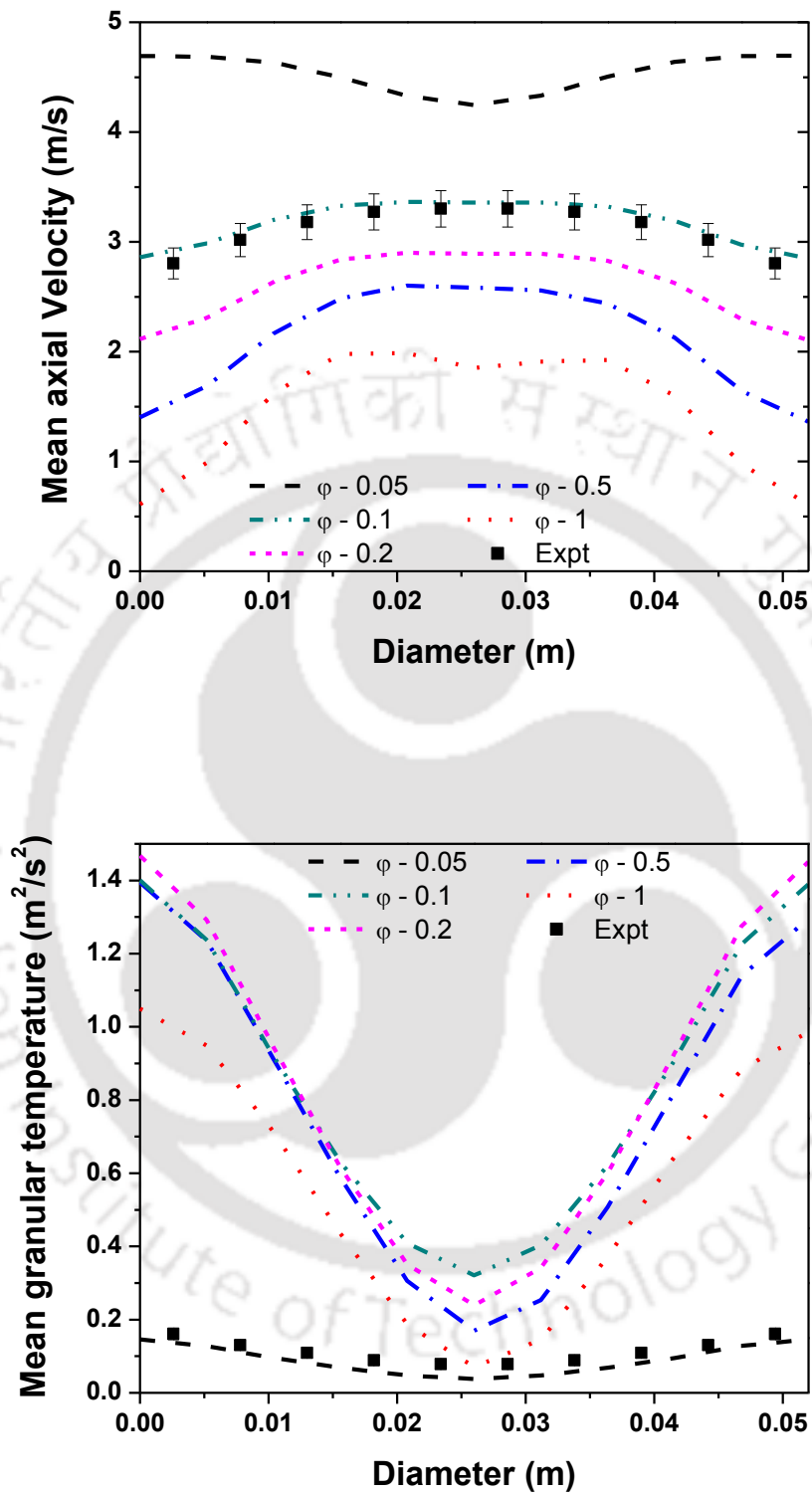


Figure 5.6 Radial profile of mean axial velocity and mean volume fraction for different specular coefficient at the height of  $H = 1.5$  m ( $U_g = 8.8$  m/s and  $G_s = 144$  kg /m<sup>2</sup>s)

## 5.5 Effect of superficial gas velocity

Figure 5.7 shows the effect of the superficial gas velocity on mean axial velocity of solids where values are compared with the experimental data. Simulation predicts the increase in axial mean velocity of solids with increase in the gas velocity. For higher velocities, experimental values are under predicted while for lower velocities, experimental values are over predicted. Simulations are not able to predict the parabolic profile of the lower velocities where the gradient is high near the wall. However, at the higher velocities, where the gradient at the wall is low, prediction is better. Further, quantitatively, values at the centre are predicted well compared to values near the wall. It should be noted that with change in the operating conditions, solid interactions changes significantly near the wall. This is mainly due to change in particle concentration near the wall which changes particle-particle and particle-wall interactions. Hence, different specular coefficient values should be used for different operating condition for better match, which is also reported by Li and Benyahia (2013).

Figure 5.8 shows the effect of superficial gas velocity on granular temperature prediction compared with the experimental values. Simulations show that granular temperature increases from the centre of the column to the wall which is in-line with experimental data. However, in simulation with increase in the gas velocity, granular temperature increases while in the case of experiments it decreases. As previously explained, laminar granular temperature is due to the particle oscillations. With increases in the velocity, particle oscillations increase due to higher gas turbulence. Thus, simulations do predict increase in the granular temperature. However, turbulent granular temperature decreases as the volume fraction decreases due to decrease in interactions and formation of metastable structures decreases as explained in the Section 3.7 and Section 3.8.

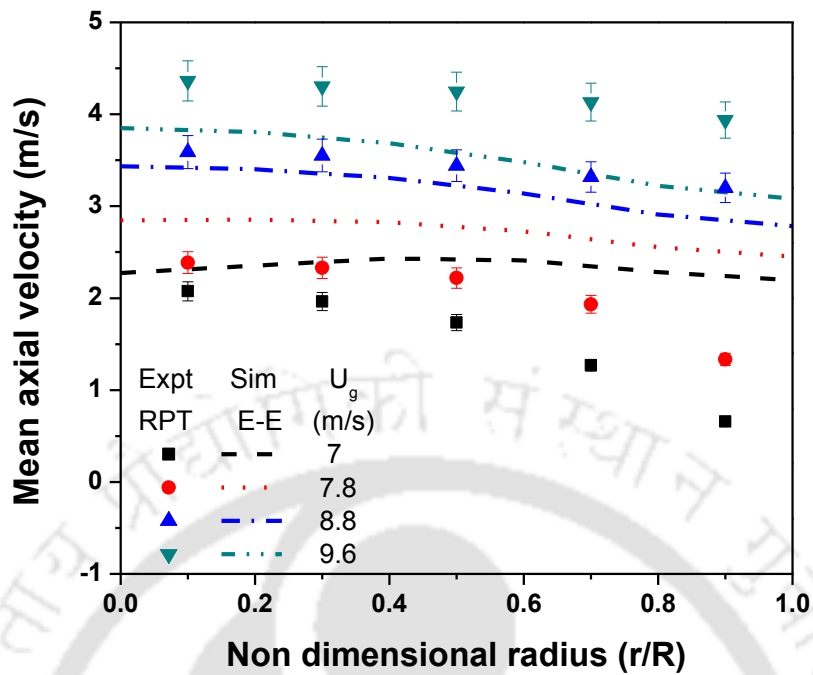


Figure 5.7 Radial profile of mean axial velocity for different superficial gas velocity at the same flux of  $110 \text{ kg/m}^2\text{s}$  at the height of  $H = 1.5 \text{ m}$

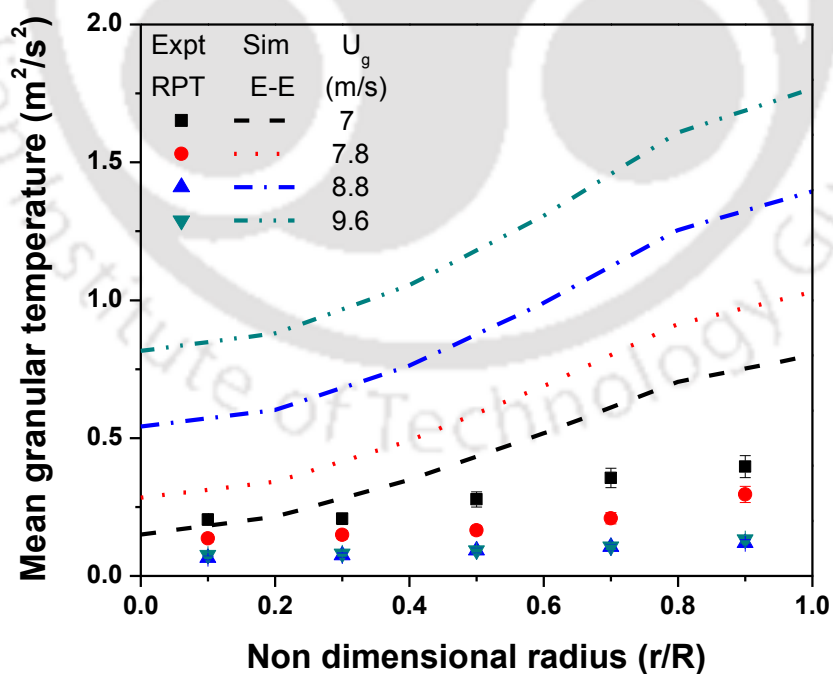
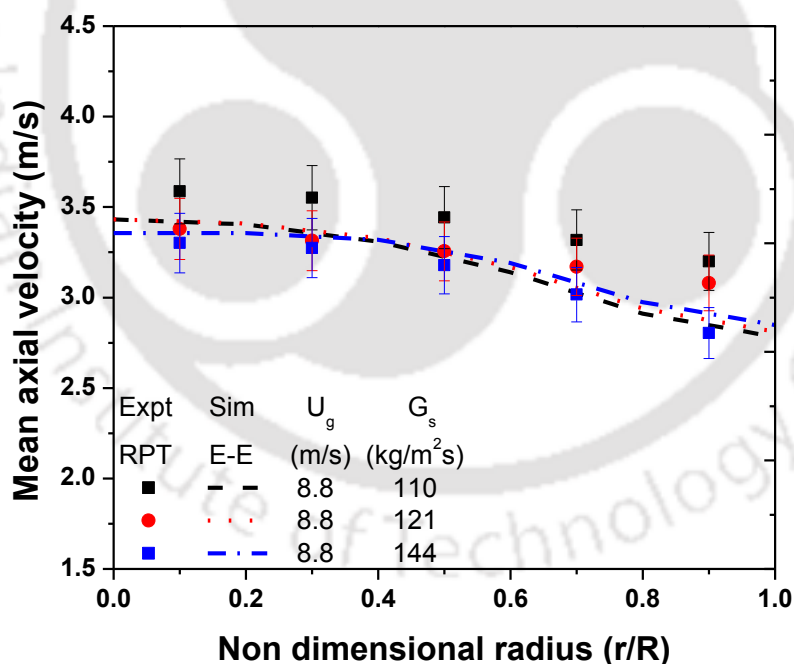


Figure 5.8 Radial profile of mean granular temperature for different superficial gas velocity at the same flux of  $110 \text{ kg/m}^2\text{s}$  at the height of  $H = 1.5 \text{ m}$

## 5.6 Effect of solid flux

Figure 5.9 shows the effect of solid flux on the prediction of the mean axial velocity of solids compared with the experimental values. Good qualitative and quantitative agreement is found between CFD simulation and experimental data except near the wall. Similar to experimental data CFD simulations also predict low change in mean velocity of solids with change in solid flux. Figure 5.10 shows the effect of solid flux on the granular temperature in comparison with the experimental values. With increase in the flux, granular temperature decreases in the simulations while it increases in the experiments. As previously explained in the effect of superficial gas velocity, simulation fluctuations are due to the particle oscillations and experiments are due to the particle interactions.



**Figure 5.9** Radial profile of mean axial velocity for different solid flux at the same superficial gas velocity of 8.8 m/s at the height of  $H = 1.5$  m

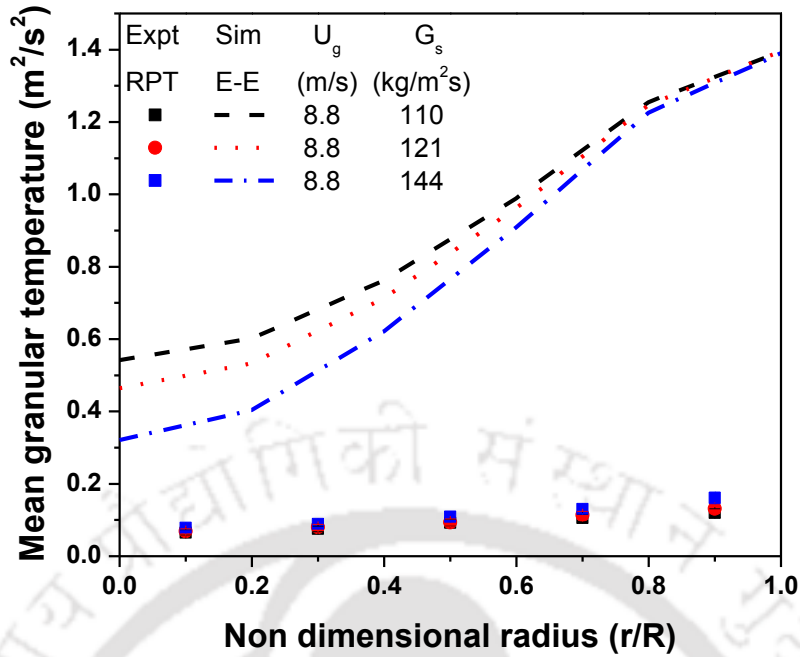


**Figure 5.10** Radial profile of mean granular temperature for different solid flux at the same superficial gas velocity of 8.8 m/s at the height of  $H = 1.5$  m

## 5.7 Pilot scale setup

Simulations were conducted with the same model parameters as developed for the laboratory scale setup, thus evaluating the performance of CFD simulations for scale up studies.

### Grid independency

Computational domain used for pilot scale study is shown in the Figure 5.11. Uniform grid of  $10 \times 500$ ,  $20 \times 392$ ,  $30 \times 594$ ,  $35 \times 670$ ,  $40 \times 784$  (radial  $\times$  axial) divisions are checked for grid convergence. Figure 5.11 shows the mean axial velocity and mean granular temperature for different grids. Except coarse grids,  $10 \times 500$  and  $20 \times 392$ , all the other grids gave similar results. Since significant differences are not observed in other grids. Relatively coarse grid,  $30 \times 594$  is used for further simulations to reduce computation time.

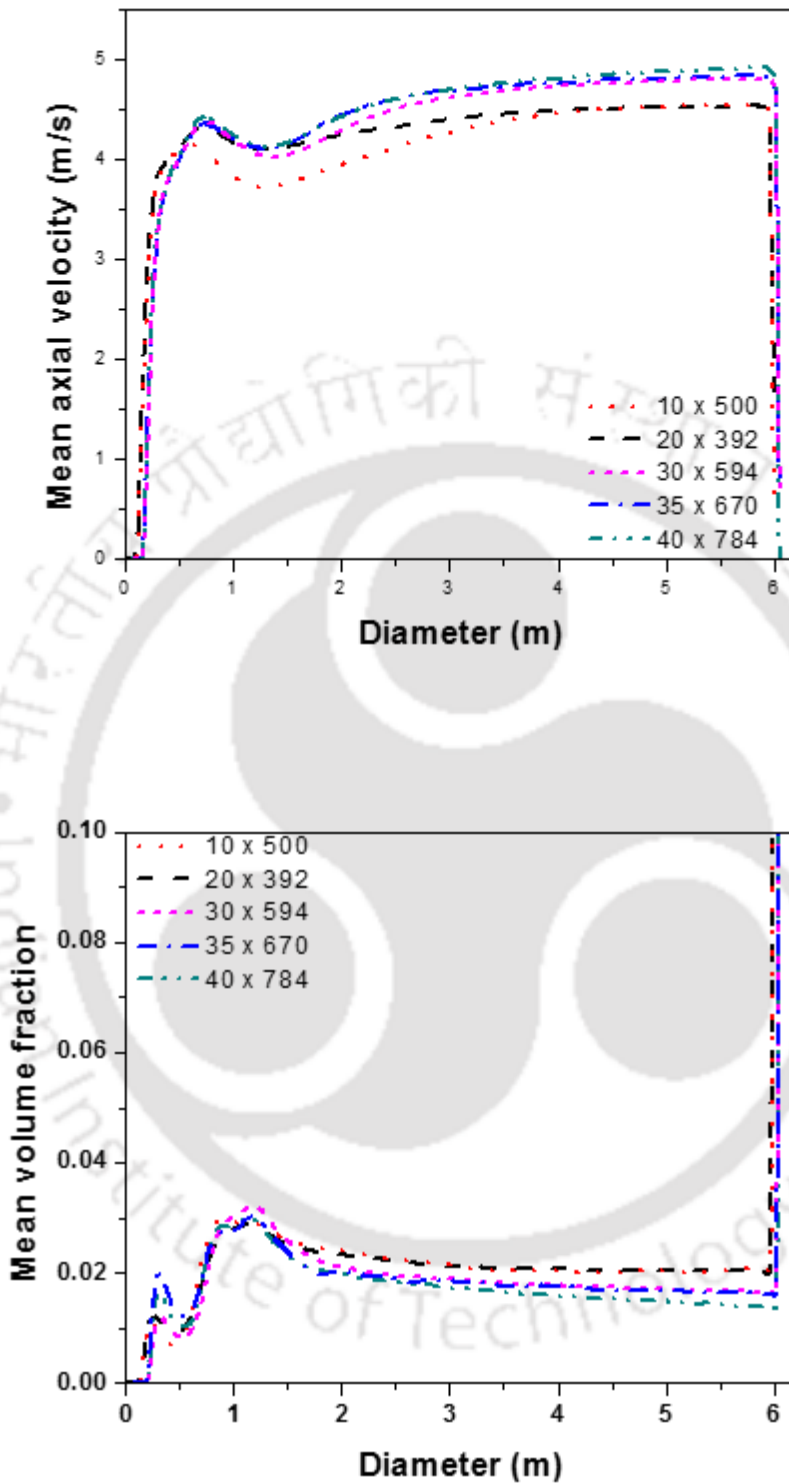
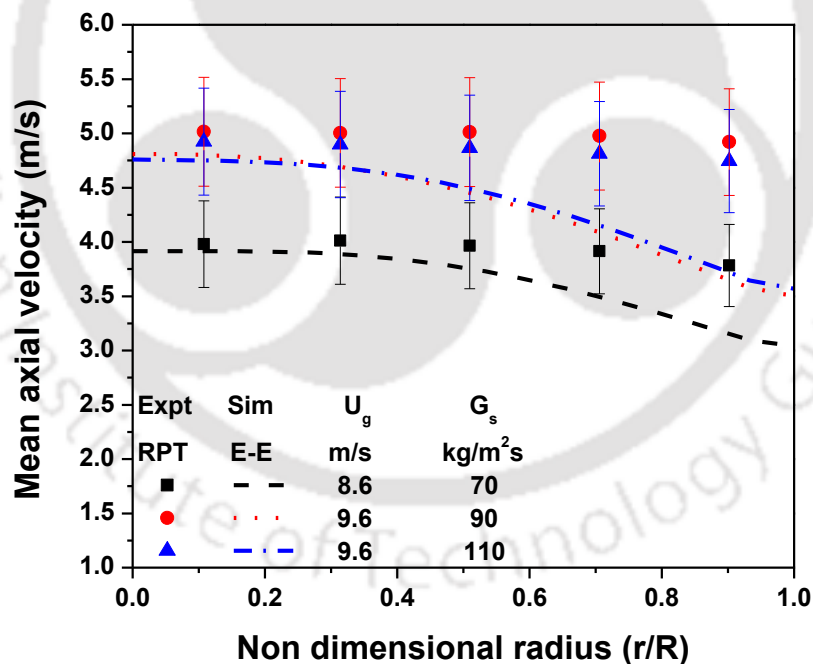


Figure 5.11 Axial profile of the mean axial velocity and mean volume fraction for different grids at the axis of the riser

## Scale up

Figure 5.12 shows the axial mean velocity of solids at different operating conditions at pilot scale setup. Except near the wall, simulations predictions are matching well with experiments, both qualitatively and quantitatively. Trends of the experiments are also predicted by the simulations. Figure 5.13 shows the granular temperature for different operating conditions at pilot scale setup. Predicted granular temperature values are twice of the experiments in the centre of the column and thrice of the experiments near the wall. Cross over observed in the experiments for the case of  $U_g = 8.6$  m/s and  $G_s = 70$  kg/m<sup>2</sup>s is not predicted by the simulations as the mechanism of phenomena is different in case of simulation compared to experiments.



**Figure 5.12 Radial profile of mean axial velocity for different operating conditions at the pilot plant scale setup at the height of  $H = 4$  m**

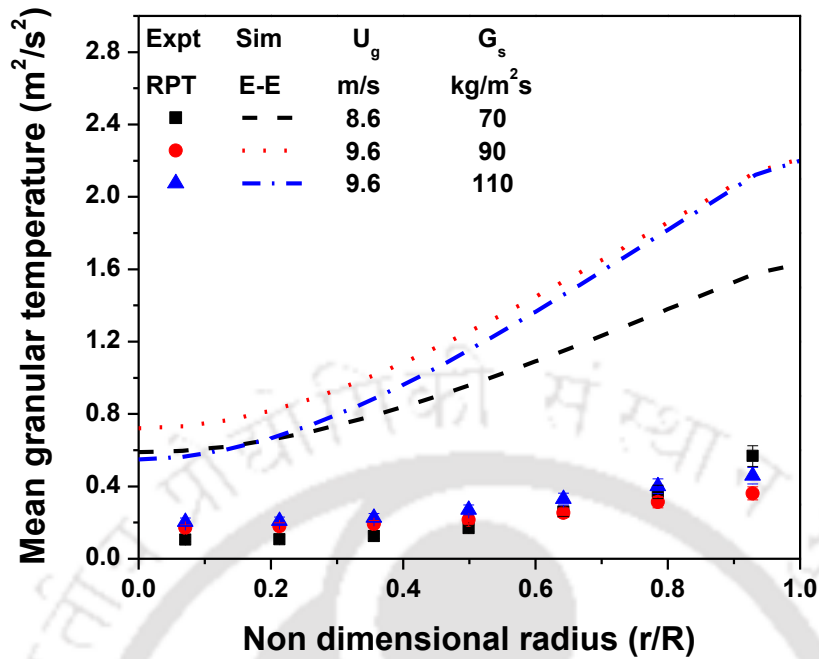


Figure 5.13 Radial profile of mean granular temperature for different operating conditions at the pilot plant scale setup at the height of  $H = 4$  m

## 5.8 Summary

In this chapter, Euler – Euler simulations of gas solid riser are presented in detail. The main objective of this chapter is to study the performance of the Euler – Euler model as the design and scale up tool. To this goal, effect of gas velocity, effect of solid flux and effect of scale were presented. It is found that developed CFD simulations are able to qualitatively and quantitatively predict the experimental data for most of the conditions. In addition to the first order moments, second order moments are also validated. Main conclusions from the results are as follows:

- Developed model is able to predict the mean axial velocity (first order moments) fairly well.

- Accuracy of prediction varies with the operating conditions, particularly near the wall. This emphasizes the need of the tuning parameters based on the operating conditions. As suggested by Li and Benyahia (2013), accounting variable specular coefficient with the operating conditions might improve the accuracy of the prediction.
- Simulations are able to predict increase in the axial solid velocity with increase in the gas velocity and decrease in the axial solid velocity with increase in the solid flux.
- Simulations are able to predict the profile of granular temperature correctly, where the granular temperature is low in the centre and high near the wall.
- Granular temperature values predicted are in the same order as of the experimental prediction, however the predicted values are higher than the experimental values.
- With increase in the flux, granular temperature decreases while experimental values are increasing. However, with increase in the gas velocity, granular temperature increases while the experimental values are decreasing. This is because the classical granular temperature predicted by the simulations is laminar granular temperature which accounts for the particle oscillations. Thus, with increases in the velocity, classical granular temperature increases. Since turbulent granular temperature are obtained from the experiments (which accounts for the clusters and other solid – solid interactions), considerable variation are observed.
- With increase in the scale, mean axial velocity are predicted reasonably. Granular temperature predictions are of the same order as of the experiments and higher than the experimental values which follows the similar trend as of the laboratory scale.

Overall, developed model is able to predict the mean velocity at different operating conditions and scale. To improve the predictions, tuning parameters must be expressed as

the function of the operating conditions. A model based on particle-particle interaction may be more suitable instead of using a single value of specular coefficient. Further, model based on Euler-Lagrangian approach may provide better accuracy in expense of massive computational requirement, particularly for complete riser simulation. One can reduce the computational domain by using periodic boundary condition at the inlet and outlet for developed region (Naren and Ranade, 2011). However, finding the development length itself is very challenging in CFB as it changes with change in operating conditions.

## Notations

|            |   |                             |
|------------|---|-----------------------------|
| $C_D$      | Drag coefficient,   | [-]                         |
| $C_\mu$    | Constant in k- $\epsilon$ model                             | [-]                         |
| $d_p$      | Particle diameter   | [ $\mu\text{m}$ ]           |
| $e_{ss}$   | Coefficient of restitution between solid particles          | [-]                         |
| $e_{sw}$   | Coefficient of restitution between solid particles and wall | [-]                         |
| $\vec{F}$  | Other forces  | [ $\text{Kgm/s}^2$ ]        |
| $G_s$      | Solid mass flux   | [ $\text{kg/m}^2\text{s}$ ] |
| $\vec{g}$  | Acceleration due to gravity                                 | [ $\text{m/s}^2$ ]          |
| $g_0$      | Radial distribution function                                | [-]                         |
| $g_{0,ss}$ | Solids radial distribution function                         | [-]                         |
| $k$        | Constant  | [-]                         |
| $k_s$      | Kinetic energy per unit mass of solids                      | [ $\text{m}^2/\text{s}^2$ ] |
| $K_{sf}$   | Momentum exchange coefficient                               | [ $\text{kgm}^3/\text{s}$ ] |
| $k_{tf}$   | Kinetic energy of turbulence per unit mass of liquid        | [ $\text{m}^2/\text{s}^2$ ] |

|                      |  |                                   |
|----------------------|--|-----------------------------------|
| $k_s$                | Granular conductivity or Diffusion coefficient of granular energy  | [kg/ms]                           |
| $P$                  | Pressure   | [N/m <sup>2</sup> ]               |
| $q$                  | Granular kinetic energy flux   | [kg/s <sup>3</sup> ]              |
| $U_g$                | Superficial gas velocity   | [m/s]                             |
| $\vec{u}$            | Velocity   | [m/s]                             |
| $\vec{u}_f$          | Ensemble averaged time smoothed velocity   | [m/s]                             |
| $y_p$                | Distance from the wall far enough so that bulk flow may be assumed                                       | [m]                               |
| <b>Greek letters</b> |  |                                   |
| $\varepsilon$        | Volume fraction (holdup)   | [-]                               |
| $\varepsilon_{if}$   | Turbulent kinetic energy dissipation rate  | [m <sup>2</sup> /s <sup>3</sup> ] |
| $\rho$               | Density  | [kg/m <sup>3</sup> ]              |
| $\bar{\tau}$         | Stress-strain tensor   | [N/m <sup>2</sup> ]               |
| $\tau_f$             | Total shear stress   | [N/m <sup>2</sup> ]               |
| $\Theta_s$           | Granular temperature   | [m <sup>2</sup> /s <sup>2</sup> ] |
| $\eta$               | Index on realizations  | [-]                               |
| $\varphi_{fs}$       | Term modelling solids energy dissipation by correlations between solids and liquid velocity fluctuations | [kg/ms <sup>3</sup> ]             |
| $\gamma_{\Theta_s}$  | Collisional dissipation of energy  | [kg/ms <sup>3</sup> ]             |
| $\mu_f^{turb}$       | Turbulent viscosity of fluid   | [kg/ms]                           |
| $\mu$                | Viscosity  | [kg/ms]                           |
| $\mu_s$              | Solids phase shear viscosity   | [kg/ms]                           |

$\lambda_s$  Bulk viscosity [kg/ms]

### Subscript

$f$  Fluid

$g$  Gas

$i$  Projection subscript

$k$  Phase index

$p$  Particle

$s$  Solids

### References

- Adamczyk, W.P., Klimanek, A., and Czakiert, T., 2014. Comparison of the standard Euler Euler and hybrid Euler Lagrange approaches for modeling particle transport in a pilot scale circulating fluidized bed. *Particuology* 17, 139-137.
- Agrawal, K., Loezos, P.N., Syamlal, M. and Sundaresan, S., 2001. The role of meso-scale structures in rapid gas–solid flows. *Int. J. Fluid Mech.* 445, 151–185.
- Anderson, T.B., Jackson. R., 1967. A fluid mechanical description of fluidized beds. *Ind. Eng. Chem. Fundamen.* 6, 527- 535.
- Andrew, A.T. IV., Loezos, P.N., Sundaresan, S., 2005. Coarse-grid simulation of gas-particle flows in vertical risers. *Ind. Eng. Chem. Res.* 44, 6022–6037.
- Arastoopour, H., Gidaspow, D., 1979. Analysis of IGT pneumatic conveying data and fast fluidization using a thermohydrodynamic model. *Powder Technol.* 22, 77–87.
- Benyahia, S., Arastoopour, H., Knowlton, T.M., Massah, H., 2000. Simulation of particles and gas flow behavior in the riser section of a circulating fluidized bed using the kinetic theory approach for the particulate phase. *Powder Technol.* 112, 24-33.

- Chalermsoonsuwan, B., Piumsoomboon, P., Gidaspow, D., 2009. Kinetic theory based computation of PSRI riser : Part I — Estimate of mass transfer coefficient. *Chem. Eng. Sci.* 64, 1195–1211.
- Chalermsoonsuwan, B., Gidaspow, D., Piumsoomboon, P., 2014. In-depth system parameters of transition flow pattern between turbulent and fast fluidization regimes in high solid particle density circulating fluidized bed reactor. *Powder Technol.* 253, 522–536.
- Chapman, S. and Cowling, T.G., 1990. *The Mathematical Theory of Non-Uniform Gases.* 3rd Ed., Cambridge University Press.
- Dai, Q., Chen, C., Qi, H., 2015. A generalized drag Law for heterogeneous gas-solid flows in fluidized beds. *Powder technol.* 283, 120–127.
- Deen, N.G., Annaland, M.V.S., van Der Hoef, M.A., Kuipers, J.A.M., 2007. Review of discrete particle modeling of fluidized beds. *Chem. Eng. Sci.* 62, 28–44.
- Ding, J. and Gidaspow, D., 1990. A Bubbling Fluidization Model Using Kinetic Theory of Granular Flow. *AIChE J.* 36, 523–538.
- Drew, D.A., 1983. Mathematical modelling of two-phase flow. *Annu. Rev. Fluid Mech.* 15, 261-292.
- Dudukovic, M.P., Larachi, F., Mills, P.L., 1999. Multiphase reactors - revisited. *Chem. Eng. Sci.* 54, 1975–1995.
- Dudukovic, M.P., 2010. Reaction engineering: Status and future challenges. *Chem. Eng. Sci.* 65, 3–11.
- Elgobashi, S. E., Abou-Ara, T.W., 1983. A two-equation turbulence model for two-phase flows. *Phys. Fluids* 26, 931-938.
- Ergun, S., 1952. Fluid flow through packed columns. *Chem. Eng. Prog.* 48, 89-154.
- Gao, X., Wang, L., Wu, C., Cheng, Y., Li, X., 2012. Steady-state simulation of core-annulus flow in a circulating fluidized bed (CFB) riser. *Chem. Eng. Sci.* 78, 98–110.
- Gidaspow, D., Bezburuah, R., Ding, J., 1992. Hydrodynamics of circulating fluidized beds: Kinetic theory approach in *Fluidization VIII*, 75-82.

- Gidaspow, D., 1994 *Multiphase Flow and Fluidization: Continuum and Kinetic Theory Descriptions*, first ed. Academic Press, San Diego.
- Gidaspow, D., Jung, J., Singh, R.K., 2004. Hydrodynamics of fluidization using kinetic theory : an emerging paradigm: 2002 Flour-Daniel lecture, *Powder Technol.* 148, 123–141.
- Gibilaro, L.G., Di Felice, R., Waldram, S.P., Foscolo, P.V., 1985. Generalized friction factor and drag coefficient correlations for fluid particle interactions. *Chem. Eng. Sci.* 40, 1817-1823.
- Hartge, E., Ratschow, L., Wischnewski, R., Werther, J., 2009. CFD-simulation of a circulating fluidized bed riser. *Particuology* 7(4), 283–296.
- Huilin, L., Gidaspow, D., 2003. Hydrodynamic Simulations of Gas - Solid Flow in a Riser. *Ind. Eng. Chem. Res.* 42, 2390–2398.
- Ibsen, C.H., Helland, E., Hjertager, B.H., Solberg, T., Tadriss, L., Occelli, R., 2004. Comparison of multifluid and discrete particle modelling in numerical predictions of gas particle flow in circulating fluidised beds. *Powder Technol.* 149, 29–41.
- Johnson, P.C., Jackson, R., 1987. Frictional-Collisional Constitutive Relations for Granular Materials, with Application to Plane Shearing. *J. Fluid Mech.* 176, 67–93.
- Jung, J., Gidaspow, D., Gamwo, I.K., 2005. Measurement of Two Kinds of Granular Temperatures , Stresses , and Dispersion in Bubbling Beds. *Ind. Eng. Chem. Res.* 44(5), 1329–1341.
- Knowlton, T.M., Karri, S.B.R., Issangya, A., 2005. Scale-up of fluidized-bed hydrodynamics. *Powder Technol.* 150, 72–77.
- Kuipers, J.A.M., van Swaaij, W.P.M., 1997. Application of computational fluid dynamics to chemical reaction engineering. *Rev. Chem. Eng.* 13, 1–118.
- Lauder, B.E., Spalding, D.B., 1972. *Lectures in Mathematical Models of Turbulence*. Academic Press, London, England.
- Lauder, B., Spalding, D., 1974. The numerical computation of turbulent flows. *Comput. Methods Appl. Mech. Eng.* 3, 269-289.

- Leung, L.S., 1980. The Ups and Downs of Gas-Solid Flow: A Review. in Fluidization (J. R. Grace and J. M. Matsen, eds.), Plenum Press.
- Li, J., 2003. Euler-lagrange simulation of flow structure formation and evolution in dense gas solid flows (Ph.D. Thesis). University of Twente, Enschede, Netherlands.
- Li, T., Benyahia, S., 2012. Revisiting Johnson and Jackson boundary conditions for granular flows. *AIChE J.* 58, 2058–2068.
- Li, T., Benyahia, S., 2013. Evaluation of Wall Boundary Condition Parameters for Gas – Solids Fluidized Bed Simulations. *AIChE J.* 59, 3624-3632.
- Li, D., Ray, M.B., Ray, A.K., Zhu, J., 2013. A comparative study on hydrodynamics of circulating fluidized bed riser and downer. *Powder Technol.* 247, 235–259.
- Li, T., Dietiker, J.-F., Shadle, L., 2014a. Comparison of full-loop and riser-only simulations for a pilot-scale circulating fluidized bed riser. *Chem. Eng. Sci.* 120, 10–21.
- Li, T., Gel, A., Pannala, S., Shahnam, M., Syamlal, M., 2014b. CFD simulations of circulating fluidized bed risers part I Grid study. *Powder Technol.* 254, 170–180.
- Liu, W., Li, H., Zhu, Q., Zhu, Q., 2015. A new structural parameters model based on drag coefficient for simulation of circulating fluidized beds. *Powder Technol.* 286, 516–526.
- Lu, B., Wang, W., Li, J., 2011. Eulerian simulation of gas-solid flows with particles of Geldart groups A, B and D using EMMS-based meso-scale model. *Chem. Eng. Sci.* 66, 4624–4635.
- Lu, B., Zhang, N., Wang, W., Li, J., 2012. Extending EMMS-based models to CFB boiler applications. *Particuology* 10, 663–671.
- Lun, C.K.K., Savage, S.B., Jeffrey, D.J., Chepurny, N., 1984. Kinetic theories for granular flow: inelastic particles in couette flow and slightly inelastic particles in a general flow field. *J. Fluid Mech.* 140, 223-256.
- Luo, K.M., 1987. Experimental gas-solid vertical transport (PhD thesis). Illinois institute of Technology, Chicago, Illinois.

- Naren, P.R., Ranade, V. V, 2011. Scaling laws for gas – solid riser flow through two-fluid model simulation. *Particuology* 9, 121–129.
- Neri, A., Gidaspow, D., 2000. Riser Hydrodynamics : Simulation Using Kinetic Theory. *AIChE J.* 46(1), 52-67.
- Nieuwland, J.J., Meijer, R., Kuipers, J.A.M., van Swaaij, W.P.M., 1996. Measurements of solids concentration and axial solids velocity in gas-solid two-phase flows. *Powder Technol.* 87(2), 127–139.
- Nieuwland, J., Huizenga, P., Kuipers, J.A.M., van Swaaij, W.P.M., 1994. Hydrodynamic modelling of circulating fluidized beds. *Chem. Eng. Sci.* 49(24), 5803–5811.
- Panday, R., Shadle, L.J., Shahnam, M., Cocco, R., issangya, A., Spenik, J.S., Ludlow, J.C., Gopalan, B., Shaffer, F., Syamlal, M., Guenther, C., Karri, S.B.R., Knowlton, T., 2014. Challenge Problem : 1. Model Validation of Circulating Fluidized Beds. *Powder Technol.* 258, 370-391.
- Pita, J.A. and Sundaresan S. 1993. Developing Flow of a Gas-Particle Mixture in a Vertical Riser. *AIChE J.*, 39, 541–552.
- Pope, S.B., 2000. *Turbulent flows*. Cambridge University press, Cambridge.
- Richardson, J.F., Zaki, W.N., 1954. Sedimentation and fluidization: Part 1. *Trans. Inst. Chem. Eng.* 32, 35-53.
- Roy, S., 2000. Quantification of Two-Phase Flow in Liquid-Solid Risers (Ph.D. thesis). Washington University, USA.
- Shah, M.T., Utikar, R.P., Evans, G.M., Tade, M.O., Pareek, V.K., 2011. CFD simulations of gas-solid flows in a CFB riser : Effect of inlet boundary conditions. 19th International Congress on Modelling and Simulation, 12–16.
- Shah, M.T., Utikar, R.P., Evans, M., Tade, M.O., Pareek, V.K., 2012. Effect of Inlet Boundary Conditions on Computational Fluid Dynamics (CFD) Simulations of Gas Solid Flows in Risers. *Ind. Eng. Chem. Res.* 51, 1721–1728.
- Syamlal, M., O'Brien, T. J., 1989. Computer simulation of bubbles in a fluidized bed. *AIChE Symp. Ser.* 85, 22-31.

- Sinclair, J.L., Jackson, R., 1989. Gas-particle flow in a vertical pipe with particle-particle interactions. *AIChE J.* 35, 1473–1486.
- Sundaresan, S., 2003. Instabilities in fluidized beds. *Annu. Rev. Fluid Mech.* 35, 63–88.
- Tartan, M., Gidaspow, D., 2004. Measurement of Granular Temperature and Stresses in Risers 50, 1760–1775.
- Tartan, M., Gidaspow, D., 2004. Measurement of granular temperature and stresses in risers. *AIChE J.* 50, 1760–1775.
- Tennekes, H., Lumley, J.L., 1972. *A First Course in Turbulence*, MIT Press.
- Tsuji, Y., Morikawa, Y., Tanaka, T., Nakatsukas, N., Nakatani, M., 1987. Numerical simulation of gas-solid two-phase flow in a two dimensional horizontal channel. *Int. J. Multiph. Flow* 13, 671–684.
- Tsuo, Y.P. and Gidaspow, D., 1990. Computation of flow patterns in circulating fluidized beds. *AIChE J.* 36, 885–896.
- Upadhyay, M., Park, J.-H., 2015. CFD simulation via conventional Two-Fluid Model of a circulating fluidized bed riser: Influence of models and model parameters on hydrodynamic behavior. *Powder Technol.* 272, 260–268.
- Vaishali, S., Roy, S., 2007. Numerical Simulation of Gas - Solid Dynamics in a Circulating Fluidized-Bed Riser with Geldart Group B Particles. *Ind. Eng. Chem. Res.* 46(25), 8620–8628.
- Vaishali, S., 2009. Gas-Solids flows in downers: hydrodynamics and reactor modelling (PhD Thesis). IIT Delhi, India.
- van der Hoef, M.A., van Sint Annaland, M., Kuipers, J.A.M., 2005. Computational fluid dynamics for dense gas-solid fluidized beds: a multi-scale modelling strategy. *China Particuology* 3, 69–77.
- Wallis, G. G., 1969. *One-Dimensional Two-Phase Flow*. McGraw-Hill, New York.
- Wang, J., Ge, W., Li, J., 2008. Eulerian simulation of heterogeneous gas – solid flows in CFB risers : EMMS-based sub-grid scale model with a revised cluster description 63(6), 1553–1571.

- Wang, X., Jiang, F., Xu, X., Wang, S., Fan, B., Xiao, Y., 2009. The Simulation and Experimental Validation on Gas-Solid Two Phase Flow in the Riser of a Dense Fluidized Bed. *J. Therm. Sci.* 18(2), 137–141.
- Wang, X., Jiang, F., Lei, J., Wang, J., Wang, S., Xu, X., Xiao, Y., 2011. A revised drag force model and the application for the gas e solid flow in the high-density circulating fluidized bed. *Appl. Therm. Eng.* 31, 2254–2261.
- Wen, C.Y., Yu, Y.H., 1966. *Mechanics of fluidization*. The Chemical Engineering Progress Symposium Series 162, 100-111.
- Yang, N., Wang, W., Ge, W., Li, J., 2003. CFD simulation of concurrent-up gas–solid flow in circulating fluidized beds with structure-dependent drag coefficient. *Chem. Eng. J.* 96, 71–80.
- Yang, N., Wang, W., Ge, W., Wang, L., Li, J., 2004. Simulation of Heterogeneous Structure in a Circulating Fluidized-Bed Riser by Combining the Two-Fluid Model with the EMMS Approach. *Ind. Eng. Chem. Res.* 43(18), 5548–5561.
- Zhang, N., Lu, B., Wang, W., Li, J., 2010. 3D CFD simulation of hydrodynamics of a 150 MWe circulating fluidized bed boiler. *Chem. Eng. J.* 162(2), 821–828.
- Zhang, Y., Lei, F., Wang, S., Xu, X., Xiao, Y., 2015. A numerical study of gas–solid flow hydrodynamics in a riser under dense suspension upflow regime. *Powder Technol.* 280, 227–238.

## Chapter 6

### Conclusions and Recommendations

All the previous chapters gave summary and conclusions with respect to the research findings in respective chapters. In this chapter, broader conclusions from this thesis and recommendations are given.

#### 6.1 Conclusions

The overall aim of the current thesis was to understand the flow behavior of gas-solids circulating fluidized bed at two different scales. The work has three different aspects. The first aspect was to implement RPT technique at a relatively high velocity system. To the best of author's knowledge this is the first time RPT is implemented at 10 m/s velocity. A considerable improvement in RPT regarding the way of calibration, data acquisition frequency and post processing was done to implement RPT at high velocity. The second aspect of the work was to implement RPT in a gas-solid circulating fluidized bed to understand the flow dynamics of CFB as a function of operating conditions at two different scales. The final aspects of the current work was to understand the scale-up issues of CFB both by using a newly developed scaling law in current work and through CFD simulations. The specific conclusions of each chapter are individually given at the end of each chapter. This Chapter is intended to summarize the key findings and hopefully evolve some broader conclusions and future directions of research. The broader conclusions of the current thesis are as follows:

- In current work it has been established that RPT technique can be used to investigate the flow dynamics in high velocity system with judicious selection of data acquisition frequency. A complete map of data acquisition frequency vs

accuracy in position reconstruction and velocity measurement is provided in current work.

- There is always a “trade – off” between the position accuracy and velocity accuracy. Stationary bias plays significant role. However the dominating factor at high velocity conditions is dynamic bias. It has been found that 80Hz frequency is sufficient to achieve an accuracy of 4 mm in position reconstruction and 0.4 m/s in velocity measurement.
- Mean velocity of the solids increases with increase in gas inlet velocity and decrease in solid flux. However, axial RMS velocity of the solids increases with decrease in gas inlet velocity or increase in solid flux for both laboratory and pilot plant scale.
- Flow behavior of gas-solid CFB predominantly depends on gas inlet velocity compared to solid flux. Further, it has been established that mean motion of the solids are mainly depends on gas-solids interaction, i.e. drag. However, particle fluctuations are dominant by solid-solid interactions. The critical thing is that even the extent of solid-solid interactions depends on the distribution of solids which is governed by the gas-solids interaction.
- Despite the dilute flow conditions, metastable structures (clusters) are observed in all the conditions. Thus, multi-scale interactions are important characteristics of CFB even for the dilute flow. Cluster characteristics are the function of operating conditions. Solid mixing studies reveal that major contribution of macromixing is mainly due to the solid clusters and solid diffusivity contribution is negligible. Major contribution of the dispersion is bottom region of the riser (entry region).

- Similar characteristics of velocity and RMS have observed in the pilot scale studies too. For the same conditions, pilot plant scale axial solid velocities are higher and fluctuations increased twice. Diffusivity and dispersion is higher in the pilot plant scale for the same operating conditions. With increase in the scale, axial solid velocity and RMS increases for the similar operating conditions. Validation of hydrodynamic similarity law of Qi et al. (2008) reveals that the microstructure similarity fails as the RMS velocity differs and highly depends on the solid-solid interaction.
- Most of the scaling laws available in literature are not able to predict the flow behavior at pilot plant scale. Hence, a new scaling laws is developed to predict the solid velocity with change in scale and operating conditions. It has been found that newly proposed scaling law is able to predict current data and data available in literature within 30% limit.
- Numerical simulation as a scale up tool is promising. However, requirement of suitable closure limits the use of CFD simulations, particularly Euler-Euler simulation. However, with careful validation of each closure Euler – Euler are able to predict the mean velocity of solids with reasonable accuracy. Even the dominant of superficial gas velocity over the solid flux also predicted correctly. However, RMS velocity prediction still requires better closure probably based on variable restitution and specular coefficient or model based on particle collision.

In addition, scarcity of detailed data on solid velocity and fluctuations is partly addressed in this thesis. Overall, solid interactions play a significant role in the fluctuations and mean solid velocity is influenced by the gas velocity. Mixing is

majorly contributed in the bottom section and solids diffusivity are negligible compared with the dispersion.

## 6.2 Recommendations and future directions

Future recommendations are integral part of any research work. As one works on a research topic, on the way to reach their objectives, one always realize the amount of unknowns more than the known. Here given are few set of recommendations.

- One need to be careful with choice of data acquisition frequency in RPT experiments, particularly either for very high velocity system or very low velocity system. Accuracy of measurement for very low velocity systems is limited with resolution and accuracy for high velocity systems is limited with dynamic bias. In case of high velocity system, where relatively high data acquisition frequency is required, one need to think about accuracy in position reconstruction as well as accuracy of velocity measurement.
- It is very difficult to achieve the exact position of the tracer particle with high fidelity every time. Hence there can be some error in position reconstruction at some stances. This small error in position reconstruction will severely affect the accuracy of velocity measurement for very high data acquisition frequency. Hence, data acquisition frequency should be judiciously chosen. As established in current work, there is always an optimal window of data acquisition frequency exist, where both accuracy in position reconstruction and velocity measurement can be optimized. Further, between this windows one should chose that data acquisition frequency which can cover most of the time scale exist in the system of interest for better understanding of flow physics in system of interest.

- Accuracy experiments studied in current work consider only axial direction motion. It can be extended to 3D flow. Applications of the RPT experiments are ever increasing due to its versatility. Thus, generalized accuracy map can be of great help for new users.
- Axial RMS velocity reported in the literature and in current study does give information about the specific systems. However, characteristic of axial RMS velocity profile for different particle properties and column geometry cannot be determined from the current data. RMS velocity profile reported in literature are varied widely. Increasing towards the wall (this work; He et al., 2009; Pantzali et al., 2013), decreasing towards the wall (Bhusparau et al., 2006; Wei et al., 1998), flat along the column and decrease/increase near the wall (Gopalan and Shaffer, 2013; Caloz, 2000). Since RMS quantifies fluctuations due to the particle – particle interactions, metastable structures, gas turbulence on particles, particle – wall collisions. Even the fluctuations due to particle – particle interactions have two competitive mechanisms, due to the mean free path and due to particle – particle collisions, which depends upon the distribution of solids in CFB. A detailed analysis of particle properties and column geometry other than operating conditions are required.
- More studies are required for finding the dominant mechanism in a particular set of conditions. Foremost way is doing the experiments at the column size of more than 200 mm where the wall effects are lower (Knowlton, 2000). Systematic study of decoupling the dominant regions of the particle – particle interactions, gas turbulence and metastable structures is also required. This decoupling will be of great help in development of a better computational model.

- Particle motion should be studied in the bottom and top region of CFB including the cyclone. Even though few studies are available (Chan et al., 2010, Pantzali et al., 2013). More studies are needed for complete characterization.
- Scaling laws should also be developed based on the RMS velocities to account for meso-scale structures for better accuracy in prediction.
- High density CFB (solid flux more than 400 kg/m<sup>2</sup>s) should be investigated and data should be compared with low density CFB to find the difference between both the CFBs. In high density CFB meso-scale meta-stable structures role may be even more dominating. Suitable comparisons can reveal the importance of meso-scale meta-stable structures and probably help in decoupling the effect of these structures with bulk scale phenomena.

## References

- Bhusarapu, S., Al-Dahhan, M.H., Duduković, M.P., 2006. Solids flow mapping in a gas–solid riser: Mean holdup and velocity fields. *Powder Technol.* 163, 98–123.
- Caloz, Y.P., 2000. Experimental investigation of local solids Fluid dynamics in different industrial-scale circulating fluidized beds with optical probes (Ph.D. Thesis). Swiss Federal Institute of Technology, Zurich.
- Gopalan, B., Shaffer, F., 2013. Higher order statistical analysis of Eulerian particle velocity data in CFB risers as measured with high speed particle imaging. *Powder Technol.* 242, 13–26.
- He, Y., Deen, N.G., Annaland, M.V.S., Kuipers, J.A.M., 2009. Gas - Solid Turbulent Flow in a Circulating Fluidized Bed Riser: Experimental and Numerical Study of Monodisperse Particle Systems. *Ind. Eng. Chem. Res.* 2009, 8091–8197.
- Knowlton, T.M., Karri, S.B.R., Issangya, A., 2005. Scale-up of fluidized-bed hydrodynamics. *Powder Technol.* 150, 72–77.

- Pantzali, M.N., Marino, J.M., Marin, G.B., Heynderickx, G.J., 2016. Three-Component Solids Velocity Measurements in the Outlet Section of a Riser. *AiChE J.* 62, 3575–3584
- Qi, X., Zhu, J., Huang, W., 2008. Hydrodynamic similarity in circulating fluidized bed risers 63, *Chem Eng Sci.*, 63, 5613–5625.
- Wei, F., Lin, H., Cheng, Y., Wang, Z., Jin, Y., 1998. Profiles of particle velocity and solids fraction in a high-density riser. *Powder Technol.* 100, 183–189.



## BIO-DATA

### Premkumar K

**Date of Birth** 12.02.1986

**Place of Birth** Ambur, India

**Degrees** B.Tech, Pharmaceutical Engineering and Technology, June 2007.  
School of Engineering and Technology,  
Bharathidasan university, Trichy, India.

M.Tech, Chemical Engineering, June 2012.

A.C.College of Technology,  
Anna University, Chennai, India.

Ph. D, Chemical Engineering (Expected)

Indian Institute of Technology Guwahati, India.

### Publications

#### Journals

Premkumar Kamalanathan, H.J. Pant and Rajesh K. Upadhyay, "Effect of dynamic bias on accuracy of radioactive particle tracking technique at different data acquisition frequencies" Appl. Radiat. Isot., (Submitted).

Premkumar Kamalanathan, Trilokpati Tribedi and Rajesh K. Upadhyay, "Effect of superficial gas velocity on hydrodynamics in Circulating Fluidized Bed (CFB)", Powder Technol., (submitted).

Premkumar Kamalanathan, Trilokpati Tribedi and Rajesh K. Upadhyay, “Effect of solid flux on velocity and their fluctuations in Circulating Fluidized Bed (CFB) using radioactive particle tracking technique:” Powder Technol., (Submitted).

Premkumar Kamalanathan, Trilokpati Tribedi, Hrish J. Pant and Rajesh K. Upadhyay, “Pilot plant scale studies of CFB: Velocity measurement and scale-up.” (Under preparation).

Premkumar Kamalanathan, Trilokpati Tribedi, Hrish J. Pant and Rajesh K. Upadhyay, “Comparison of variation in residence time distribution and axial dispersion coefficient at laboratory and pilot plant scale CFB.” (Under preparation).

Premkumar Kamalanathan and Rajesh K. Upadhyay, “Scale-up of circulating fluidized bed system through CFD simulation: A strategy with experimental validation.” (Under preparation).

### **International Conferences**

Premkumar Kamalanathan, H.J.Pant, Rajesh K. Upadhyay, “DDPM and Euler-Euler simulations of circulating fluidized bed and experimental validation through radiotracer techniques”, **ISCRE 23**, Bangkok, Thailand, Sep 2014.

Premkumar Kamalanathan and Rajesh K. Upadhyay, “Numerical and experimental investigation of circulating fluidized bed (CFB) at high solid fluxes”, **Camure 9**, Lyon, France, December 2014.

Premkumar Kamalanathan, Trilokpati Tribedi and Rajesh K. Upadhyay, “Experimental study of Circulating Fluidized Bed (CFB) using radioactive particle tracking technique”, **GLS 12**, Newyork, USA, July 2015.

Premkumar Kamalanathan, Trilokpati Tribedi and Rajesh K. Upadhyay, “Investigation of circulating fluidized bed using radioactive particle tracking and Euler - Euler simulations”, **3<sup>rd</sup> INDO GERMAN Workshop**, Guwahati, India, February 2016.

### **National Conferences**

Premkumar Kamalanathan and Rajesh K. Upadhyay, “Comparative studies of conventional and EMMS based drag closures for prediction of meso- scale structures in circulating fluidized bed”, CHEMCON, December 2013.

Rajani Kant Boro, Premkumar Kamalanathan and Rajesh K. Upadhyay, “Experimental verification of EMMS drag model for heterogenous gas – solid flows in a CFB riser with gamma densitometry”, CHEMCON, December 2014.

Premkumar Kamalanathan, Trilokpati Tribedi and Rajesh K. Upadhyay, “Dense discrete phase model (DDPM) simulations of circulating fluidized bed riser”, CHEMCON, December 2015.

Trilokpati Tribedi, Premkumar Kamalanathan and Rajesh K. Upadhyay, “Simulation of gas -solids circulating fluidized bed riser using EMMS drag model”, CHEMCON, December 2015.